

AN EXPERIMENTAL STUDY OF THE ELECTRIC FIELD DRIFT OF
POSITRONS IN SOLID MEDIA AND ITS APPLICATION TO THE

DEVELOPMENT OF FIELD ASSISTED MODERATION OF FAST POSITRONS
MODERATORS

A thesis submitted to the University of London
for the degree of Doctor of Philosophy

Richard Iain Simpson
Department of Physics and Astronomy
University College London

March 1990

ProQuest Number: 10797782

All rights reserved

INFORMATION TO ALL USERS

The quality of this reproduction is dependent upon the quality of the copy submitted.

In the unlikely event that the author did not send a complete manuscript and there are missing pages, these will be noted. Also, if material had to be removed, a note will indicate the deletion.



ProQuest 10797782

Published by ProQuest LLC (2018). Copyright of the Dissertation is held by the Author.

All rights reserved.

This work is protected against unauthorized copying under Title 17, United States Code
Microform Edition © ProQuest LLC.

ProQuest LLC.
789 East Eisenhower Parkway
P.O. Box 1346
Ann Arbor, MI 48106 – 1346

ABSTRACT

The primary aim of this work was to investigate the possibility of developing more intense laboratory-based slow positron (e^+) beams. Conventionally, these are formed by moderating β^+ particles *in vacuo* using metal foils and meshes. e^+ thermalise in the metal bulk and a fraction subsequently diffuse to a surface where they are re-emitted with eV energies.

It is proposed that a new type of moderator could be developed based on the electric field drift of e^+ in semiconductors or insulators. A solution to the diffusion equation is derived, which includes terms describing positron implantation, drift and annihilation. Using published mobility data for Si, the expression is used to estimate the fraction of e^+ drifted to a surface or interface. For a 50 μm Si crystal cooled to 80K, efficiencies of up to 10% are predicted. It is suggested that the trapping of e^+ in defects in the thin contact required to generate the electric field can be reduced by using an epitaxially grown NiSi_2 layer on a Si(111) substrate.

A new method of measuring positron mobility, μ_+ , using a modified e^+ lifetime spectrometer was developed. Changes in the lifetime spectra are related to the electric field drift of e^+ from the Si bulk into an annihilation state associated with the Au contact or Au-Si interface. Values of μ_+ calculated from the data are in good agreement with other published measurements.

The re-emission of e^+ from clean and oxygen exposed Si(111) and Si(100) surfaces bombarded with β^+ particles was measured in ultra high vacuum. The data suggest that the Si(111) and Si(100) samples studied have positive positron work functions and the small yield of slow e^+ measured is attributed to the escape of non-thermal e^+ from the surface. Measurements of positron yield versus oxygen exposure are consistent with a changing surface dipole arising from oxygen adsorption.

It is concluded that Si is not suitable as a positron moderator and that other materials need to be evaluated to establish whether a practical field assisted moderator can be developed.

TABLE OF CONTENTS

	Page
ABSTRACT	2
TABLE OF CONTENTS	3
LIST OF FIGURES	7
LIST OF TABLES	14
ACKNOWLEDGEMENTS	15
CHAPTER 1 Introduction	
1.1 Introduction	17
1.2 Basic Positron Properties	22
1.3 Positron Dynamics In Solid Media	27
1.3.1 Introduction	27
1.3.2 Interaction Of Incident e^+ with Surfaces	28
1.3.3 Thermalisation	32
1.3.4 Ps Formation in Insulators	40
1.3.5 Diffusion	42
1.3.6 Bulk Defect Trapping	44
1.3.7 Positron-Surface Processes	49
a) Prompt emission of slow e^+	51
b) Re-emission of non-thermal e^+	52
c) Positronium emission	57
d) Surface state trapping	61
e) Positrons at interfaces	62

	1.4 Experimental Techniques	64
	1.4.1 Angular Correlation	64
	1.4.2 Doppler Measurements	67
	1.4.3 Positron Lifetime Spectroscopy	68
	1.4.4 Positron Beams	71
	a) Sources for slow positron beams	73
	b) Positron moderators	76
	c) Beam transport	78
	d) The interaction chamber	80
	1.5 Scope Of The Current Work	80
CHAPTER	2 Positron Motion In An Externally Applied Electric Field	
	2.1 Introduction	83
	2.2 The Effect Of An Electric Field On Positron Implantation	84
	2.3 Equilibrium Positron Motion - Positron Mobility	87
	2.4 Experimental Measurements Of Positron Mobility	92
	2.5 Measurement Of Positron Mobility By A Lifetime Method - Theory	111
CHAPTER	3 Measurement Of Positron Mobility In Silicon By A Lifetime Method	
	3.1 Introduction to Positron Lifetime Method	117
	3.2 Design Characteristics	121
	3.2.1 Design and Optimisation of the Spectrometer	121
	3.2.2 Additional Electronics	126
	3.2.3 Source	127
	3.3 Data Analysis	130

	3.3.1 Resolution	130
	3.3.2 Centroid Shifts	145
	3.4 Experimental Procedure	147
	3.5 Results	154
	3.5.1 RESOLUTION	154
	3.5.2 Centroid Shifts	159
	3.6 Discussion	162
	3.7 Conclusion	165
CHAPTER	4 Field Assisted Moderators	
	4.1 Introduction	167
	4.1.1 Conventional Positron Moderators	167
	4.1.2 Field Assisted Moderators	175
	4.2 Solution Of The Diffusion Equation	179
	4.3 Requirements Of A Field Assisted Moderator	185
	4.4 Silicon Field Assisted Moderators	186
	4.5 Other Possibilities	192
	4.5.1 Polar Insulators	192
	4.5.2 Rare Gas Solids	193
	4.6 Conclusion	200
CHAPTER	5 A Study Of Slow Positron Re-Emission From Surfaces in Ultra High Vacuum	
	5.1 Introduction	203
	5.1.1 Metallic Surfaces	203
	5.1.2 Insulating and Semiconducting Surfaces	213
	5.2 Silicon Surface Structure	217

5.3	Experimental Details	225
5.4	Sample Preparation	230
5.4.1	Nickel	232
5.4.2	Silicon	233
5.5	Results	234
5.5.1	Nickel	234
5.5.2	Silicon	245
a)	Results	245
b)	Discussion	249
5.6	Conclusion	253
CHAPTER 6	Conclusion	255
APPENDIX 1	Application Of The Diffusion Equation To Mono-Energetic Positron Implantation Into Single Crystal Foils	261
REFERENCES		268

LIST OF FIGURES

	Page
1.1 Interaction of a keV energy e^+ beam with a solid surface and the underlying bulk	23
1.2 Feynman diagram representation of electron-positron annihilation into a) one, b) two and c) three photons	24
1.3 Variation of back-scatter coefficient, B , with atomic number, Z . (MacKenzie <i>et al</i> 1983)	29
1.4 Variation of e^+ back-scattering coefficient, B , with e^+ implantation energy into Al	31
1.5 Rate of energy-loss, $\left(\frac{dE}{dt}\right)$, versus energy, E , for e^+ thermalisation in Al for several lattice temperatures, T (Nieminen and Oliva 1980)	33
1.6 e^+ thermalisation time in Al versus lattice temperature (K). (Nieminen and Oliva 1980)	35
1.7 Distribution of trajectory endpoints projected onto the y-z plane, for 2keV positrons implanted into Al. (Valkealahti and Nieminen 1983)	35
1.8 Angular scan of 50keV e^+ transmission through a thin Si(100) crystal. (Logan <i>et al</i> 1988)	39
1.9 Shift, ΔS , in lineshape parameter, S , as a function of incident e^+ energy for 30, 90 and 180keV energies (Lynn <i>et al</i> 1985)	47
1.10 Re-emitted e^+ energy spectra from insulating surfaces	53
a) Ionic insulators (Mills and Crane 1984)	
b) Rare gas solids (Gullikson and Mills 1986)	

1.11	Positron re-emitted yield, R , and Ps field, f , versus e^+ implantation energy for a 15 000Å solid Ar film. (Gullikson and Mills 1986)	54
1.12	Studies of epithermal e^+ re-emission. (Nielsen <i>et al</i> (1986)	56
1.13	Time of flight spectra for triplet Ps annihilation at distances, a) $z=10\text{mm}$ and b) $z=50\text{mm}$ in front of the Cu target. (Mills and Pfeiffer 1979)	58
1.14	Normal component of kinetic energy of Ps emitted from clean and oxidised Al(111) surfaces	60
1.15	2D ACAR contour plots for an Al(110) surface	62
1.16	Variation of lineshape parameter, S , with e^+ implantation energy for a thermally grown SiO_2 layer on Si. (Nielsen <i>et al</i> 1987)	63
1.17	ACAR measurements	66
	a) Schematic diagram of a one dimensional (1D) ACAR arrangement	
	b) Typical momentum distribution for a metallic sample showing parabolic and pedestal regions due to e^+ annihilation with free and core electrons respectively.	
1.18	Mean positron lifetimes in metals (MacKenzie 1983)	70
1.19	Schematic diagram of bunched e^+ beam used for near-surface e^+ lifetime studies (Schödlbauer <i>et al</i> 1987)	72
1.20	Source-moderator geometries	77
2.1	Effect of an applied electric field on e^+ implantation profile in polyethylene. (Heinrich 1978)	85
2.2	Fractional variation of Ps fraction, f , in polyethylene with applied electric field. (Bisi <i>et al</i> 1981)	87
2.3	Effect of an applied electric field on thermal e^+ motion	88
2.4	Change in positron drift velocity, v_+ , as a function of bias, V_1-V_2 , applied to an Si(Li) detector sample. (Mills and Pfeiffer 1977)	96

2.5	Measurement of positron drift velocity, v_+ , in polyethylene as a function of the internal electric field. (Mills <i>et al</i> 1986)	98
2.6	Electric field effects in paraffin wax. (Stone <i>et al</i> 1989)	103
2.7	Experimental arrangement for measuring e^+ implantation profiles in solids. (Brandt and Paulin 1977)	104
2.8	Relative shift in e^+ annihilation profile and corresponding drift velocity as a function of applied electric field. (Brandt and Paulin 1977)	105
2.9	A variable energy study of e^+ electric field drift in Si. (Corbel <i>et al</i> 1989)	108
2.10	Measurement of the electric field drift of e^+ in a solid by a lifetime method	113
3.1	Leading edge discriminator walk effects as a function of pulse amplitude	119
3.2	Constant fraction pulse shaping	120
3.3	Schematic diagram of the lifetime spectrometer used for mobility measurements	122
3.4	Compton profiles measured using plastic scintillator/photo-multiplier arrangement	124
3.5	Positron lifetime spectra	125
3.6	Time to amplitude convertor calibration spectrum	126
3.7	Variation of signal to noise ratio, R and fractional error, Δ , with source strength, s	129
3.8	Effect of the number of gaussians on fitted parameters	136
3.9	Effect of start channel on one, two and three gaussian fits to a three component generated spectrum	137
3.10	Variation of fitted parameters with total counts in spectrum. Three lifetime components	139

3.11	Variation of fitted parameters with total counts in spectrum. Four lifetime components.	140
3.12	Variation of fitted parameters with background for a three component spectrum	141
3.13	Variation of fitted parameters with FWHM of the resolution function for a three component spectrum	143
3.14	Variation of fitted parameters with FWHM of the resolution function for a four component spectrum	144
3.15	Sample mounts and Au contact tracks	148
3.16	Current-voltage characteristics for an Au-Si-Al sample used for e^+ mobility measurements in Si	149
3.17	Variation of the electric field with position for a reverse biased Au-nSi-Al sample	150
3.18	Variation of electric field, ξ , at the Si-Au interface with applied bias for the $10k\Omega\text{cm}$ n-type samples used in the present study. A bias of 286V is required to deplete the sample fully	151
3.19	Sample/source arrangement used for e^+ measurements	152
3.20	Cryostat used for low temperature measurements	153
3.21	Determination of the Si-Au interfacial lifetime component, τ_4	156
3.22	Variation in intensity of the Si-Au interfacial lifetime component with applied voltage	158
3.23	Stability of centroid measurements	160
3.24	Positron drift velocity in Si versus applied electric field, ξ , calculated from centroid data	161
3.25	Variation of χ^2 with μ_+ for linear and Shockley expression fits to the low temperature Si data	162
3.26	Experimental measurements of positron mobility, μ_+ , in Si at a temperature, T	164

4.1	Re-emitted positron energy spectra for a tantalum-mica-gold moderator. (Costello <i>et al</i> 1972)	169
4.2	Re-emitted positron energy spectra for 1000Å W(100) foils (Jacobsen <i>et al</i> 1990 and Chen <i>et al</i> 1987)	172
4.3	Schematic diagram of a field assisted positron moderator	177
4.4	Energy levels for a Si-NiSi ₂ field assisted moderator	178
4.5	Variation of e ⁺ probability density, $n(x,t)$ with time following implantation of a δ function profile at $t=0$	180
4.6	Transmitted slow positron yield versus Si film thickness for e ⁺ drift velocities of 5×10^4 and $1 \times 10^5 \text{ms}^{-1}$	187
4.7	Transmitted slow positron yield with applied electric field for a 50 μm Si film	189
4.8	Avalanche photodiode structures	189
4.9	Transmission electron micrograph of an 18Å NiSi ₂ layer on Si(111). (Van Loenen <i>et al</i> 1985)	191
4.10	Re-emitted energy distribution, $R(E)$, for e ⁺ from Ar for several different initial energy distributions, $P(E,0)$. Data obtained from Monte Carlo simulations	196
4.11	Re-emitted energy distribution, $R(E)$, for e ⁺ implanted into Ar with energies of .5, 2, 5keV and β^+ energies. Data obtained from Monte Carlo simulations	197
4.12	Re-emitted energy distribution, $R(E)$ for e ⁺ from Ar stressed by electric fields of 0, 1×10^6 , 5×10^6 and $1 \times 10^7 \text{Vm}^{-1}$	199
4.13	Re-emitted slow positron yield versus applied electric field. Data obtained from Monte Carlo simulations	200
4.14	Variation of Ps fraction in Ar with applied electric field	201
5.1	Electron and positron energy levels near to a metallic surface	205
5.2	Retarding potential curves of e ⁺ re-emission from clean Al(100), Cr and Si(100) surfaces. (Mills <i>et al</i> 1978)	206

5.3	Studies of e^+ re-emission from Ni(100) surfaces (Fischer <i>et al</i> 1986)	208
5.4	The variation of slow e^+ yield with work function, ϕ_+ , for K exposed Cu(111) and Ni(100) surfaces. (Gullikson <i>et al</i> 1988)	210
5.5	Positron re-emission from a clean 250Å CoSi ₂ layer on Si(111) (Gullikson <i>et al</i> 1987)	212
5.6	Difference between angular distributions of annihilation γ -rays, $\Delta f(\theta) = f_2(\theta) - f_1(\theta)$ for n- and p-type doped Si(100). (Gol'danski <i>et al</i> 1988)	215
5.7	a) Surface energy levels, work function, ϕ_- , and photoelectric threshold, ϕ_{PE} for an "ideal" Si surface without surface states b) Variation of ϕ_- and ϕ_{PE} predicted by the "ideal" model	219
5.8	Measurements of work function, ϕ_- , and photoelectric threshold, ϕ_{PE} versus bulk doping (Allen and Gobeli 1962)	221
5.9	Electron energy levels in Si	222
5.10	Electron distribution curves obtained from an ultraviolet photoelectron spectroscopic (UPS) study of a degenerate n^{++} Si(111) surface. (Wagner and Spicer 1974)	224
5.11	a) Position of the Fermi level relative to the valence band maximum for p^{++} , n^- and n^{++} doped samples as a function of oxygen exposure b) Electron affinity, χ , versus oxygen exposure (Wagner and Spicer 1974)	224
5.12	Schematic diagram of the experimental arrangement used to study e^+ re-emission from Ni, Si(111) and Si(100) surfaces	226
5.13	Slow positron count rate, R , versus sample potential for coil currents of 0.2 to 1.0A	235

5.14	Variation of slow positron yield with source potential for a 15000Å Ni(100) layer grown epitaxially on a NaCl substrate	236
5.15	Slow positron yield and slow to fast e ⁺ ratio versus CEM cone potential	237
5.16	a) Annealing cycle used for a polycrystalline Ni sample heated to 720K b) Slow positron yield from a polycrystalline Ni sample versus annealing time at 720K	238
5.17	a) Retarding potential spectrum for a polycrystalline Ni sample annealed at 720K for 15minutes b) Re-emitted e ⁺ energy spectrum obtained by differentiation of the data in Figure 5.17a)	242
5.18	Slow positron yield versus annealing time for a sputtered polycrystalline Ni sample	244
5.19	Slow positron yield versus oxygen exposure for a 10kΩcm p-type Si(111) sample	247
5.20	Slow positron yield versus oxygen exposure for a 4-6Ωcm Si(100) sample. The carrier type is unknown	248
5.21	Energy distribution of epithermal e ⁺ in Si	252
A1.1	Calculated slow e ⁺ yields and fast e ⁺ transmission probabilities for Cu foils	263
A1.2	Calculated slow e ⁺ yields and fast e ⁺ transmission probabilities for W foils	264
A1.3	Comparison of theoretical and experimental e ⁺ moderation efficiencies for a 1500Å Ni(100) foil	265
A1.4	Brightness gain, G, and optimum primary beam energy as functions of foil thickness for Ni(100)	266

LIST OF TABLES

	Page
1.1 Positron Surface Probes	21
1.2 Chronology of Positron Surface Science	50
1.3 Properties of Some e^+ Emitting Sources	74
2.1 Charge Carrier Properties in Silicon	91
2.2 Measurements of Positron Mobility	101
3.1 Generated Positron Lifetime Spectra	134
4.1 Positron Moderator Efficiencies	176
5.1 Positron Surface Properties	241
A1.1 Parameters Used In Transmission Moderator Efficiency Calculations	265

ACKNOWLEDGEMENTS

I wish to thank everyone who has contributed in any way to the present work. I am especially grateful to the following:

Dr. C.D. Beling, Dr. M. Charlton, Dr. S.A. Davies, Professor T.C. Griffith, Dr. F.M. Jacobsen, G.O. Jones, Dr. G. Laricchia, Professor M.G. Stewart, Professor Y.Y. Wang, N.Zafar and the staff of the Physics and Astronomy Department, UCL, for their continual encouragement, discussion and assistance;

B. Humm, A.G. Walker, I. Rangué, E. Oldfield and the staff of the Physics and Astronomy Department main workshop for invaluable technical assistance;

The SERC for financial assistance.

Special thanks are due to Mike and Sally for their comments, criticism and corrections to the typescript and to Thorn EMI Central Research Laboratories for the use of word processing facilities.

To Sally, my family
and friends

CHAPTER 1

INTRODUCTION

1.1 INTRODUCTION

The existence of antimatter was first predicted by Dirac (1930a), who considered the consequences of negative solutions of the relativistic expression

$$E^2 = m_0^2 c^4 + p^2 c^2 \quad 1:1$$

developed by Einstein to describe the variation of a particle's energy, E , with rest mass, m_0 , and momentum, p . c is the velocity of light *in vacuo*. These solutions were generally rejected as being unphysical. However, in the case of electrons, Dirac offered a physical interpretation. In his model, energy levels below $-m_0 c^2$ are occupied by an infinite sea of electrons. With these states completely filled, the Pauli principle excludes the transition of "normal" electrons with positive energy into these states. However, if energy greater than $2m_0 c^2$ is supplied to an electron in a negative state, it can be promoted to positive energy, leaving behind a hole with positive mass and charge. This process is the now familiar "pair production". Dirac was unwilling to propose the existence of a new particle, so he associated the holes with protons, believing that the difference in mass between protons and electrons was a consequence of the Coulomb force between electrons in the sea. However, Weyl (1931) showed that the hole had to correspond to a particle with the same mass as the electron. This new particle was termed the positron, e^+ , in recognition of its antielectron-like nature. Experimental observation of the e^+ was subsequently reported by Anderson (1932) and Blackett and Occhialini (1933) in photographs of cosmic ray tracks.

In the sixty years following the predictions of Dirac, positron physics has been a rapidly developing field of research. Much of the early interest in e^+ studies can be attributed to

the e^+ being the first form of antimatter to be observed experimentally. However, the subsequent discovery of many more exotic antiparticles has diminished this role and most present day studies are concerned with the use of positrons as a sensitive probe of atomic and solid state structure. In many cases positron investigations have been used to augment existing techniques: one obvious example being atomic scattering. At first thought, e^+ -atom scattering might appear to be very similar to e^- -atom scattering, apart from a difference in sign of the charge of the incident particle. However, the consequences of this sign change are of great significance. Positrons are distinguishable from the target atom electrons and are therefore not subject to the complications of exchange effects. On the other hand, e^+e^- correlations arise, including the creation of e^+e^- bound states - positronium formation. Frequently these correlations are more important than electron exchange so e^+ -atom scattering can provide a more demanding test of theory than its electron analogue. A further advantage of e^+ -atom studies results from the partial cancellation of the static and polarisation potentials which comprise the overall interaction. This reduces the total cross section for the e^+ process and makes its measurement much more sensitive to uncertainties in the calculated values of the polarisation potential. Further discussion of atomic scattering is beyond the scope of this work; extensive reviews of this area have been published by Charlton (1985), Griffith (1986) and Humberston (1979).

Following the theoretical prediction of positronium (Ps) by Mohorovicic (1934), and the first experimental observation by Deutsch (1951), in one of the earliest applications of positron lifetime spectroscopy (PLS), Ps has been the subject of many theoretical and experimental investigations. It is one of the simplest purely leptonic electromagnetically bound state and thus lends itself well to the study of bound state applications of quantum electrodynamics (QED). Measurements of Ps energy levels and annihilation rates provide stringent tests of QED theory. It is not possible to discuss this important field in detail here, apart from mentioning that a recent measurement of the ortho-positronium

annihilation rate by Westbrook *et al* (1987) is some ten standard deviations above the best present theoretical prediction. Further work, both experimentally and theoretically, will be necessary to resolve this discrepancy. Experimental and theoretical studies of Ps have been extensively reviewed by Berko and Pendleton (1980) and DeBenedetti and Corben (1954).

In solid state physics, positron studies have made many notable contributions. Specific examples include the mapping of Fermi surfaces in metals and alloys by the observation of annihilation gamma rays, and the study of defects using both beam and lifetime techniques. The present work is largely concerned with the interaction of positrons with solid media and some of these techniques will be discussed below in more detail. Reviews of solid state positron physics have been presented by Brandt and Dupasquier (1983), Hautojärvi, ed., (1979), Dupasquier and Zecca (1985) and Schultz and Lynn (1988).

Recently, the advent of well defined intense positron beams has opened up the field of positron surface physics. Low energy positron diffraction (LEPD) has been demonstrated (Lynn and Dickman 1978, Mills and Platzman, 1980 and Rosenberg *et al*, 1980) and can be considered as complementary or possibly as an alternative to low energy electron diffraction (LEED). LEPD and LEED both rely on coherent scattering to probe the structure of the diffracting lattice, but LEPD data are easier to interpret because of the absence of exchange. Also, differences in scattering cross sections make LEPD more surface local, avoiding the need for pseudo-potentials to describe the long range interactions arising from the atomic planes beneath the surface layer. However these advantages must be offset against the inferior intensity and resolution of current positron beams. Observations of low energy positronium diffraction (LEPsD) from LiF surfaces have been reported by Weber *et al* (1989). LEPsD has some significant advantages over other types of diffraction, including LEED and LEPD. The high break up probability of Ps in solids ensures that the technique is highly surface sensitive, unlike LEED. The

principal advantage of LEPsD over conventional neutral atom scattering is in the projectile energy, E_i , required to give a de Broglie wavelength, λ_{dB} , approximately equal to one atomic spacing in the diffracting lattice (typically several Å). For He atoms $E_i \approx .1\text{eV}$ for $\lambda_{dB} = 1\text{Å}$. Consequently these atoms are turned back far enough from the surface to be predominantly scattered by the average surface potential. For Ps with $\lambda_{dB} = 1\text{Å}$, $E_i \approx 100\text{eV}$ and Ps atoms approach close enough to the surface to interact with the ion core potential of the individual surface atoms. Consequently LEPsD gives more localised information about the surface. Unfortunately Ps beams of good resolution and intensity are difficult to produce, although progress is being made in this area (Laricchia *et al* 1987 and Weber *et al* 1989). Table 1.1 lists the important surface sensitive positron techniques together with their electron analogues, where applicable.

A significant new area of positron related research is the production of antihydrogen ($\bar{\text{H}}$) by the interaction of antiprotons with positrons or positronium. Measurement of the properties of $\bar{\text{H}}$ including electronic energy levels, fine structure, Lamb shift and hyperfine structure are considered important tests of CPT invariance, which is one of the fundamental laws of particle physics. The motion of antimatter in gravitational fields has also generated considerable interest. Several collaborations (Poth 1987, Rich *et al* 1987 and references therein, and Deutch *et al* 1988) are currently pursuing research programmes with the intention of producing $\bar{\text{H}}$ atoms within the next few years.

This section has demonstrated some areas of research where positron studies are making significant contributions. In many cases further progress is hindered by the resolution, and intensity available with current beam technology. Possible progress in this area is discussed in Chapter 4. The remainder of this chapter is an introduction to basic positron properties and current experimental techniques. Emphasis is placed upon solid state positron physics, as this is most relevant to the present work.

TABLE 1.1
Positron Surface Probes

Method	Surface Property Probed	e ⁻ Analogue	Advantages of e ⁺ Technique
Low energy positron diffraction (LEPD) ^{a), b), c)}	Surface structure	Low energy electron diffraction (LEED)	Simpler theoretical calculations
Re-emitted Positron energy- loss spectroscopy (REPELS) ^{d)}	primarily adsorbed surface atoms/ molecules	Electron energy- loss spectroscopy (EELS)	Possibility of superior intensity and resolution at low energies. Possibility of spin polarised studies of paramagnetic molecules
Positronium diffraction (LEPsD) ^{e)}	Surface structure, adsorbates	none	-
Positron Auger electron spectroscopy (PAES) ^{f)}	Surface chemical composition	Auger electron spectroscopy	Reduction in secondary electron background
Positron microscopy ^{g), h), i), j)}	Surface structure, defects	Electron microscopy	Possible improvements in resolution
Surface angular correlation (ACAR) ^{k), l)}	electron surface state momentum	no direct equivalent	-
Surface lifetime spectroscopy ^{m)}	Surface defects, electronic states	none	-
Spin polarised positron studies ⁿ⁾	Surface magnetism	none	-

References

- a) Lynn, and Dickman, (1978)
- b) Mills and Platzman, (1980)
- c) Rosenberg, Weiss and Canter, (1980)
- d) Fischer, Lynn and Gidley, (1986)
- e) Weber, Tang, Berko, Brown, Canter, Lynn, Roellig and Viescas (1989)
- f) Weiss, Mayer, Jibaly, Lei, Mehl and Lynn (1989)
- g) Hulett, Dale and Pendyala (1984)
- h) Brandes, Canter, Horsky and Mills (1988b)
- i) Rich and Van House (1988)
- j) Brandes, Canter, Horsky, Lippel and Mills (1988a)
- k) Lynn, Mills, West, Berko, Canter and Roellig (1985)
- l) Howell, Mayer, Rosenberg and Fluss (1985b)
- m) Schödlbauer, Kögel, Sperr and Triftshäuser (1987)
- n) Gidley, Köymen, and Capehart (1982)

1.2 BASIC POSITRON PROPERTIES

Most of this discussion will be concerned with the interaction and annihilation of positrons in solid media. Interactions in gases are in many ways similar, although in the latter case electron densities are much lower and positron lifetimes consequently longer. Also the probability of Ps formation is higher in gaseous media and is indeed excluded from metallic and semiconducting substances.

When energetic positrons are implanted into solid media, they undergo a variety of rapid energy-loss processes until they reach near thermal equilibrium. Their subsequent motion is determined by the properties of the surrounding medium and the existence of any externally applied fields (see Chapter 2). A summary of the nature and timescale of common e^+ processes occurring in a solid is shown schematically in Figure 1.1.

Annihilation is of great significance since, not only does it mark the destruction of the e^+ , the γ -ray signature also holds information on the final state of the annihilating pair. By considering conservation of charge parity, Yang (1950) showed that the selection rule for e^+ annihilation into n photons is

$$(-1)^n = (-1)^{L+S} \quad 1:2$$

where L and S are respectively the total orbital angular momentum and spin of the e^+e^- pair. Figure 1.2 shows the Feynman diagram representation of e^+e^- annihilation into 1, 2 and 3 gamma rays. In this scheme the annihilation rate is proportional to α^n where α is the fine structure constant given by

$$\alpha = \frac{e^2}{4\pi\epsilon_0\hbar c} \approx \frac{1}{137} \quad 1:3$$

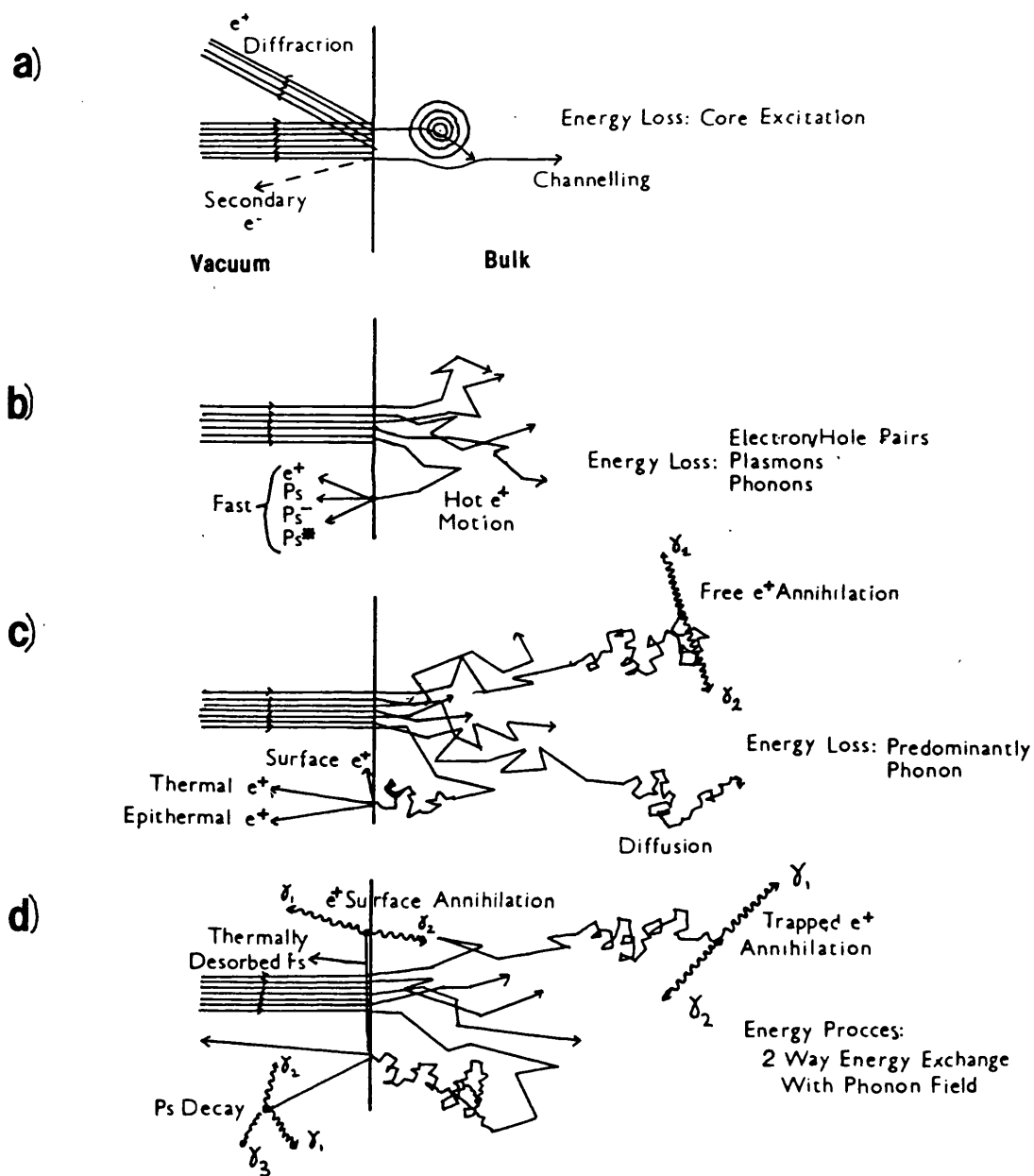


Figure 1.1 Interaction of a keV energy e^+ beam with a solid surface and the underlying bulk.

- a) First encounter ($0 \leq t \leq 10^{-15}$ s)
- b) Thermalisation ($0 \leq t \leq 10^{-12}$ s)
- c) Thermal e^+ processes ($0 \leq t \leq 10^{-10}$ s)
- d) Long lived processes ($0 \leq t \leq 10^{-7}$ s)

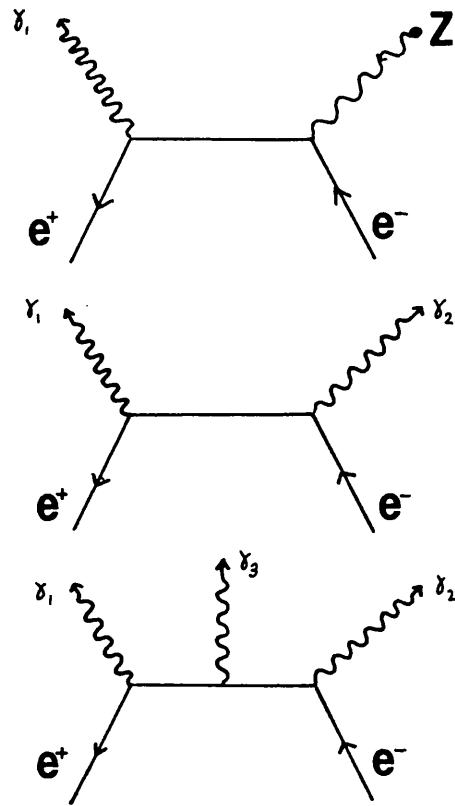


Figure 1.2 Feynman diagram representation of electron-positron annihilation into a) one, b) two and c) three photons.

Here, e , ϵ_0 , \hbar and p are respectively the electronic charge, permittivity of free space, Planck's constant and the number of photon emission/absorption vertices. The above expression would suggest that the ratio of 1:2:3 γ processes is $\alpha^3:\alpha^2:\alpha^3$. However, for the one photon process, the presence of a third body is required to achieve momentum and energy conservation, which results in an additional factor of α^3 . Consequently 2 and 3 gamma modes are most common, with decays into more than 3 quanta increasingly improbable because of an additional α factor for each extra photon. Detailed calculations performed by Ore and Powell (1949) give the 2:3 γ ratio as 1:370 so the latter process can generally be neglected.

For positronium, Yang's selection rule must be applied to determine the correct γ decay mode. As mentioned above, Ps is the e^+e^- bound state. Its gross structure is similar to that of the hydrogen atom, although there is a reduction in binding energy (6.8eV compared with 13.6eV for H) and a doubling of the Bohr radius, a_0 , as a result of the reduced mass of the Ps atom. Ground state ($L=0$) Ps may occur in one of two states, which reflect the relative orientation of the positron and electron spins. For para-positronium (p-Ps) these spins are antiparallel giving a total angular momentum, $J=L+S=0$, whereas for ortho-positronium (o-Ps) the spins are parallel and $J=1$. Consequently, o-Ps is a triplet state with three substates corresponding to $m_s=1, 0, -1$ and p-Ps a singlet state with $m_s=0$. In the absence of a magnetic field the ratio of triplet to singlet states is therefore 3:1. According to Equation 1:2, o-Ps decays into three γ -rays, the two γ mode being forbidden and p-Ps decays into two but not three γ -rays.

The 2γ annihilation rate Γ of a positron with probability density, $\rho_+(r_+)$, at position, r_+ , in a medium with a local electron density, $\rho_-(r_-)$, at position, (r_-) , is given by (Dirac 1930b)

$$\begin{aligned}\Gamma &= \pi r_0^2 c \int d^3r_- d^3r_+ \rho_+(r_+) \rho_-(r_-) \delta(r_- - r_+) \\ &= \pi r_0^2 \hat{\rho}_-\end{aligned}\tag{1:4}$$

where

$$\hat{\rho}_- = \int d^3r_+ \rho_+(r_+) \rho_-(r_+)$$

and r_0 is the classical electron radius given by

$$r_0 = \frac{e^2}{4\pi\epsilon_0 m_0 c^2}\tag{1:5}$$

Hence the annihilation rate is a measure of the local electron density $\hat{\rho}_-$ sampled by the positron. This expression is not strictly valid since it fails to allow for the enhancement of $\rho_-(r_-)$ through the Coulomb interaction. The correlation between $\rho_+(r_+)$ and $\rho_-(r_-)$ is in

fact a major problem in determining the properties of condensed matter from e^+ studies. In metals e^+ correlation with the conduction electrons can be treated in a simplified fashion using a free electron gas model and considering a dimensionless quantity, r_s , the one electron radius (in units of a_0), such that

$$\frac{4}{3}\pi r_s^3 a_0^3 \rho_- = 1 \quad 1:6$$

Using this approach Brandt and Rheinheimer (1970,1971) calculated the enhancement factor $h(\rho_-)$, which relates the true steady state density ρ_- to the correlated density $\hat{\rho}$, to be

$$h(\rho_-) = \frac{\hat{\rho}}{\rho_-} = 1 + \frac{r_s^3 + 10}{6} \quad 1:7$$

and consequently the mean positron lifetime in the metal, τ , is given by

$$\tau = \Gamma^{-1} \approx \frac{r_s^3}{2(16 + r_s^3)} \quad (\text{ns}) \quad 1:8$$

For Al, $r_s \approx 2.1$, $h(\rho_-) \approx 5$ and $\tau \approx 180\text{ps}$ which is in agreement with experiment. In the low electron density limit where $r_s \gg 1$, $\tau \rightarrow 500\text{ps}$, which is the spin average positronium lifetime. In insulators, where electron densities are low, 3γ annihilations are indeed observed. However, in most cases, the radius of the positronium atom is larger than the lattice constant of the host medium, so the Ps atom is significantly perturbed and pick-off processes with surrounding electrons become highly probable. Although there are strong similarities between e^+e^- pairs in solids and "real" positronium in vacuum, there are also significant differences in annihilation rate, for example, so Ps in solids is often referred to as q-Ps or quasi-positronium. In alkali halides q-Ps lifetimes are $\approx 600\text{ps}$, whereas in polymers, lifetimes of the ortho-positronium state of up to 5ns have been reported. This

area has been reviewed in some detail by Dupasquier (1983). Ps formation during e^+ thermalisation is discussed briefly in Section 1.3.4 and the variation in Ps formation probability in electric fields is considered in Chapter 2.

Although positron lifetimes are relatively short ($\tau \approx 10^{-10}$ s) they are long compared to most microscopic interaction times in solids. For example, lattice and electronic relaxation times are of the order of 10^{-13} and 10^{-16} s respectively. Furthermore, as discussed in Section 1.3.3, e^+ thermalisation times are typically between 1 and 10% of the e^+ lifetime in a solid, so most e^+ attain equilibrium with the lattice long before annihilation. Although short lived on a macroscopic timescale, e^+ can be used to probe processes which are slow compared to their lifetime. One such example is the study of defect annealing by the positron annihilation technique. In these studies, the resolution of the experiment is determined by the count rate and statistics required to observe the transient process.

1.3 POSITRON DYNAMICS IN SOLID MEDIA

1.3.1 Introduction

In this section the motion of e^+ in solid media is followed from initial implantation through to annihilation or re-emission from a surface. An understanding of these processes is required to determine the efficiency of current and new moderation arrangements used to produce mono-energetic e^+ beams. It also provides the basis for using e^+ techniques as a probe of bulk and surface structure. A proportion of incident e^+ interact directly with the surface, particularly at low energies. Consequently, these processes are considered first. A summary of e^+ interactions in solids and at surfaces is given in Figure 1.1.

1.3.2 Interaction of Incident e^+ with Surfaces

The interaction of a flux of positrons with a surface is strongly dependent on the incident energy. At high energies ($\geq 10\text{keV}$), the predominant process is penetration deep into the bulk and subsequent complete thermalisation. At lower energies the mean implantation depth becomes small and a non-negligible proportion of e^+ return to the surface before thermalisation. The interaction of these so called epithermal positrons is considered in Section 1.3.7b). At even lower energies ($\approx 100\text{eV}$), where the positron de Broglie wavelength is approximately equal to the crystal lattice spacing, coherent scattering from the first few atomic layers gives rise to the diffraction patterns discussed briefly above. At all energies, inelastic scattering occurs including the production of secondary electrons, which is of practical importance since it provides the mechanism for e^+ detection by channel electron multipliers (CEMs).

The fractional loss of positrons from the incident surface is characterised by the back-scattering coefficient, B , which depends both on the e^+ energy and the atomic number, Z , of the target. B is of particular relevance to calculations of efficiencies of positron moderators, used in the production of slow positron beams. It is also one of the factors which determine the absorption of e^+ in source supporting foils used in positron annihilation techniques such as PLS. The variation of B with atomic number Z for a β^+ positron source has been measured by MacKenzie *et al* (1973) over the range $3 \leq Z \leq 92$ using a technique based on recording annihilation γ -rays in a Ge(Li) detector. This method overcomes some of the uncertainties encountered in methods which rely on direct detection of e^+ . The data were found to be well fitted by the expression

$$B = 0.342 \log_{10} Z - 0.146 \quad 1:9$$

as shown in Figure 1.3.

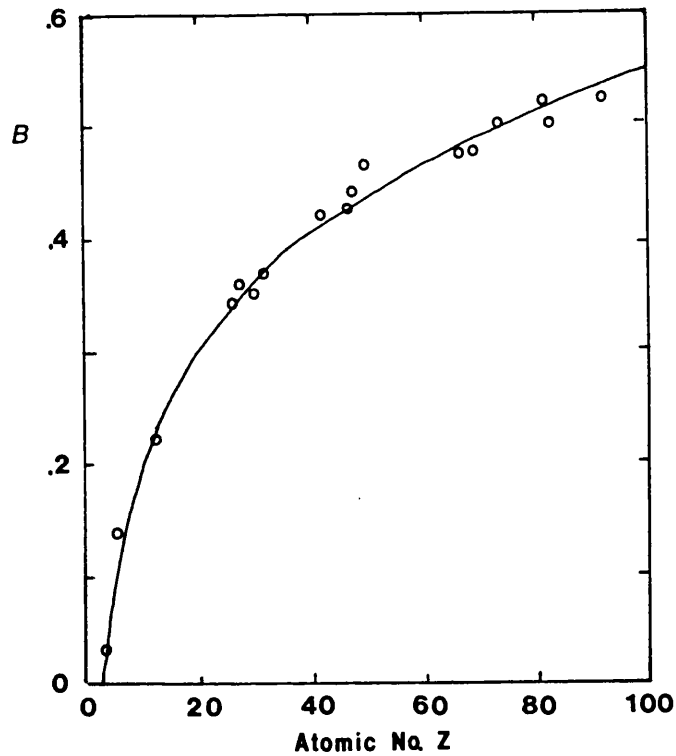


Figure 1.3 Variation of back-scatter coefficient, B , with atomic number, Z . Data fitted by the expression

$$B = 0.342 \log_{10} Z - 0.146$$

(MacKenzie *et al* 1983)

Valkealahti and Nieminen (1983, 1984) performed Monte Carlo investigations of positron thermalisation from keV energies in Al, Cu, W and Au. Their calculations included terms describing elastic scattering, based upon exact cross sections of effective crystalline potentials, and inelastic scattering based on Gryzinski's excitation function (Gryzinski 1965a,b,c). The simulation procedure involved calculating the mean free path, l_T , at a particular energy from the mean free paths of the individual processes and assigning a randomised distance, s , between collisions according to

$$s = -l_T \log_e R$$

where R is a uniform random number. Another random number determined which type of scattering event occurred at the end of path s . For each elastic scattering event, the scattering angle was determined from the relevant cross section by assigning another random number and the energy-loss following an inelastic event determined in a similar fashion. The path of the thermalising positron was followed down to a termination energy of 20eV, which typically involved several hundred scattering events. The simulation was repeated between 1000 and 2000 times for a particular set of input parameters, to give satisfactory statistical accuracy.

The variation of B with incident energy for Al obtained from these simulations is shown in Figure 1.4 together with the experimental data described below. For Al, there was a slow increase in B with energy, whereas for e^- the opposite trend was observed. In contrast a significant increase in B for both e^+ and e^- was calculated for Au. In all cases a higher proportion of e^- were back-scattered than e^+ . Agreement between the calculations and experimental studies was found to be good.

In an experiment described further below, Mills and Wilson (1982) measured the integral longitudinal energy spectrum of e^+ back-scattered from an Al foil target and found an increase in B from 4-10% between 0.5 and 2.9keV (see Figure 1.4). Mills and Wilson (1982) observed that more than 90% of back-scattered e^+ had longitudinal energy less than half that of the incident e^+ . However the measured energies represent a lower bound on the total back-scattered energy because of the transverse momentum component, which was not recorded.

Recently, Baker and Coleman (1988) measured back-scattering coefficients for thick Al, Cu, Ag and W targets in the energy range 0.5 to 30keV. In this study, mono-energetic positrons were accelerated and magnetically guided to the samples through an ExB filter, which caused only a slight deflection in their path. The e^+ annihilation rate was monitored by a Ge detector positioned in close proximity to the samples. Back-scattered positrons

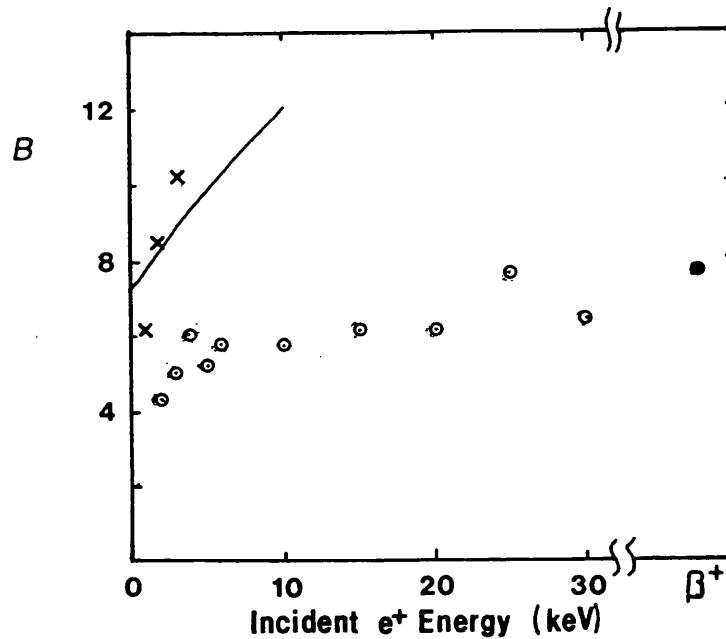


Figure 1.4 Measurements of e^+ back-scattering coefficient, B , for low-energy e^+ implantation into Al.

- Baker and Coleman (1988) (Experiment)
- × Mills and Wilson (1982) (Experiment)
- Kuzminikh and Vorobiev (1979) β^+ implantation (Experiment)
- Valkealahti and Nieminen (1984) (Theory)

returned through the \mathbf{ExB} field and were deflected off the beam axis, so that they annihilated at an aperture plate. This plate was sufficiently distant from the Ge detector to ensure that the annihilation rate of e^+ back-scattered from the samples was not recorded. The incident e^+ flux at a particular energy was determined by monitoring the annihilation rate in an Al sample located behind a biased mesh, from which no back-scattered e^+ could escape. For the back-scattering measurements, the samples were biased at -10V to prevent the escape of work function and epithermal e^+ (see Section 1.3.7 for a discussion of e^+ re-emission processes). Values of B determined in this study are presented in Figure 1.4 together with the other back-scattering data for Al described above.

The significant discrepancy between experimental and theoretical values suggests that further work in this area is required. The variation of B with sample thickness is of particular importance in the determination of transmission moderator and remoderator efficiencies. Extension of the detailed measurements of Baker and Coleman (1988) to 1000-10 000Å thin metal foils would therefore be worthwhile.

1.3.3 Thermalisation

In most instances positrons penetrate the target without undergoing surface reflection, rapidly lose energy and then attain thermal equilibrium with the surrounding medium. The processes involved are similar to those for electrons, although some differences are observed. At energies of a few MeV, radiative stopping (Bremsstrahlung) dominates, in which X-rays are emitted during e^+ -nucleus interactions. For β^+ particles, which have a mean energy of ≈ 0.2 MeV, relativistic scattering dominates at high energies. In this energy range, differences in e^+ and e^- energy-loss occur primarily as a result of collisions with large energy transfer. Also the upper limit for e^+ energy-loss is 100% compared with 50% for e^- due to the indistinguishability of the incident and target particles. These effects explain the difference in B discussed above. At eV energies different scattering mechanisms for metals, semiconductors and insulators are important. In metals, electron interactions can occur at all energies, although below the Fermi energy they become inefficient and are replaced as the dominant energy-loss mechanism by phonon processes. The calculated variation of $\left(\frac{dE}{dt}\right)$ with E obtained by Nieminen and Oliva (1980) for Al is shown in Figure 1.5. The onset of phonon scattering below ≈ 0.2 eV can clearly be seen. In non metals, electron-hole pair production (ionisation) cannot occur once e^+ have cooled below the band-gap. Consequently, phonon interactions become important below several eV. In insulators, e^+ cooling into the Ore gap can form Ps. This process is considered briefly in Section 1.3.4.

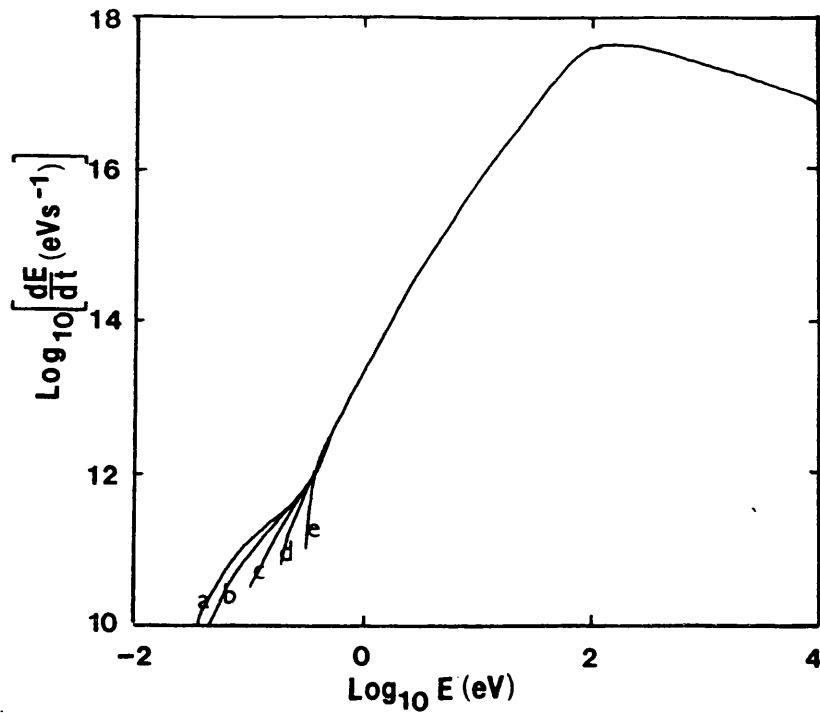


Figure 1.5 Rate of energy-loss, $\left(\frac{dE}{dt}\right)$, versus energy, E , for e^+ thermalisation in Al for several lattice temperatures, T (Nieminen and Oliva 1980).

- | | |
|---------|---------|
| a) 15K | d) 600K |
| b) 100K | e) 900K |
| c) 300K | |

Positron thermalisation times, t_{th} , in solid media are difficult to deduce from experimental data. Kubica and Stewart (1975) performed high resolution angular correlation of annihilation radiation (ACAR) measurements in several metals down to low temperatures. From the sharpness of the Fermi surface obtained from the momentum spectra, they concluded that e^+ thermalisation in K, Mg, Al and Na to temperatures of $(25 \pm 25)K$, $(10 \pm 10)K$, $(30 \pm 35)K$ and $(50 \pm 30)K$ respectively occurred. Although the latter metal appeared to show incomplete thermalisation, the result is made uncertain by the possible presence of defects.

Since phonon interactions provide a weaker energy-loss mechanism than electronic excitations, t_{th} is generally longer in insulators than in metals. In wide band-gap insulators

such as rare gas solids a significant proportion of e^+ may escape from the sample before complete thermalisation. This process is discussed further in Section 1.3.7b) and in Chapter 4.

Thermalisation time has been determined from slowing down calculations performed by Carbotte and Arora (1967) and Nieminen and Oliva (1980). These calculations show that initial energy-loss to eV energies is rapid ($\leq 10^{-12}$ s) and that it is the subsequent cooling to the lattice temperature which governs t_{th} . Consequently, t_{th} is strongly temperature dependent. This effect is seen in the calculations of Nieminen and Oliva (1980) for 1keV positrons thermalising in Al (see Figure 1.6).

The spatial distribution of e^+ trajectory endpoints, calculated by Valkealahti and Nieminen (1984), is shown in Figure 1.7 for 2keV e^+ implanted into Al. The concept of a trajectory endpoint at which slowing down processes give way to thermal motion is in fact idealised since there is a gradual transformation, with a two way exchange of energy with the phonon field. However this notion is convenient since it provides a starting point for calculations of subsequent e^+ motion (see Beling *et al* 1987a, for example). The depth distribution of trajectory endpoints is given by the stopping profile $P(x)$, where x is the penetration depth perpendicular to the surface. The absorption of β^{\pm} particles into materials of differing Z has been studied in detail both theoretically and experimentally (for example Knop and Paul 1966) and is well described by an exponential profile of the form

$$P(x) = \alpha \exp(-\alpha x) \qquad 1:11$$

where α is termed the absorption coefficient. Values of α are similar for β^+ and β^- emitters with the same endpoint energy, E_E , although positron penetration is typically 10% greater due to the effect of particle indistinguishability. The variation of α with E_E is given by the empirical formula (Evans 1955).

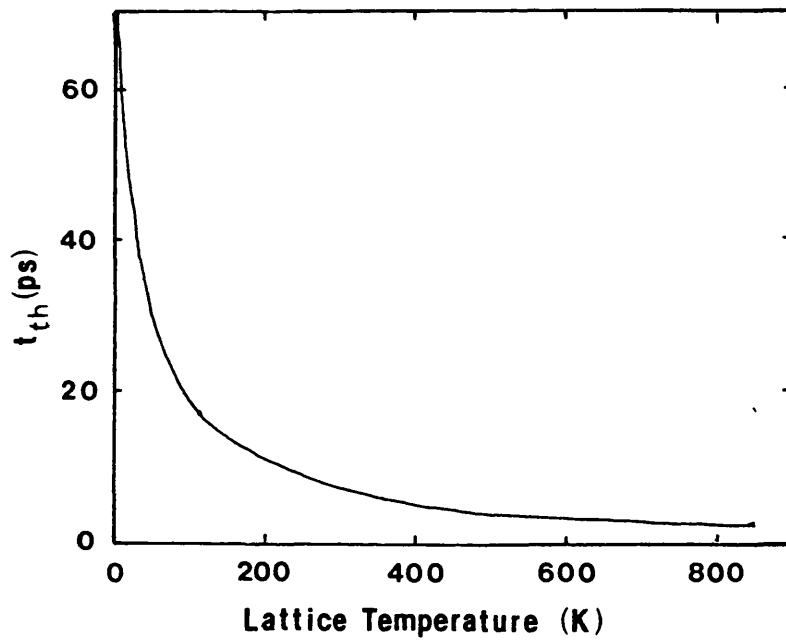


Figure 1.6 e^+ thermalisation time in Al versus lattice temperature (K). (Nieminen and Oliva 1980).

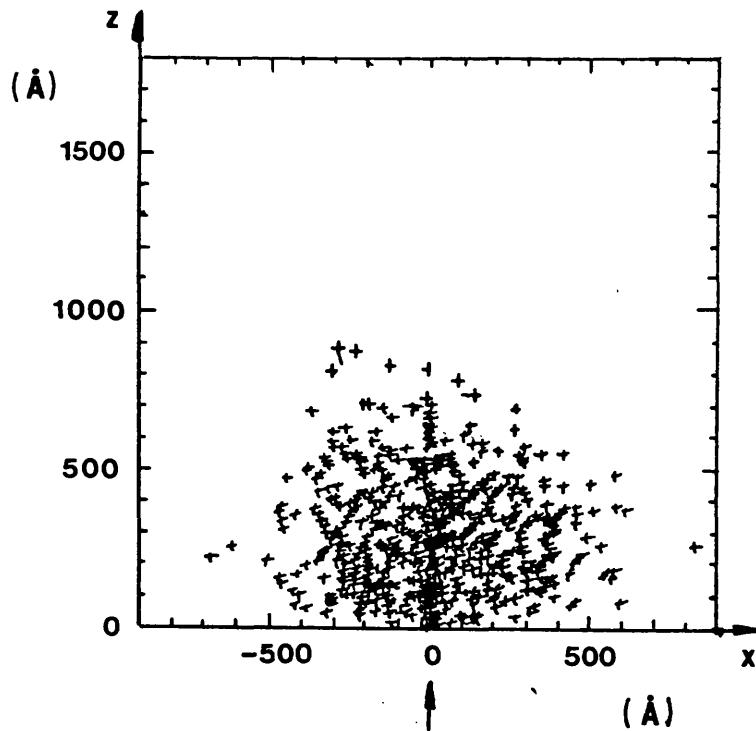


Figure 1.7 Distribution of trajectory endpoints projected onto the y-z plane for 2keV positrons implanted into Al. (Valkealahti and Nieminen 1983).

$$\alpha = 1.7E^{-1.14}$$

1:12

Brandt and Paulin (1977) used the apparatus described in Chapter 2 to measure implantation profiles in a large number of materials of differing Z . They found $\frac{\alpha_+}{\rho} = (29 \pm 1) \text{cm}^2 \text{g}^{-1}$ for all samples studied, where ρ is the target density. Subsequently, Mourino *et al* (1979) made further measurements by a similar method and found overall agreement with Brandt and Paulin (1977). However, a slow variation of α_+ with Z was observed. Fits to the data gave

$$\frac{\alpha_+}{\rho} = \frac{1.1Z^{0.25}}{E^{1.58}} \quad \text{cm}^2 \text{g}^{-1} \quad 1:13$$

for ^{68}Ga and ^{64}Cu isotopes and

$$\frac{\alpha_+}{\rho} = \frac{2.8Z^{0.15}}{E^{1.19}} \quad \text{cm}^2 \text{g}^{-1} \quad 1:14$$

for ^{22}Na . In this case \bar{E} is the mean β^+ energy (.26MeV for ^{22}Na , for example). The energy dependence of these formulae was thought to reflect variations in back-scattering brought about by changes in the source supporting material.

The implantation of lower energy (keV) e^+ into solids has been less well studied: the only experimental study being that of Mills and Wilson (1982). In this work, the transmission of 1-6keV e^+ through Al, Cu and Si was measured as a function of the foil thickness. The thickness graded Al and Cu films were formed by evaporation of the metals onto carbon substrates, which were subsequently bent into semicircles and mounted on a stepper motor in the beamline. The stepper motor gradually rotated the samples so that portions

of varying thickness were presented to the beam. The transmitted e^+ intensity was recorded by monitoring the e^+ annihilation rate at an Al target situated 15cm behind the sample.

When the foil thickness was expressed in terms of specific mass (mass per unit area), e^+ transmission probabilities in Al and Cu were in agreement to within 10%. The median e^+ penetration depth, \bar{x} , in both materials was found to vary with energy, E , according to

$$\bar{x} = AE^n \quad 1:15$$

with $n=1.60$ and 1.43 respectively for Al and Cu. These data were in disagreement with the earlier calculations of Nieminen and Oliva (1980), presumably because the theory had neglected the important effect of large angle scattering. However, subsequent Monte Carlo simulations performed by Valkealahti and Nieminen (1983, 1984) were in good agreement with this experimental data: the small differences could be explained by the effect of neglecting back-scattering in the experimental study. Calculated values of A and n for different materials varied slightly but were typically $4\mu\text{gcm}^{-2}$ and 1.6 respectively. Valkealahti and Nieminen (1983, 1984) also demonstrated that their calculated stopping profiles were well fitted by a profile originally introduced by Makhov (1960a, b, c) to describe electron penetration into solids. This expression takes the form

$$P(x) = \frac{mx^{m-1}}{x_0^m} \exp\left[-\left(\frac{x}{x_0}\right)^m\right] \quad 1:16$$

where x_0 is related to \bar{x} , the mean penetration depth, by the gamma function, $\Gamma(z)$, expression

$$\bar{x} = \Gamma\left(1 + \frac{1}{m}\right)x_0 \quad 1:17$$

Over the range 1-10keV, m was found to be nearly constant (≈ 1.9) for the Al, Cu, Si and Au targets studied, although a slight increase in m with energy was noted for Al and Cu. Valkealahti and Nieminen (1983, 1984) demonstrated the importance in choosing the correct stopping profile for near-surface studies involving the implantation and re-emission of e^+ (or positronium). They stated that use of an exponential rather than a Makhovian profile resulted in a substantial underestimate of the diffusion constant, D_+ , in Al obtained from this type of study. Subsequently Nielsen *et al* (1985) found that in Si an exponential profile failed to give a satisfactory fit to the data over a wide range of positron energies. The value of D_+ thus obtained in Si was found to be about 40% less than that obtained using a Makhovian fit. This experiment is described in more detail in Section 2.4. Further studies of low energy e^+ implantation are required to confirm the Monte Carlo calculations. Precise measurements of A , n and m in a large range of solids will improve the accuracy of many applications of low energy e^+ studies and may show small material dependent variations.

Vehanen and Mäkinen (1985) demonstrated the consistency of the Makhovian and exponential profiles for monoenergetic and β^+ implantation respectively by convoluting the former with the energy distribution for a ^{22}Na β^+ source. The resulting profiles for Al, Cu and W were found to be exponential at depths greater than about $10\mu\text{m}$.

When positrons are implanted into a solid in a direction close to that of a major crystallographic plane, they undergo correlated small angle scattering which tends to channel them through open regions of the lattice. In this case, their mean penetration depth is increased due to a reduction in large angle e^+ -ion core scattering. Unlike electrons, positrons are repelled by the lattice ion cores, so e^+ channelling is stronger and extends to lower energies. Using a variable energy positron beam and a surface barrier detector, Logan *et al* (1988) measured the normalised e^+ yield transmitted through a thin Si(100) crystal and obtained the distributions shown in Figure 1.8 with the detector on and off axis. In the former case, an increased yield was observed corresponding to

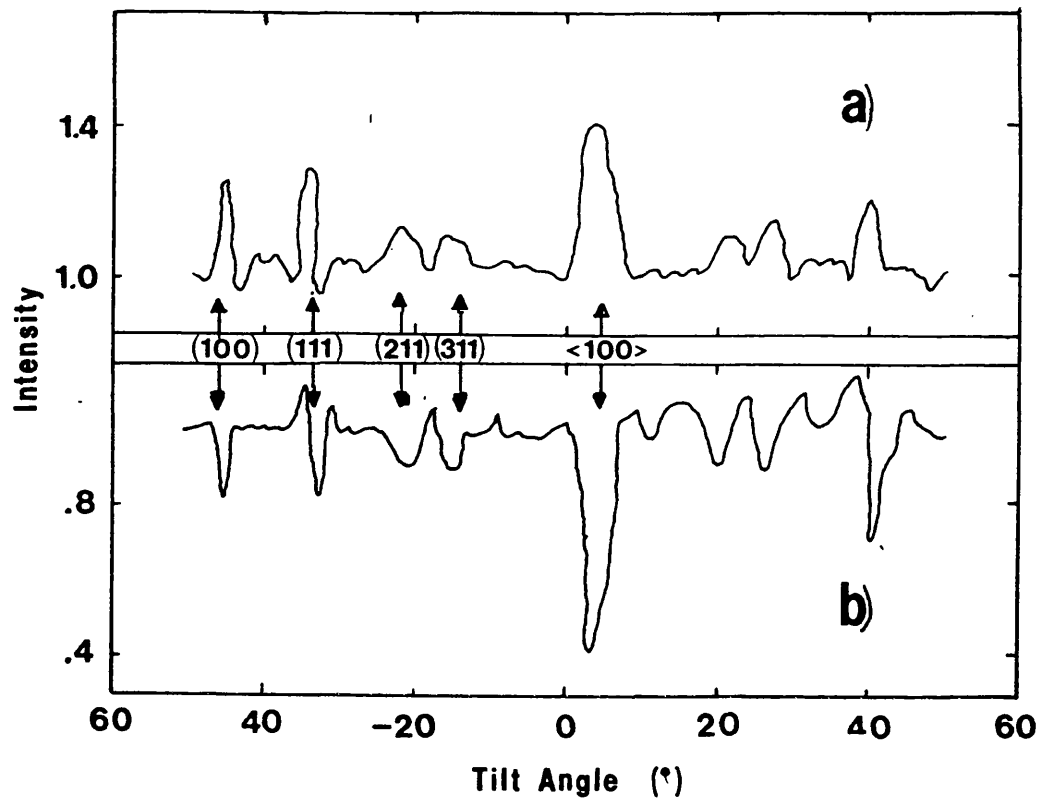


Figure 1.8 Angular scan of 50keV e^+ transmission through a thin Si(100) crystal.

a) Surface barrier detector on axis.

b) Surface barrier detector off axis.

(Logan *et al* 1988).

channelling along the principal (100) plane. Channelling in other lower order planes can also be seen. In the latter geometry, a decrease in positron yield was observed at the same tilt angles, which is due to a reduction in large angle scattering for channelled e^+ . The authors suggest that positron channelling may provide a useful probe of crystal structure.

As a result of channelling, the implantation of e^+ into single crystal foils may be significantly different to that observed in polycrystalline samples. This effect might be important in determining the optimum thickness for transmission moderators and remoderators. The theoretical calculations of Valkealahti and Nieminen (1983, 1984) should therefore be extended to include this effect.

1.3.4 Ps Formation in Insulators

In insulators a significant proportion of e^+ annihilate as Ps. For example e^+ lifetime measurements by Hyodo and Stewart (1984) and variable energy beam studies by Mills and Crane (1984) suggest that the Ps formation fraction, f , in NaF is $\approx 60\%$. Since the electrons in insulators are tightly bound to the ion cores in the lattice, Ps formation can only occur during, or as a direct result of e^+ thermalisation. Two models have been proposed to describe this process.

1. The Ore model

This model was originally developed by Ore (1949) to predict values of f in gases and has subsequently been applied to Ps formation in solids. In this model Ps is assumed to be formed as a direct process in which thermalising e^+ pick off electrons from the surrounding atoms. This mechanism is only energetically favourable over a discrete range of e^+ energies, which is termed the Ore gap. The lower limit, E_l , of the gap is determined by the requirement that the kinetic energy of the Ps formed is ≥ 0 . Hence

$$E_l = E_{gap} - E_b \quad 1:18$$

where E_{gap} is the band gap energy and E_b the Ps binding energy in the solid. If $E_+ > E_{gap}$ the kinetic energy of the Ps atom is greater than its binding energy, so the atom is unstable and a free e^+e^- pair is formed instead. The upper limit for stable Ps formation, E_u , is thus given by

$$E_u = E_{gap} \quad 1:19$$

and the Ore gap defined by the inequality

$$E_{gap} - E_b \leq E_+ \leq E_{gap} \quad 1:20$$

In these expressions, E_+ , E_u and E_l are defined relative to the e^+ ground state energy in the solid. Consequently the Ore gap is shifted by $-\phi_+$, if it is defined in terms of e^+ beam energy. Using the Ore model, Ps formation in gases (Jacobsen 1986) and solids (Eldrup *et al* 1985) has been studied using Monte Carlo methods. These simulations assume that e^+ lose energy by electronic excitation as well as by the formation and break-up of energetic Ps through collisions with the host medium. The calculation is terminated when stable Ps is formed in the Ore gap or the e^+ energy is reduced below E_l . The process is repeated for a large enough number of events to give a statistically reliable estimate of f .

2. The Spur Model

A second mechanism, proposed by Mogensen (1974), considers Ps formation as a two step process. Ps is formed in radiation spurs created as an energetic e^+ slows down in the surrounding medium. Besides the positron, the radiation spur also contains free electrons, positive ions and other reactive species. Ps formation therefore occurs in competition with other recombination processes and diffusion of particles out of the spur. The importance of these other processes means that the model is substantially more difficult to develop than the Ore model.

There has been considerable debate concerning the relative importance of the two processes under different experimental conditions. In general, spur formation of Ps is more probable in dense media whereas the Ore process tends to dominate in low density gases. Using a variable energy positron beam, Eldrup *et al* (1985) studied Ps formation in ice over a range of energies up to 4.5keV and compared the results with Monte Carlo calculations which included the effects of four electron energy bands. They concluded that at low energies Ps formation was predominantly through the Ore process and at higher energies an increase in Ps formation resulted from spur processes. Eldrup *et al*

(1985) suggested that further studies were required to establish the detailed relationship between electron structure and Ps yield. One important test of theory is the variation of f with applied electric field. This is discussed in Section 2.2.

1.3.5 Diffusion

Following thermalisation, the motion of e^+ over distances greater than their de Broglie wavelength can be described by a classical random walk, characterised by a diffusion constant, D_+ , defined by

$$D_+ = \frac{1}{3} v_{th}^2 t_s \quad 1:21$$

where v_{th} is the thermal root mean square velocity and t_s the mean free time between collisions. t_s is determined by the scattering processes experienced by the e^+ (Bergersen *et al* 1974). Theory predicts that in metals above about 25K, impurity scattering ceases to be important and acoustic phonon scattering dominates, resulting in a $T^{-0.5}$ variation in D_+ .

In general, experimental methods of determining D_+ measure the diffusion length, L_+ , which is related to D_+ by

$$L_+ = \sqrt{D_+ \tau} \quad 1:22$$

where τ is the mean lifetime in the solid. For a general implantation profile, $P(x)$, the probability, P_s , of a e^+ returning to a surface is given by

$$P_s = \int_0^{\infty} P(x) \exp\left(-\frac{x}{L_+}\right) dx \quad 1:23$$

In defect free metals, $L_+ \approx 1000 \text{ \AA}$ which is significantly less than the mean implantation depth for β^+ ($\approx 10^5 - 10^6 \text{ \AA}$). In this case, P_s is small, which explains the relatively poor efficiency of primary e^+ moderators (see Section 1.4.4b) and Chapter 4). However, in finely divided powders with grain sizes $\leq 10\,000 \text{ \AA}$, a significant proportion of e^+ stop within one diffusion length of the surface and $P_s \geq 1\%$. This effect was exploited in early measurements of D_+ using positron lifetime spectroscopy, as discussed in Chapter 2.

At keV energies, the mean positron implantation depth, \bar{x} , is comparable with L_+ and P_s is sufficiently large for significant e^+ or Ps re-emission to occur. Measurements of D_+ have been made with variable energy positron beams by determining P_s as a function of implantation energy. In this case $P(x)$ is given by Equation 1:16 above. An exact solution to Equation 1:23 can only be obtained for $m=1$ (exponential profile) or $m=2$ (gaussian profile). In the former case, Equations 1:11 and 1:15 hold and L_+ can be related to an energy E_0 , by the expression

$$L_+ = AE_0^n \quad 1:24$$

In beam experiments the quantity normally measured is the Ps fraction, f . In this case

$$f = f_0 \frac{1}{1 + \left(\frac{E}{E_0}\right)^n} \quad 1:25$$

where f_0 is the surface branching ratio for Ps. For $1 < m < 2$, exact solutions cannot be obtained and L_+ is determined by performing a lengthy fitting procedure to Equation 1:23. In addition to the uncertainty in implantation profile, difficulties arise in determining the reference states of 0 and 100% Ps formation required to determine f from the measured data. Difficulties encountered in the determination of D_+ by variable energy beam methods have been discussed by Lynn (1983) and Jorch *et al* (1984).

Early measurements of e^+ diffusion to surfaces confirmed theoretical predictions of a $T^{-0.5}$ variation in D_+ (Lynn and Lütz 1980). However, the first systematic compilation of data for L_+ in several different materials as a function of temperature (Schultz *et al* 1985) indicated a stronger temperature dependence. Subsequently Huomo *et al* (1987) suggested that back diffusion measurements made at low implantation energies may be subject to errors arising from the re-emission of epithermal positrons (see Section 1.3.7b)). they presented measurements in Mo and Ag which were in agreement with theory. As a result of this work the earlier measurements of Schultz *et al* (1985) may now need to be reevaluated.

In insulators, Ps produced during e^+ thermalisation may also be delocalised. Early lifetime measurements in powders showed a long-lived lifetime component with an intensity which increased with decreasing grain size. This behaviour was attributed to the motion of Ps to the powder surface where it subsequently annihilated with a lifetime longer than that in the bulk. More recently, variable energy e^+ beams have been used to study the motion of bulk Ps to surfaces. Using this technique, values of $\approx .05$ (Sferlazzo *et al* 1985) and $.02\text{cm}^2\text{s}^{-1}$ (Eldrup *et al* 1985) have been reported for the Ps diffusion constant in quartz and ice respectively.

1.3.6 Bulk Defect Trapping

In non-perfect materials, e^+ may become trapped in defects. This process may be observed experimentally by

1. a change in ACAR profile (Berko and Erskine 1967).
2. a change in lineshape parameter, S , of the 511keV annihilation γ peak (Jackman 1974, MacKenzie 1983).

3. A change in mean positron lifetime, or a change in intensity of a particular lifetime component (MacKenzie *et al* 1967)
4. A reduction in the thermal positron flux returning to a surface (for example Lynn 1979).

A thermal positron typically scans 10^9 atoms before annihilation. Provided that the trapping probability is high once the positron encounters a defect site, the process can be observed experimentally even for low concentrations of defects. In metals, e^+ are repelled by the positive ion cores in the crystal lattice and therefore tend to become localised at voids in the material. Once trapped, the escape probability is generally low (e^+ binding energy $\approx 1\text{eV}$) and e^+ annihilate with a lifetime characteristic of the electron density in the defect. In voids, this density is low in comparison to that of the perfect lattice and an extra long-lived lifetime component, or an increase in mean lifetime, is observed. For a homogeneous distribution of defects, characterised by a trapping rate, κ , the positron lifetime, τ , is replaced by τ^* in Equation 1:22 where,

$$\tau^* = (\tau^{-1} + \kappa)^{-1} \quad 1:26$$

In Al, a vacancy defect concentration of 20ppm is sufficient to bring κ close to τ^{-1} , reducing L_+ by a factor of $\sqrt{2}$. The effect of the defect concentration can thus be observed by a measurement of either L_+ or τ^* . In many instances trapping is diffusion limited, and κ is related to D_+ by

$$\kappa = 4\pi r_v D_+ C n_A \quad 1:27$$

where r_v is the vacancy capture radius (≈ 1 atomic spacing), n_A the atomic density, and C , the defect concentration. For non-homogeneous defect distributions, κ will depend on the geometry of the system (Brandt and Paulin 1972 and Chapter 2).

In some non metals (for example GaAs and paraffin wax) the binding energy of e^+ to defects is comparable to thermal energies. In these cases, detrapping can occur and e^+ "hop" from one defect site to another. Experimental observations of thermally activated transport are discussed in Section 2.4.

Following pioneering work by MacKenzie *et al* (1967), PLS, has become a well established probe of defect concentrations. Although this work is not discussed further here, much of the material has been reviewed in Brandt and Dupasquier (1983) and a more recent overview of work in this field can be found in the Proceedings of the Eighth International Conference on Positron Annihilation (ICPA8) (Dorikens-Vanpraet *et al*, eds., 1989).

The advent of variable energy e^+ beams has opened up the possibility of studying near surface defect profiles. One example is the study of Ni implanted with He ions reported by Lynn *et al* (1986). In these experiments, the annihilation of e^+ was monitored by an intrinsic Ge detector for different e^+ implantation energies. The shape of the 511keV annihilation peak, characterised by the lineshape parameter, S , (see Section 1.4.2) was used to determine the fraction of e^+ annihilating in open volume defects produced by the implantation of He ions. Lynn *et al* (1986) determined the difference, ΔS , between S parameter values measured in annealed (defect free) and samples implanted with 30, 90 and 180keV $^4\text{He}^+$ ions. The shift of the ΔS distributions to increasing e^+ energy, at high He implantation energies (Figure 1.9) demonstrates that the data contain information on the depth of the defect distribution.

Lynn *et al* (1986) assumed a defect distribution defined by

$$\begin{aligned} \kappa(x) &= \kappa & x_1 \leq x \leq x_2 \\ \kappa(x) &= 0 & x < x_1 ; x > x_2 \end{aligned} \qquad 1:28$$

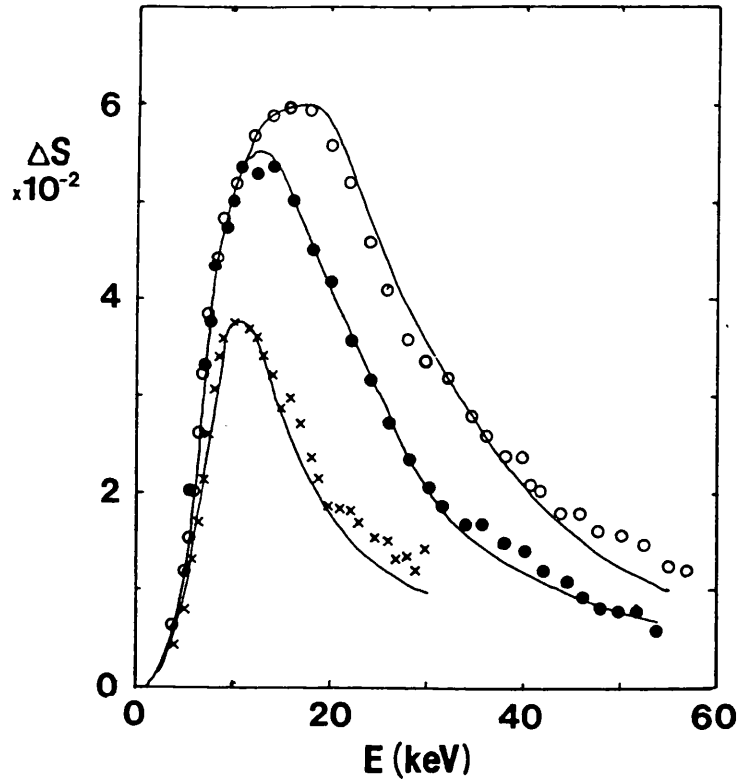


Figure 1.9 Shift, ΔS , in lineshape parameter, S , as a function of incident e^+ energy for 30, 90 and 180keV energies.

- 180keV
- 90keV
- × 30keV

(Lynn *et al* 1986)

and fitted the data to a theoretical expression derived in the paper to give x_1 and x_2 . The results were in reasonable agreement with the He induced damage profiles calculated by an established Monte Carlo method. Differences were believed to be due to the presence of a tail in the defect distribution, extending to the sample surface. As a result of the high He fluences used to produce the voids, saturation trapping of e^+ occurred into this tail, giving a broader apparent defect distribution. Consequently, the authors concluded that better agreement between theory and experiment would be obtained if lower He fluences

were used. In this case, the square-like profile assumed would be a poor description of the true defect distribution, so a more sophisticated fitting procedure would be required. Alternatively, square-like profiles could be produced using variable energy $^4\text{He}^+$ implantation.

Lynn *et al* (1986) also used the S parameter method to study the annealing of the He induced defects. Between 770 and 970K, a strong increase in ΔS was observed, which was attributed to the agglomeration of bubbles. Above 970K, ΔS decreased, indicating that migration and destruction of the bubbles at the surface had occurred.

Other variable energy e^+ studies of near-surface defect profiles have been reviewed by Schultz and Lynn (1988).

The possibility of prethermalisation trapping of e^+ into defects has been subject to some debate and, in general it was concluded that this process was not significant (Hodges 1970). However, measurements of the energy distribution of e^+ re-emitted from Al(111) and Cu(100) surfaces, undertaken by Nielsen *et al* (1986) (see Section 1.3.7b)) showed that non-thermal e^+ with energies $\geq 1\text{eV}$ have a relatively high probability of trapping into vacancy type defects, generated either thermally at 800K or by implantation of Ar^+ ions. These observations bring into question the reliability of previous measurements of bulk defect concentrations using e^+ techniques. These data should now be reevaluated, taking into account both thermal and non-thermal trapping. Theories describing the latter process have recently been developed (Lynn *et al* 1987a, Puska and Manninen 1987, and Shirai and Takamura 1987). Measurements of near-surface defect profiles using variable energy e^+ beams should be carried out at high enough energies to ensure that e^+ have completely thermalised before returning to the defected region.

1.3.7 Positron-Surface Processes

Positrons returning to a surface from the underlying bulk can undergo a variety of processes with probabilities dependent on the physical and chemical properties of the surface and near-surface bulk. The importance of non thermal e^+ processes at surfaces has also been realised. A chronology of e^+ -surface studies is given in Table 1.2.

In the simple work function model developed to explain e^+ re-emission from metallic surfaces (see Section 5.1.1), e^+ are viewed as passing over a step of height ϕ_+ situated at the surface, where ϕ_+ is the positron work function. The problem can be solved quantum mechanically by matching the e^+ wave functions in vacuum and bulk at the surface. This leads to a transmission probability, P , for e^+ leaving the bulk given by

$$\text{where } P = \frac{4kT}{|\phi_+|} \quad 1:29$$
$$kT \ll |\phi_+|$$

Here, T is the lattice temperature and k , is Boltzmann's constant. The total probability of e^+ escape can be determined by considering the possibility of multiple approaches of reflected e^+ to the surface. For example, at 300K, a surface with $\phi_+ = -1\text{eV}$ has $P \approx 10\%$. At low temperatures, P decreases rapidly, and the effect should be recorded in experimental measurements of the e^+ surface branching ratio, y_0 (see Section 1.3.7a)). Early experimental measurements (Schultz and Lynn 1982) failed to show a strong temperature dependency in y_0 , which suggested that e^+ emission was not a direct process. Many bodied effects (Wilson 1983) and multiple approaches to the surface of e^+ from the bulk have been offered as possible explanations of this discrepancy. However, recent measurements reported by Britton *et al* (1989) showed decreasing e^+ and Ps yields for clean Cu(111) and Al(110) surfaces below 300K. For both surfaces the yields disappeared at 0K, as predicted by the simple quantum mechanical model. The authors therefore concluded that e^+ are reflected by the surface potential and suggested that the

TABLE 1.2
Chronology of Positron Surface Physics

Year	Event	Reference
1950	First attempt to observe re-emission of thermal e^+	Madansky and Rasetti (1950)
1970	Observation of e^+ surface effects in powdered Si samples	Gainotti and Ghezzi (1970)
1972	Negative e^+ re-emission mechanism proposed	Costello (1972a, b) Tong (1972)
1974	Observation of Ps emission from surfaces	Canter <i>et al</i> (1974)
1978	First study of e^+ re-emission from characterised surfaces in UHV	Mills <i>et al</i> (1978)
1978	Observation of e^+ diffraction effects	Lynn and Dickman (1978)
1980	Variation in e^+ work function correlated to change in surface dipole moment	Murray <i>et al</i> (1980)
1981	Observation of positronium negative ion (Ps^-)	Mills (1981)
1982	Profiling of near-surface defects	Triftshäuser and Kögel (1982)
1983	Observation of e^+ energy-loss to surface adsorbed molecules	Fischer <i>et al</i> (1983)
1984	Study of e^+ re-emission from ionic insulator surfaces	Mills and Crane (1984)
1985	Measurement of surface ACAR spectra	Lynn <i>et al</i> (1985a) Howell <i>et al</i> (1985b)
1986	Observations of e^+ re-emission from rare gas solid films. Hot positron emission mechanism proposed.	Gullikson and Mills (1986)
1986	Studies of epithermal e^+ re-emission from metal surfaces. Observation of epithermal e^+ trapping	Nielsen <i>et al</i> (1986)
1987	High resolution e^+ surface lifetime studies	Schödlbauer (1987)
1988	Studies of e^+ re-emission from multilayer structures	Gidley and Frieze (1988)
1989	Observation of e^+ reflection from the surface potential	Britton <i>et al</i> (1989)
1989	Observation of Ps reflection from LiF	Weber <i>et al</i> (1989)

failure of earlier experiments to observe this effect was a result of incomplete e^+ thermalisation prior to re-emission from the surface (see Section 1.3.7b)). Generally, it is considered that for negative positron work function surfaces, the probability for low energy e^+ re-emission, trapping into surfaces and Ps emission are approximately equal. These processes are described in the following subsections.

a) *Prompt emission of slow e^+*

For many metals and some insulators, the spontaneous re-emission of thermal e^+ is an energetically favourable process. This phenomenon is explained by a negative e^+ work function mechanism, originally proposed by Tong (1972) to explain early measurements of e^+ re-emission from several metallic surfaces (Costello *et al* 1972a, b). Tong's theory and the subsequent thorough experimental investigations of this process are described in detail in Chapter 5. In the ideal case, the energy distribution of e^+ re-emitted from a surface is peaked at $-\phi_+$ and has an angular spread of $\Delta\theta$ related to the thermal spread of e^+ in the bulk by

$$\Delta\theta \approx \left(\frac{kT}{2\phi_+} \right)^{\frac{1}{2}} \quad 1:30$$

where ϕ_+ is the positron work function of the surface. However, in practice, most experimentally obtained retarding field spectra show a greater increased energy spread due to e^+ -surface energy-loss processes and an increased angular spread caused by the microscopically rough surface. Inelastic surface processes involving e^+ include plasmon and adsorbate excitation; the latter being demonstrated by Fischer *et al* (1983, 1986) to be a novel probe of surface contamination.

The surface branching ratio, y_0 , is defined as the fraction of e^+ leaving the surface as low energy positrons. Values of y_0 are listed in Table 5.1.

b) Re-emission of non-thermal e^+

Studies of e^+ re-emission from wide band gap insulators including MgO, Al_2O_3 and LiF (Mills and Crane 1984) have been reported. In these studies e^+ implanted into the samples with intermediate energy ($\leq 10\text{keV}$) were observed to be re-emitted with a large spread of energies, comparable to the band-gap of the particular material (see Figure 1.10a). Hence, the data could not be explained by the work function mechanism of Tong (1972), discussed above and in Chapter 5. Mills and Crane (1984) therefore interpreted their data in terms of the migration and break-up of Ps at the sample surface, resulting in the emission of the positron via an Auger-like process. The electron was assumed to be trapped in a vacant surface state.

In comparison with ionic insulators, the solid rare gas films studied by Gullikson and Mills (1986) have simpler structures, which enabled a clearer interpretation of the e^+ re-emission process to be established. These authors were therefore able to conclude that their data were inconsistent with a Ps break-up mechanism and a "hot positron" model was proposed instead to describe the re-emission process (see Figure 1.10b)). Energetic e^+ entering a solid rare gas rapidly lose energy by electronic excitation. However, once e^+ have cooled below the band-gap, this process can no longer occur and, apart from the possibility of Ps formation in the Ore gap, further reduction in e^+ energy continues only via weak acoustic phonon interactions. The maximum phonon energy is $\approx 10\text{meV}$, so the energy-loss per collision is small and the diffusion constant large. Consequently, there is a substantial probability of e^+ reaching a surface with sufficient energy to overcome an unfavourable potential barrier arising from a positive positron work function.

Experimental measurements of re-emitted positron spectra (see Figure 1.10b) extend up to a value E_{th} , which was associated with the lowest e^+ inelastic threshold. As the implantation energy was increased, e^+ penetrated deeper into the solid and therefore

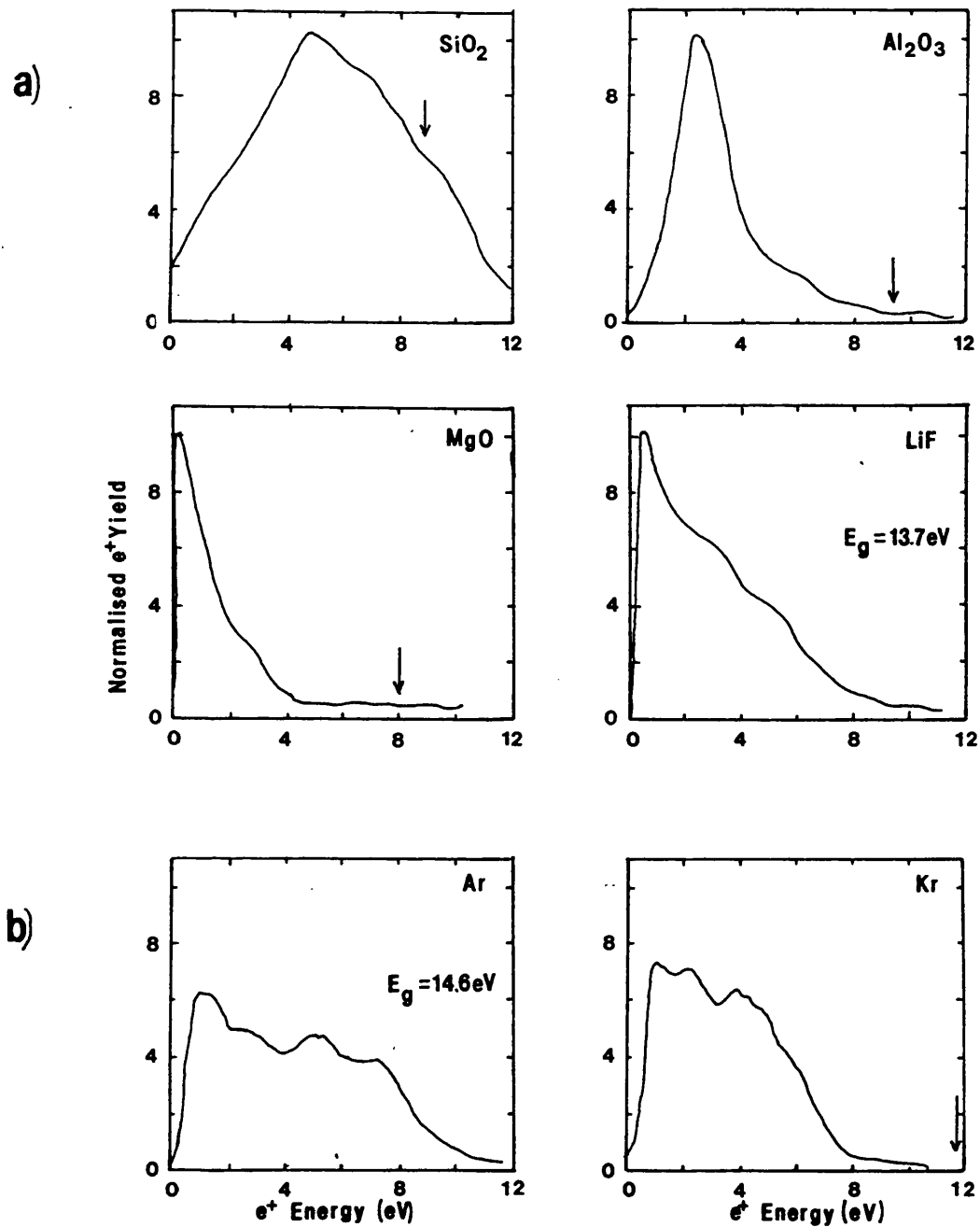


Figure 1.10 Re-emitted e⁺ energy spectra from insulating surfaces.

a) Ionic insulators (500eV incident e⁺ energy) (Mills and Crane 1984)

b) Rare gas solids (1800eV e⁺ energy) (Gullikson and Mills 1986)

Arrows indicate the band-gap energy, E_g , of the solid

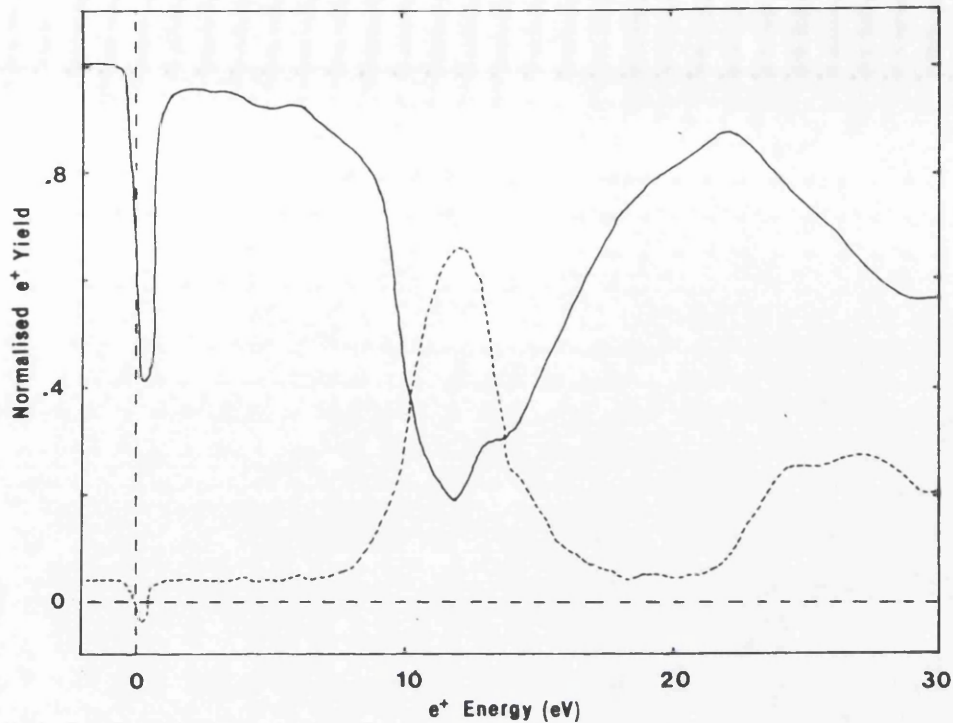


Figure 1.11 Positron re-emitted yield, R (solid line), and Ps yield, f (broken line), versus e^+ implantation energy for a 15 000 Å solid Ar film (Gullikson and Mills 1986)

underwent more energy-loss before returning to the surface. Consequently, a shift of the re-emitted e^+ energy distribution to lower energies and a lower total e^+ yield were observed, in agreement with the model.

Detailed measurements of re-emitted e^+ and Ps yields, R and f at low implantation energies (see Figure 1.11) enabled Gullikson and Mills (1986) to determine the inelastic thresholds for Ps, exciton and electron-hole pair formation. The onset of the former process at E_{th} governed the maximum re-emitted e^+ energy shown in Figure (1.10a). The sharp dip in positron yield at low energies was attributed to e^+ energy-loss to the phonon field. Using a Monte Carlo routine to simulate the slowing down of e^+ , the mean energy-loss per collision, δE , was deduced from ΔE . Measurements of R versus film

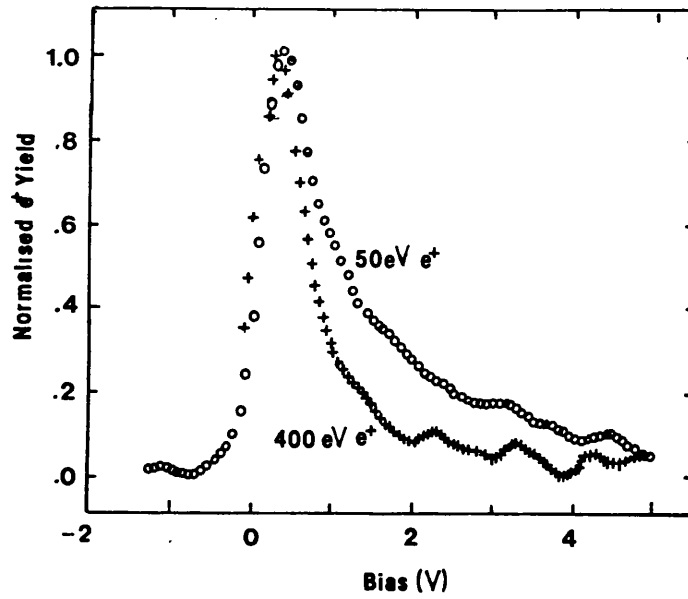
thickness enabled the energy dependent positron mean free path, l , to be determined in Ar. Using this result and the value of δE , the positron diffusion length in Ar was estimated to be $\approx 5000\text{\AA}$, which is a factor of five greater than in metals.

These measurements provided conclusive proof of the hot positron mechanism for e^+ re-emission from rare gas solids. The model is now considered to apply to other wide band-gap insulators (Lynn and Nielsen 1987, Gullikson and Mills 1986), although in most cases, the existence of an optical branch in the phonon dispersion relation increases energy-loss, thereby reducing the probability of re-emission.

Nielsen *et al* (1986) measured the energy distribution of e^+ re-emitted from Al(111) and Cu(100) surfaces following implantation at low energies ($\leq 500\text{eV}$). These surfaces were studied because their slightly positive positron work functions ($0 < \phi_+ < 0.1\text{eV}$) ensured that whilst no thermal e^+ could escape, the energy distributions of non-thermal e^+ were not appreciably distorted. Energy spectra for an Al(111) surface at 500K bombarded by 50 and 400eV incident e^+ are shown in Figure 1.12a). About 20% of 50eV incident e^+ were emitted as non-thermal e^+ and approximately 80% of this yield had energies $< 5\text{eV}$. With the implantation energy increased to 400eV, the re-emitted fraction was $< 10\%$ and the energy distribution depleted at high energies ($> 1\text{eV}$) in comparison with the 50eV data. The similarity between the two spectra at low re-emitted e^+ energies shows that the e^+ energy-loss rate below 1eV is substantially less than at higher energies. From the data, Nielsen *et al* (1986) estimated that e^+ typically thermalise to 1eV in $\approx 10^{-13}\text{s}$ and to near-thermal energies in $\approx 10^{-12}\text{s}$. These results are in agreement with theoretical calculations (see Section 1.3.3) which assume that energy-loss is dominated by electronic excitations down to energies of $\approx 1\text{eV}$ and phonon interactions at lower energies.

Re-emitted e^+ energy spectra for clean and oxidised (5\AA Al_xO_y) surfaces are shown in Figure 1.12b). The broad energy distribution measured for the latter surface is explained

a)



b)

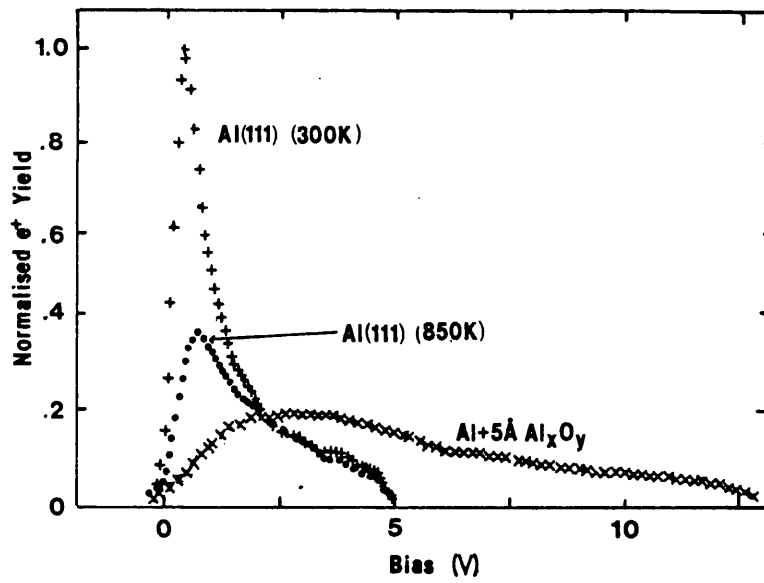


Figure 1.12 Studies of epithermal e⁺ re-emission

- a) Energy distribution of e⁺ re-emitted from the surface of Al(111) at 500K after implantation at 50 and 400eV
- b) Energy distribution of e⁺ re-emitted from clean and oxygen exposed Al(111) surfaces after implantation at 50eV

(Nielsen *et al* 1986)

by the presence of a wide band-gap in the insulating oxide layer, which excludes any electronic excitations once e^+ have slowed below the positronium formation threshold. This is the essence of the hot positron model described earlier in this section.

In metals with negative positron work functions, both thermal and epithermal re-emission can occur. At low implantation energies ($\leq 500\text{eV}$) a high energy tail is observed on the usual thermal re-emitted e^+ energy distribution (for example, Fischer *et al* 1986). The re-emission of e^+ from clean and oxygen exposed Si surfaces reported in Chapter 5 is considered to be a result of a non-thermal e^+ process. In this case the relatively narrow Si band-gap (1.1eV) results in a low positron yield from the surface. In Chapter 4, the results of Monte Carlo simulations are presented, which show that the energy distribution of epithermal e^+ re-emitted from rare gas solids can be changed by the presence of an electric field in the film.

c) Positronium emission

Energetically, Ps emission is favoured over e^+ re-emission because its binding energy more than compensates for the minimum energy required to remove the electron from the solid (the electron work function, ϕ). The high electron densities in metals and semiconductors preclude Ps formation in the bulk, so this process is expected to occur several Å from the surface, where the electron density has fallen below a critical limit. In this case, the concept of a positronium work function is therefore unphysical and the process should be described in terms of a Ps formation energy, E_{Ps} . Ps formation occurs within 10^{-18}s , which is much shorter than typical energy relaxation times, so for thermal e^+ , the re-emitted energy spectrum, $E_{Ps}(k)$, will be determined largely by the electron density of states $f(k)$ at energy $E(k)$ below the Fermi level in the bulk. This results in the expression

$$E_{Ps} = 6.8 - (\phi_+ + \phi_-) - E(k) \quad 1:31$$

where 6.8 is the Ps binding energy in eV.

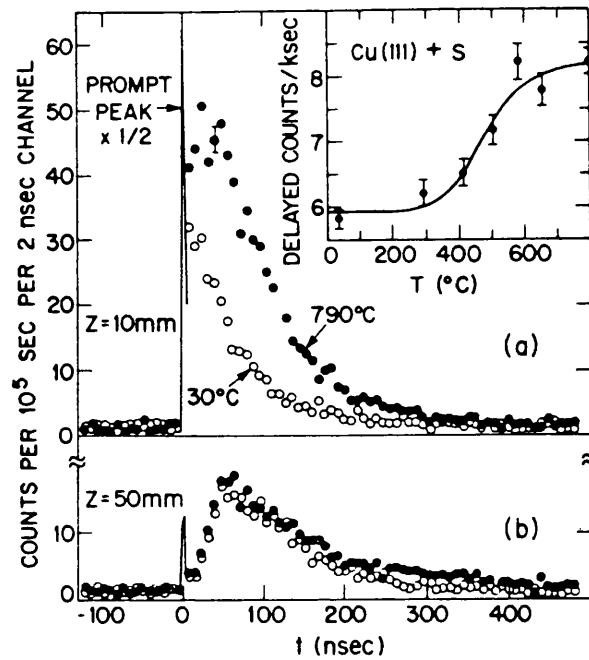


Figure 1.13 Time of flight spectra for triplet Ps annihilation at distances

a) $z=10\text{mm}$

b) $z=50\text{mm}$

in front of the Cu target. $t=0$ corresponds to the arrival of e^+ bunches at the target. Inset shows the variation of the total delayed component with temperature. The solid line is an exponential Arrhenius fit to the data (Mills and Pfeiffer 1979a)

Substantial Ps emission from an MgO coated gold target bombarded with eV energy e^+ was reported by Canter *et al* (1974). Subsequently, Mills and Pfeiffer (1979a) used a time of flight method to measure the velocity distribution of Ps emitted from a Cu(111) surface. Timing was accomplished by deriving start signals from a pulsed positron beam and stop signals from the annihilation of emitted Ps recorded at a fixed distance, z , from the sample, by a collimated scintillator/photomultiplier arrangement. With $z=10\text{mm}$, the lifetime spectra shown in Figure 1.13a) were collected at 300 and 1050K. The large peaks at $t=0$ are produced by e^+ annihilations in the Cu target and the prompt decay of para-positronium, whereas the delayed part of the spectrum is due to decay of the

ortho-positronium state. With the target at 1060K, a decrease in prompt peak and increase in apparent decay time were recorded, which suggested that the extra Ps was emitted from the heated surface with a lower mean energy than that emitted at 300K. With z increased to 50mm, identical spectra were obtained at the two temperatures (Figure 1.13b), which indicated that the additional slow Ps had decayed before it reached the region monitored by the detector. Consequently, the data could be subtracted to give a spectrum associated only with thermal Ps. Mills and Pfeiffer (1979a) concluded that two Ps emission mechanisms occurred. The temperature dependent part, described by an Arrhenius variation (see inset to Figure 1.13) was believed to be due to the thermal desorption of Ps formed from e^+ trapped in the surface potential well (see Figure 5.1). The other part of the distribution was attributed to Ps formed by slow e^+ emitted directly from the surface without trapping. The energy distribution of Ps formed by the latter process is given by Equation 1:31 above.

Using a similar time of flight arrangement, Mills *et al* (1983) measured the differential energy distribution of Ps emitted from clean and oxygen exposed Al(111) surfaces. Their data, shown in Figure 1.14 is in good agreement with the results derived from a simple e^- density of states model, demonstrating the validity of Equation 1:31. The discrepancy between theory and experiment at low Ps energies may be due to the effect of annihilation on the walls of the cell.

More recently, Howell (1987) reported Ps time-of-flight (TOF) measurements, obtained using a linac based beam (see Section 1.4.4a). These studies confirmed the existence of both fast and thermal Ps production mechanisms and also demonstrated that Ps may be formed as a result of electron pick-up by non-thermal e^+ , which have scattered out of the metal samples (Howell *et al* 1986).

Nieminen and Oliva (1980) argued that the probability of Ps formation, f_0 , at a surface depends on the e^+ transit time, and hence its velocity through the region where e^- capture

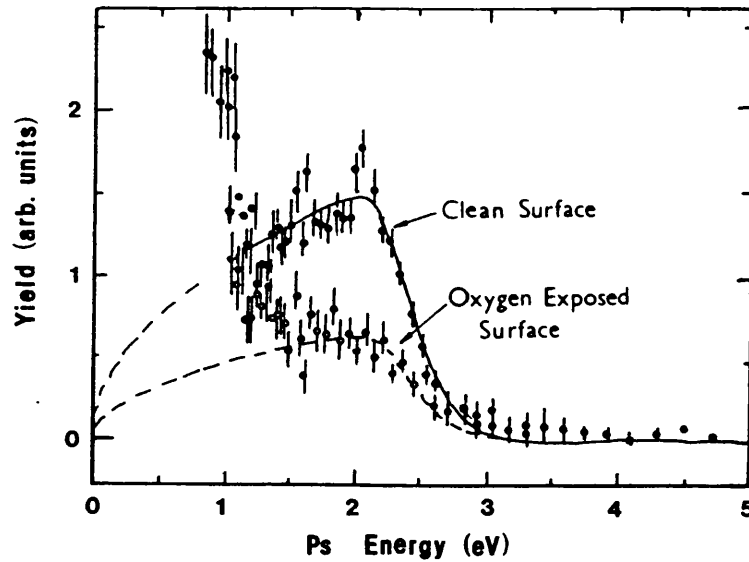


Figure 1.14 Normal component of kinetic energy of Ps emitted from clean and oxidised Al(111) surfaces. Solid lines are fits to the data assuming a simple local density of states model. (Mills *et al* 1983).

occurs. A correlation between f_0 and ϕ_+ might therefore be expected, although a strong trend is not observed experimentally, suggesting that other effects such as the electron density of states, dominate the formation process.

In insulators, Ps formed in the bulk can diffuse to a surface and be spontaneously emitted into vacuum. In this case, it is meaningful to assign a Ps work function, ϕ_{Ps} , analogous to ϕ_+ and ϕ_- . For this process

$$\phi_{Ps} = \phi_+ + \phi_- - 6.8(\text{eV}) \quad 1:32$$

and is negative for most materials. Work function emission of Ps from ice (Eldrup *et al* 1985), quartz and MgO (Sferlazzo *et al* 1987) and ionic solids (Mills and Crane 1984) have been reported, although the latter measurement has now been reinterpreted in terms of the "hot positron model" described above.

d) Surface state trapping

Early theories of e^+ surface states were developed to explain the long lifetimes associated with positrons localised in radiation induced voids (Hodges and Stott 1973). Models generally considered that these states arose from e^+ trapping in the surface potential well (see Figure 5.1). Platzman and Tzoar (1986) have advanced an alternative mechanism in which e^+ are assumed to be trapped as physisorbed Ps, bound to the surface by Van der Waals forces.

Since e^+ are bound in the potential well with eV energies, the most energetically favourable method of escape is through Ps formation. Measurements of thermally desorbed Ps by Mills and Pfeiffer (1979a), discussed above, provided the first direct confirmation of e^+ localisation at surfaces. The idea of e^+ trapping in the surface potential well minimum suggests that these e^+ are only localised perpendicular to the surface, and may therefore possess large transverse momenta. However, 2D angular correlation of annihilation radiation (ACAR) measurements of e^+ residing in these states (Lynn *et al* 1985a, Howell *et al* 1985b, Chen *et al* 1987) showed nearly isotropic momentum distributions (see Figure 1.15), similar to those recorded for bulk e^+ traps. It has therefore been suggested that e^+ may become localised at surface defects or impurity sites. Lou *et al* (1989) have calculated 2D ACAR distributions for the Al(100) surface and found a nearly isotropic momentum distribution, in agreement with Lynn *et al* (1985a). Using a mixed density approximation, Brown *et al* (1987) obtained an ACAR spectrum significantly more anisotropic (Figure 1.15). Subsequent calculations presented by Brown *et al* (1989) indicated that e^+ trapping at vacancy sites may provide the best explanation for the isotropic experimental data. The authors noted that these calculations are strongly model dependent and suggested that further work is necessary to establish irrevocably the dominant surface trapping mechanism.

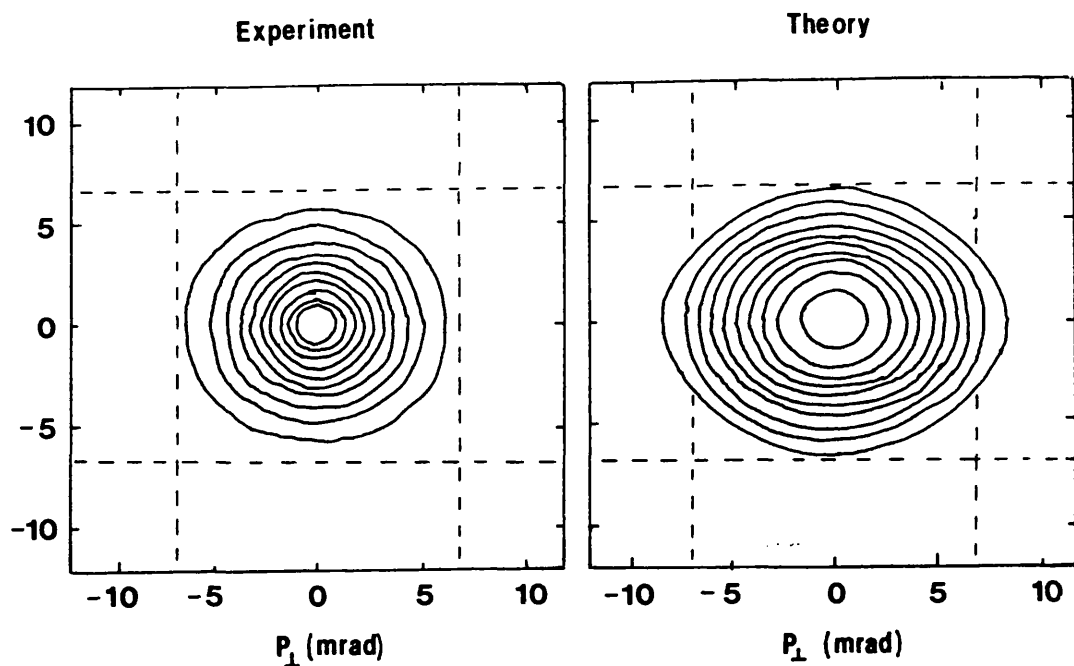


Figure 1.15 Two dimensional contour plot for an Al(110) surface. The experimental and theoretical data are respectively from Chen *et al* (1987) and Brown *et al* (1987).

e) Positrons at interfaces

The behaviour of positrons at many solid-vacuum and solid-gas interfaces (for example radiation induced He bubbles in Al) is quite well understood. Investigations of e^+ motion at a buried solid-solid interface has only recently been developed, although experimental results published so far suggest that positron studies may provide a useful probe of interface structure.

The first observation of e^+ trapping at interfacial defects was reported by Schultz *et al* (1983) for a structure comprising a thin epitaxially grown layer of Cu on a W(110) substrate. Only 30% of the expected re-emitted yield of 2keV e^+ implanted into the sample was measured. On annealing at 1225K the yield was restored to its expected

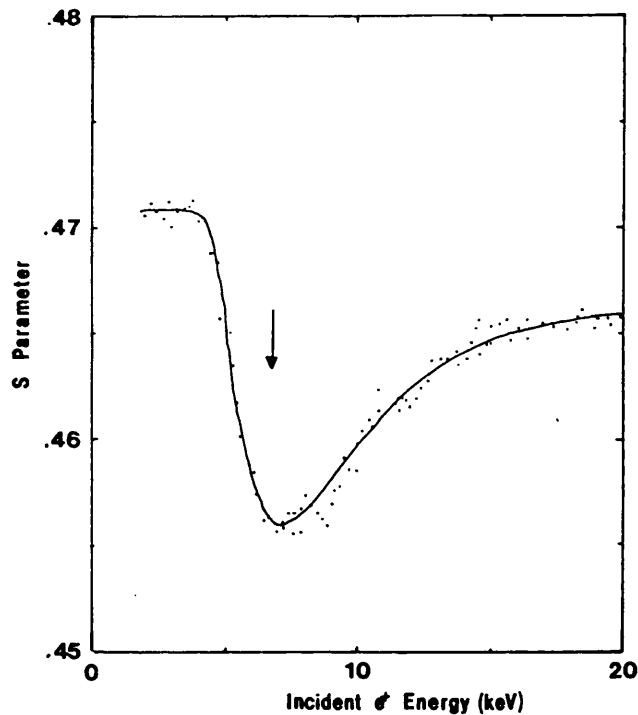


Figure 1.16 Variation of lineshape parameter, S , with e^+ implantation energy for a thermally grown SiO_2 layer on Si. Arrow indicates the position of the Si- SiO_2 interface. The solid line is a theoretical fit to the data (Nielsen *et al* 1987).

value. Since this coincides with the temperature required to cause thermal activation of the first Cu layer on W(110), it was concluded that positrons were being trapped at the interface.

Nielsen *et al* (1987) measured the S parameter as a function of incident positron energy in Si(110) with a 3500\AA oxide overlayer and obtained the distribution shown in Figure 1.16. The minimum of the distribution was attributed to e^+ annihilations in an interfacial state and the curved regions on either side of the minimum to e^+ diffusion from the Si(110) and SiO_2 layers to the interface. Although the nature of the e^+ annihilation state at the interface was not established, it was noted that previous studies of similar interfaces using other techniques showed the existence of a variety of defect and impurity states. The technique has subsequently been applied to other systems including the Si-Si(100)

interface (Schultz *et al* 1988) and the AlGaAs-GaS interface (DeWald *et al* 1988). Given the limited number of available techniques suited to the study of buried interfaces, positron methods may well have a promising future.

1.4 EXPERIMENTAL TECHNIQUES

1.4.1 Angular correlation

Through the conservation of momentum, the motion of an annihilating e^+e^- pair manifests itself in two ways.

1. a slight departure in the co-linearity of the annihilation γ -rays due to the momentum component, p_{perp} , perpendicular to the direction of emission given by

$$\sin \theta = \frac{p_{perp}}{m_0 c} \quad 1:33$$

2. an unequal distribution of the energy of the emitted γ -rays (Doppler shift) arising from the momentum component p_{para} , in the direction of emission given by

$$\Delta E = \frac{1}{2} p_{para} c \quad 1:34$$

where $m_0 c^2 + \Delta E$ and $m_0 c^2 - \Delta E$ are the emitted γ -ray energies and $(\pi - \theta)$, the angle between them.

The first of these effects is exploited by angular correlation of annihilation radiation (ACAR) systems to obtain information on centre of mass motion of the annihilating pair. Generally, e^+ attain thermal equilibrium with the surrounding medium prior to annihilation, so ACAR distributions are predominantly determined by the motion of the

more energetic electrons. For example, the first one dimensional (1D) measurements in metals and semiconductors (DeBenedetti *et al* 1950, Lang and DeBenedetti 1957 and Berko and Hereford 1956) showed distributions comprising a parabolic portion, which could be explained in terms of a simple Fermi gas model, imposed on top of a broader "pedestal", attributed to annihilations with energetic core electrons (see Figure 1.17b). The important effect of defect trapping on ACAR distributions was not realised until later (Berko and Erskine 1967).

A schematic diagram of a 1D ACAR system is shown in Figure 1.17a). The technique involves measuring the coincidence rate $N(\theta)$, between two detectors as the angle θ is varied. $N(\theta)$ distributions typically have milliradian widths, so high resolution is required to generate useful data. Consequently, the sample/counter separation is large (several metres) and the collimated slit width small (\approx mm). Since the system only measures a 1D projection of the annihilation pair momentum, in the z direction, a long slit geometry can be used, as shown in the figure. Adequate counting rates are achieved by using several tens of mCi of ^{22}Na and ^{58}Co as a source (see Table 1.3).

It was realised that an extension of 1D ACAR measurements into two dimensions would yield significant additional information. In principal, 2D resolution can be achieved by reducing the long slit configuration to a "point slit" geometry, albeit with a substantial loss in count rate. However, it was only with the development of multiple detector arrays or position sensitive counters that practical 2D ACAR systems were developed (for example Berko and Mader 1975). Subsequently ACAR measurements have become an important source of information on 2D Fermi surfaces in metals and alloys. Reviews on the ACAR technique have been published by Berko (1983) and West (1973).

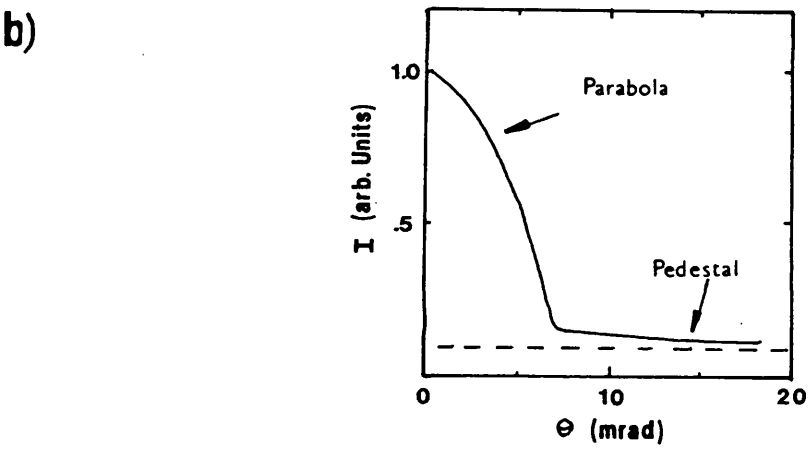
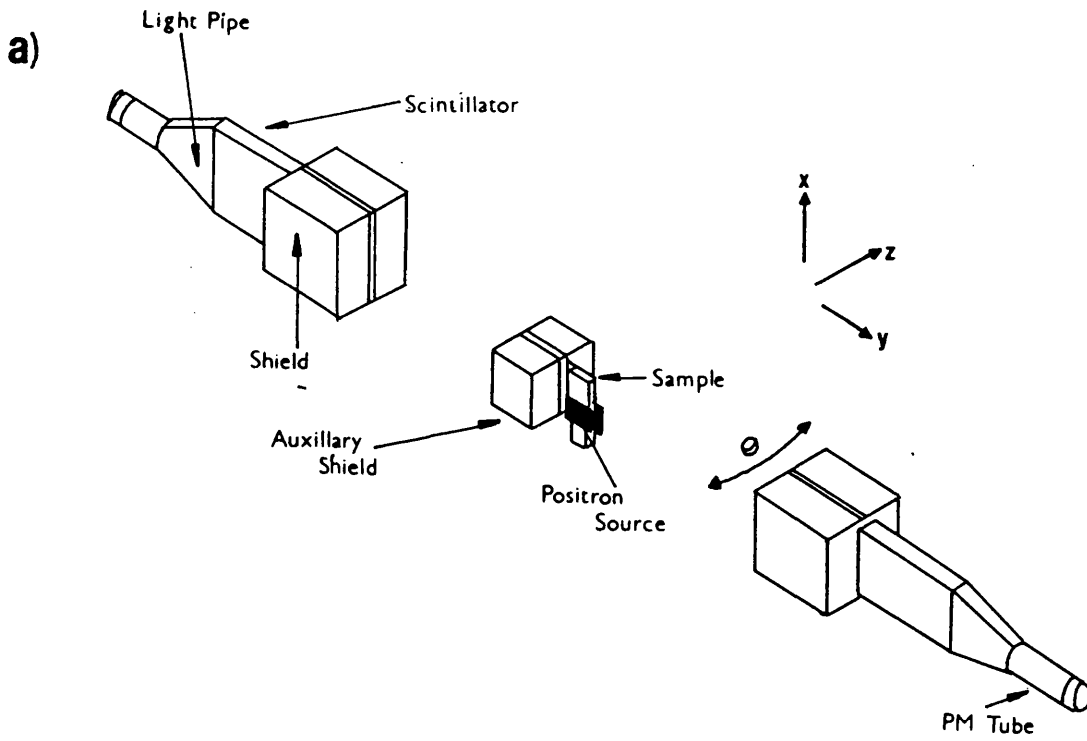


Figure 1.17 ACAR measurements.

- a) Schematic diagram of a one dimensional (1D) ACAR arrangement.
- b) Typical momentum distribution for a metallic sample showing parabolic and pedestal regions due to e^+ annihilation with free and core electrons respectively. Dashed line indicates background arising from random coincidences.

1.4.2 Doppler Measurements

Measurement of Doppler shift given by Equation 1:34 above essentially provides information on the third momentum component not resolved in 2D ACAR studies. Simultaneous measurement of all three components is impractical, so ACAR and Doppler methods are viewed as being complementary. In studies of positron mobility using the Doppler technique, the 511keV photopeak is observed to be either red or blue shifted depending on the orientation of the detector and electric field. However, in experiments such as defect studies, the shift in gamma energy is isotropic, so the Doppler peak appears both red and blue shifted. This technique is therefore referred to as Doppler broadening rather than Doppler shift. Modern Ge detectors have resolutions of $\approx 1\text{keV}$ which corresponds to an ACAR resolution of about 4mrad. Although this is a factor of ten less than that routinely attained by the latter technique, the high data acquisition rates achieved by solid state detectors make Doppler studies suitable for time dependent studies such as defect annealing.

Although it is possible to unfold the resolution function which typically has a width comparable to the required γ energy distribution, analysis of Doppler broadening data by simpler procedures such as S and W parameter determination is more commonplace. The S parameter is defined as the fraction of events in the spectrum residing in a pre-selected group of channels at the peak and W, the fraction of events lying in the wings of the distribution (that is events with large momentum shifts). These parameters can be considered to hold energy related information on the e^+e^- annihilation state. Consequently changes in S parameter have been related to defect trapping in solid media (for example see MacKenzie 1983). Differences in the electronic states of various materials can be exploited to determine the fraction of e^+ annihilating in a particular substance. For example, this method has been used to determine the effective β^+

implantation profile in Ni by sandwiching foils of varying thickness between reflectors of different Z (Linderoth *et al* 1984). A similar approach has been used by MacKenzie *et al* (1973) to measure the back-scattering coefficient, B , as a function of Z .

In the above studies, the positron source was generally a small deposit of the isotopes ^{22}Na or ^{68}Ge supported in a thin foil sandwich and placed between two identical samples. However, the Doppler technique has also been used in conjunction with e^+ beams to determine the vacancy concentration arising from He ion implantation (see Section 1.3.6), and to study defect concentrations at SiO_2 -Si interfaces (Nielsen *et al* 1987 and Section 1.3.7c)). Other beam measurements based upon the Doppler broadening technique have been reviewed by Schultz and Lynn (1988).

In studies of positron motion in electric fields, the e^+ gain sufficient energy from the field to produce a measurable centroid shift in the 511keV annihilation peak, as observed by a Ge detector. These measurements are discussed in Chapter 2.

Gamma energy spectra are frequently used to determine the surface Ps fraction in variable energy beam studies and the bulk Ps fraction in insulators (see Dupasquier 1983). Although not a Doppler method, these measurements rely on finding the ratio of 2-3 γ -ray annihilations by determining the area of the 511keV peak relative to the continuous 3γ background using a Ge or NaI detector (Lynn 1983) and therefore rely on the good energy resolution of the γ -ray detector.

1.4.3 Positron Lifetime Spectroscopy

This technique involves measuring the time interval between the emission of a positron and its subsequent annihilation in the medium under study. By repeating the procedure for a large number of events, a e^+ lifetime spectrum is generated. This data can be subsequently deconvoluted to yield information on the various e^+ annihilation states in the

medium under study. Following its initiation by Shearer and Deutsch (1949), this method has proved to be a powerful instrument for the study of e^+ -gas interactions (for reviews see Griffith and Heyland 1978 and Charlton 1985).

Subsequently, positron lifetime spectroscopy (PLS) has been applied to other states of matter. The earliest measurements in solid media originate from about 1960 when e^+ lifetimes in elemental metals were published. Before 1967 confusion arose from the failure to realise the significance of e^+ -defect trapping, a process which was indeed first observed by PLS (MacKenzie *et al* 1967).

Figure 1.18 shows the mean positron lifetime for annealed metals at room temperature. As discussed in Section 1.2 the annihilation rate is determined by the overlap integral of the electron and positron wave functions. In metals contributions arise from both core and conduction electrons. Although the former are generally more numerous than the latter, e^+ are repelled from the positively charged ion cores, so the relative effect of the outermost electrons is enhanced. The similarity between the periodic variation in mean positron lifetime with atomic number, Z , and that observed for other chemical and physical properties is therefore not surprising.

Although the underlying experimental principles have largely remained unchanged since the early PLS measurements in gases, present day lifetime spectrometers have benefited from considerable advances both in instrumentation and data handling. In the latter case, data reduction by computer using specifically developed software has become common practice, increasing both the speed and accuracy of the analysis procedure. The principles of modern e^+ lifetime spectroscopy are discussed in Chapter 3 and the first direct application of this technique to the determination of e^+ mobility in solids developed in Chapters 2 and 3. The PLS technique and its application to solid state defect and positronium studies have been discussed in the relevant chapters of Brandt and

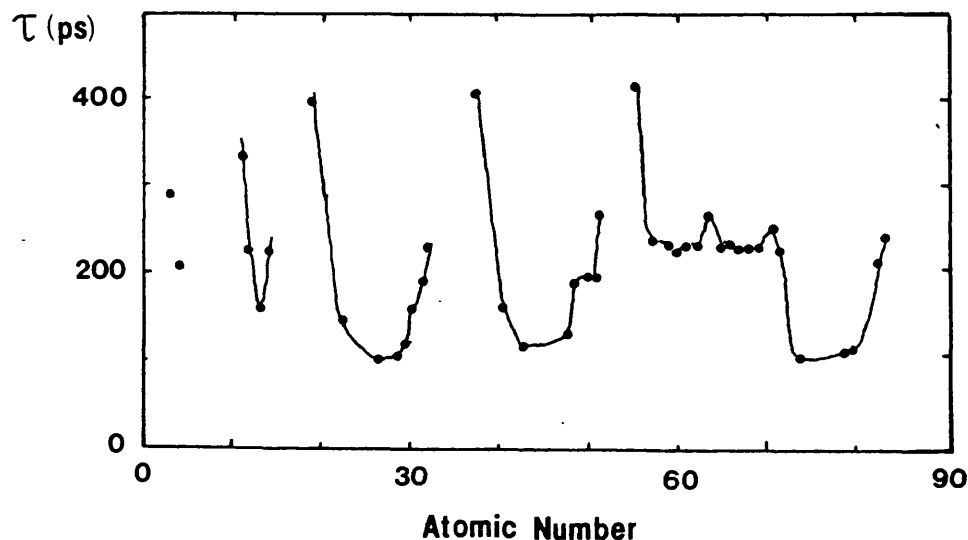


Figure 1.18 Mean positron lifetimes in metals (MacKenzie 1983)

Dupasquier (1983). A survey of current research programmes based around this technique can be obtained from the ICPA8 proceedings (Dorikens-Vanpraet *et al*, eds., 1989).

In terms of characterising the e^+e^- annihilation state in various media, PLS can be viewed as being complementary with Doppler and ACAR measurements. Sen and MacKenzie (1977) hoped that combination of the former two techniques to obtain momentum spectra as a function of positron lifetime in the solid might provide additional information on e^+ annihilation in polymers. They developed an instrument capable of recording such information although this technique has yet to make a significant contribution to this field.

For lifetime studies requiring spatial resolution, the mean positron implantation depth needs to be controlled. Conventional fast timing arrangements using β^+ emitters are therefore unsuitable and another means of deriving a prompt signal is required. Various methods of timing e^+ beams have been developed (for example the system used by Mills and Pfeiffer (1979a) to measure Ps time of flight spectra as discussed in Section 1.3.7c)). Schödlbauer *et al* (1987) have developed a system based around a variable energy pulsed

positron beam to study e^+ trapping in near surface defects. The experimental arrangement, shown schematically in Figure 1.19, incorporates both a beam chopper and buncher to reduce the e^+ pulse width to ≈ 100 ps. A BaF_2 scintillator coupled to a photomultiplier tube monitors e^+ annihilation at the target and is used to drive the start signal input of the time to amplitude convertor (TAC). Stop pulses are derived from the RF signal supplied to the beam buncher and are suitably delayed to ensure they arrive at the TAC after the corresponding start signal. The time resolution of the instrument is ≈ 240 ps with a counting rate of 70 events per second, which compares favourably with conventional fast timing systems. The facility has been used to obtain information on the spatial distribution of defects produced in metals by helium and nitrogen ion implantation (Schödlbauer *et al* 1987, McGervey *et al* 1989).

1.4.4 Positron Beams

Until about 1970 positron studies were performed using fast e^+ from radioactive sources. Whilst this method was adequate for bulk Fermi surface measurements and studies of homogeneous defect concentrations by Doppler and lifetime techniques, it was only with the advent of monoenergetic low-energy beams that e^+ studies of surface structure and non homogeneous defect distributions became feasible. The important application of e^+ beams to e^+ -gas scattering has been reviewed elsewhere (for references see Section 1.1). Early e^+ beam studies were generally carried out in non ultra high vacuum (UHV) conditions, with uncharacterised sample surfaces. Whilst such experiments provided information on the types of e^+ interaction occurring at surfaces (for example the negative work function mechanism for e^+ re-emission by Costello *et al* (1972a, b) and observations of Ps emission by Canter *et al* 1974) a good understanding of the behaviour of e^+ at metallic surfaces only began to be developed with the initiation of experimental arrangements which permitted the preparation and characterisation of clean surfaces *in situ* (for example Mills *et al* 1978 and the other studies described in Chapter 5). The development of e^+ beams is reviewed in Chapter 4.

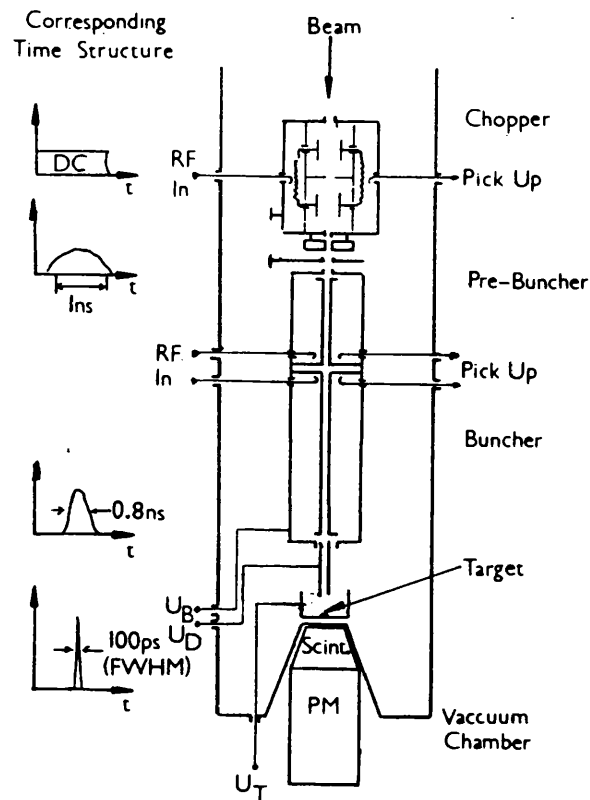


Figure 1.19 Schematic diagram of bunched e^+ beam used for near-surface e^+ lifetime studies (Schödlbauer *et al* 1987).

Positron beams can be considered to comprise four main components:

1. a source of energetic positrons
2. a moderator which converts a small fraction of the incident high energy e^+ spectrum into a nearly monoenergetic low-energy distribution
3. a e^+ transport system which transfers e^+ from the moderator to the interaction chamber and controls the energy and profile of the beam. This part of the system is also important in reducing the γ -ray and fast e^+ backgrounds at the sample
4. an interaction chamber equipped with positron/ γ -ray detectors, and containing the solid target (or gas cell in atomic scattering studies).

The main parameters which characterise the beam properties and the suitability of the instrument for a particular application are

1. the intensity of e^+ (e^+s^{-1} reaching the sample)
2. the angular and spatial spread of the beam
3. the final energy and energy spread of the e^+ reaching the target
4. the magnitude of the γ -ray and fast e^+ backgrounds at the target
5. the time dependence of the beam (that is pulsed or continuous operation).

These points are generally determined by the first three components of the beam, listed above.

a) Sources for slow positron beams

High energy positrons are produced either by β^+ decay of radioactive sources or by pair production from high energy γ -rays. In the former case, the resulting beam is continuous in time, although beam bunching can be achieved using magnetic or electric fields (for example Mills *et al* 1983, discussed above).

The properties of some positron emitting isotopes are listed in Table 1.3. ^{22}Na and ^{58}Co are most commonly employed for e^+ beam production. Their relatively long half lives permit commercial production and subsequent transportation to the beam line. ^{22}Na is supplied either as a sealed source with a thin metal window, or as NaCl solution, which can be used to prepare, by deposition, small sources for specific applications. ^{58}Co has the advantage of a higher specific activity (activity per unit mass) than ^{22}Na , which makes it particularly suitable if the source moderator configuration is arranged in back scattering geometry. Consequently, this isotope is frequently supplied diffused in to a thin Cu ribbon.

TABLE 1.3
Properties of Some e⁺ Emitting Sources

Isotope	Half-life	e ⁺ per decay (%)	End-point energy (MeV)	Fiducial gamma -ray energy	gamma-ray per e ⁺ (%)		Optimum specific surface activity (Cicm ⁻²)
					Fiducial	Others	
¹¹ C	20min	99	.96	-	0	0	-
¹³ N	9.96min	100	1.20	-	0	0	-
¹⁵ O	123s	100	1.74	-	0	0	-
¹⁸ F	110min	97	.635	-	0	0	-
¹⁹ Ne	17.4s	100	2.22	-	0	0	-
²² Na	2.6yr	90	.545	1.275	100	11	.012
²⁶ Al	8.0x10 ⁵ yr	85	1.17	1.81	100	11	-
⁴⁴ Ti	47yr	94	1.47	1.156	100	8	-
⁴⁸ V	16d	50	.696	1.31, .983	200	220	-
⁵⁷ Ni	36h	46	.85	1.37	100	115	-
⁵⁸ Co	71d	15	.474	.811	100	580	.17
⁶⁴ Cu	12.8h	19	.573	-	0	2.5	6
⁶⁸ Ge	275d	88	1.90	1.078	1.7	3	.06
⁸⁹ Zr	79h	22	.90	-	0	250	-

Other sources such as ¹¹C and ⁶⁴Cu have short half lives, and therefore require either continuous or at least frequent replenishment. Consequently they can only be utilised if the beam line is located close to a high flux reactor (Lynn and Frieze 1984) or particle accelerator (Stein *et al* 1974). Their principal advantage is that sources of higher activity than commercially available, (up to ≈100 Ci) can be prepared.

The maximum surface specific activity of a particular source material (expressed as activity per unit area) is determined by its specific activity, which is material dependent and the effect of self-absorption, which is nearly independent of the isotope and limits the maximum useful thickness of the source. This quantity is listed in Table 1.3 for some of the common isotopes used in e^+ beam production. In practice, the maximum surface activity for ^{58}Co is limited by technological difficulties to $\approx 1\text{Ci cm}^{-2}$.

The choice of source support is important in determining the efficiency of a particular source-moderator configuration. In most cases, the solid angle subtended at the source by the moderator is less than 2π , so more than 50% of fast e^+ from the source would be lost if it were not for the effect of back-scattering. The activity is therefore deposited on a high Z backing such as tungsten, which back-scatters up to about 50% of incident e^+ . Furthermore, it has long been realised that lower energy e^+ are more efficiently moderated than those at high energies. Since a proportion of e^+ are back-scattered with substantial energy-loss, this component enhances the moderator efficiency by more than would be expected from a simple geometrical consideration of back-scattering.

Bremsstrahlung emitted by rapid deceleration in a metallic convertor of MeV energy e^- from a linear accelerator (linac) provide the usual source of energetic γ -rays for e^+e^- pair production. The resulting fast e^+ are then moderated in a similar fashion to β^+ particles. Since linacs are pulsed, the final e^+ beam is pulsed as well, unless beam debunching using a magnetic storage ring or "bottle" is included between the moderator and interaction chamber. In some instances, particularly timed e^+ applications, the short ($\approx\text{ns}$) pulse duration of a linac is advantageous. However a major disadvantage is that the benefit of a high instantaneous e^+ intensity (up to $10^6 e^+$ per pulse) can only be fully utilised in the study of infrequent processes, which ensure that the detector systems are not swamped. The development of position sensitive detector arrays with subsequent readout may be a useful addition to linac based beams (Charlton and Jacobsen 1987).

b) Positron moderators

The development of high efficiency e^+ moderators has been the result of a substantial number of experimental and theoretical studies. Each successive improvement in moderator efficiency permitted more precise studies of positron behaviour, particularly their interactions at surfaces, to be performed. These, in turn, resulted in the development of better e^+ moderators, culminating in the relatively high efficiency single crystal metal and solid rare gas configurations currently in use. This progress is reviewed in Chapter 4.

The important steps in the moderation process for metallic materials, namely rapid thermalisation, diffusion and vacuum re-emission at a surface have been discussed briefly in Section 1.3. The latter process is discussed further in Chapter 5. For solid rare gas films, and presumably other insulators such as MgO, the moderation process is different, and is explained by the "hot positron model" developed by Gullikson and Mills (1986) and Mills and Gullikson (1986). This was discussed in Section 1.3.7a). A list of moderator efficiencies is given in Table 4.1.

Source-moderator configurations may be arranged in either back-scattering or transmission geometry (see Figure 1.20). The former has been found to be the most efficient configuration because of the relative ease in producing defect-free, single crystal moderators in semi-infinite rather than thin film form. Furthermore, the shape of the positron implantation profile results in a greater fraction of e^+ diffusing to the incident surface than to any other. However, the major disadvantage of this geometry is the shadowing effect of the source, which reduces the effective moderator area, and difficulties in separating incident and outgoing e^+ beams, particularly in the case of secondary moderator arrangements using electrostatic optics.

Transmission mode moderation was originally achieved using vane moderators (Figure 1.20b)); for example, the MgO moderator developed by Canter *et al* (1972). Subsequently, metallic meshes, polycrystalline foils and, more recently, thin

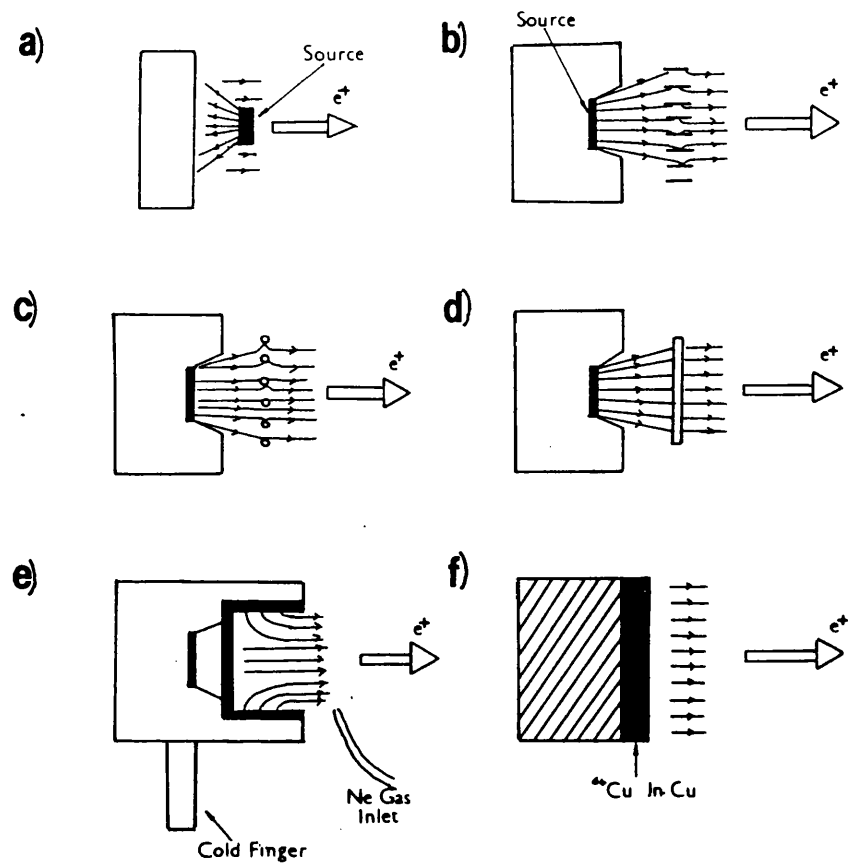


Figure 1.20 Source-moderator geometries.

- a) Metal single crystal: back-scattering geometry.
- b) Vane transmission moderator.
- c) Grid transmission moderator.
- d) Thin polycrystalline/single crystal foil: transmission geometry.
- e) Solid rare gas film moderator.
- f) ^{64}Cu in Cu self moderator.

(1000-20 000Å) single crystal moderators have been developed. Theoretical calculations (see Appendix 1) suggest that the efficiency of the latter foils is slightly less than for similar materials employed in back scattering geometry. Although substantial improvements in efficiency have been reported (for example see Zafar *et al* 1988, 1989 and Gramsch *et al* 1987) they have yet to attain these predicted values. Despite this fact, practical advantages of thin film moderators, particularly in the case of brightness enhancement, will ensure that the transmission configuration becomes more widespread.

c) *Beam transport*

Both magnetically and electrostatically guided e^+ beams have been developed. In the former type, the field is normally created by a solenoid or a series of discrete coils separated by their radius (Helmholtz configuration) to ensure a uniform guiding field. Additional electromagnets or small permanent magnets may also be incorporated to permit fine adjustment of the beam position or to optimise the transport efficiency. Bent solenoids or \mathbf{ExB} deflectors are included to permit the interaction chamber to be located out of line of sight of the source. With appropriate shielding, this arrangement reduces the fast e^+ and γ backgrounds at the sample. The major advantage of magnetic systems is their simple design and the ability to confine e^+ emitted from the moderator with a large range of angles and energies. This property also applies to e^+ scattered in a gas cell, which makes magnetic confinement particularly suitable for some types of cross section measurement (for example Ps formation), although consequently less suitable for angular scattering measurements and studies requiring beams with small energy spreads. For surface physics applications the principal disadvantage of this magnetic transport is that e^+ re-emitted from surfaces spiral in the field resulting in a loss of information on their transverse momentum in a retarding potential analysers. However, by locating a permanent magnet behind the sample, the angular divergence of e^+ moving from the strong field produced by the permanent magnet into the weaker guide field is reduced, so a retarding field analyser records a greater proportion of the total e^+ momentum. \mathbf{ExB} effects also degrade the resolution of retarding grid systems and exclude the use of more sophisticated energy selectors such as hemispherical analysers. An UHV system designed for e^+ solid state studies has been described by Schultz (1988).

For experiments which require a high degree of control of the e^+ beam quality, electrostatic guidance is normally employed (for example Canter *et al* 1986, 1987, 1989). In electrostatic systems, the e^+ beam is guided, accelerated and focussed by a series of lenses each comprising three or more elements maintained at different potentials. Energy

selectivity of incident and scattered e^+ beams can be achieved using hemispherical or cylindrical mirror analysers, which may also serve to reduce the γ -ray and fast e^+ background arising from the source.

Although electrostatic systems permit greater control of beam parameters such as diameter, d , energy, E , and angular divergence, θ , than is possible using simple magnetic arrangements, the performance of both methods of transport is limited by Liouville's theorem, which states that a swarm of particles under the influence of conservative forces occupies a constant volume in phase space. For a particle beam this implies

$$\sin^2 \theta d^2 E = \text{constant} \quad 1:35$$

so the brightness per unit energy, R , of a beam of intensity, I , defined by

$$R = \frac{I}{\sin^2 \theta d^2 E} \quad 1:36$$

is also a conserved quantity. Consequently, the diameter of the beam, which is normally governed by the source/moderator dimensions and geometry needed to give the required intensity, can only be reduced at the expense of increasing θ , or reducing E and/or I . However, as proposed by Mills (1980), the process of moderation is non-conservative and therefore not constrained by Liouville's theorem. A e^+ beam can therefore, be focussed down to a small spot on a secondary moderator and the remoderated e^+ beam will have a significantly reduced diameter whilst still maintaining the original energy and angular spread of the primary beam. Although there is a reduction of $\approx 50\text{-}75\%$ in intensity of the final beam after each stage of remoderation due to e^+ losses in the foil, an increase in R of a factor of 10 or more can be achieved. The process can be repeated a number of times to give substantial improvements in R . The technique has been successfully applied by several research groups (for example Canter *et al* 1989) to produce micron sized beams suitable for use as a e^+ microscope.

d) The interaction chamber

The design of the interaction chamber and associated γ -ray or e^+ detectors is determined by the specific application of the system. For solid state studies, the chamber may be equipped with a means of surface preparation such as ion sputtering and electron beam annealing. Standard surface analysis instrumentation such as LEED/Auger may be included to characterise samples prepared *in situ*. Alternatively, these facilities may be incorporated in an adjacent preparation chamber, and the sample introduced into the beamline using a precision transfer system.

Slow positrons in beam studies can be detected either directly or from their annihilation γ -rays. Direct detection is generally achieved using channel electron multipliers (CEMs) or CEM arrays (micro-channel plates) which operate by secondary electron amplification following e^+ impact. γ -ray events are recorded using scintillation detectors coupled to photomultiplier tubes, or solid state germanium detectors, which are particularly suitable for defect studies because of their superior energy resolution. Position sensitive 2D γ systems are used in conjunction with intense positron beams to measure ACAR spectra at surfaces.

1.5 SCOPE OF THE CURRENT WORK

An introductory review of positron interactions in solid media has been given and the various techniques developed to observe these processes discussed.

The development of e^+ beams in the late 1960's and subsequent rapid improvements in this technique have opened up the possibility of studying the interactions of positrons at surfaces and in the near-surface bulk. Beams with intensities of 10^5 - $10^6 e^+s^{-1}$ are in use in several laboratories (for example Schultz 1988). Stronger beams require dedicated linacs (Howell *et al* 1985a) or access to a high flux reactor (Lynn *et al* 1987b) to produce intensities up to $10^9 e^+s^{-1}$. Whilst these facilities are clearly of considerable value in

advancing research with e^+ , their widespread use is limited by expense. Further experimental and theoretical work is still required before a complete understanding of e^+ processes at surfaces can be achieved. In many cases more detailed measurements demand substantial improvements in current technology, particularly the development of more intense beams with better spatial and energy resolution. Novel probes of surface structure, such as REPELS and LEPD have begun to be evaluated and results compared to conventional e^- methods (see Table 1.1). Potential advantages of e^+ techniques have to be offset against experimental difficulties and the extra expense of producing good quality e^+ beams of adequate intensity in comparison to commercially available electron beams with μA currents.

The main motivation behind the present work is the desire to produce more intense laboratory based beams. Conventional positron moderators rely on diffusion to transport a small fraction ($\approx 1\%$) of implanted e^+ to a surface, where they can be re-emitted into vacuum, guided and accelerated to produce a beam. The processes governing positron diffusion including the important effect of e^+ trapping in defects are well understood and as discussed in Chapter 4, there appears to be little scope for further improvements in efficiency of conventional moderators. Furthermore shielding requirements, commercial availability and expense limit the strength of β^+ sources to $\approx 100\text{mCi}$, so development of laboratory based e^+ beams with intensities significantly greater than $\approx 10^6 e^+ s^{-1}$ is unlikely with current technology.

The motion of positrons in electric fields is considered in Chapter 2 and a review of previously published work on this subject presented. These studies show that in some materials e^+ acquire a substantial drift velocity, v_+ , which is usually related to the applied field, ξ , by the expression

$$v_+ = \mu_+(\xi)$$

where μ_+ is the positron mobility. A new method of determining μ_+ using a positron lifetime technique is proposed. In Chapter 3 measurements of μ_+ in Si by this method are described. These results show that at 100K, up to 8% of e^+ implanted into a high purity Si crystal can be drifted to an interface. This is approximately a factor of eight greater than that expected by diffusion alone.

The first suggestion of using an electric field to enhance the motion of e^+ to the surface of a moderator is attributed to Lynn and McKee (1979). However their attempt to produce a "field assisted moderator" using a thin Si surface barrier detector, were unsuccessful. In Chapter 4, field assisted moderation is considered in detail and calculations presented which show that up to 10% of e^+ implanted into Si from a ^{22}Na source can be drifted to a contact. It is suggested that the problem of e^+ trapping in the metal contact might be overcome using a conducting layer formed epitaxially on a semiconductor or insulator surface. The $\text{NiSi}_2\text{-Si}$ structure is considered to have many of the properties required for a working field assisted moderator. The possibility of improving the efficiency of rare gas solid moderators by the application of electric fields is also considered.

In Chapter 5, the negative work function mechanism for e^+ re-emission from surfaces is discussed and experimental results for metals and insulators reviewed. Although several measurements of the e^+ work function for Si have been reported, these results are inconsistent. Measurements of positron re-emission from clean and oxygen exposed Si(111) and (100) surfaces in ultra high vacuum are described and it is concluded that the small yields of e^+ recorded are a result of a non-thermal rather than a negative work function mechanism.

Chapter 6 is a summary and conclusion to the present work. Scope for further work on field assisted moderation is suggested.

CHAPTER 2

POSITRON MOTION IN AN EXTERNALLY APPLIED ELECTRIC FIELD

2.1 INTRODUCTION

In Chapter 1 non-equilibrium (thermalisation) and equilibrium (thermal transport) e^+ motion were briefly reviewed. In this chapter the discussion is extended to cases where e^+ motion is influenced by an externally applied electric field. In general, the effect of an E-field on positron motion is to:

1. change the e^+ thermalisation time;
2. raise the effective equilibrium positron temperature above that of the lattice; and
3. impart a drift velocity onto the random thermal motion of the e^+ .

The relative importance of these effects depends on both the magnitude of the applied electric field and the properties of the host solid. The motion of e^+ in equilibrium with the field has been studied in several materials (see Section 2.4) and is particularly relevant to the understanding of slow positron beam formation and the interaction of e^+ with vacancies in crystalline solids. The possibility of developing more efficient (field assisted) moderators provides motivation for further work in this area (Beling *et al* 1987b and Chapter 4). The effect of high electric fields on positron thermalisation in solid matter has received less attention. Measurements of this type promote a better understanding of slowing down processes and may provide an explanation for the apparent discrepancies in measured e^+ mobilities as determined by different techniques.

2.2 THE EFFECT OF AN ELECTRIC FIELD ON POSITRON IMPLANTATION

In all practical cases, e^+ supplied to a solid initially possess energies significantly greater than those associated with a thermal e^+ ensemble. However, in most materials, e^+ rapidly cool to the lattice temperature by a combination of electron excitations and phonon interactions. The total thermalisation time depends on the properties of the surrounding bulk and its temperature, but is typically between 3 and 60ps (Nieminen and Oliva 1980). Although hot e^+ effects during this period determine quantities such as the e^+ implantation profile and positronium fraction, most e^+ annihilate or escape into vacuum from a surface after attaining thermal equilibrium with the lattice. Consequently most experiments measure properties relating to cool or thermal e^+ . A notable exception to the above argument is the observation of hot e^+ re-emission from rare gas solids first reported by Gullikson and Mills (1986) as discussed in Section 1.3.7b).

Only one direct study of the influence of an electric field on the positronium implantation profile has been published. Heinrich (1978) employed a collimated slit detection system to monitor the γ -rays produced by positron annihilation in polyethylene samples, following implantation from a 200mCi ^{64}Cu source. The experimental arrangement is similar to that used by Brandt and Paulin (1977), which is shown in Figure 2.7. The samples were mounted on a micrometer screw to enable the singles and coincidence count rates to be recorded as a function of depth in the sample, x . The whole implantation profile could thus be recorded. With an applied electric field of 100kVcm^{-1} , the relative change in singles counting rate, $\left(\frac{\Delta N}{N}\right)_A$, reproduced in Figure 2.1, is strongly dependent on x and is therefore inconsistent with the view that the only effect of the electric field is to drift thermalised e^+ . Instead Heinrich (1978) concluded that the dominant change in $\left(\frac{\Delta N}{N}\right)_A$ was due to a depth dependent e^+ absorption coefficient, α_+ , and that after allowing for this effect, the post-thermalisation drift of e^+ was in fact negative. No explanation for this surprising behaviour has been offered. It would be useful to repeat these measurements to see whether the changes in implantation profile occur in other materials.

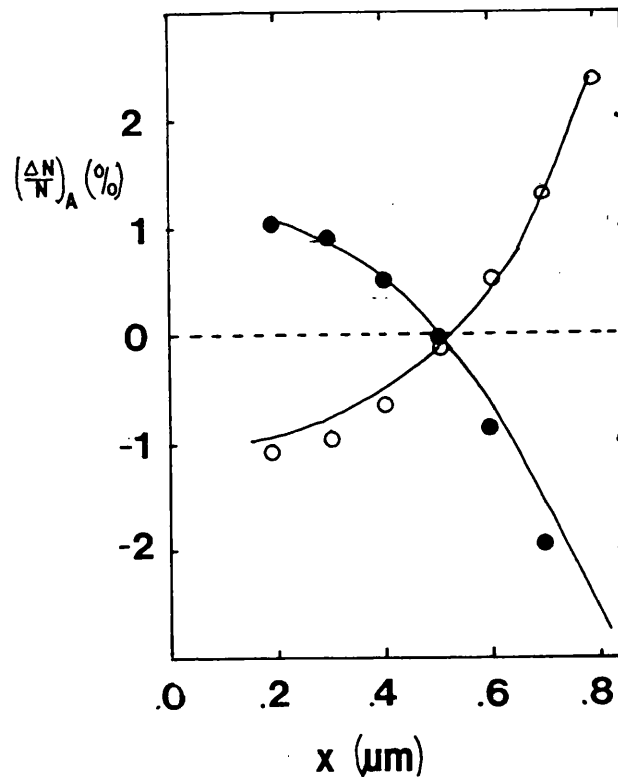


Figure 2.1 Effect of an applied electric field on e^+ implantation profile in polyethylene. Relative change in count rate $(\frac{\Delta N}{N})_A$ produced by the field.

○ +100kVcm⁻¹

● -100kVcm⁻¹

Curves are fits which allow for the effect of the field during thermalisation. (Heinrich 1978)

With the application of large electric fields ($\geq 0.1\text{MVcm}^{-1}$), thermalisation times are increased and e^+ spend a significant proportion of their lifetime at non-thermal energies. The equilibrium energy attained by the e^+ is governed by the relative rates of energy loss due to scattering and the energy gain from the field between collisions. In insulators, where fields $\approx 10\text{MVcm}^{-1}$ can be sustained, equilibrium energies of the order of several eV are expected and heating of e^+ following partial thermalisation can occur.

Measurements of the electric field dependence of positronium formation in polyethylene reported by Bisi *et al* (1981) may show the effect of e^+ heating. Experimental values of the Ps yield, f , are shown in Figure 2.2 together with a theoretical fit performed by Brandt (1982). These data show that following an initial decrease at low fields, f passes through a minimum at about 0.4MVcm^{-1} . At higher fields f increases rapidly and finally tends asymptotically towards 100% Ps formation. The theoretical treatment performed by Brandt (1982) indicated that a simple Ore model describes the variation of f . With no applied electric field, e^+ which cool below the positronium threshold ($\approx 3.2\text{eV}$ in polyethylene) annihilate as free e^+ , whereas those residing within the Ore gap form Ps and subsequently annihilate in this bound state. At high electric fields, e^+ are heated into the Ore gap increasing the Ps fraction until it saturates at 100%. Mogensen (1983) subsequently disputed this interpretation and suggested that positron detrapping from shallow defect sites and charging effects should be taken into account. It is possible that the thin foils used for the high field measurements may have introduced substantial errors into the measured Ps yields. Mogensen (1983) concluded that e^+ heating to energies sufficient to repopulate the Ore gap was unlikely and that the measurements were not inconsistent with the spur model for Ps formation even if heating of e^+ occurred.

In an experiment described in detail in Section 2.4, MacKenzie and Ghorayshi (1985) measured e^+ mobility, μ_+ , and positronium fraction, f , in several insulating materials stressed by electric fields up to $\approx 10\text{kVcm}^{-1}$. For all materials studied, they found that f either remained constant or decreased with increasing electric field. This behaviour could not be related to the usual classification of the insulators into categories such as ionic crystals, polar and non polar polymers. For materials with a significant positron mobility, a decrease in f with increasing μ_+ was always observed. No physical interpretation of this behaviour was offered and the authors suggested that further studies, with well characterised samples are necessary before a complete understanding of positron behaviour in electric field stressed polymers can be established.

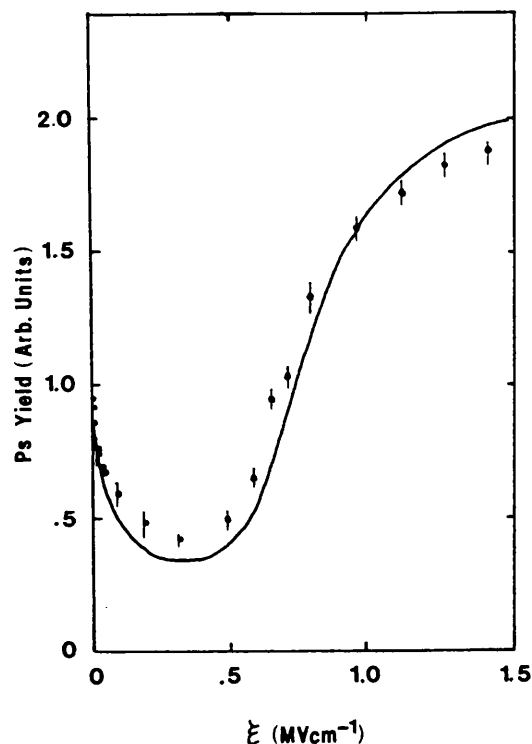


Figure 2.2 Fractional variation of Ps fraction, f , in polyethylene with applied electric field

- Experimental data (Bisi *et al* 1981)
- Theoretical fit based on simple Ore model of Ps formation (Brandt 1982)

2.3 EQUILIBRIUM POSITRON MOTION - POSITRON MOBILITY

The electric field motion of conventional charge carriers (electrons and holes) has been extensively studied in many materials, mainly through its importance in developing semiconductor devices and understanding dielectric breakdown phenomena in insulators. In general, transport behaviour of positrons is expected to be similar to that of holes, and experimental results tend to support this viewpoint.

At low or intermediate electric fields, e^+ implanted into solid media will attain near thermal equilibrium with the lattice in times comparable to those for zero-field

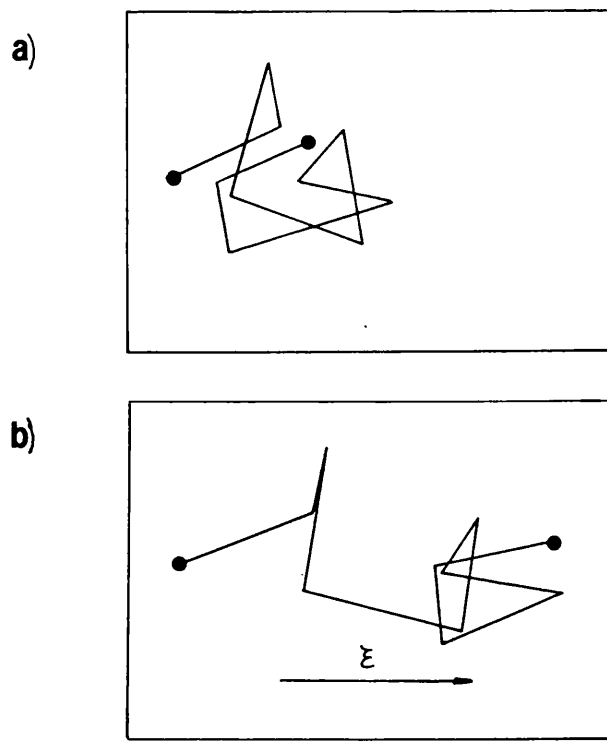


Figure 2.3 Effect of an applied electric field on thermal e^+ motion

a) e^+ random thermal motion

b) electric field induced drift velocity imposed on e^+ random thermal motion

thermalisation. Subsequently the electric field superposes a constant drift velocity, v_+ , on the normal thermal motion of the e^+ (see Figure 2.3). v_+ is usually related to the applied E-field, ξ , by the expression

$$v_+ = \mu_+(\xi) \xi \quad 2:1$$

where $\mu_+(\xi)$ is the field dependent positron mobility. An elementary treatment of free carrier mobility at low fields can be developed by ascribing a mean free path, l , between scattering events. In this case, their thermal velocity of motion, v_T , is approximated by

$$v_T \approx \left(\frac{2kT}{m^*} \right)^{\frac{1}{2}} \quad 2:2$$

where m^* is the charge carrier effective mass, which crudely takes into account the overall effect of band structure, and the mean free time between collisions is

$$\tau = \frac{l}{v_T} \quad 2:3$$

The electric field accelerates the carriers at a rate

$$a = \frac{e \xi}{m^*} \quad 2:4$$

and imparts a velocity $a\tau$ in one mean free time. Collisions are assumed to be spherical, so the effect of the E-field is lost after each scattering event. The drift velocity, v_c , is thus approximately given by,

$$v_c = \left(\frac{el}{m^* v_T} \right) \xi \quad 2:5$$

and comparing (2:5) with (2:1) gives

$$\mu_c = \frac{el}{m^* v_T} \quad 2:6$$

μ_c , the carrier mobility, is expected to be temperature dependent, mainly through the variation in l . Measurements of μ_c with temperature for all carrier types show that this dependency can be expressed as a power law of the form

$$\mu_c \propto T^{-n} \quad 2:7$$

To a good approximation, $l \propto T^{-1}$ so from 2:6 and 2:7, $n = 1.5$. However, experimental measurements for electrons, holes and positrons in Si (see Table 2.1) give different values of n . This is mainly due to the effects of a more complicated band structure and contributions from other scattering processes apart from the acoustic phonon mode.

For non-degenerate cases, μ_c is related to the diffusion constant, D_c , via the Einstein relation

$$D_c = \mu_c \frac{kT}{e} \quad 2:8$$

In degenerate cases and at high fields this expression is not strictly valid, although approximations may still hold. For positrons, measured values of both D_+ and μ_+ provide evidence of complete thermalisation in silicon. These experiments are described in Section 2.4.

At intermediate fields, free carriers are unable to dissipate the energy supplied by the field and their average temperature rises above that of the lattice. In this case it is necessary to equate the power input from the electric field to the power loss due to scattering. Continuation of the above approach to carrier drift leads to a

$$v_c \propto \xi^{\frac{1}{2}} \quad 2:9$$

variation. Shockley (1951) performed a more detailed treatment of the motion of non-degenerate particles in semiconductors and derived an expression for the acoustic phonon limited drift velocity:

$$v_c = \sqrt{2} \mu_c \xi \left\{ 1 + \sqrt{1 + \left(\frac{3\pi}{8} \right) \left(\frac{\mu_c \xi}{v_l} \right)^2} \right\}^{-\frac{1}{2}} \quad 2:10$$

TABLE 2.1
Charge Carrier Properties in Silicon and Germanium

	Electron	Hole	Positron
Charge	-1	+1	+1
Silicon			
Effective mass (m_e)	.98 (trans.) .19 (long.)	.016(light) .49(heavy)	-
Mobility (300K) $\text{cm}^2\text{V}^{-1}\text{s}^{-1}$	1500	450	$\approx 80^a$ ($T^{-1.5}$ extrap.) 104(12) ^b 80 ^c 430(100) ^d $\approx 50^e$
n (see Equation 2:7)	2.42 (300K)	2.2(300K)	1.2(.1) ^a (80-184K) 1.3(.1) ^e (100-300K)
Germanium			
Effective mass (m_e)	1.64 (long.) .052(trans.)	.044 (light) .28 (heavy)	1.23(.17) ^f
Mobility (300K) $\text{cm}^2\text{V}^{-1}\text{s}^{-1}$	3900	1900	$21^g(T^{-1.5}$ extrap.) 8-20 ^h
n (see Equation 2:7)	1.66 (300K)	2.33(300K)	$\approx 1.9^h$ (200-500K) 1.1(.1) ^g

References

- a) Mills and Pfeiffer (1977)
- b) Nielsen, Lynn, Vehanen and Schultz (1985)
- c) Present work; Simpson, Stewart, Beling and Charlton (1989)
- d) Brandt and Paulin (1977)
- e) Corbel, Hautojärvi, Makinen, Vehanen and Mathiot (1989)
- f) Shulman, Beardsley and Berko (1975)
- g) Mills and Pfeiffer (1976)
- h) Jorch, Lynn and McMullen (1984)
- other data from Sze (1981)

where v_c is the longitudinal sound velocity ($=8.43 \times 10^5 \text{ cm s}^{-1}$ in Si). The positron drift measurements of Mills and Pfeiffer (1976, 1977) discussed in Section 2.4 are well fitted by this expression. In semiconductors, more efficient optical phonon scattering becomes important at higher fields. In Si and Ge this process ultimately leads to the saturation of hole and electron drift velocities at values approximately corresponding to half the energy required to create an optical phonon. Theoretical treatments of charge transport at high electric fields are difficult to perform exactly, although various approaches have been adopted which provide a good description of experimental measurements. This has been the subject of a review by Jacobini and Reggiani (1979). Measurements of positron mobility at high fields have yet to be reported, but should provide an interesting test of this theory.

2.4 EXPERIMENTAL MEASUREMENTS OF POSITRON MOBILITY

The earliest measurement of positron mobility, μ_+ , reported by Lang and DeBenedetti (1957), involved measuring a shift, $\delta\alpha$, in the e^+ angular correlation spectrum due to the presence of an electric field. The e^+ drift velocity, v_+ , is related to $\delta\alpha$ by

$$v_+ = c \delta\alpha \frac{m}{m_+} \quad 2:11$$

where c is the velocity of light and m_+ the positron effective mass. Because of its high electron mobility, Lang and DeBenedetti (1957) chose diamond for their study in the hope that e^+ might prove to be similarly mobile. A thin layer of aquadag (colloidal graphite) was applied to the flat faces of several 1mm thick diamonds and a 60Hz, 100V potential applied between these and the metallic diamond supports. Using a 1D angular correlation apparatus, coincidence signals derived during positive and negative parts of the voltage cycle were recorded on separate scalars A and B. Data were accumulated at angular

95

settings of -5, 0 and +5 milliradians during a 50minute cycle. The resulting distribution B was found to be shifted by .073mrad with respect to A, in the correct direction for the field. However the derived value for μ_+ of $(120\pm 160)\text{cm}^2\text{V}^{-1}\text{s}^{-1}$ was zero within the statistical accuracy of the experiment, so Lang and DeBenedetti (1957) concluded that there was no evidence of positron motion due to the E-field. One explanation given for this negative result was that e^+ might be trapped in non-mobile states, so the authors proposed repeating their measurements with better characterised samples.

Sueoka and Koide (1976) repeated these measurements in diamond and found for $m_+^* = m_e$, $\mu_+ < 20\text{cm}^2\text{V}^{-1}\text{s}^{-1}$ at 291 and 90K: an order of magnitude less than their Wigner Seitz method calculation. This discrepancy may have been due to positron trapping in defects although it was considered unlikely, since the measured angular correlation curves closely resembled those obtained for annealed diamond, despite the samples being unannealed. Another possible explanation is that the calculation is in error due to the uncertainty in m_+^* . For example, an increase in m_+^* from m_e to $2m_e$ reduces μ_+ by a factor of 10. In principle m_+^* can be determined from angular correlation measurements (Shulman *et al* 1975). However, in diamond the broad angular distribution renders this approach practically impossible. The reason for the disagreement between theory and experiment therefore remains unresolved although Sueoka and Koide (1976) believed that their experimental measurements were reliable. In an appendix to this work, similarly obtained values for μ_+ of <15 and $<80\text{cm}^2\text{V}^{-1}\text{s}^{-1}$ in synthetic quartz and BaTiO_3 respectively were reported. From these results Sueoka and Koide (1976) infer that e^+ mobilities in insulators are smaller than those of electrons and holes.

An alternative method of determining μ_+ by γ -ray spectroscopy is to measure the Doppler shift of the 511keV annihilation line due to positron drift in an applied E-field. This shift was first observed by MacKenzie and Campbell (1972) by measuring the centroid shift of

the single escape γ peak in a coaxial Ge(Li) detector. On changing the detector bias by 600V, a 50eV shift in the peak energy was observed. The Doppler shift, δ , is related to the positron drift velocity by the expression

$$\delta = \frac{\Delta E}{E} = \frac{v_+}{2c} \quad 2:12$$

where ΔE is the shift at energy, E . The value of ΔE measured by MacKenzie and Campbell (1972) implies an improbably high positron mobility in Ge, so the origin of the 50eV shift remains unclear, although the argument that e^+ motion can Doppler shift γ -ray peaks has subsequently been shown to be valid.

Mills and Pfeiffer (1976) published the first quantitative measurement of positron mobility by a Doppler method. A large coaxial intrinsic Ge (IG) detector was used to monitor the 511keV peak produced by e^+ annihilating in a second planar IG detector. Event signal pulses associated with the thermalisation of e^+ entering the second detector were applied to the coaxial detector as a gating pulse. Since the expected Doppler shift was small ($\frac{\Delta E}{E} \approx 1 \times 10^{-5}$) highly stable electronics were required. To minimise the effect of electronic drift, the bias voltage, V , applied to the planar detector was switched between 2 values, V_1 and V_2 , every 1000s in an eight step cycle (1,2,2,1,2,1,2,1). The data were stored in a multichannel analyser (MCA) and read out at the end of each 1000s interval. A reference peak was collected simultaneously by feeding pulses from a stable pulser into the preamplifier test input. This peak was used to correct the energy distribution data for small gain drifts in the system. These were typically 1 part in 10^5 . Data were analysed in two ways: by performing a gaussian fit to the V_1 and V_2 peaks and calculating the centroid shift or by subtracting the two area normalised curves point by point and performing a suitable fit to the resulting distribution. Both methods were found to be in agreement.

Data were obtained for different values of V_1 and V_2 at $(95\pm 5)\text{K}$ (LN_2 in the dewar) and $(36\pm 5)\text{K}$ (LH_2 in the dewar). Although there was some evidence of non linearity at 36K, the data were well fitted by straight lines, giving values of $\mu_+(36\text{K}) = (350\pm 17)\text{cm}^2\text{V}^{-1}\text{s}^{-1}$ and $\mu_+(93\text{K}) = (124\pm 10)\text{cm}^2\text{V}^{-1}\text{s}^{-1}$. As a control experiment, the planar detector was rotated through 90° so that the bias field was perpendicular to the momentum of the γ rays monitored by the second detector. As expected, no Doppler shift was observed.

Mills and Pfeiffer (1976) concluded that after accounting for the difference in effective mass, positron motion in Ge under the influence of an E-field is similar to that of holes. Although acoustic phonon interactions are assumed to be the dominant e^+ scattering process, the low temperature data showed some evidence of velocity saturation, which may have been due to the effect of optical phonon generation. The low value of 1.2 obtained for n from the ratio of μ_+ at the two different temperatures could also be a result of this process. Alternatively, the rise in μ_+ with decreasing temperature might be limited by the increasing importance of impurity scattering at low temperatures.

Mills and Pfeiffer (1977) repeated these measurements in silicon and found $\mu_+(80\text{K}) = (460\pm 20)\text{cm}^2\text{V}^{-1}\text{s}^{-1}$ and $\mu_+(184\text{K}) = (173\pm 15)\text{cm}^2\text{V}^{-1}\text{s}^{-1}$. The low temperature data showed strong evidence of velocity saturation so the data were fitted to Equation 2:10 to determine the true low field positron mobility. As observed in Ge, the ratio of mobilities at the two temperatures gave a value for $n < 1.5$, which suggests that some non-acoustic phonon scattering was taking place. The data obtained by Mills and Pfeiffer (1977) in Si is reproduced in Figure 2.4.

More recently, the technique was refined by Mills *et al* (1986) to measure the much lower positron mobility in polyethylene. $2\times 2\times 0.092\text{cm}^3$ samples with painted aquadag contacts were placed on either side of a $20\mu\text{Ci}$ source and the arrangement clamped between stainless steel plates. The Ge detector used to monitor the 511keV γ peak was situated behind a lead collimator so that solid angle corrections could be neglected. Pulses from

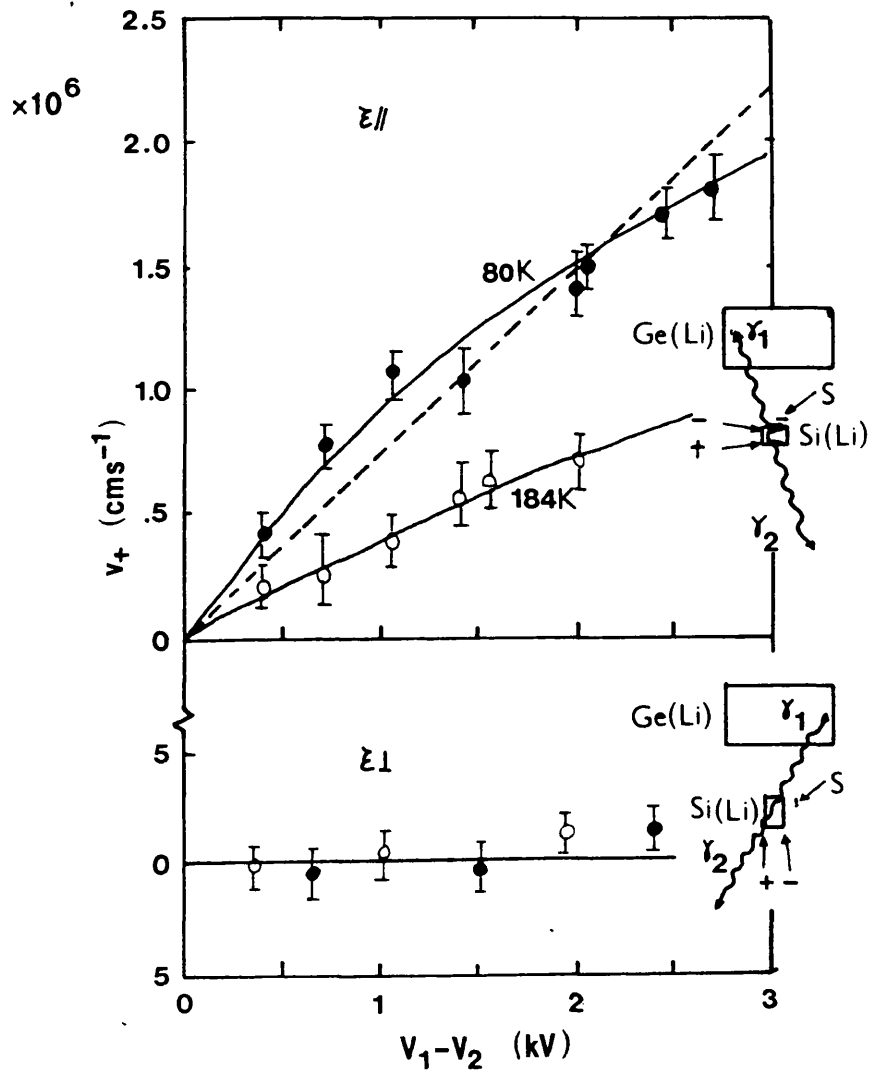


Figure 2.4 Change in positron drift velocity, v_+ , as a function of bias, V_1-V_2 applied to an Si(Li) detector sample of active thickness 0.43cm

- a) Field applied parallel to momentum of γ -rays monitored by the second detector
- b) Field applied perpendicular to momentum of γ -rays monitored by the second detector. As expected no Doppler shift was observed in this orientation

(Mills and Pfeiffer 1977)

the detector were sent to two single channel analysers set on the upper and lower halves of the 511keV photopeak. The amplitude gain was adjusted automatically by a long time constant feedback loop that sensed the difference in A and B count rates. These rates were recorded on a dual input MCA operating in multi-channel scaling mode, which enabled the channel number at which the counts were being added to be swept up and down with a 1ms dwell time. A systematic sawtooth waveform corresponding to the channel number was amplified to a 100V signal and, together with its inverse, applied to the two sides of the samples.

A Doppler shift of the 511keV photopeak caused equal and opposite changes in the count rates A and B. To calibrate the system, fixed changes in the amplifier gain were introduced and the corresponding changes in count rate noted. Checks were performed to ensure that the line centre shift was due to a velocity Doppler effect and not some other systematic effect proportional to the magnitude of the applied field.

The measured variation in positron drift velocity is shown in Figure 2.5. In this case the internal field has been used which includes the effect of the dielectric constant ($\epsilon = 2.26$ for polyethylene). A value of $(10.3 \pm 1.5) \text{cm}^2 \text{V}^{-1} \text{s}^{-1}$ for μ_+ was obtained from the slope of the data. As expected, data collected with the applied electric field perpendicular to the line joining the samples to the detector showed no Doppler shift.

MacKenzie and Ghorayshi (1985) measured μ_+ and the electric field variation of the positronium fraction, f , in several insulators using an experimental arrangement which facilitated simultaneous collection of annihilation γ -ray, time and energy spectra.

A signal oscillator drove a transformer, which supplied the electric field to the samples. The period of the oscillator was long enough to ensure that the E-field was effectively constant during one e^+ lifetime, yet short enough to average the effects of electronic instability or polarisation relaxation of the field. The oscillator also fed an analyser x-axis

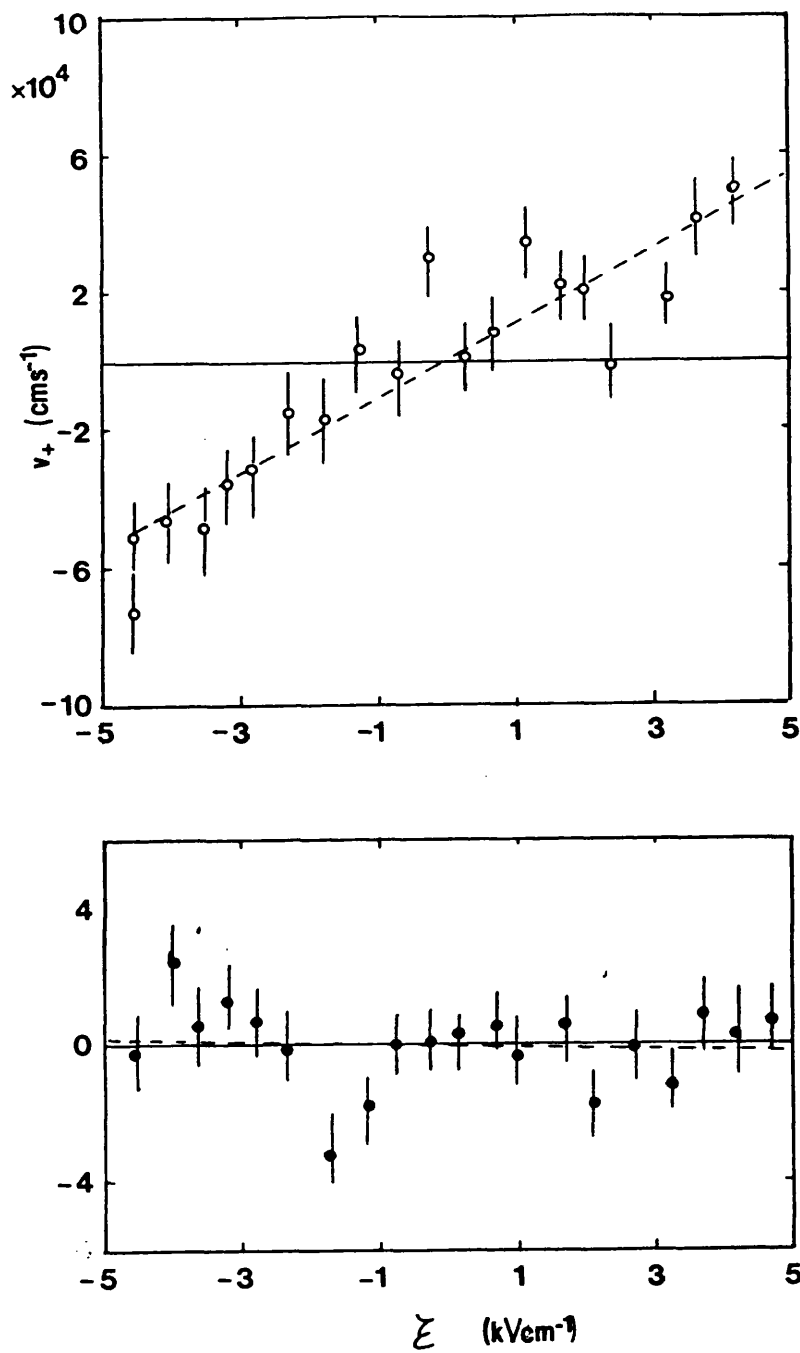


Figure 2.5 Measurement of positron drift velocity, v_+ , in polyethylene as a function of the internal electric field

- Electric field applied parallel to line, d, joining samples and detector
- Electric field perpendicular to d. No significant Doppler shift was observed for this orientation

(Mills *et al* 1986)

analogue to digital convertor (ADC), so that time or energy pulses supplied to the y-axis ADC input were stored in one of 32 parts of the analogue memory according to the instantaneous applied field.

The positronium fraction, f , was derived from the lifetime spectra by calculation of the intensity of the o-Ps component. These results have already been discussed in this section. The positron mobility, μ_+ , was deduced from the centroid shifts in the 511keV annihilation peak recorded in the γ spectra. The authors noted that, apart from a Doppler shift in this peak, which is described by Equation 2:12 above, an additional shift arises from Ps formation. These two effects can be distinguished by collecting data, both with the field parallel and perpendicular to the line joining the samples and detector. In the latter case only the shift caused by Ps formation is observed. Alternatively, using just the parallel alignment, the Doppler component can be recognised because it is antisymmetric, whereas the Ps formation related shift is symmetric with applied field.

The values of μ_+ measured by MacKenzie and Ghorayshi (1985) are listed in Table 2.1, together with the other published measurements. Apart from polyethylene and paraffin wax, low mobility values were recorded. In polyethylene, μ_+ , was significantly greater than that obtained by Mills *et al* (1986). This discrepancy may arise from the effect of the dielectric constant on the internal field, which was neglected by MacKenzie and Ghorayshi (1985). Another possibility is that large variations in μ_+ may be exhibited by different polyethylene samples, suggesting that the measurements should be repeated for better characterised samples. No explanation of the surprisingly high value of μ_+ in paraffin wax was offered.

Ball *et al* (1989) made a more detailed study of positron mobility in paraffin wax over the temperature range 274-311K. The data were corrected for the non-mobile Ps fraction, f , using the expression

$$\mu_+ = \frac{\mu_m}{1-f} \quad 2:13$$

where μ_m is the measured value of μ_+ .

The internal field was calculated in the local field approximation to be

$$\xi = \xi_a \frac{(2+\epsilon)}{3} \quad 2:14$$

where ξ is the applied electric field and ϵ the zero frequency dielectric constant. Over the measured temperature range, μ_+ increased from 10.9 at 274K to 78.7cm²V⁻¹s⁻¹ at 311K, suggesting a thermally activated transport mechanism. In this case

$$\mu_+ \propto \exp\left(-\frac{E_b}{kT}\right) \quad 2:15$$

where E_b is the binding energy of the trapped e^+ state. PLS results published by Dannefaer *et al* (1989) suggest that a similar mechanism describes e^+ transport in GaAs. In this case, the traps are possibly boron or nitrogen impurity sites with a positron binding energy of 23meV.

Polarisation effects in insulators may be a significant problem in studies of positron motion, and indeed may explain differences in mobility values published for the same material. If substantial polarisation effects do occur, the internal field may be time dependent, with a relaxation time comparable to the run time required to measure μ_+ . In this case the time dependent field is difficult to determine and will therefore lead to uncertainties in μ_+ .

TABLE 2.2
Measurements of Positron Mobility

Material	μ_e (cm ² V ⁻¹ s ⁻¹)	Method
Polyethylene	10.3(1.5)	Doppler ^{a)}
	27.7(2.4) [low density] 31.0(2.1) [high density]	" ^{b)}
	≈10	Implantation ^{c)}
Silicon	460(20) [80K] 173(15) [184K]	Doppler ^{d)}
	104(12)	Measurement of D ₊ using variable energy beam ^{e)}
	≈50	Variable energy beam. S parameter measurement ^{f)}
	100(18) 400(60)	Positron lifetime study ^{g)}
	430(100) 320(160)	Implantation ^{h)} e ⁺ lifetime. e ⁺ diffusion to surfaces of powdered samples ⁱ⁾
Germanium	350(17) [36K] 124(10) [93K]	Doppler ^{j)}
	≈8-20	e ⁺ beam ^{k)}
Diamond	120(160)	Angular correlation ^{l)}
	<20	" " ^{m)}
	160(80)	Implantation ^{h)}
	80(40)	e ⁺ lifetime. Powdered samples ⁿ⁾
SiO ₂ (quartz)	<15	Angular correlation ^{m)}
BaTiO ₃	<80	Angular correlation ^{m)}
InP	15(5)	e ⁺ lifetime ^{o)}
Paraffin wax	≈11-78 [274-311K]	e ⁺ lifetime/Doppler ^{p)}
PTFE (Teflon)	<2	Implantation ^{h)}
	3.5(2.1)	Doppler ^{b)}
Kapton	.38(.75)	Doppler ^{b)}
KCl crystal	.35(3.3)	Doppler ^{b)}
Mylar	.38(1.0)	Doppler ^{b)}
Glass	2.7(2.6)	Doppler ^{b)}
Various metals and alloys	40(20)	e ⁺ lifetime. Powdered samples ^{q)}

References

- a) Mills, Gullikson, Pfeiffer and Rockward (1986)
- b) MacKenzie and Ghorayshi (1985)
- c) Mourino and Brandt (1979)
- d) Mills and Pfeiffer (1977)
- e) Nielsen, Lynn, Vehanen and Schultz (1985)
- f) Corbel, Hautajarvi, Makinen, Vehanen and Mathiot (1989)
- g) Present work
- h) Brandt and Paulin (1977)
- i) Gainotti and Ghezzi (1970)
- j) Mills and Pfeiffer (1976)
- k) Jorch, Lynn and McMullen (1984)
- l) Lang and DeBenedetti (1957)
- m) Sueoka and Koide (1977)
- n) Fieschi, Gainotti, Ghezzi and Manfredi (1968)
- o) Beling, Simpson, Stewart, Wang, Fung, Wai and Sun (1987b)
- p) Ball, MacKenzie and Stone (1989)
- q) Paulin, Ripon and Brandt (1973)

Stone *et al* (1989) performed PLS studies in paraffin wax as a function of time after application of a 25kVcm^{-1} electric field. Data were collected using a highly efficient fast lifetime spectrometer with a coincidence rate of 3000 counts per second, which enabled statistically reliable spectra to be generated in 80s. Transient behaviour was observed by collecting a series of 80s runs with no field applied, followed by a further series with the field switched on. Data were analysed by taking the ratio of intensities of short to long lived lifetime components. The latter component was associated with pick-off annihilations of o-Ps in the samples. The recorded transient behaviour after application of the field shows a short term polarisation with a time constant of several minutes (see Figure 2.6a)). A second transient variation with a period of about one day was also observed.

Values of μ_+ for different oscillator periods determined by the Doppler method described above are shown in Figure 2.6b). The data are uncorrected for the immobile Ps fraction. Since the reduction in μ_+ was substantially greater than the 6% transient in the Ps fraction, the variation was attributed to an increase in e^+ trapping. The polarisation was found to persist after removal of the electric field, so the authors concluded that μ_+ depended on the electric field history of the sample. In extending mobility measurements to other materials, these observations should be taken into consideration.

Using a different approach, Brandt and Paulin (1977) related electric field induced changes in positron implantation profiles to the positron mobility in silicon and diamond. Their apparatus, which was essentially a modified γ -ray angular correlation spectrometer, is shown schematically in Figure 2.7. The count rate due to positron annihilations at different depths was monitored by advancing the sample platform with a micrometer screw. The system could be operated in either mode 1 (singles counting) or mode 2 (coincidence counting), although only mode 1 was used for mobility measurements. The

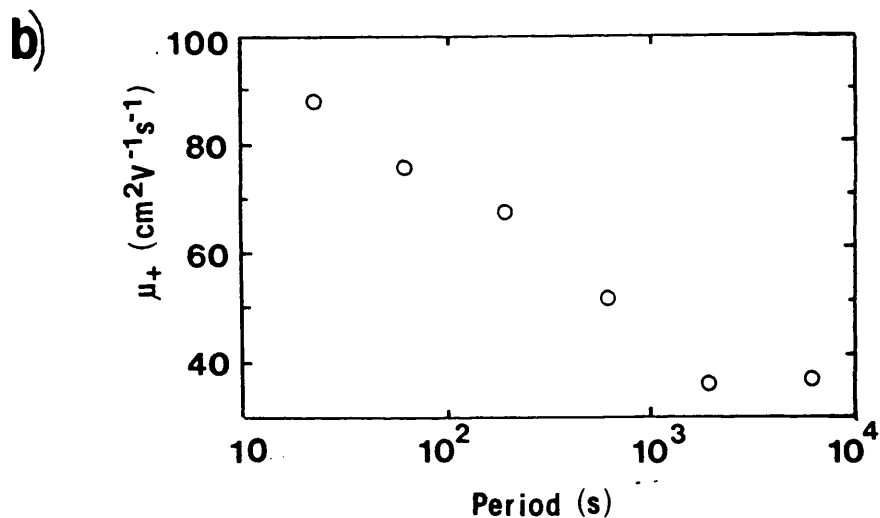
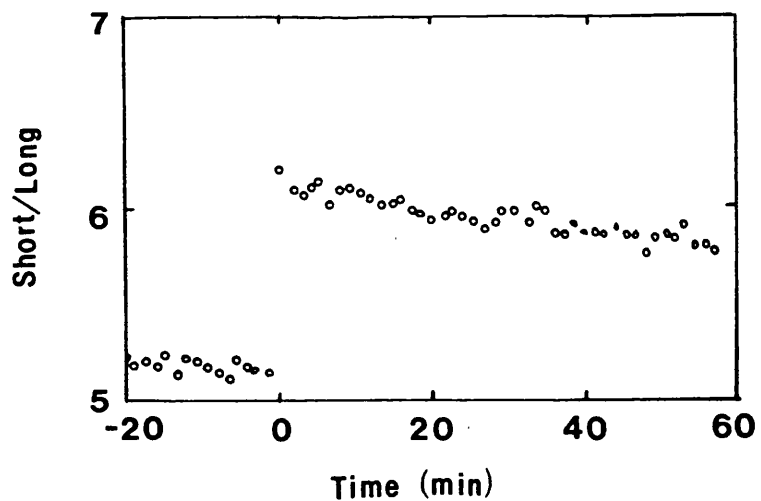


Figure 2.6 Electric field effects in paraffin wax

- a) Change in ratio of integrated areas of short to long lifetime components after application (at $t=0$) of a 2.5MVcm^{-1} electric field to paraffin wax at 296K. Transient behaviour of positron annihilation in the wax is clearly shown
- b) Positron mobility in paraffin wax as a function of period of applied field

(Stone *et al* 1989)

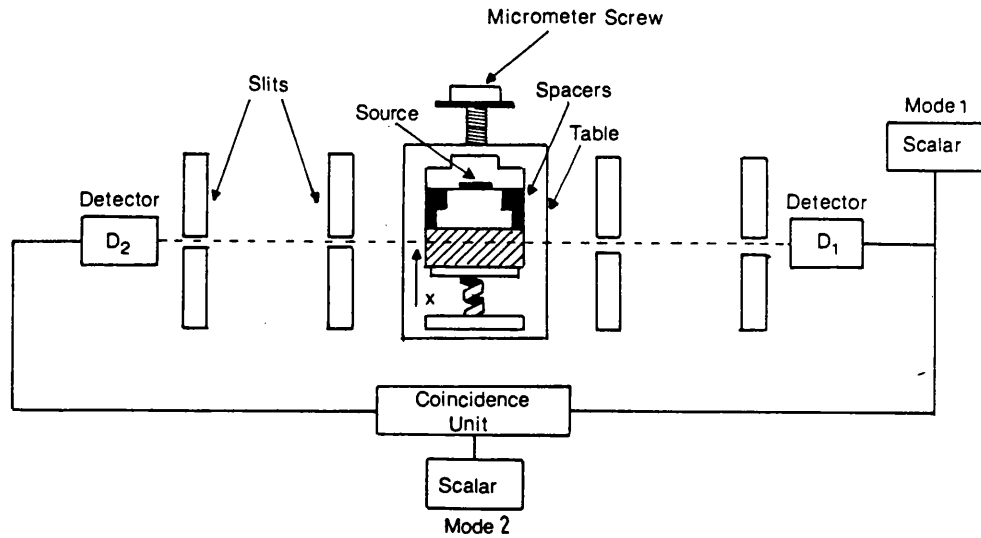


Figure 2.7 Experimental arrangement for measuring e^+ implantation profiles in solids. (Brandt and Paulin 1977)

change in count rate, $\Delta N(\xi)$ with applied field, is related to the positron drift velocity by

$$v_+ = \frac{1}{\alpha_+ \tau} \frac{\Delta N(\xi)}{N} \quad 2:16$$

where, α_+ and τ , are the e^+ absorption coefficient for the emitter and the mean positron lifetime in the sample, respectively. The measured shifts and corresponding e^+ drift velocity are shown in Figure 2.8 After correcting for Joule heating at high fields, the data were fitted by Equation 2:16 and a value of $\mu_+ = (430 \pm 100) \text{cm}^2 \text{V}^{-1} \text{s}^{-1}$ obtained. In diamond, the increase in velocity at low fields corresponded to $\mu_+ \approx 200 \text{cm}^2 \text{V}^{-1} \text{s}^{-1}$, whereas at high fields the e^+ drift velocity saturated, possibly as a result of defect trapping. These measurements are not inconsistent with those of Lang and DeBenedetti (1957) and Sueoka and Koide (1976), especially if defect concentrations were limiting e^+ drift. However, a $T^{-1.5}$ extrapolation of the Doppler measurements of Mills and Pfeiffer (1977)

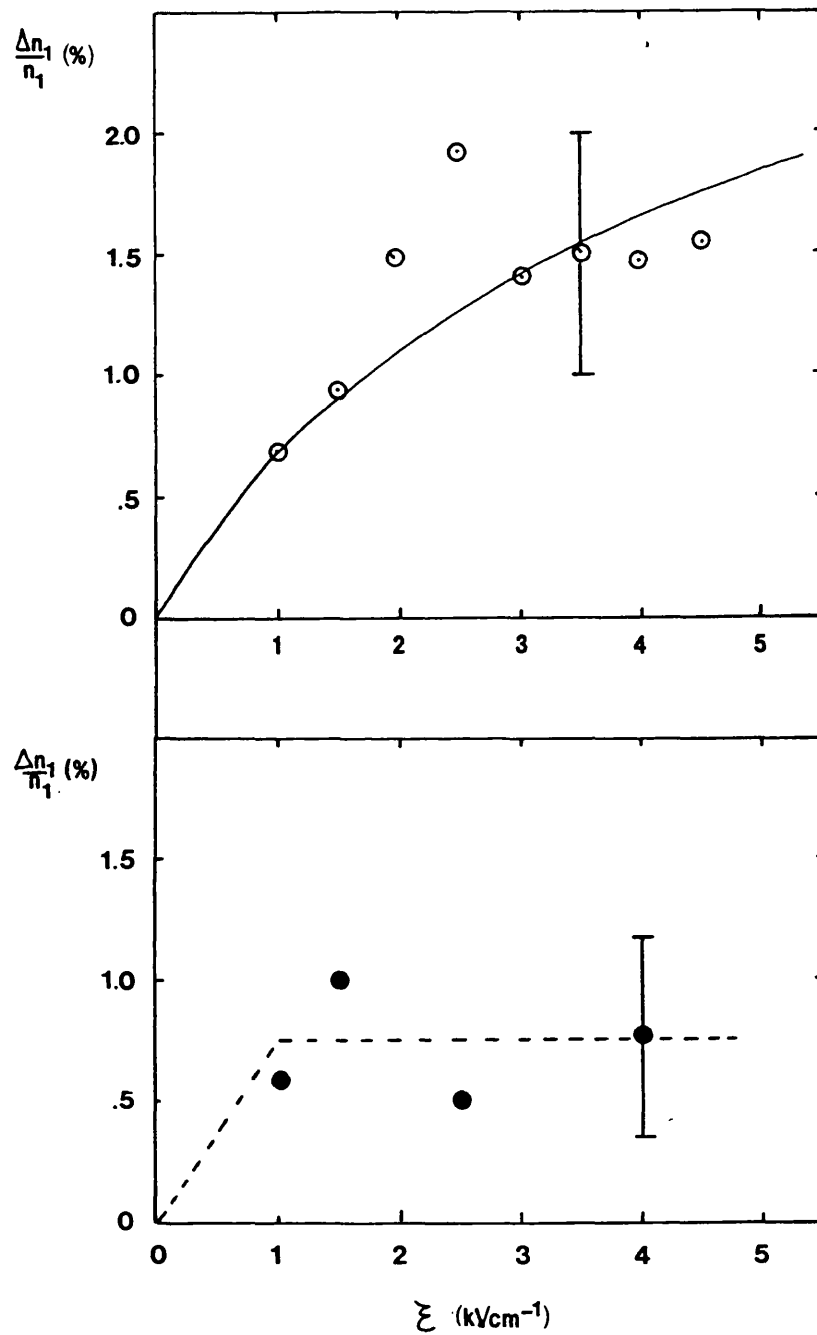


Figure 2.8 Relative shift $\frac{\Delta n_1}{n_1}$ in e^+ annihilation profile, and corresponding drift

velocity as a function of applied electric field, ξ

○ Si (300K)

● Diamond (300K)

(Brandt and Paulin 1977)

gives $\mu_+ \approx 80 \text{cm}^2 \text{V}^{-1} \text{s}^{-1}$: significantly less than that of Brandt and Paulin (1977) in Si. The reason for this discrepancy is unclear. Mills and Pfeiffer (1977) suggest that experiments which measure mobilities by e^+ displacement, which includes the method employed by Brandt and Paulin (1977), may be subject to errors caused by the prethermal drift of positrons. They suggested use of a prethermalisation mobility,

$$M = \frac{el}{m_e c} \quad 2:17$$

where l is the e^+ mean free path at velocities close to the speed of light, c . The mean free time between collisions is a function of velocity during slow down and l decreases from 10^{-4} to 10^{-8}m with a change in positron energy from 10 to 0.1 eV. Mills and Pfeiffer (1977) quote a value of $M = 900 \text{cm}^2 \text{V}^{-1} \text{s}^{-1}$ for the ^{64}Cu source used by Brandt and Paulin (1977). If η is the fraction of time spent in the prethermalisation state, the mobility, μ'_+ , measured in a e^+ displacement experiment may be expressed as

$$\mu'_+ = (1 - \eta)\mu_+ + \eta M \quad 2:18$$

With $\eta \approx 10\%$, it is difficult to see how μ_+ would change from the "true" value measured by Mills and Pfeiffer (1977) to that obtained by Brandt and Paulin (1977). In an errata Mills and Pfeiffer (1979b) acknowledged that this effect is unlikely to explain the observed difference in these two measured values of μ_+ . Subsequently Mills *et al* (1986) compared their value of μ_+ , determined by Doppler shift measurement in polyethylene, with a displacement method value previously reported by Mourino and Brandt (1979) and concluded that the two methods are in agreement. However, the studies of Heinrich (1978), discussed above in Section 2.2, continue to provide evidence in doubt of the reliability of e^+ displacements methods, if prethermalisation effects are not carefully considered. In a further publication, this problem was addressed by Heinrich and Schiltz (1982), who demonstrated that in molecular liquids, post- and pre-thermal effects can be

separated, leading to a more reliable measurement of μ_+ by a positron implantation method. Unfortunately, no further measurements of μ_+ in solids by this improved technique have been reported.

Using a variable energy e^+ beam, Corbel *et al* (1989) studied positron motion in a biased Au-Si Schottky barrier diode, by measuring the S-parameter of the 511keV e^+ annihilation peak (S is defined in Section 1.4.2). The variation of S with applied field is shown in Figure 2.9a for both forward ($V>0$) and reverse ($V<0$) bias. The e^+ implantation energy is 10keV. At large negative biases all e^+ implanted into the Si drifted to the interface and S saturated. For forward bias potentials $\geq 0.3eV$, the effect of the electric field on e^+ motion was negligible. Figure 2.9b) shows the S parameter versus e^+ implantation energy, E, for several different bias voltages. For $E \leq 3keV$, e^+ are implanted into the 100Å Au layer and are therefore unaffected by the junction bias. Between 5 and 10keV the S parameter distributions recorded under large reverse bias conditions show a broad minimum. In this region all e^+ implanted into the diode are drifted into the Au-Si interface by the large electric field established across the depletion region. For $V \geq 0.35V$, the effect of the electric field in the depletion region is negligible and positron motion to the interface is dominated by diffusive transport.

Since the carrier concentration in the Si used to fabricate the diode was known, Corbel *et al* (1989) could make a rough estimate of the positron mobility in Si using the data shown in Figure 2.9b). They found $\mu_+ \approx 50cm^2V^{-1}s^{-1}$, which is in fair agreement with a $T^{-1.5}$ extrapolation to 300K of the data of Mills and Pfeiffer (1977) and the value obtained from the present study at 295K.

Positron mobility can be deduced from measurements of D_+ by application of the Einstein relation (Equation 2:8). The earliest measurements of D_+ were derived from e^+ lifetime measurements in powders. In such samples, where the grain size is significantly less than the mean positron implantation depth for the β^+ source used, e^+ thermalise uniformly

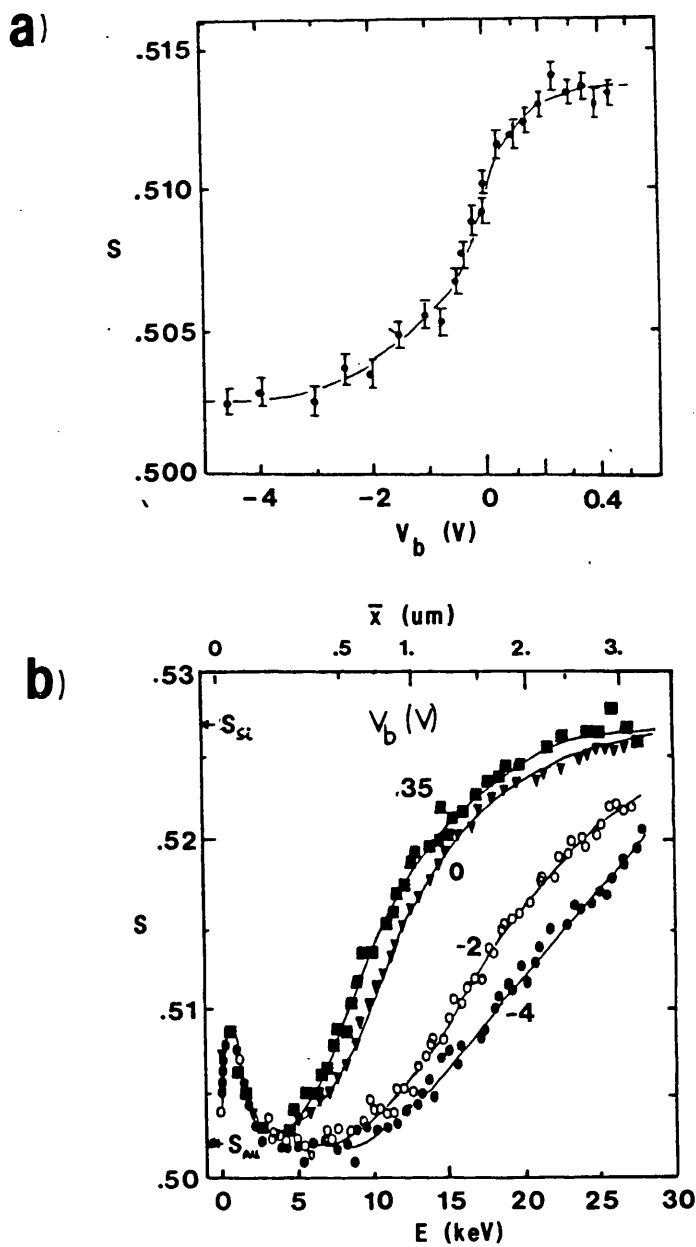


Figure 2.9 A variable energy study of e^+ electric field drift in Si.

a) Variation of line shape parameter, S , with bias applied to Au-Si Schottky barrier.

b) S parameter as a function of e^+ implantation energy for various bias voltages applied to an Au-Si Schottky barrier. The mean implantation depth, \bar{x} , as a function of e^+ incident energy is given along the top scale.

(Corbel *et al* 1989)

throughout the grains. In metallic samples e^+ diffuse freely until they annihilate in the metal bulk, in bulk defects or in surface states. In non metallic substances extra components due to positronium formation are observed, which may also be mobile (see Chapter 1). On changing the grain size, the intensity of the lifetime component associated with the third annihilation mechanism is expected to change and can be related to D_+ . If individual lifetime components cannot be resolved, a change in $\bar{\tau}$, the mean lifetime, is observed. Brandt and Paulin (1972) performed a theoretical study of this problem and derived relationships for the surface related component under different conditions. In a subsequent publication, Paulin *et al* (1973) reported lifetime measurements made in several metallic powders. From this data the authors concluded that D_+ in metals $\approx (1.0 \pm 0.5)\text{cm}^2\text{s}^{-1}$. The data suggested that the internal reflection coefficient of e^+ at the surface, r , was non-zero, which led to an underestimate of D_+ since the theory assumed $r=0$. However, provided $r < 0.5$, the error introduced in D_+ due to reflection is less than the compounded errors arising from the lifetime data and was therefore neglected.

Gainotti and Ghezzi (1970, 1972) performed similar measurements in powdered Si and Ge samples. In both cases they observed two components, the first of which corresponded to the e^+ lifetime measured in single crystal samples and was independent of grain size and sample doping. The intensity, I_2 , of the second, slower component increased with decreasing grain size and had a lifetime similar to that of the respective semiconductor oxide ($(520 \pm 20)\text{ps}$ for Si and $(410 \pm 10)\text{ps}$ for Ge). It was therefore attributed to the annihilation of e^+ in a surface oxide layer following migration from the interior of the grain. In Ge, Gainotti and Ghezzi (1972) observed differences in I_2 with doping level which they described in terms of positron transport in an electric field arising from charge trapped in the surface layer. In n-type samples, this field enhanced e^+ motion towards the surface oxide potential well, increasing I_2 , particularly at low resistivities. In p-type grains, the direction of the field was reversed and I_2 reduced. However in n-type Si grains,

I_2 was smaller at low rather than high resistivities. The reason for this discrepancy was unclear. In Ge, where the band bending $\Delta V_s \approx kT$, the variation of I_2 with temperature was predicted to vary as

$$I_2 \propto \exp\left(-\frac{\Delta V_s}{kT}\right) \quad 2:19$$

In $0.4\mu\text{m}$ radius p-type grains, I_2 was found to double from 10% at 78K to 20% at 403K, although the data were not of sufficient accuracy to test the validity of Equation 2:19. However, the data suggested a value for $\Delta V_s \approx 0.8 \times 10^{-3} \text{eV}$, which was in agreement with the band bending calculated for the surface state density recorded in the literature. As expected, in low resistivity n-type samples this behaviour was not observed and I_2 was approximately constant with temperature. In this case, ΔV_s is negative and the penetration of the field is negligible. Consequently D_+ could, in principle, be calculated from the measured variation of I_2 with grain size. However the expression given in the paper is only valid when the grain radius $R \gg L_+$, the positron diffusion length. Under these conditions I_2 is too small for an accurate measurement of D_+ , although it can be inferred from the data that D_+ is significantly greater than the values reported by Paulin *et al* (1973).

More reliable determinations of D_+ became possible with the advent of intense slow positron beams. Using a technique based around a 0-5keV variable energy positron beam, Jorch *et al* (1984) monitored the fraction of incident e^+ which, after thermalisation in a Ge crystal and diffusion back to the surface, were subsequently re-emitted as positronium. Knowledge of the energy dependency of the e^+ implantation profile enabled a fitting procedure to be carried out and D_+ to be deduced. It was possible to extend measurements to high temperatures (up to 1020K), beyond the range attainable by current techniques for holes and electrons, thus demonstrating the inadequacy of conventional phonon scattering theories which satisfactorily explain the low temperature behaviour. An extrapolation of

this data to low temperatures gave reasonable agreement with the value of μ_+ measured by Mills and Pfeiffer (1976). Using the same technique, Nielsen *et al* (1985) found D_+ in silicon to be $(2.7 \pm .3) \text{cm}^2 \text{s}^{-1}$ at 300K which corresponds to a mobility of $(104 \pm 11) \text{cm}^2 \text{V}^{-1} \text{s}^{-1}$, in good agreement with an extrapolation of the Doppler measurement of Mills and Pfeiffer (1977) discussed above.

Table 2.2 summarises the available mobility measurements. From the above review it is concluded that whilst there is reasonable agreement between values of μ_+ determined by different techniques, there are some discrepancies which have yet to be adequately explained, especially those found when comparing Doppler and displacement measurements. Further studies are therefore necessary and it would be of interest to extend these to new materials to obtain a better understanding of e^+ motion.

2.5 MEASUREMENT OF POSITRON MOBILITY BY A LIFETIME METHOD - THEORY

Systems in which positrons can be transferred from one annihilation state to another can be used to determine positron transport properties. Two such examples are:

1. Diffusion of positrons from bulk to surface in small grain size powders (for example Paulin *et al* 1973).
2. Trapping of positrons at defect sites in crystals (Beling *et al* 1987b).

The transition rates will depend on the positron diffusion constant as well as particle size in the first example and defect size and concentration in the second. In both instances conditions can be achieved which ensure that the trapping rate is of the same order as the bulk annihilation rate, and it can thus be deduced from changes in measured lifetime spectra. If large electric fields are applied to single crystals, it is possible to drift a significant fraction of e^+ to an interface, where they annihilate in a state distinct from that

of the bulk. Measurement of this fraction as a function of field can be used to deduce the bulk positron mobility and provides the basis for the experimental method described in Chapter 3. The problem can be treated theoretically by assuming a two state system (see Figure 2.10a, b)) for which the rate equations are

$$\frac{dn_b}{dt} = -\lambda_b n_b - J(t)$$

and

$$\frac{dn_i}{dt} = -\lambda_i n_i + J(t)$$
2:20

Here, λ_b and λ_i are respectively the annihilation rates in state $|b\rangle$, the bulk state and state $|i\rangle$, the interface state. $J(t)$, the e^+ flux between the states, can be expressed as κn_b where κ is the transition rate from $|b\rangle$ to $|i\rangle$. The exact form of κ will depend on the nature and geometrical form of the problem (Brandt and Paulin 1972). The electric field drift of e^+ to an abrupt planar interface situated at $x = 0$ (Figure 2.10b)) can be evaluated by solving the one dimensional continuity equation

$$\frac{\partial n_b(x, t)}{\partial t} = -v_+ \frac{\partial n_b(x, t)}{\partial x} - \lambda_b(x, t)$$
2:21

This first order differential equation is variable separable, that is a solution of the form

$$n(x, t) = X(x)T(t)$$
2:22

exists. Therefore

$$X \frac{dT(t)}{dt} = -v_+ T(t) \frac{dX(x)}{dx} - \lambda_b X(x)T(t)$$

and

$$\frac{1}{T(t)} \frac{dT(t)}{dt} = -\frac{v}{X(x)} \frac{dX(x)}{dx} - \lambda_b = -q$$
2:23

where q is an arbitrary constant.

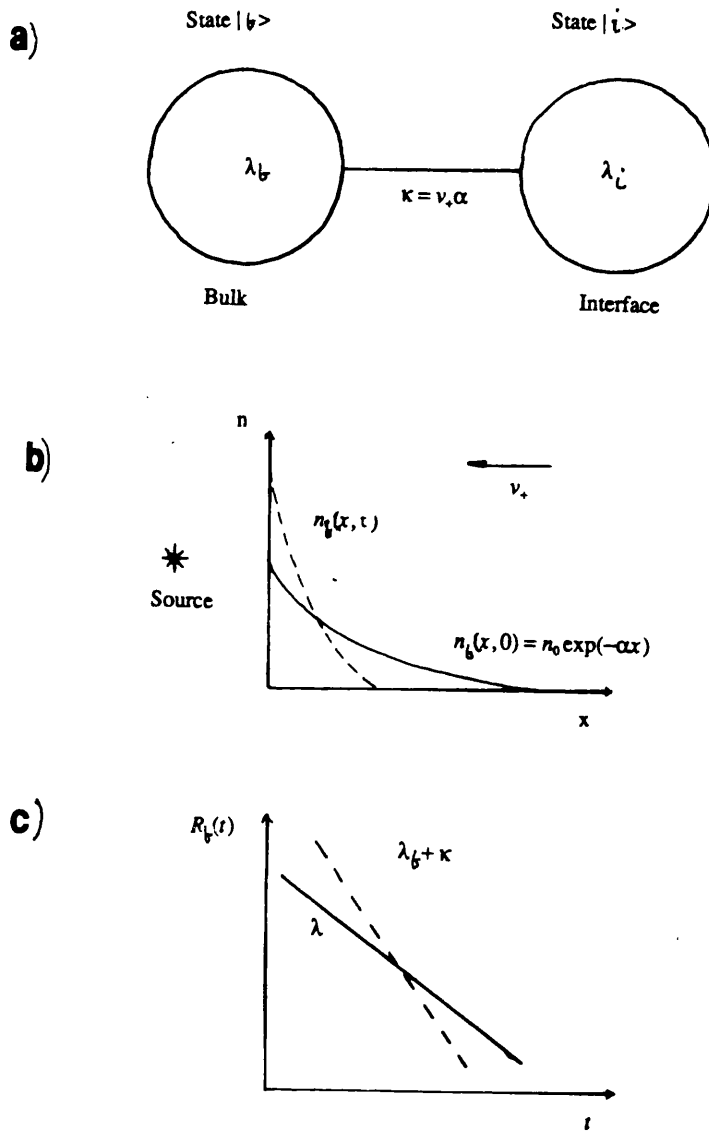


Figure 2.10 Measurement of the electric field drift of e^+ in a solid by a lifetime method

- a) Two state system used to describe the drift and annihilation of e^+ in an interface state
- b) Geometrical arrangement showing e^+ implantation profile $n_b(x, 0)$ and subsequent profile $n_b(x, t)$ after e^+ drift and annihilation
- c) Change in apparent bulk e^+ annihilation rate due to e^+ drift into an interface state distinct from that of the bulk.

Hence

$$\begin{aligned} \text{and} \quad T &= T_0 \exp(-qt) \\ X &= X_0 \exp\{(-q + \lambda_b)x\} \end{aligned} \quad 2:24$$

Imposing the boundary conditions

1. No e^+ exist at infinite time

$$\text{ie } n \rightarrow 0 \text{ as } t \rightarrow \infty \quad 2:25$$

2. e^+ are implanted with an exponential stopping profile

$$n_b(x, 0) = n_0 \alpha \exp(-\alpha x) = X_0 T_0 \exp\left(-\frac{q - \lambda_b}{v_+} x\right) \quad 2:26$$

$$\text{provides } \alpha_+ = \frac{q - \lambda_b}{v_+}$$

$$\text{that is } q = \alpha_+ v_+ + \lambda_b$$

$$\text{therefore } n_b = n_0 \alpha_+ \exp\{-(\lambda_b + \alpha_+ v_+)t\} \exp(-\alpha_+ x) \quad 2:27$$

The total number of e^+ present in $|b\rangle$ at time t is given by

$$n_b = n_0 \exp\{-(\lambda_b + \alpha_+ v_+)t\} \int_0^\infty \alpha_+ \exp(-\alpha_+ x) dx = n_0 \exp\{-(\lambda_b + \alpha_+ v_+)t\} \quad 2:28$$

Hence the rate equation for n_b is

$$\begin{aligned} \text{and} \quad \frac{dn_b(t)}{dt} &= -\lambda_b n_b(t) + \alpha_+ v_+ n_b(t) \\ \frac{dn_i(t)}{dt} &= -\lambda_i n_i(t) - \alpha_+ v_+ n_b(t) \end{aligned} \quad 2:29$$

These are equivalent to Equation 2:20 with

$$\kappa = \alpha_+ v_+ \quad 2:30$$

Performing algebraic manipulation on Equation 2:29 and integrating gives

$$n_b = n_0 \exp\{-(\lambda_b + \alpha_+ v_+)t\}$$

and

$$n = \frac{\alpha_+ v_+ n_0}{\lambda_b - \lambda_i + \alpha_+ v_+} [\exp\{-\lambda_i t\} - \exp\{-(\lambda_b + \alpha_+ v_+)t\}] \quad 2:31$$

So, taking $n_i(0) = 0$,

$$n(t) = n_b(t) + n(t)$$

$$\text{and} \quad = n_0 \exp\{-(\lambda_b + \alpha_+ v_+)t\} + \frac{\alpha_+ n_0 v_+}{\lambda_b - \lambda_i + \alpha_+ v_+} [\exp\{-\lambda_i t\} - \exp\{-(\lambda_b + \alpha_+ v_+)t\}] \quad 2:32$$

$$\frac{n(t)}{n(0)} = \left\{ 1 - \frac{v_+}{\lambda_b - \lambda_i + \alpha_+ v_+} \right\} \exp\{-(\lambda_b + \alpha_+ v_+)t\} + \frac{\alpha_+ v_+}{\lambda_b - \lambda_i + \alpha_+ v_+} \exp\{-\lambda_i t\}$$

The counting rates are

$$R_b(t) = \lambda_b n_b(t)$$

and

$$R_i(t) = \lambda_i n_i(t)$$

2:33

$$R(t) = R_b(t) + R_i(t)$$

The fraction (intensity) of e^+ annihilating in states $|b\rangle$ and $|i\rangle$ are given by

$$\text{and} \quad I_b = \int_0^\infty \frac{1}{n_0} R_b(t) dt = \frac{\lambda_b - \lambda_i}{\lambda_b - \lambda_i + \alpha_+ v_+} \quad 2:34$$

$$I_i = \int_0^\infty \frac{1}{n_0} R_i(t) dt = \frac{\alpha_+ v_+}{\lambda_b - \lambda_i + \alpha_+ v_+}$$

Also $I_b + I_c = I$ as expected. Under these conditions, lifetime spectra will show two components, (I_b, λ'_b) and (I_c, λ_c) , where $\lambda'_b = \lambda_b + \alpha_+ \nu_+$. ν_+ can be deduced either by deconvolution of spectra into individual components or by calculating the centroid shift between field on and field off spectra. Both methods of data reduction are considered in the next chapter.

CHAPTER 3

MEASUREMENT OF POSITRON MOBILITY IN SILICON BY A LIFETIME METHOD

3.1 INTRODUCTION TO POSITRON LIFETIME METHOD

This method involves measuring the time interval between the emission of a positron from the radioactive source and its subsequent annihilation in the medium under study. By repeating this procedure for a large number of events, a e^+ lifetime spectrum is generated. The data can be subsequently analysed to give j individual lifetime components, each with a lifetime τ_j and intensity, I_j . These components relate to the different e^+e^- annihilation states in the sample under study. In some applications, the data are analysed in a less sophisticated fashion, such as centroid shift determination. Both methods of analysis are discussed in Section 3.3.

Although the principles of positron lifetime spectroscopy (PLS) have essentially remained unchanged since its initiation by Shearer and Deutsch (1949), a continuous desire to improve resolution and/or counting efficiency has stimulated a large amount of research in this area. The importance of contributions from

1. the scintillator/photomultiplier arrangement and
2. the method of electronic processing of the phototube output pulses

have been realised. Much of the progress in these areas has been reviewed by Moszynski and Bengtson (1979).

The purpose of the scintillator/photomultiplier arrangement is to detect incident γ -rays and provide fast pulses for the subsequent timing circuits. γ -rays interact with the scintillating medium predominantly through the Compton process in which a scattered γ -ray liberates a high energy electron. This electron subsequently excites the optical states

of a large number of atoms. On decay, UV or visible photons are produced which trigger the photomultiplier. The time response of the scintillator is governed by the decay of the excited optical states, the scintillator dimensions and the type of coating applied to reflect the light at the scintillator surfaces (de Vries *et al* 1985). Fast timing systems have generally used plastic scintillators such as Pilot U and NE111, or in some cases liquid scintillators, although recently the advantages both in resolution and efficiency offered by dense crystals such as BaF₂ (Laval *et al* 1982) and CsF (Eldrup *et al* 1989) have been realised.

In the photomultiplier, photons striking the photocathode liberate electrons, which are subsequently multiplied by acceleration and liberation of secondary electrons at a series of dynodes. The resulting event signal is extracted either at the anode or in some cases at an intermediate dynode (de Vries 1987), with an overall gain of typically 10^7 - 10^8 . Important quantities which determine the suitability of the photomultiplier for fast timing applications are:

1. the quantum efficiency of the photocathode;
2. the spread in transit time of the photoelectrons from the photocathode to the first dynode and
3. variations in the electron multiplication process.

Several photomultiplier types have been found suitable for fast timing. These include the Philips XP2020Q and more recently the Hamamatsu R2083Q with its superior timing properties (de Vries *et al* 1989).

Most fast timing applications including PLS require energy discrimination. In photomultiplier arrangements this is accomplished by applying voltage discrimination to the phototube output pulses. Leading edge discriminators (LEDs), which are the simplest means of deriving a time pick-off signal, produce an output logic pulse when the input

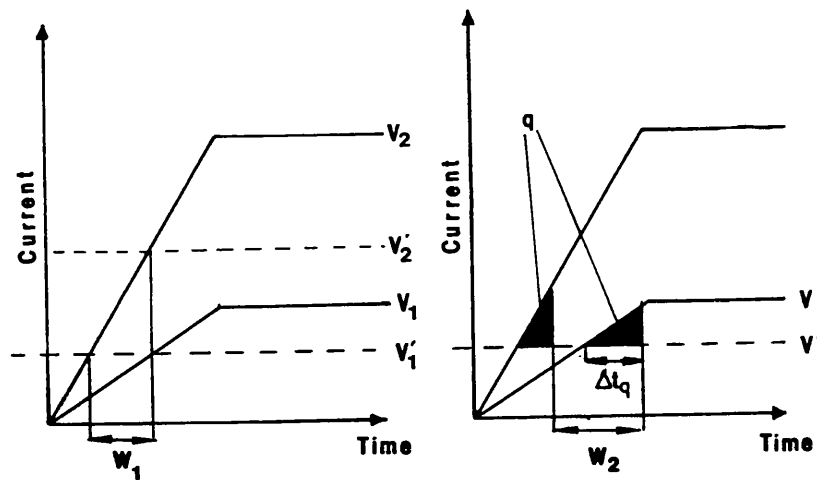


Figure 3.1 Leading edge discriminator walk effects as a function of pulse amplitude

- a) amplitude walk, W_1
- b) amplitude and charge walk, W_2

level crosses a fixed threshold. A primary disadvantage of this technique is that the time of occurrence of the output pulse from the LED is dependent on the amplitude and rise time of the input signal (see Figure 3.1). The former effect is termed amplitude dependent walk. Once the signal exceeds threshold a finite amount of charge, q , is required to trigger the discriminator leading to an additional walk time, Δt_q , which also depends on the pulse amplitude, as shown in the figure. This second effect is termed charge dependent walk. The figure also shows that the amplitude walk can be removed, if the discriminator is set to trigger at a constant fraction $F = \frac{V'}{V}$. Additionally, the effect of statistical variations (jitter) in the pulse can be minimised if the correct choice of F is made.

Consequently, constant fraction timing (CFT) has been developed to lessen the above effects. In CFT the photomultiplier pulse is split and shaped as shown in Figure 3.2. If the discriminator triggering is arranged to occur at the zero crossing point of the resulting CF bipolar pulse, it will be independent of the original pulse amplitude. The choice of attenuation and delay can be selected to ensure optimum timing for all input pulses.

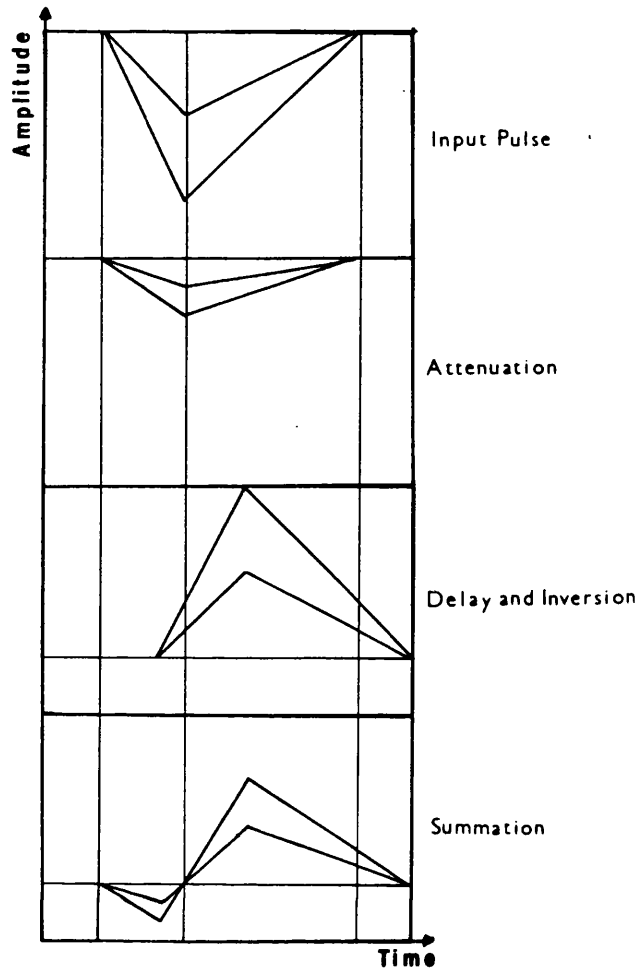


Figure 3.2 Constant fraction pulse shaping

Amplitude and rise time compensated (ARC) discrimination is a modified version of CFT which compensates for rise-time dependent walk as well as amplitude dependent time walk. It is not normally necessary to use ARC timing in PLS applications.

Improved timing resolution has been achieved using photomultiplier dynode pulses, which have shorter risetimes than the corresponding anode pulses. In this case, the pulses are inverted prior to reaching conventional CFT circuits, or special CFT discriminators developed which accept positive rather than negative pulses. Dynode pulses are bipolar and can therefore be used in conjunction with zero crossing discriminators to give an

arrangement equivalent to CFT (de Vries and Kelling 1987, 1988). This technique is termed internal fraction shaping, since the bipolar pulses are shaped by adjusting the potential to the photomultiplier dynodes to achieve optimum timing.

It is unlikely that design developments in the other components of a positron lifetime spectrometer will significantly improve its overall performance. Time to amplitude convertors (TACs) of good linearity and stability, are now commercially available. The development of personal computer based multichannel analysers (MCAs) facilitate improved data handling and offers the possibility of on-line correction of instabilities (for example Teixeira Dias *et al* 1989).

3.2 DESIGN CHARACTERISTICS

3.2.1 Design and Optimisation of the Spectrometer

The lifetime spectrometer employed for the current measurements of positron mobility in silicon is shown schematically in Figure 3.3. The system used 12° coned Pilot U scintillators coupled to twelve stage Philips XP2020Q photomultipliers to monitor the gamma rays from the source (STARTS) and subsequent annihilations in the sample (STOPS). To improve performance, timing pulses were taken from the ninth dynode and, after inversion, presented to Ortec 583 constant fraction discriminators. Figures 3.4a) and b) show the measured Compton profiles for ^{60}Co and ^{22}Na sources, respectively, produced by gamma ray interactions in one of the scintillators. For ^{22}Na , the Compton edges for 511keV and 1.28MeV γ events can clearly be seen. Knowledge of these profiles enabled the discriminators' voltage windows to be set. The fast negative timing outputs from the discriminators were fed to the TAC. The stop signal was delayed by a suitable amount to ensure that the TAC operated in its linear region. The TAC provides a bipolar pulse for every accepted start-stop pair and these events were stored, according to amplitude, in a 1024 channel Northern ECON II series MCA. Scalars connected to the positive output of

the stop discriminator and the TAC true start output, recorded the total number of stop and start signal events, respectively. Gating pulses from the MCA were used to inhibit the TAC whenever the MCA was busy.

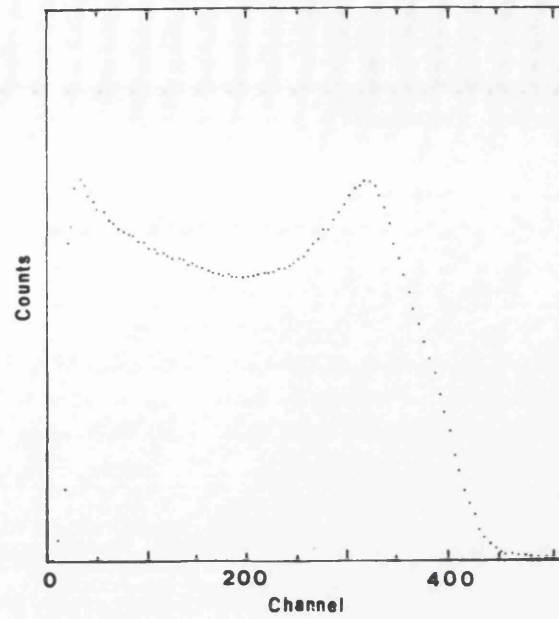
The overall performance of the spectrometer was determined using a ^{60}Co source which emits 1.17 and 1.33 MeV γ -rays in near coincidence. ^{60}Co spectra only show signal from prompt events and therefore can be used to measure the resolution function of the instrument. Another useful calibration source consists of ^{22}Na deposited on "Kapton". Provided sufficient Kapton was used to stop all β^+ particles, its e^+ lifetime spectrum shows a single lifetime component of $\approx 380\text{ps}$, which has been measured to good accuracy (Plotkowski *et al* 1988). This component is sufficiently long lived to permit its separation from the resolution function by standard analysis methods, such as the computer code RESOLUTION, described below. This spectrum can therefore be used to determine both the resolution function and time calibration for the system. Typical ^{60}Co and ^{22}Na in Kapton spectra are shown in Figure 3.5a) and b). Using these sources, adjustments of photomultiplier voltage, CF discriminator levels and walk settings were made to optimise the time resolution, whilst still maintaining a good coincidence rate.

Accurate time calibration of the system was achieved by applying pulses from a signal generator to the stop line; the start signal still being derived from a phototube in the usual way. In this instance only random events were built up in the MCA and the time per channel, t_{ch} , given by

$$t_{ch} = \frac{TD_i}{N_1N_2} \quad 3:1$$

where D_i is the data in the i^{th} channel, T the run time and N_1, N_2 the number of stops and starts. This method also served to test the linearity of the TAC/MCA arrangement. A typical calibration run is shown in Figure 3.6.

a)



b)

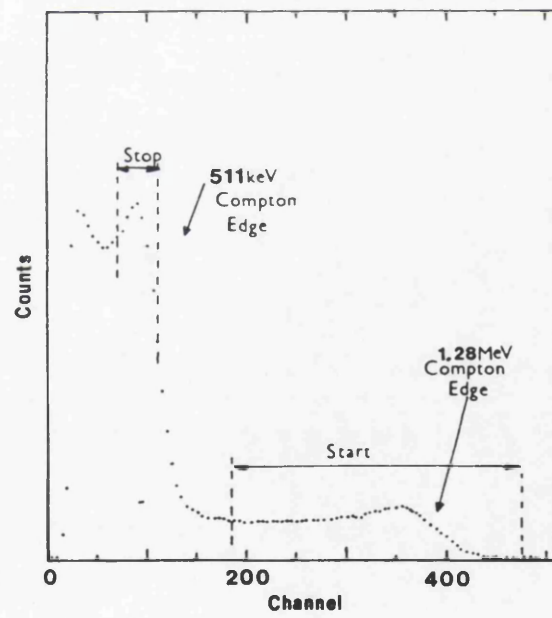


Figure 3.4 Compton profiles measured using plastic scintillator/photomultiplier arrangement

a) ^{60}Co source

b) ^{22}Na source

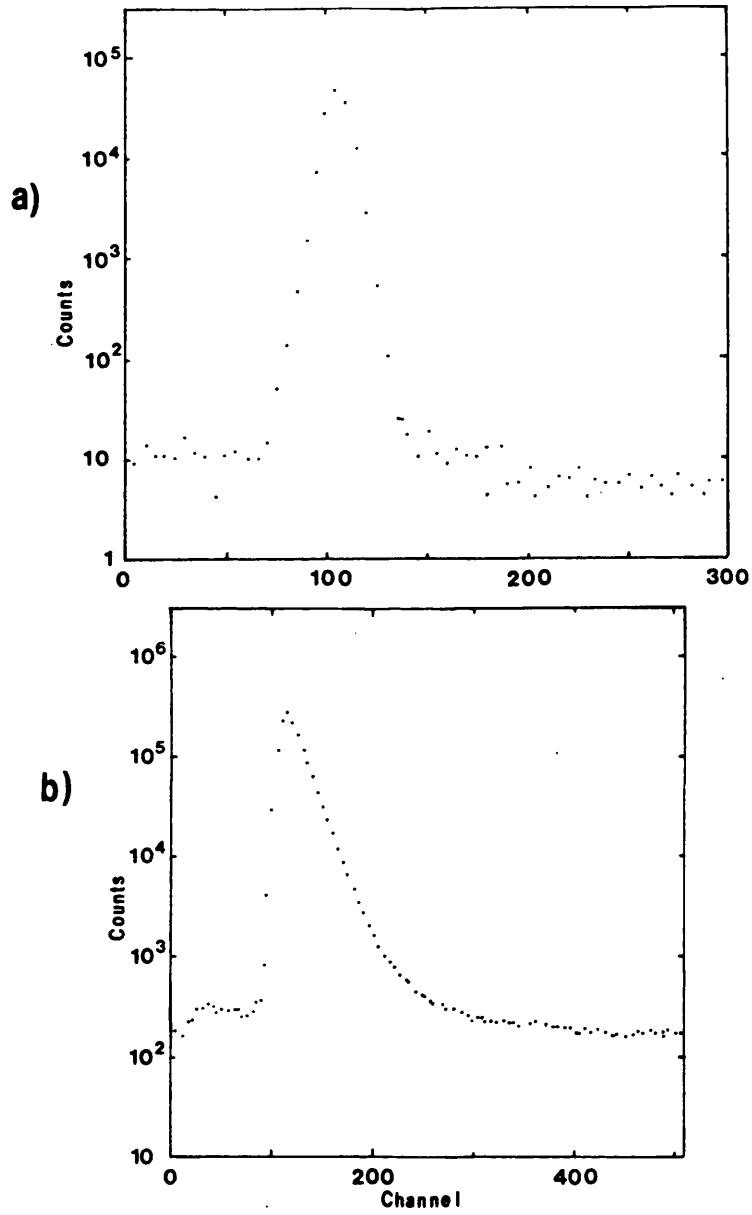


Figure 3.5 Positron lifetime spectra

a) ^{60}Co source

b) ^{22}Na in "Kapton" $\tau_2 \approx 380\text{ps}$ (99.3%)

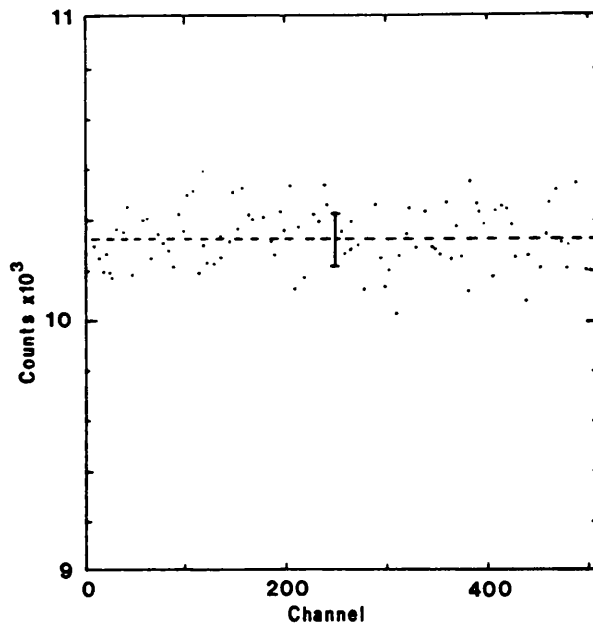


Figure 3.6 Time to amplitude convertor calibration spectrum. 24.4ps per channel. Error bar signifies statistical error.

3.2.2 Additional Electronics

Ambient temperature changes are generally considered to be the dominant source of electronic drift effects in fast electronic systems, so the experiments described below were carried out in an air-conditioned laboratory at a temperature of $(294 \pm 0.5)\text{K}$. In the current study, small changes between field on and field off spectra were related to positron drift in the Si samples. If the spectra are collected consecutively this change can be masked by the adverse effect of electronic drift. However, if pairs of field on/field off spectra are collected concurrently, the latter effect deteriorates both spectra to a similar extent, leaving the field dependent differences relatively unchanged. Therefore, a two step (field on/ field off) switching cycle was incorporated into the arrangement. With an electric field applied to the samples, data were collected in the first half of the MCA memory. After about 800s the field was switched off and the data routed to the second half of the memory. After a further 800s, this cycle was repeated. The "active" periods

were separated by 90s "dead" periods to ensure that the field applied to the samples had stabilised. This switching operation was performed by a system controller supplied by Miller Systems Limited. The stability of the lifetime spectrometer is discussed in Section 3.5.

3.2.3 Source

For these experiments, a small ^{22}Na source was used to implant β^+ particles into the samples. The source strength was determined by the requirement of achieving adequate statistical accuracy without increasing the signal to background ratio to an unacceptable level. Ideally these factors can be improved simultaneously by the choice of a weak source and long run time, although this generally results in degradation of the time resolution by electronic instabilities and puts an unreasonable timescale on the duration of the experiment.

Green and Lee (1964) have shown that the signal to background ratio, R , is given by

$$R = \frac{\phi}{\beta} = \frac{1}{st} \quad 3:2$$

where ϕ is the fraction of events corresponding to real coincidences, β , the fraction of events arising from random (background) coincidences, s is the source strength in e^+s^{-1} and t is the time interval over which the spectrum is measured (the TAC range). Killeen (1975) showed that the fractional error, Δ , in ϕ is given by

$$\Delta = c \left(\frac{1}{2s} + t \right)^{\frac{1}{2}} \quad 3:3$$

where

$$c = (e_1 e_2 w_1 w_2 T)^{\frac{1}{2}}$$

Here, e_1 , e_2 , w_1 , and w_2 are respectively, the detection efficiencies and solid angles for γ detection at the scintillation counters and T is the run time. Figure 3.7 shows the variation of R and $\left(\frac{\Delta}{c}\right)$ with s . In this case s is expressed in microCuries (μCi), where 1Ci is 3.7×10^{10} disintegrations per second. It can be seen that R degrades rapidly with s whereas Δ tends towards its asymptotic value of $t^{1/2}$ at high s . Comparison of the predictions of Figure 3.7 with experimentally determined values of R suggests that the true source strength was less than $10\mu\text{Ci}$, so it might have been advantageous to have chosen a stronger source. However the source employed gave adequate statistical accuracy in 1-2 days ($\approx 1-2 \times 10^6$ counts per spectrum).

The source was fabricated by depositing an aqueous NaCl solution containing a proportion of ^{22}Na ions in a 3mm spot on a $8\mu\text{m}$ Kapton (polyimide) substrate. The foil was then folded in two, with the activity inside, and glued along the edges.

The source contribution, which is the fraction of e^+ annihilating in the supporting foils and the source itself, depends on the absorption and back-scattering coefficient of the source material, as well as the back-scattering co-efficient of the surrounding samples. To assess the importance of e^+ annihilation in the source deposit, de Vries (1987) measured the e^+ lifetime components in NaCl layers deposited on Mylar foils. From a three component fit to this data, lifetimes and intensities (in %) of 37ps(18%), 379(77%) and 1.5ns (5%) were obtained. For most practical cases, these intensities are expected to be small compared to the contribution from the supporting foils, which accounts for $\approx 15\%$ of the annihilations in a typical source/sample configuration. The latter contribution can be determined from published results on e^+ absorption (for example Linderoth *et al* 1984, for Ni and Plotkowski *et al* 1988 for Kapton) and fixed during analysis of the experimental data. However, in practice, uncertainties in the back-scattering and absorption coefficients of a particular source/sample configuration makes calculation of the source contribution by this method unreliable. Consequently, a full analysis of the measured lifetime spectra is

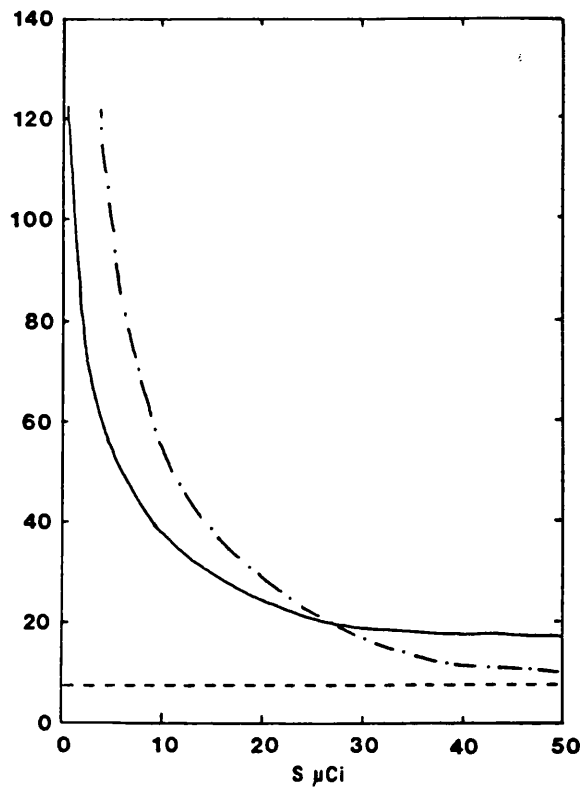


Figure 3.7 Variation of signal to noise ratio, R and fractional error, Δ , with source strength, s

- $\frac{\Delta}{c} (\text{ns})^{1/2}$
- · - R
- - - limit $t^{1/2} (\text{ns})^{1/2}$

often performed, in which the source component(s) is/are determined together with the components arising from e^+ annihilations in the samples. This approach was adopted in the current study and the source contribution was found to consist of two components of approximately 370ps (16%) and 1.4ns (0.7%). The latter is in agreement with the findings of de Vries (1987). The 370ps component presumably arose from a combination of contributions from the NaCl and Kapton. Its intensity was in reasonable agreement with Plotkowski (1988), who observed that 17% of e^+ were absorbed in a source configuration

consisting of two 1mgcm^{-2} Kapton foils sandwiched between Ni plates. However, the measured lifetime was significantly less than the value of $(387 \pm 7)\text{ps}$ reported by Plotkowski *et al* (1988), which may have been due to the effect of the NaCl.

3.3 DATA ANALYSIS

Data were analysed either by using the computer code RESOLUTION to determine the lifetimes and intensities of individual components, or by calculation of centroid shifts between field on (odd) and field off (even) spectra.

3.3.1 Resolution

Several published methods for the extraction of the lifetimes and intensities of the various components which make up a measured e^+ spectrum have been published. Most lifetime spectra are thought to consist of a sum of decaying exponentials with decay rates λ_j and intensities $A_j = \frac{I_{0j}}{\lambda_j}$ where I_{0j} is the time zero value of the j^{th} exponential. The decays are therefore described by

$$\begin{aligned} I_j &= I_{0j} \exp(-\lambda_j t) & t \geq 0 \\ I_j &= 0 & t < 0 \end{aligned} \quad 3:4$$

Generally, there is also a contribution to the spectrum from the resolution, $R(t)$, of the instrument and a background, B , which in many circumstances can be assumed uniform. The resolution function is often taken to comprise a summation of k gaussian distributions (gaussians) with full width half maxima (FWHM), w_k , each centred at a time, $t = T_k$, although other possibilities for $R(t)$ have been considered (for example de Vries 1987). For the gaussian case

$$R(t) = \sum_k G_k(t) = \sum_k (\sigma_k \sqrt{\pi})^{-1} \exp\left[-\left(\frac{(t-T_k)}{\sigma_k}\right)^2\right] \quad |t| \leq \infty$$

where

$$\sigma_k = \frac{\omega_k}{2\sqrt{\ln 2}} \quad 3:5$$

After subtraction of the uniform background, the model spectrum, $M(t)$, is described by a convolution of the above gaussian and exponential functions so

$$M(t) = \sum_{j,k} \int_{-\infty}^{\infty} I_j(t') G_k(t-t') dt' \quad 3:6$$

The content of the i^{th} channel, $N(\Delta t_i)$, corresponds to the time interval $\Delta t_i = t_{i+1} - t_i$, thus

$$N(\Delta t_i) = \int_{t_i}^{t_{i+1}} M(t) dt \quad 3:7$$

In a weighted least squares (WLSQ) method with n data points and l free parameters, the function ϕ , is to be minimised where,

$$\phi = \sum_{i=1}^N p_i (y_i - f_i(\bar{b}))^2 \quad 3:8$$

Here, y_i , is the data content of channel i , $f_i(t)$ is the model value obtained from Equation 3:7, p_i the statistical weight attached to channel i and \bar{b} is a vector representing the l parameters to be estimated. Several standard numerical methods have been adopted to perform this minimisation.

Of the various WLSQ methods, the programmes RESOLUTION and POSITRONFIT are probably most commonly in use. These comprise part of a library of programmes, PATFIT, developed by Kirkegaard *et al* (1982, 1989) for the analysis of positron

annihilation data from lifetime spectrometers and angular correlation systems. These programmes operate by fitting model parameters to the data using a semilinear Marquardt least squares technique. Non linear parameters such as the time-zero channel, T_0 , and the lifetime values, are solved iteratively using the Newton-Gauss-Marquardt method, whereas linear parameters are determined at the end of each iteration. This approach reduces the effective number of free parameters, thus giving more rapid convergence at the expense of slightly longer computing time for each iteration. Iterations start from an initial set of guessed parameters and are terminated when the weighted sum of squared deviations becomes stationary (that is when $\frac{\partial \chi^2}{\partial b} = 0$). This typically takes between seven and twenty-five iterations, depending on the complexity of the spectrum and the closeness of guessed initial parameters to their final values. The initial choice of parameters was found not to be critical, with the exception of T_0 , which could be estimated quite accurately from the data. Alternatively, if T_0 changed significantly during a run, the analysis was repeated with a new value of T_0 chosen to be closer to that at convergence.

The major difference between POSITRONFIT and RESOLUTION is in the treatment of the source contribution. In the former code, a fixed source contribution is subtracted prior to analysis of the full spectrum, whereas the latter code treats all components, including those arising from the source, as model parameters during the iteration procedure. RESOLUTION allows up to five gaussians in the resolution function and four lifetime components to be ascribed. Both programmes permit constraints to be imposed on individual components, gaussians and linear combinations of intensities. T_0 is always left as a free parameter and a region in the data defined from which the background is determined.

The routines which comprised PATFIT have been used successfully by many groups to analyse data from a large variety of experimental situations. As pointed out by Kirkegaard *et al* (1982), the major limitation of such analysis programmes is that fitting model parameters to experimental data is a mathematical exercise and the derived

parameters are therefore, in the first instance, mathematical quantities, which only take on physical meaning if they can be unambiguously related to positron processes. Several models can provide a good fit to a particular data set, especially if enough fitting parameters are chosen, so considerable care must be taken in the interpretation of parameters as physical quantities. One particular problem is that the number of components is not known *a priori* and indeed is often considered to be a function of the resolution of the system. In some cases, the resolution of the instrument will be insufficient for the fitting routine to separate the components required for a particular model. On the other hand, a low number of counts in the spectrum, which is often a direct consequence of improved resolution, gives poor statistical accuracy and the possibility of local minima in parameter phase space, resulting in erroneous determination of optimum parameter values. This problem can usually be overcome by varying the initial guessed parameters and checking for consistency in these quantities at convergence. The compromise between resolution and count rate depends on details of the specific problem being studied and also, to some extent, on the method of analysis.

Another complication arises from the difficulty in separating the resolution function from the lifetime components since in most cases, the full width at half maximum (FWHM) is comparable to the shortest lifetime components. This problem has been discussed at some length during recent positron conferences such as ICPA8 (Dorikens-Vanpraet *et al*, eds., 1989).

Computer generated e^+ lifetime spectra are often analysed to assist in the separation of experimental data into individual components. Lifetime spectra can be generated according to the number of parameters and/or constraints required for a particular model and the analysis compared with that of the experimental data. The input parameters of the generated programme are then varied until agreement is reached. This laborious procedure is not totally reliable and, ideally, experimental conditions should be chosen which facilitate reduction of measured spectra into the number of components required by

TABLE 3.1
Generated Positron Lifetime Spectra

	3 Component			4 Component			
Gaussians	G_1	G_2		G_3	G_4		
Intensity	25%	75%		25%	75%		
FWHM (ps)	381	279		381	279		
Displacements (ps)	-6	0		-6	0		
Lifetimes	τ_1	τ_2	τ_3	τ_1	τ_2	τ_3	τ_4
Lifetime (ps)	225	370	2123	225	370	2123	390
Intensity (%)	83.3	16	.7	80.3	16	.7	3.0
Time-zero (ch.)		100			100		
Background (cts)		35			35		

the model. Generated spectra can also be used to monitor the effects of number of gaussians chosen to represent the resolution function, start channel, total counts, background and resolution on fitted parameters and thus to assess the possibility of improving the experimental procedure by, for example, increasing run times.

The effect of the above mentioned parameters was considered by generating spectra representative of the experimental data recorded during the e^+ mobility measurements discussed below. The generation programme input parameters for three and four component spectra are shown in Table 3.1. Fitting routines, including RESOLUTION, generally decompose the resolution function of experimental spectra into gaussians. However, this does not establish conclusively that "real" resolution functions are

combinations of gaussians, only that they are approximated by this form. Generated spectra used in the current study were constructed with two gaussian resolution functions and hence may not provide the most stringent test of a routine which reduces the resolution function back to a summation of gaussians. In a similar study, de Vries (1987) constructed more realistic spectra by adding exponential lifetime components to a measured ^{60}Co spectrum, which was considered to be representative of the ^{22}Na resolution function for the instrument used. The conclusions reached from this study were similar to those discussed below, so generated spectra containing resolution functions constructed from gaussians can be considered to be adequate representations of real e^+ lifetime spectra.

1. **Number of gaussians**

The effect of the number of gaussians included in the analysis on the fitted parameters obtained from RESOLUTION is shown in Figure 3.8 for an experimentally measured three component (silicon with Kapton source) spectrum containing 2×10^6 counts. The time-zero position is approximately at channel 113.5. The data show an inferior fit and greater variation in fitted parameters with start channel for the single gaussian case. Two and three gaussian fits gave similar results and only showed large variations with start channels close to time-zero. Three gaussian fits required more iterations for convergence, particularly when the start channel was close to time-zero. Consequently, two gaussian fits were used to analyse all data recorded in the present work.

2. **Start channel**

Figure 3.9 shows one, two and three gaussian fits to a three component generated spectrum (see Table 3.1) with no statistics added. The behaviour is similar to that shown in Figure 3.8 above. The distributions show that for two and three gaussian fits, a start channel significantly less (≈ 10 channels) than time-zero should be chosen. However, in practice, experimental data were best fitted with the start

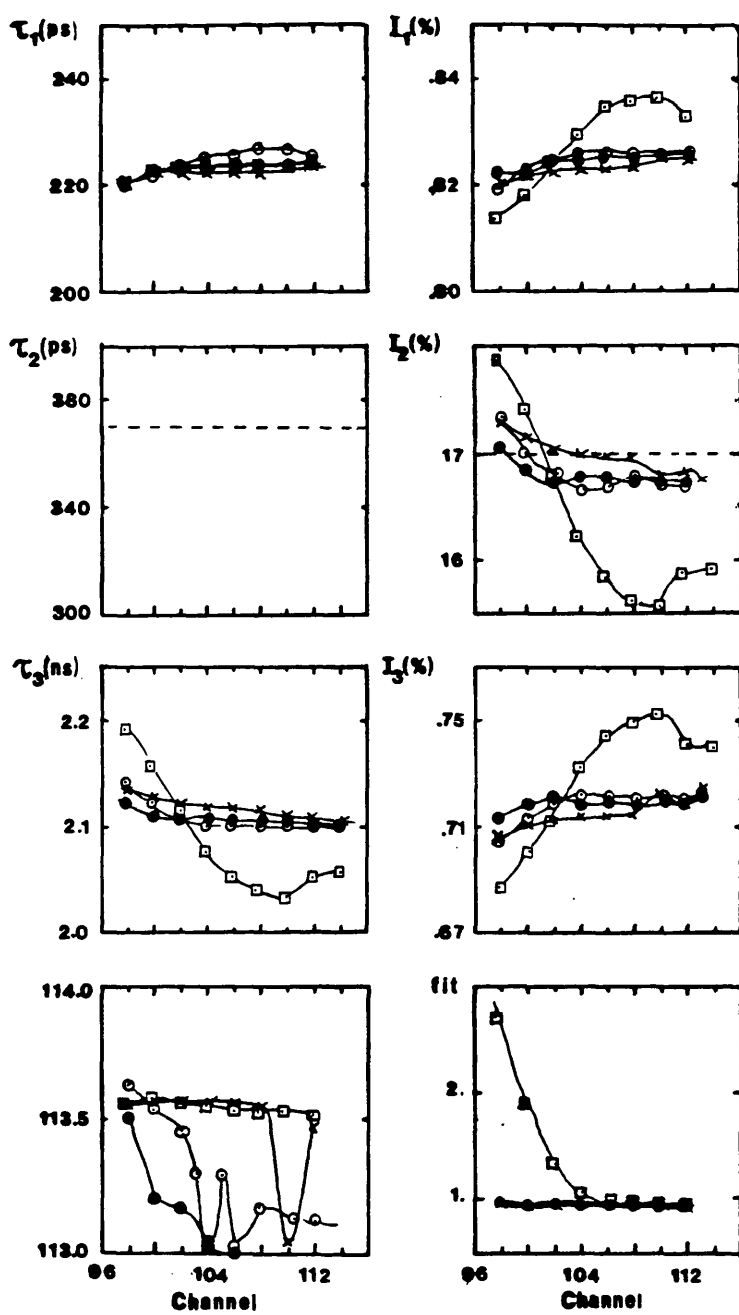


Figure 3.8 Effect of the number of gaussians on fitted parameters. ^{22}Na source in "Kapton" surrounded by Si. Three component spectrum with τ_2 fixed at 370ps

- One gaussian fit
- × Two gaussian fit
- ⊙ Three gaussian fit (Relative gaussian intensities 10%, 25% and 65%)
- Three gaussian fit (Relative gaussian intensities 30%, 30% and 40%)

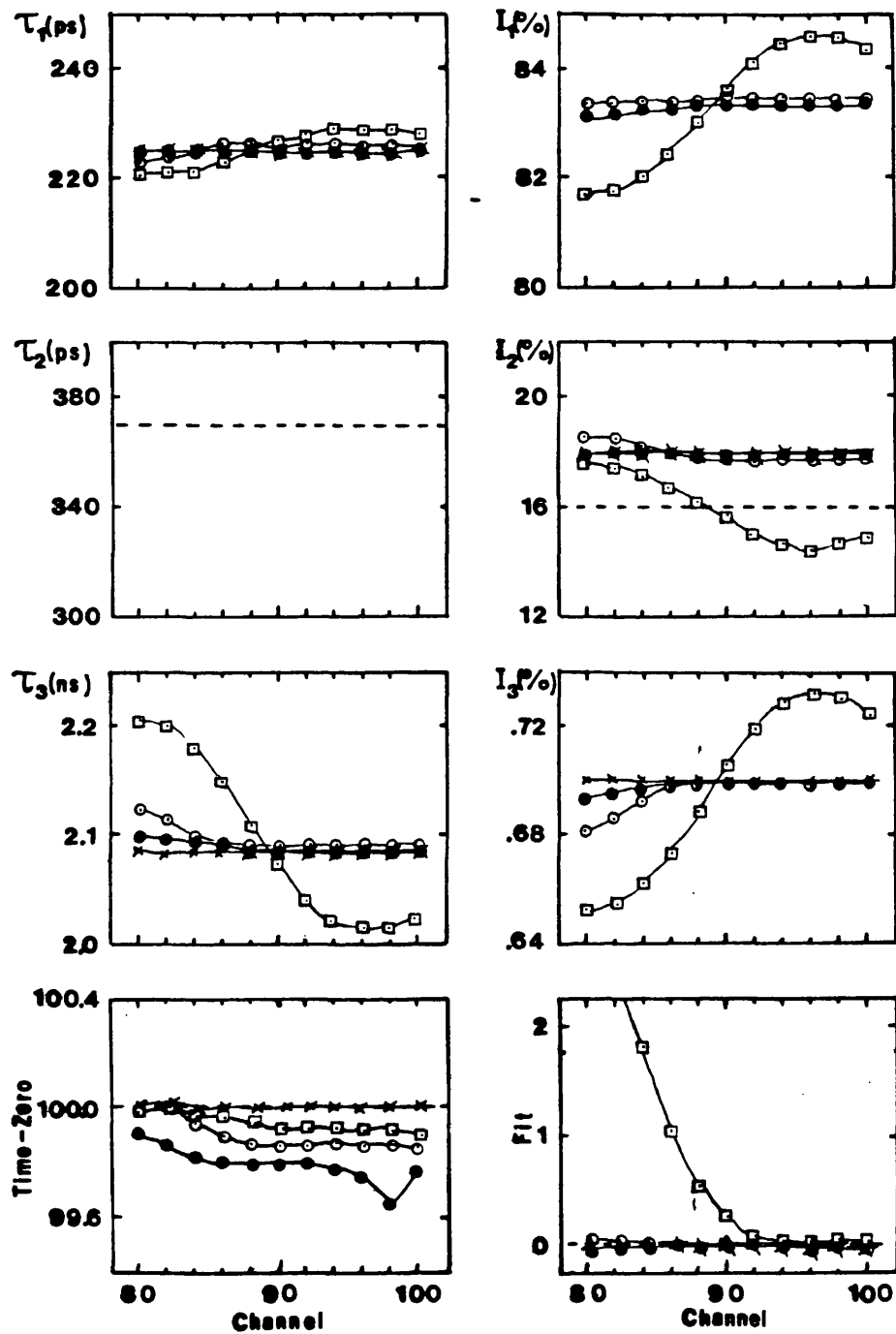


Figure 3.9 Effect of start channel on one, two and three gaussian fits to a three component generated spectrum (see Table 3.1).
 Symbols as for Figure 3.8

channel between 5 and 8 channels less than time-zero. This is probably due to the degrading effect of statistical fluctuations, and the possibility of non-gaussian components in the resolution function, which were not included in the generated spectra.

3. Total counts in the spectrum

Figure 3.10 shows the variation in fitted parameters with total number of counts for a three component spectrum. With all three lifetimes free, accurate fits were only obtained for spectra containing more than $\approx 5 \times 10^6$ counts. However, if τ_2 were fixed, fewer counts were required for reliable fitting. Figure 3.11 shows variations in fitted parameters with total number of counts for the four component spectrum in Table 3.1. For the first two sets of constraints described in the figure caption, adequate fits were obtained, even at low numbers of counts, for all parameters apart from τ_4 and I_4 . With the third set of constraints, in which I_2 was left free, poor parameter values were generally obtained. Fits to experimental mobility data were performed using the second set of parameters in which τ_4 , the interfacial lifetime was fixed (see Section 3.5.1). Consequently, good fits were expected for these spectra, which typically contained between 1.5 and 2×10^6 counts.

4. Background

The variation in the fitted parameters with the background fixed by RESOLUTION is shown in Figure 3.12 for a three component spectrum. The true background in the generated spectra is 35 counts in all cases. The strong effect of background on τ_3 can be seen. When left free, τ_2 was also affected by the background, although to a lesser extent.

From the generated spectra, it could be seen that even at high channel numbers, a significant proportion of the counts were associated with τ_3 rather than the background. Consequently the background in experimental spectra was calculated

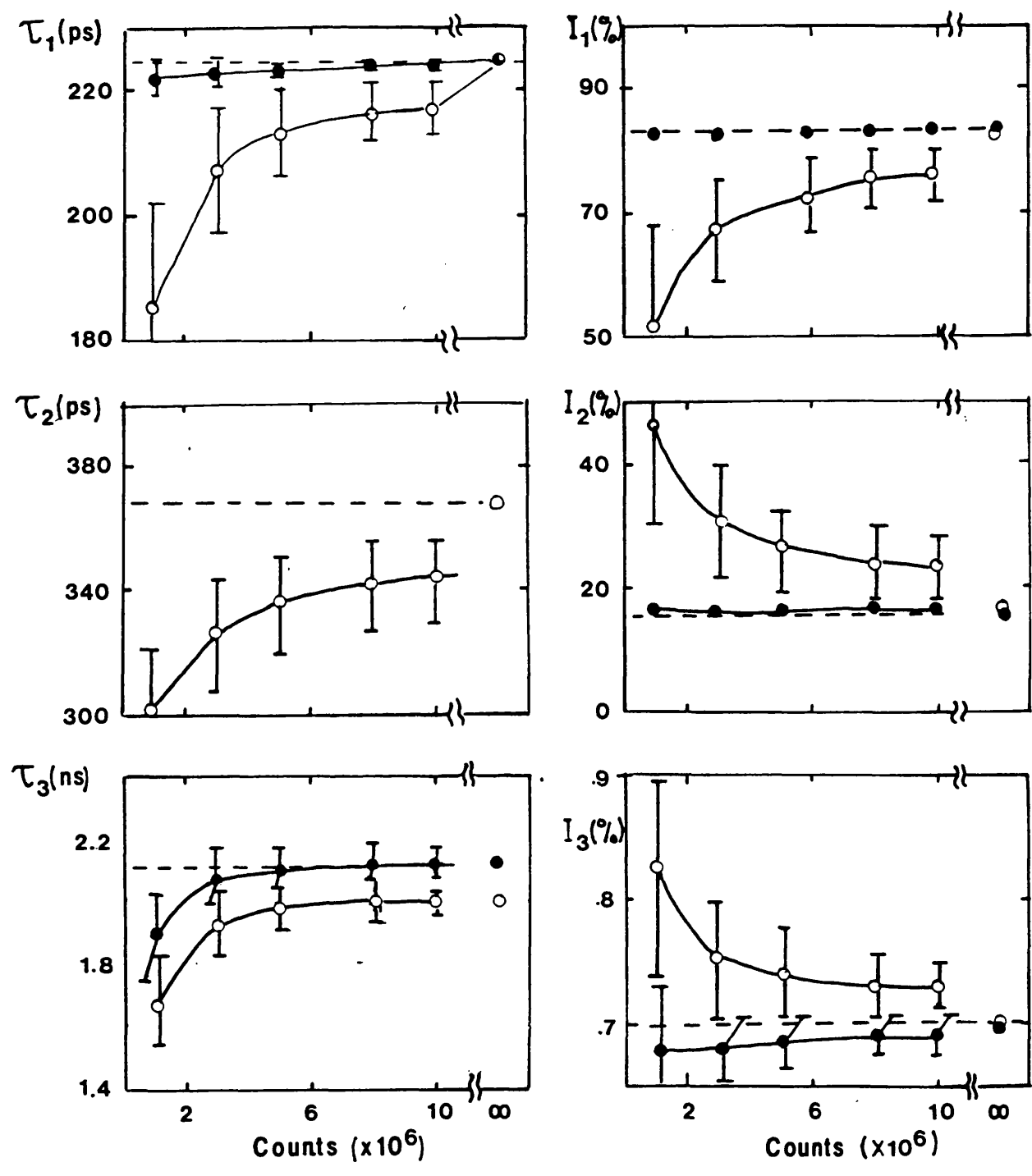


Figure 3.10 Variation of fitted parameters with total counts in spectrum. Three lifetime components (see Table 3.1)

- τ_2 fixed at 370ps
- All lifetime components left as free parameters

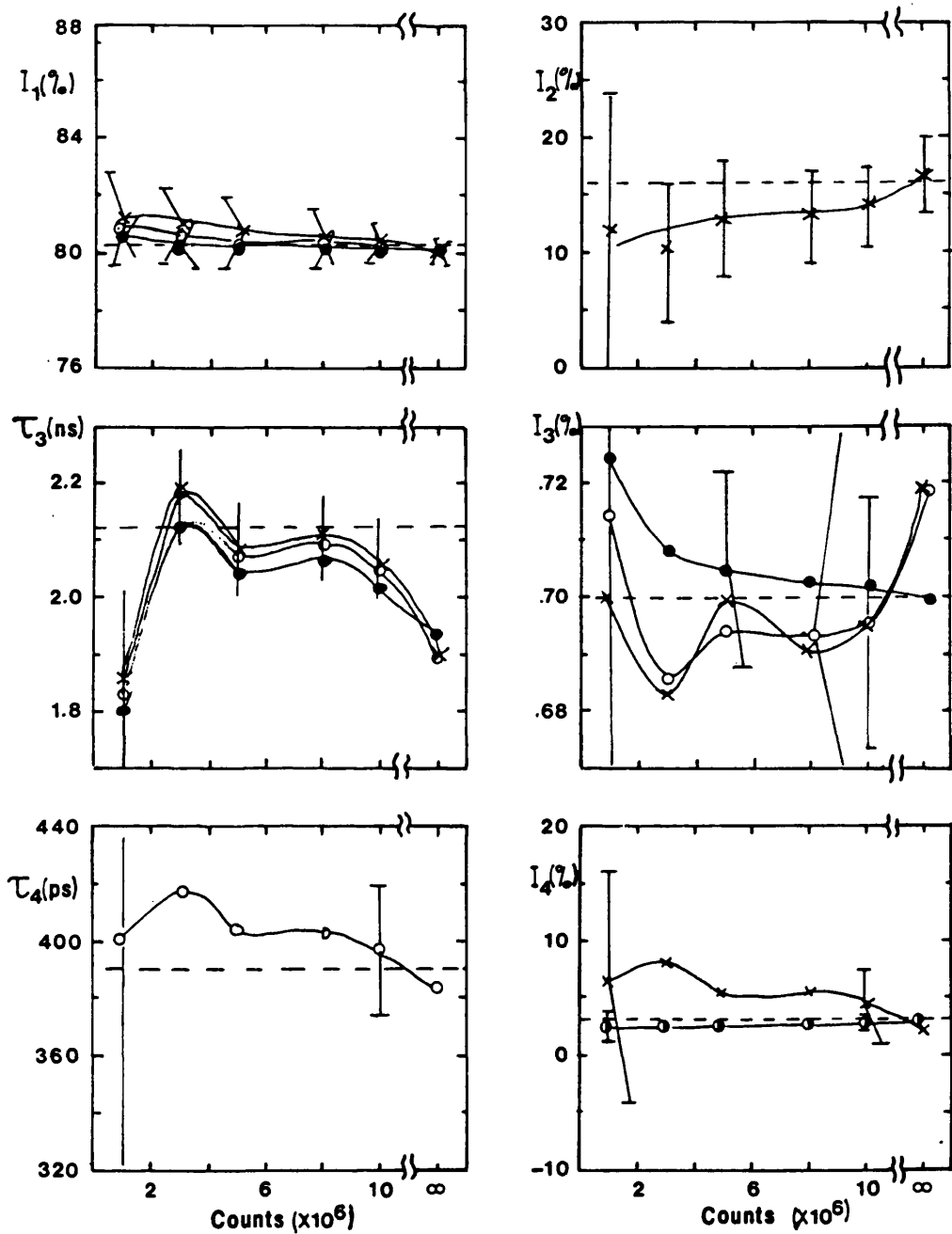


Figure 3.11 Variation of fitted parameters with total counts in spectrum. Four lifetime components (see Table 3.1)

- τ_1, τ_2, I_2 and τ_4 fixed
- τ_1, τ_2 and I_2 fixed
- × τ_1, τ_2 and τ_4 fixed

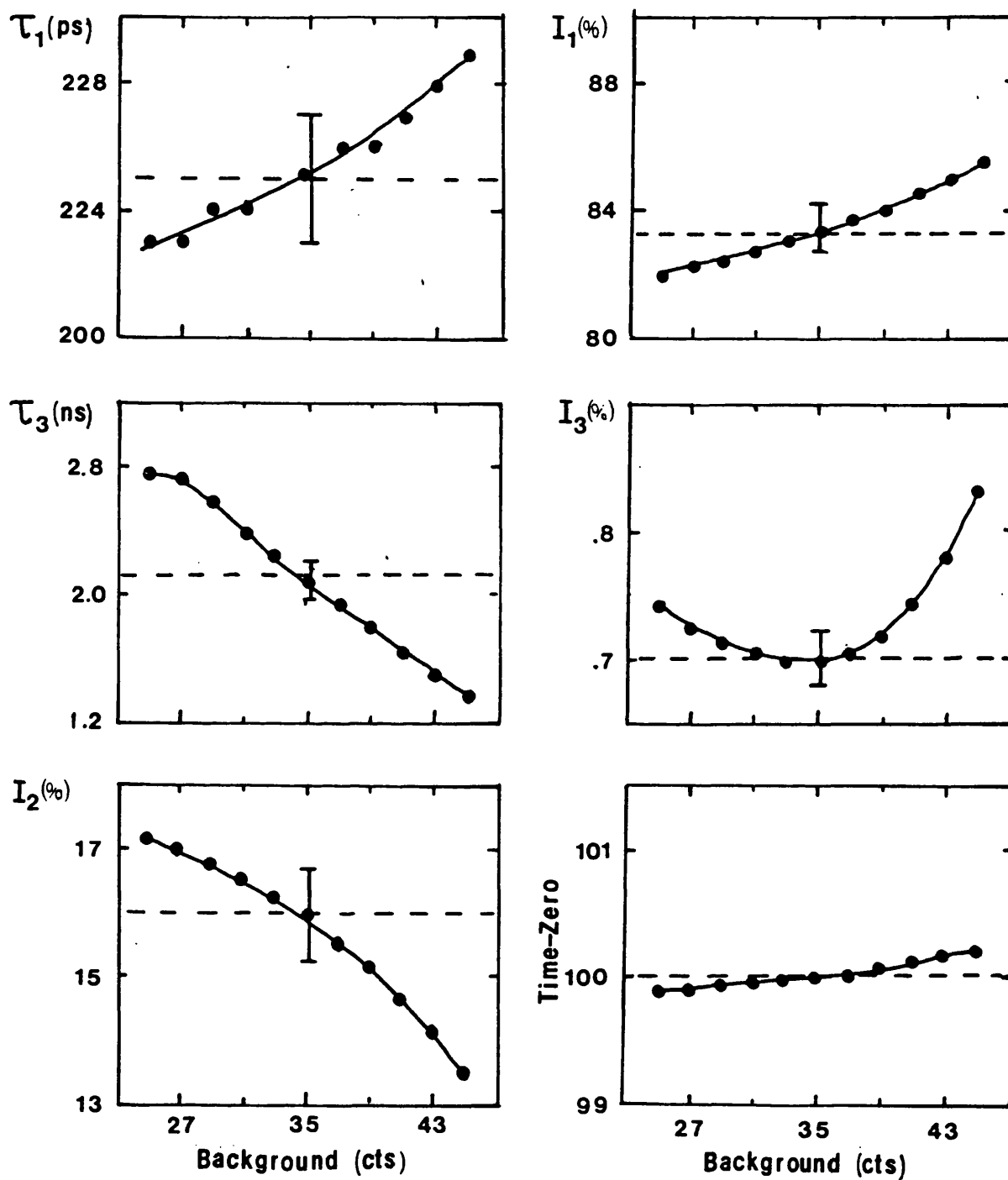


Figure 3.12 Variation of fitted parameters with background for a three component spectrum (see Table 3.1). τ_3 fixed at 370ps

from the number of stops and starts recorded on the scalars, using the expression

$$B_i = \frac{N_1 N_2 (1 - \alpha) t_{ch}}{T} \quad 3:9$$

where α is the timing efficiency (fraction of start events which produce a coincidence output from the TAC). For the present arrangement $\alpha \approx 1\%$, so the expression approximates to Equation 3:1.

Another important quantity relating to the background is its ratio to the signal in the spectrum. This was discussed in Section 3.2.3. No study of the quality of fit with this quantity was made. However, the greater experimental errors associated with the low temperature mobility data were a direct consequence of a reduction in the signal to background ratio, compared to that for room temperature measurements.

5. Resolution

The effect of resolution (FWHM) on fits to three and four component spectra are shown in Figures 3.13 and 3.14. For the three component fit, all lifetimes were left free and there was a significant improvement in accuracy with decreasing FWHM. If τ_2 were fixed at 370ps, good accuracy was achieved at all resolutions. This constraint was used for the analysis of experimental data assumed to contain three components. For the four component spectra, constraints needed to be applied to obtain reliable results. In the analysis shown in Figure 3.14, τ_2 and I_2 were fixed and good accuracy obtained for the other free components. This set of constraints was applied for the analysis of the mobility data discussed below. The statistical error on τ_4 calculated by RESOLUTION was large ($\approx 30\%$) and only decreased slowly with decreasing FWHM. This suggests that in determining τ_4 , the effect of statistics was more significant than that of resolution. The uncertainty in τ_4 was the major limitation in accuracy of the current experimental technique for the

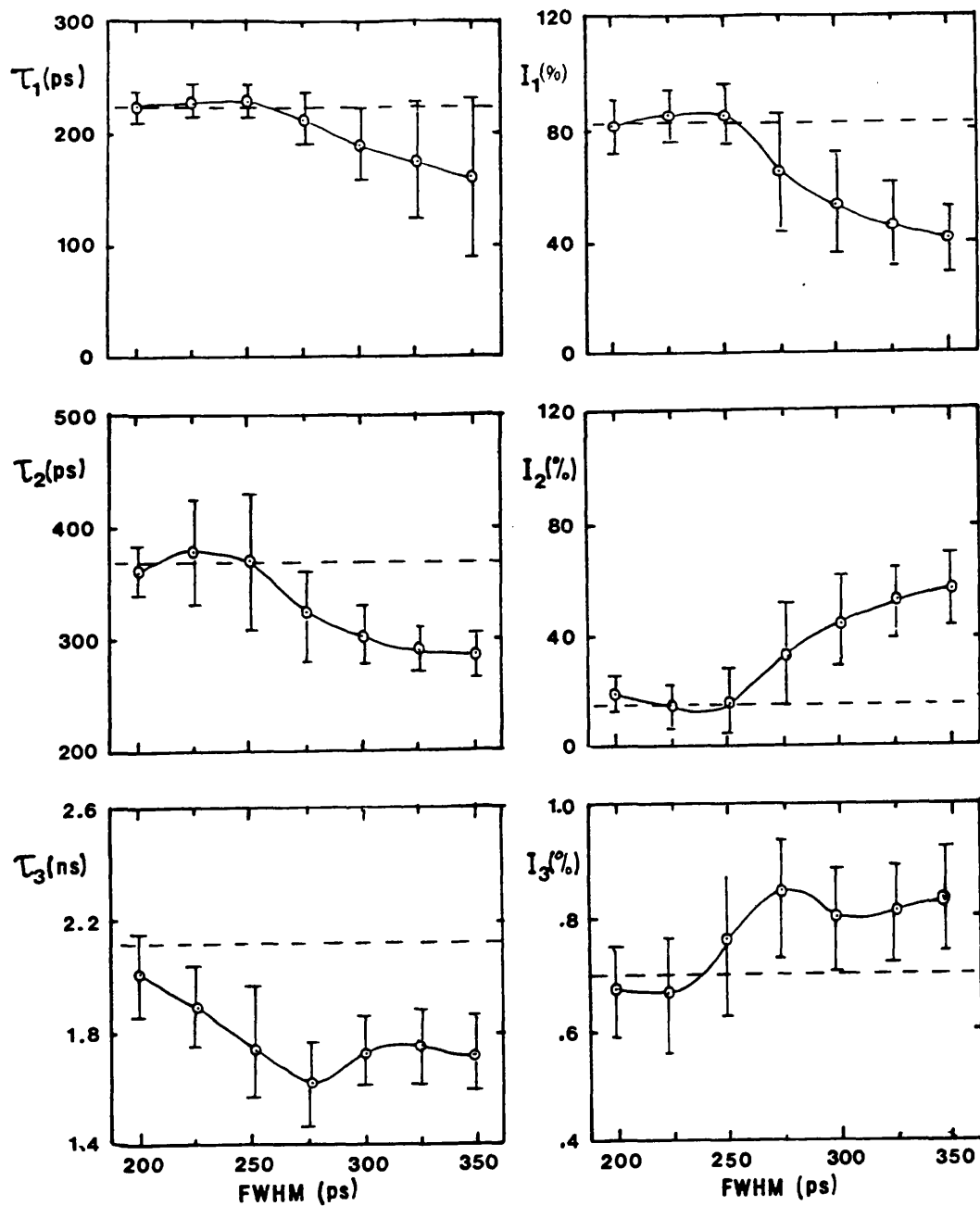


Figure 3.13 Variation of fitted parameters with FWHM of the resolution function for a three component spectrum (see Table 3.1)

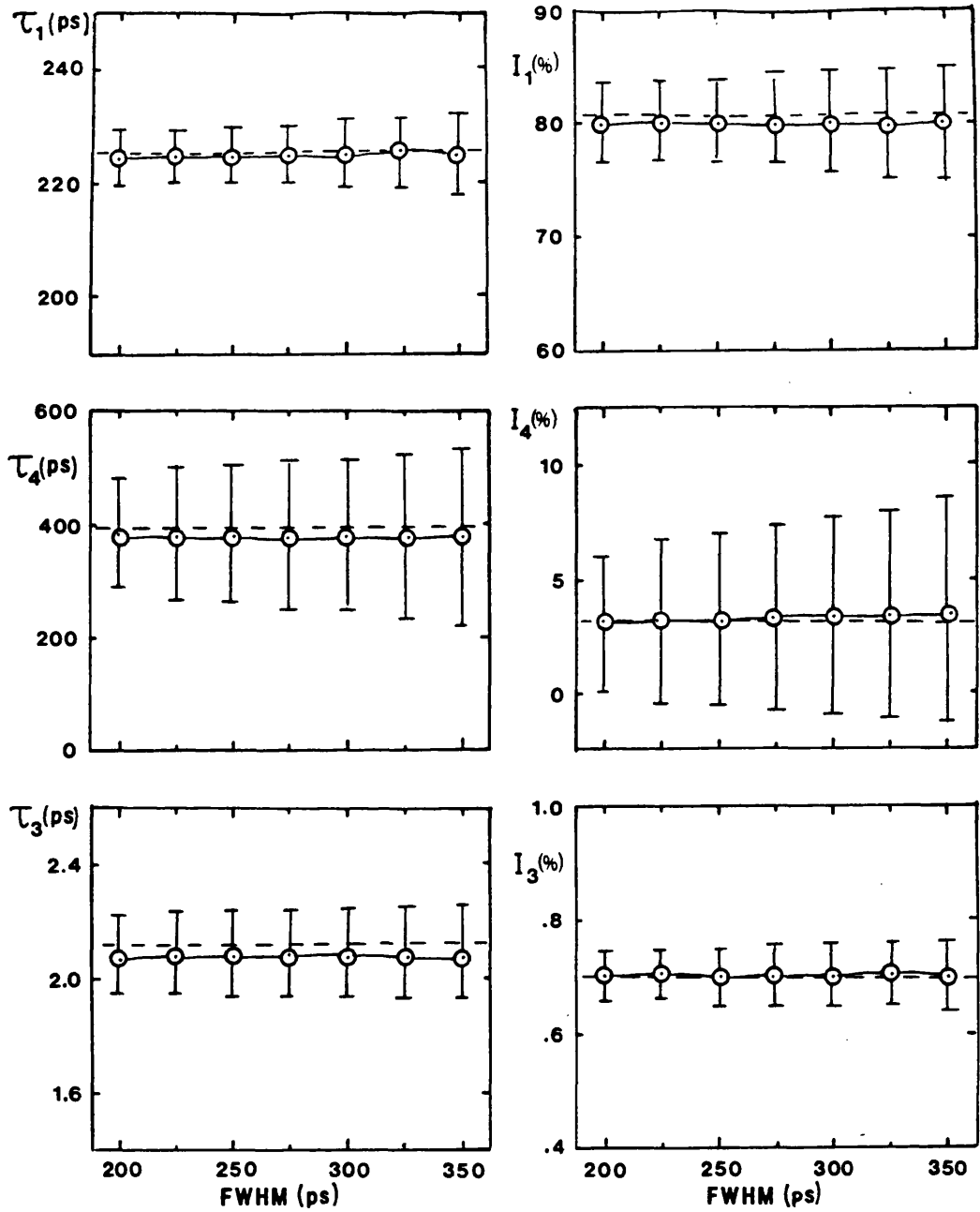


Figure 3.14 Variation of fitted parameters with FWHM of the resolution function for a four component spectrum (see Table 3.1)

determination of positron mobilities. In materials other than silicon, τ_4 may be substantially different from the other components present in the zero field spectra and greater experimental accuracy would therefore be expected.

The effect on accuracy of the fits obtained by RESOLUTION for three and four component lifetime spectra has been considered. In most cases fitted parameters agree with their true values to within the calculated errors. Significant improvements in accuracy can be achieved if constraints are applied to some of the components. However, caution must be exercised to ensure that all constraints are valid.

3.3.2 Centroid Shifts

The centroid, σ , and error, $\Delta\sigma$, of a discrete distribution of data are given by

$$\sigma = \frac{\sum_i D_i i}{\sum_i D_i}$$

and

$$\Delta\sigma = \frac{\sqrt{\sum_i (i - \sigma)^2 D_i}}{\sum_i D_i}$$

3:10

where the summation i runs over all channels of interest. Shifts in centroid position can be related to changes in lifetime or intensity of the components in a spectrum. For the current work, centroid shifts between electric field and zero field spectra were related to the positron mobility in Si. For a positron lifetime spectrum the centroid, $\bar{\tau}$, is related to the intensity and lifetimes of the various components, j , by

$$\bar{\tau} = \sum_j I_j \tau_j$$

where

$$\sum_j I_j = 1$$

3:11

Assuming four component spectra, the centroids of the field off and field on cases are respectively

$$\begin{aligned}\bar{\tau}_0 &= I_{10}\tau_1 + I_{20}\tau_2 + I_{30}\tau_3 + I_{40}\tau_4 \\ \bar{\tau}_V &= I_{1V}\tau'_1 + I_{2V}\tau'_2 + I_{3V}\tau'_3 + I_{4V}\tau'_4\end{aligned}\tag{3:12}$$

where the subscripts 1-4 correspond to Si bulk, Kapton source, long-lived source and interfacial components respectively. Subscripts 0 and V correspond to voltage off and on. The centroid shift due to the electric field is given by

$$\Delta\bar{\tau}_V = \bar{\tau}_V - \bar{\tau}_0\tag{3:13}$$

In the present case τ_2 , I_2 , τ_3 , I_3 and τ_4 are unchanged by the presence of the field. Also the intensity of the interfacial component is negligible at zero field, so $I_{40}=0$, and the centroid shift is given by,

$$\Delta\bar{\tau}_V = I_{1V} - I_{10}\tau'_1 + I_{4V}\tau'_4\tag{3:14}$$

From Chapter 2,

$$\tau'_1 = \lambda_1^{-1} = \frac{\tau_1}{1 + \alpha\nu_+\tau_1}$$

and

$$I_4 = \frac{\alpha\nu_+\tau_1\tau_4}{\tau_4 - \tau_1} \cdot \frac{1}{1 + \alpha\nu_+}\tag{3:15}$$

Substituting into Equation 3:14 and noting that

$$I_{1V} + I_{4V} = I_{10} + I_{40} = I_{10}\tag{3:16}$$

gives

$$\Delta\bar{\tau}_v = \Delta\bar{\tau}_0 + \frac{\alpha\tau_1(\tau_4 - \tau_1 I_{10})v_+}{1 + \alpha\tau_1 v_+}$$

3:17

$$\approx \Delta\bar{\tau}_0 + \alpha\tau_1(\tau_4 - \tau_1 I_{10})v_+$$

since

$$\alpha\tau_1 v_+ \ll 1$$

The centroid shift at zero field, $\Delta\bar{\tau}_0$, is included in the expression to allow for any significant shifts due to instrumental effects. The major advantage of the centroid method over RESOLUTION is that I_4 and τ_1' are constrained to give the same value for v_+ at a particular field. This was not possible using RESOLUTION.

3.4 EXPERIMENTAL PROCEDURE

For mobility measurements, 15mm diameter, 1mm thick disks of 10k Ω cm n-type Si(111) were etched in hydrofluoric acid and, after rinsing in distilled water, cemented into printed circuit board mounts using epoxy resin. 2000Å layers of gold and aluminium were evaporated onto either side of the samples and mounts, in the pattern shown in Figure 3.15. Electrical connections were made via the mount to avoid damage to the metal-silicon contacts. Electrical continuity between the two tracks joining each film was monitored throughout the experiment to ensure that the supply voltage was being supplied to the film. Typical forward (A_u positive with respect to A_l) and reverse (A_u negative with respect to A_l) bias current-voltage relationships are shown in Figure 3.16. Leakage currents through the samples increased with time. The reason for this behaviour is uncertain, but was possibly due to contamination at the metal-Si interface, which occurred during fabrication of the contacts.

The electric field across the Au-Si-Al samples can be calculated from Poisson's equation,

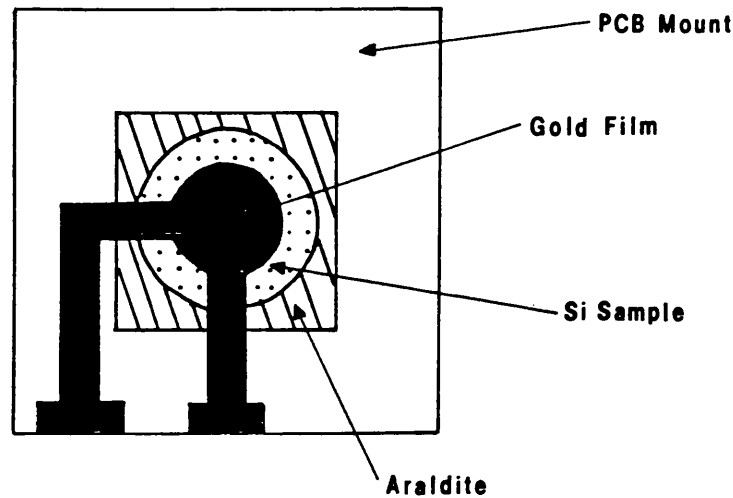


Figure 3.15 Sample mounts and contact pattern

$$-\frac{d^2V(x)}{dx^2} = q \frac{N}{\epsilon_s} \quad 3:18$$

where $V(x)$ is the voltage at position, x , in the region, q , the majority carrier charge, N , the charge donor (n-type)/acceptor (p-type) concentration and ϵ_s , the permittivity of Si (Sze, 1981, p74). The field distributions for under-depleted, fully depleted and fully depleted with over-voltage cases are shown in Figures 3.17a, b, c) respectively. The depletion voltage, V_d , is given by,

$$V_d = \frac{w^2}{2\epsilon_s \mu_c \rho} \quad 3:19$$

where w is the Si thickness, ρ its resistivity and μ_c the electron (n-type) or hole (p-type) mobility. For the samples used in the present study, $\rho=10^4 \Omega\text{cm}$ (n-type), $w=0.95\text{mm}$, $\epsilon_s=11.9\epsilon_0$ and $\mu=1500\text{cm}^2\text{V}^{-1}\text{s}^{-1}$, so $V_d = 286\text{V}$. Since the maximum e^+ drift length is

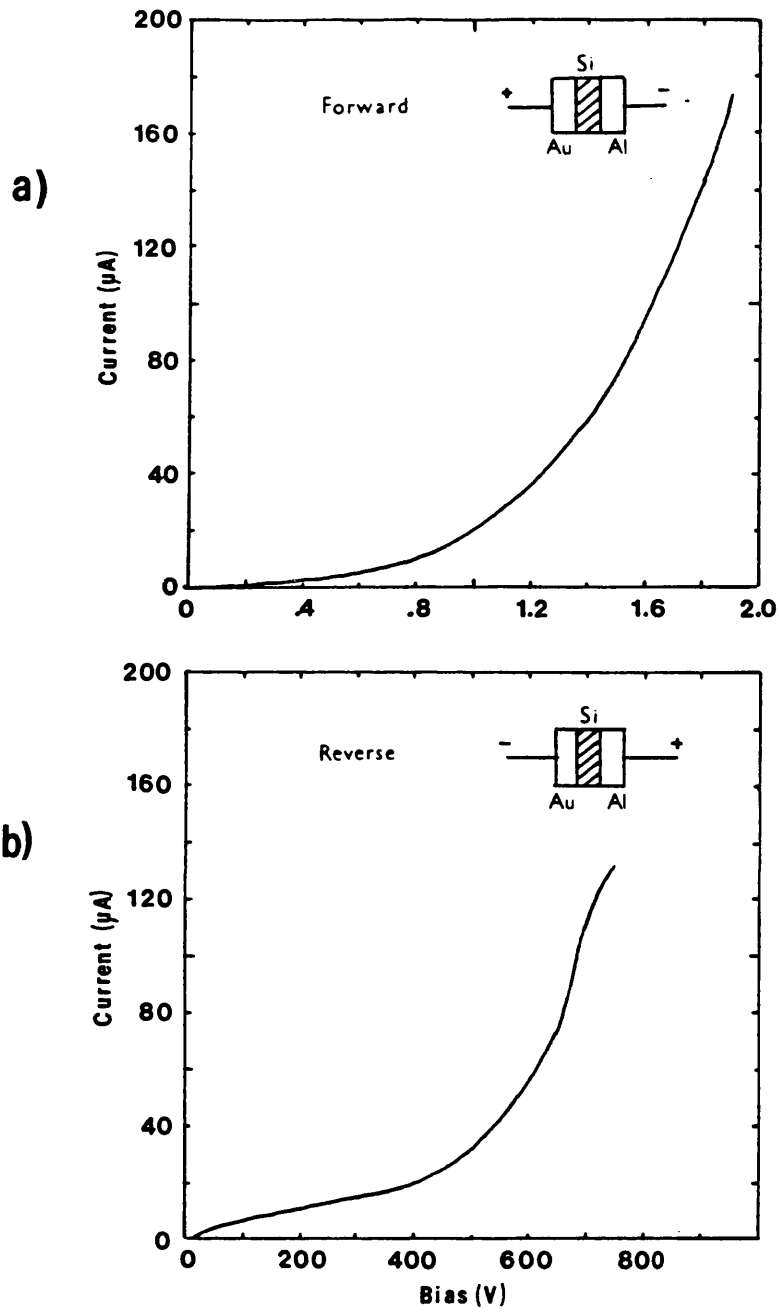


Figure 3.16 Current-voltage characteristics for an Au-Si-Al sample used for e^+ mobility measurements in Si

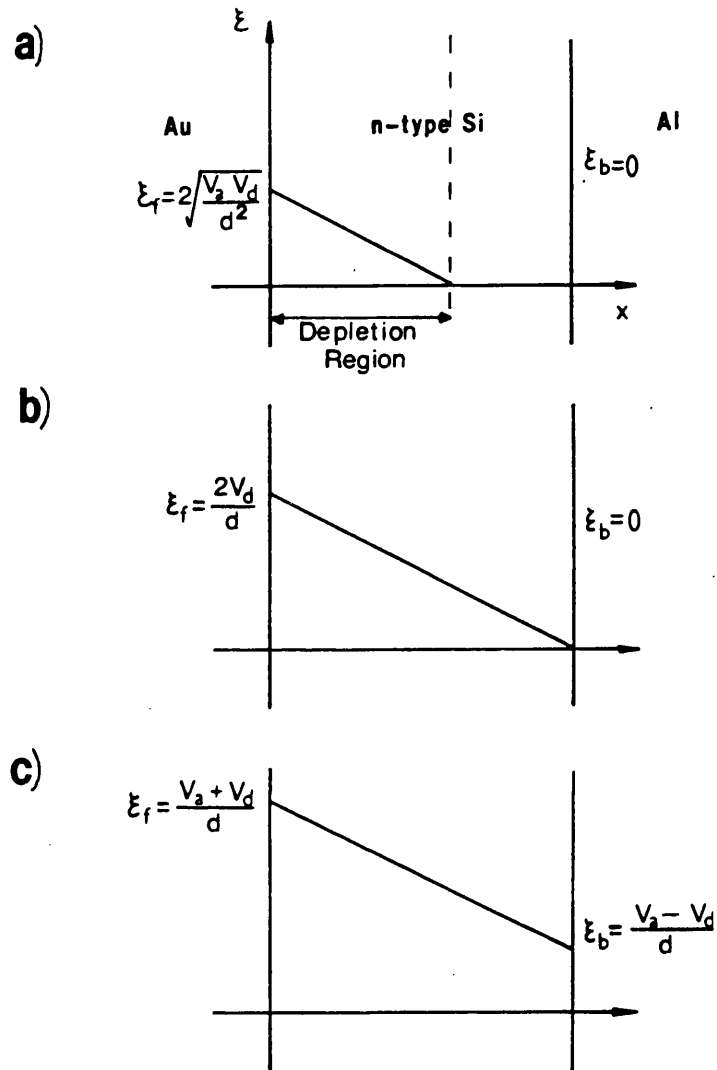


Figure 3.17 Variation of the electric field with position for a reverse biased Au-nSi-Al sample

- a) Under-depleted ($V_a < V_d$)
- b) Fully depleted ($V_a = V_d$)
- c) Fully depleted with over-voltage ($V_a > V_d$)

V_a is the potential applied across the sample, V_d , the potential required to deplete the sample fully and d , the Si thickness

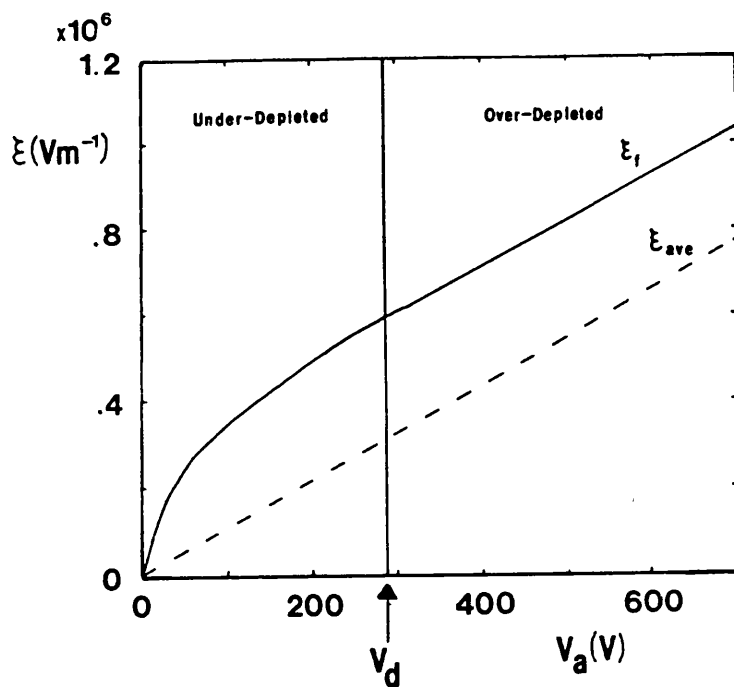


Figure 3.18 Variation of electric field, ξ , at the Si-Au interface with applied bias for the $10\text{k}\Omega\text{cm}$ n-type samples used in the present study. A bias of 286V is required to deplete the sample fully.

$\approx 10^5(\text{ms}^{-1}) \cdot 10^{-10}(\text{s}) = 10\mu\text{m}$, e^+ drifting into the Au-Si interface experience a uniform field, ξ , approximately equal to that at the interface, ξ_f . The variation of ξ_f with applied bias, V_a , is shown in Figure 3.18.

For mobility measurements, the samples were arranged with gold contacts adjacent to the source, as shown in Figure 3.19, so that, with reverse bias applied, e^+ drifted towards the source. However some data were collected with the samples reversed. In this case e^+ drifted towards the source and the observed effect of the field on the spectrum was expected to be reduced, if the (τ_d, I_d) component arose from annihilations at the Si-Au interface.

For low temperature measurements, a cryostat was constructed using an Edwards cold trap as the liquid nitrogen reservoir (see Figure 3.20). The samples were mounted in a copper holder which was maintained in good thermal contact with the reservoir via a copper cold finger. The cryostat was evacuated to 10^{-2} torr using a rotary pump.

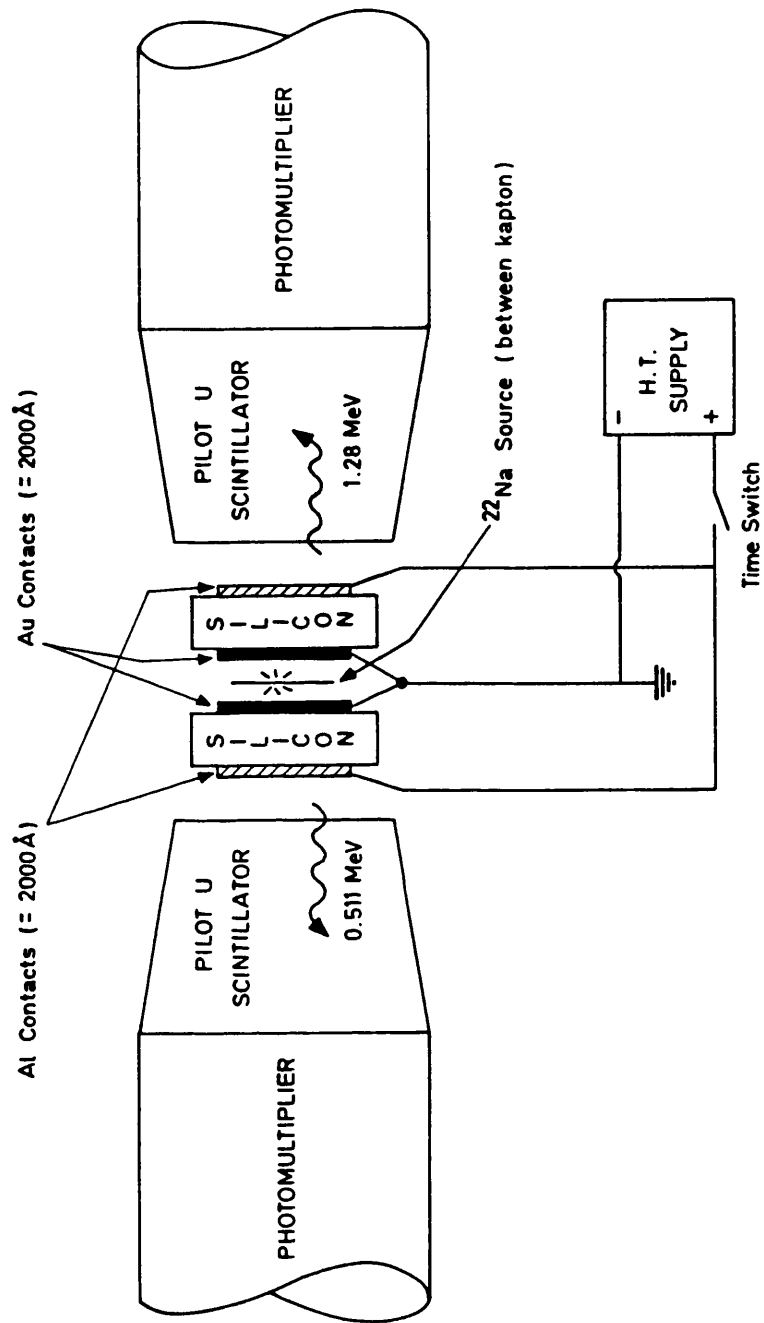


Figure 3.19 Sample/source arrangement used for e^+ measurements.

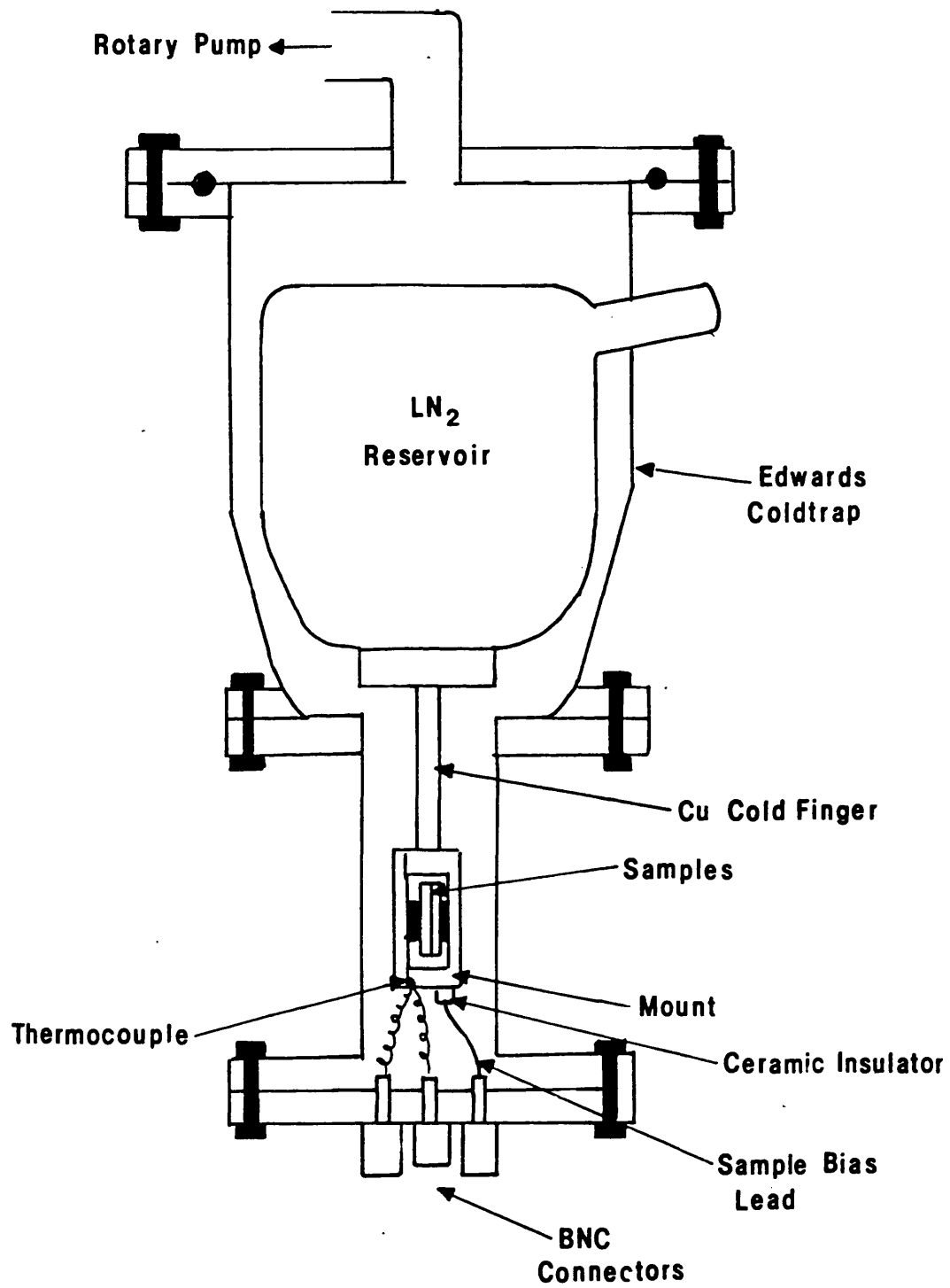


Figure 3.20 Cryostat used for low temperature measurements

For these measurements, a negative bias was applied to the gold contacts adjacent to the source; the Al contacts being held at earth potential by the copper mount. The temperature of the mount was monitored by a thermocouple which indicated a steady temperature of $(104 \pm 4) \text{K}$ with LN_2 in the cryostat reservoir. On cooling, an increase in leakage current through the samples was observed, which may have been due to cracking of the epoxy mount or stresses introduced into the samples by contraction. This made it impossible to extend measurements above 250V applied bias without significant Joule heating.

For low temperature measurements, the reduced solid angle subtended by the detectors resulted in a significantly lower count rate than that at room temperature (295K). This was partially overcome by increasing the source activity to about $20 \mu \text{Ci}$. Consequently, the signal to background ratio was reduced, increasing the error in measured parameters.

Pairs of spectra were collected by switching the active half of the MCA memory as described in Section 3.2.2. Usually a field on/field off pair was collected, followed by a field off/field off pair, which permitted the electronic stability to be monitored. During a two day run, between 1 and 2×10^6 counts were collected in each spectrum.

3.5 RESULTS

3.5.1 RESOLUTION

Zero field spectra were well fitted by three lifetime components of 224, 370 and $\approx 1500 \text{ps}$, with intensities of about 83%, 16% and 1% respectively. The first component was associated with annihilations in bulk Si whereas the second and third components arose from annihilations in the source. Electric field spectra showed a fourth component with a lifetime, τ_4 , close to that of the source-supporting Kapton foils (370ps) and an intensity which increased with applied bias. A value for this lifetime could not be determined

directly from RESOLUTION, as mentioned in Section 3.3. However, τ_4 could be deduced from the expression derived in Chapter 2 for I_4 and the effective e^+ annihilation rate in bulk Si, λ_1' , namely

$$\kappa = (\lambda_1 - \lambda_4) \frac{I_4}{1 - I_4}$$

and

$$\lambda_1' = \lambda_1 + \kappa \quad 3:20$$

where

$$\kappa = \alpha v_+$$

λ_1' and I_4 are constrained via Equations 3:17. Using a three component fit to all the zero field data, an average value for I_2 , the Kapton lifetime, was determined. Electric field spectra were subsequently analysed for a range of fixed values of τ_4 using a four component fit with I_2 and τ_2 fixed. For each value of τ_4 , values of κ and hence $\tau_1' = (\lambda_1')^{-1}$ were determined from the measured value of I_4 , using Equation 3:17.

Finally this value of τ_1' was plotted with the value determined from RESOLUTION against τ_4 . The crossing point of the two lines gave the best value of τ_4 (see Figure 3.21). This procedure was repeated for several pairs of spectra and an average value of τ_4 calculated. At 295K and 104K the average values for τ_4 were (397 ± 24) and (416 ± 23) ps respectively. Consequently τ_4 was assumed to be constant at (400 ± 30) ps for both temperatures studied. With τ_4 fixed at this value, I_4 was determined from RESOLUTION as a function of electric field. Figure 3.22a) shows the variation in I_4 with applied voltage for e^+ motion towards the source. For the data in Figure 3.22b) the direction of the field is reversed, so e^+ drift away from the source and have a negligible chance of reaching the Si-Au interface. For biases < 286 V, the samples are under-depleted and the electric field does not extend to the Al-Si contact, which is adjacent to the source in this

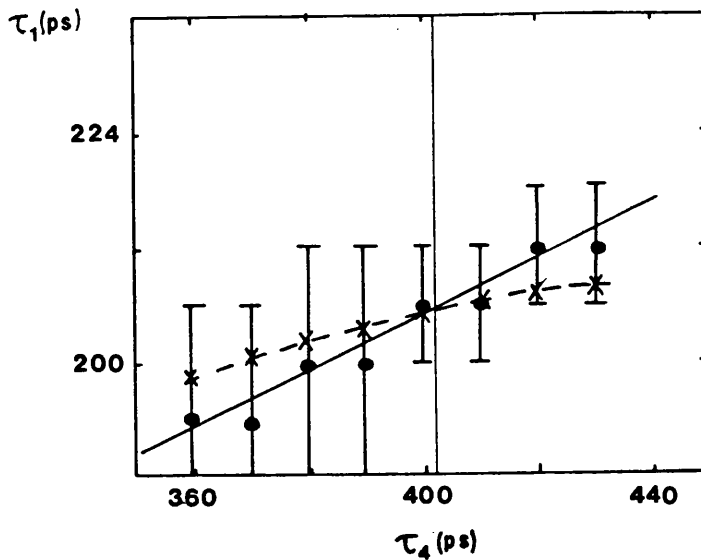


Figure 3.21 Determination of the interfacial lifetime component, τ_4

× Value of τ_1 calculated from $\tau_1 = (\lambda_1 + \kappa)^{-1}$

● Value of τ_1 determined from RESOLUTION

Intersection at $\tau_4 = 402\text{ps}$

configuration. Consequently the average field experienced by e^+ implanted into the Si bulk is substantially less than ξ_r . For higher biases, the field extends across the whole sample and the average field becomes significant. In this geometry, no significant change in I_4 with electric field was recorded, which suggests that τ_4 is associated with annihilations in an interfacial state and not with field dependent annihilation in bulk defects, for example. The exact nature of the interfacial annihilation state is uncertain, although it is expected that a significant concentration of large open volume voids (vacancy agglomerates) exist in this region, due to the non epitaxial structure of the gold contact. The measured value of τ_4 is typical of those observed for bulk voids in many metals and semiconductors. At disordered interfaces, defect concentrations approaching one per lattice site can be envisaged due to the mismatch of the crystal structure of the substrate and overlayer. It is therefore reasonable to assume that e^+ trapping into these states is governed only by the drift of e^+ to the interface and not by the trapping rate into

the defects. In a variable energy e^+ beam study discussed in Chapter 2, Corbel *et al* (1989) observed the electric field drift of e^+ from Si into an Au-Si interface using an S parameter method to monitor e^+ annihilation. Although no discussion of the nature of the interface region was given, the S parameter for e^+ annihilating at the interface was less than that measured in bulk Si or Au. This suggests that the e^+ annihilation characteristics of the interface are distinct from either bulk material.

Using the data in Figure 3.22a) values of $\mu_+(295K) = (81 \pm 17) \text{cm}^2 \text{V}^{-1} \text{s}^{-1}$ and $\mu_+(104K) = (303 \pm 65) \text{cm}^2 \text{V}^{-1} \text{s}^{-1}$ were obtained from Equation 3:17. The quoted error reflects the statistical error ($\approx 8\%$) in I_4 and an error arising from the uncertainty in τ_4 ($\approx 24\%$). Mills and Pfeiffer (1977) found that their low temperature mobility data were better fitted by the Shockley expression (Equation 2:10) rather than a linear expression. Although there appears to be some non-linearity in the present data at high fields, similar values of reduced chi squared, $\frac{\chi^2}{\nu}$, were found for both fits. However, the similarity between positron, electron and hole motion in semiconductors suggests that the Shockley expression provides the correct variation of ν_+ with ξ , as concluded by Mills and Pfeiffer (1977). Fitting this expression to the 104K data gives $\mu_+(104K) = (410 \pm 80) \text{cm}^2 \text{V}^{-1} \text{s}^{-1}$, which is significantly greater than that obtained by linear regression. At room temperature both fits gave similar values of μ_+ .

The time-zero channel is treated as a free parameter by RESOLUTION, so the main effect of electronic instability arising from temperature changes is a degradation in the resolution function (an increase in FWHM) of the spectrum. It was shown above that the effect of resolution on the parameters fitted by RESOLUTION was relatively unimportant. Consequently, analysis carried out by this method showed smaller variations due to instrument instability than those recorded in centroid shift calculations.

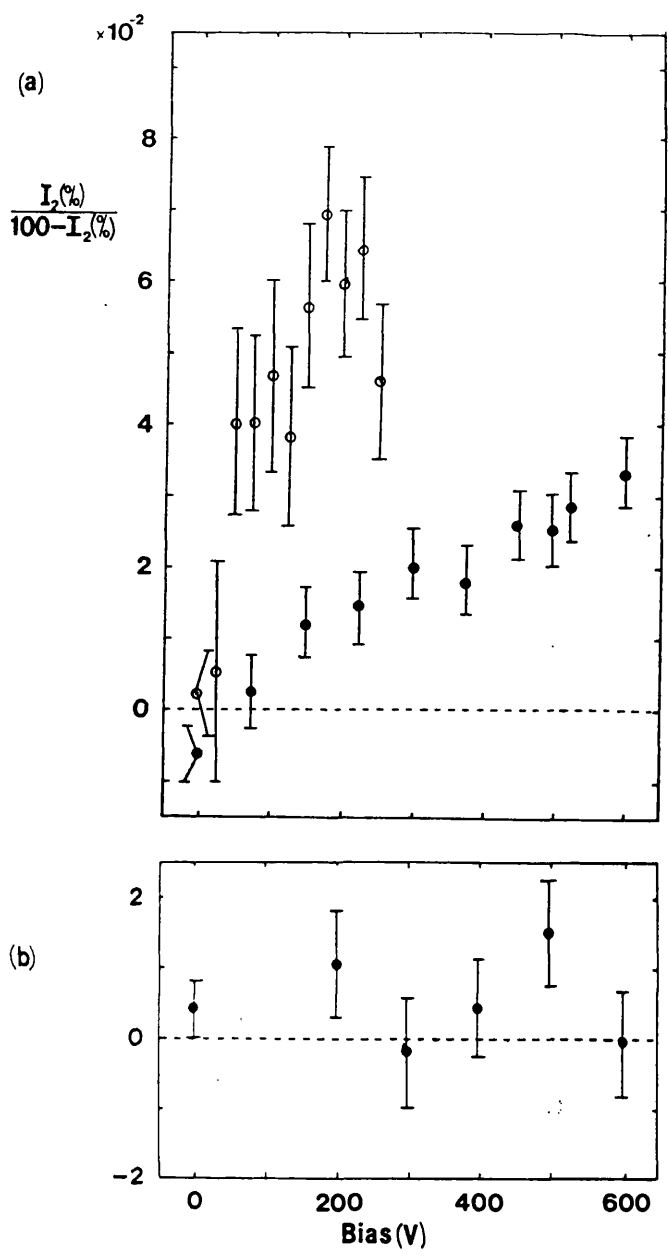


Figure 3.22 Variation in intensity of the interfacial lifetime component with electric field

a) Positron drift towards source,

● 295K

○ 104K

b) Positron drift away from source. As expected, in this case there is no statistically significant change in the lifetime spectrum with electric field,

● 295K

3.5.2 Centroid Shifts

Centroid shifts, $\Delta\bar{\tau}$, and their associated statistical errors were calculated from Equation 3:10. Figure 3.23 shows the mean centroid and centroid shift for pairs of zero field spectra, which were successively collected between each pair of field off/field on spectra. The average shift was zero to within the statistical accuracy of the data, showing that there was no systematic variation between odd and even spectra. The variation in $\Delta\bar{\tau}$ is larger than the statistical errors calculated, which suggests that these measurements were influenced by electronic instabilities in the spectrometer. However, this variation was substantially less than the corresponding change in mean centroid, which demonstrates the advantage of simultaneous collection of pairs of spectra in terms of reducing the effect of temperature induced electronic instabilities.

Figure 3.24 shows the electric field variation of ν_+ , calculated from the centroid data using Equation 3:17. A linear fit to the room temperature data gave $\mu_+(295\text{K}) = (68 \pm 11)\text{cm}^2\text{V}^{-1}\text{s}^{-1}$. The assigned error included a statistical contribution as well as those arising from uncertainties in τ_1 , I_{10} and τ_4 . As observed with the RESOLUTION data, the 104K measurements show a slight non-linear variation. Shockley and linear fits respectively gave $\mu_+(104\text{K}) = (370 \pm 80)$ and $(310 \pm 60)\text{cm}^2\text{V}^{-1}\text{s}^{-1}$. In both cases $\frac{\chi^2}{\nu} \approx \frac{13.5}{13}$, which indicates a good fit for the accuracy of the data (see Figure 3.25). A Shockley fit to the room temperature data gave a value of μ_+ in close agreement with linear regression.

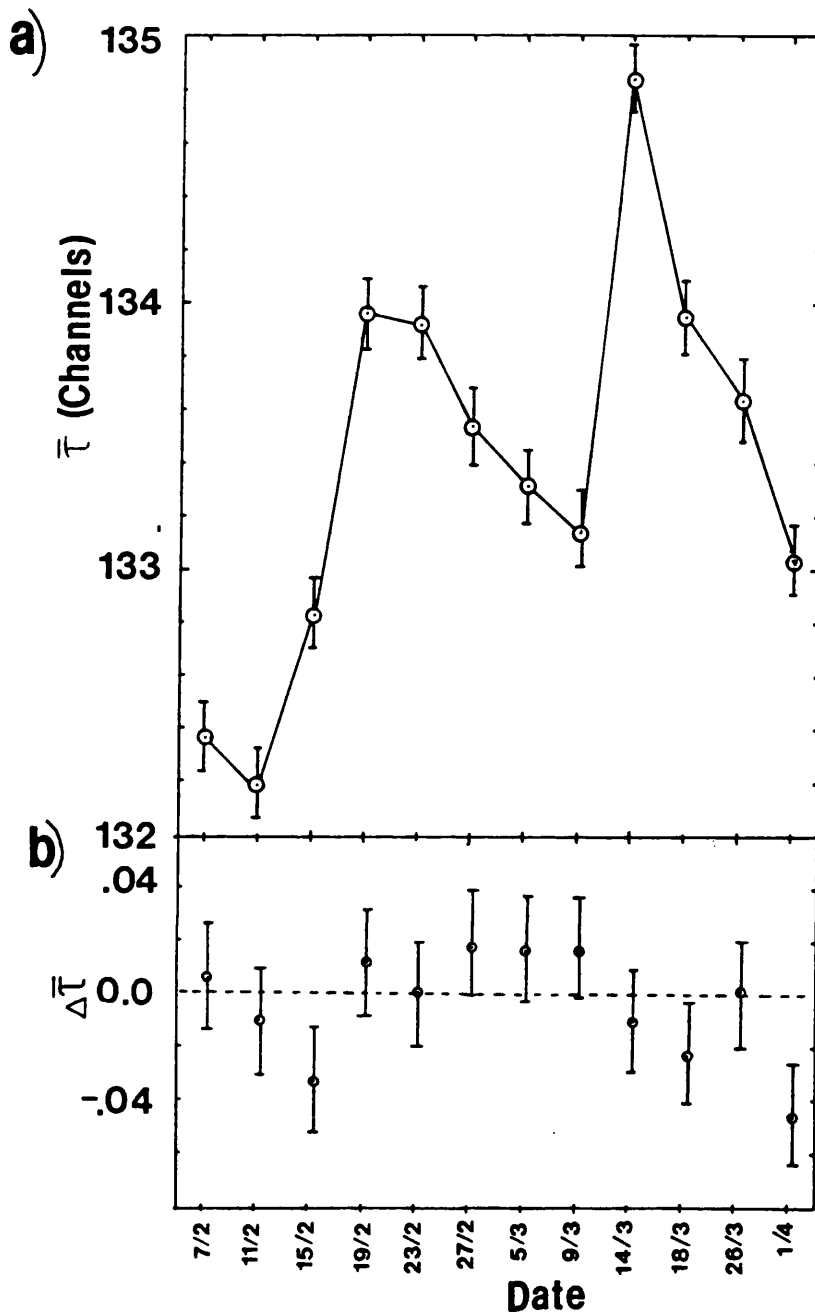


Figure 3.23 Stability of centroid measurements

- a) Variation of mean centroid position for pairs of spectra collected with no applied field
- b) Corresponding variation in centroid shift

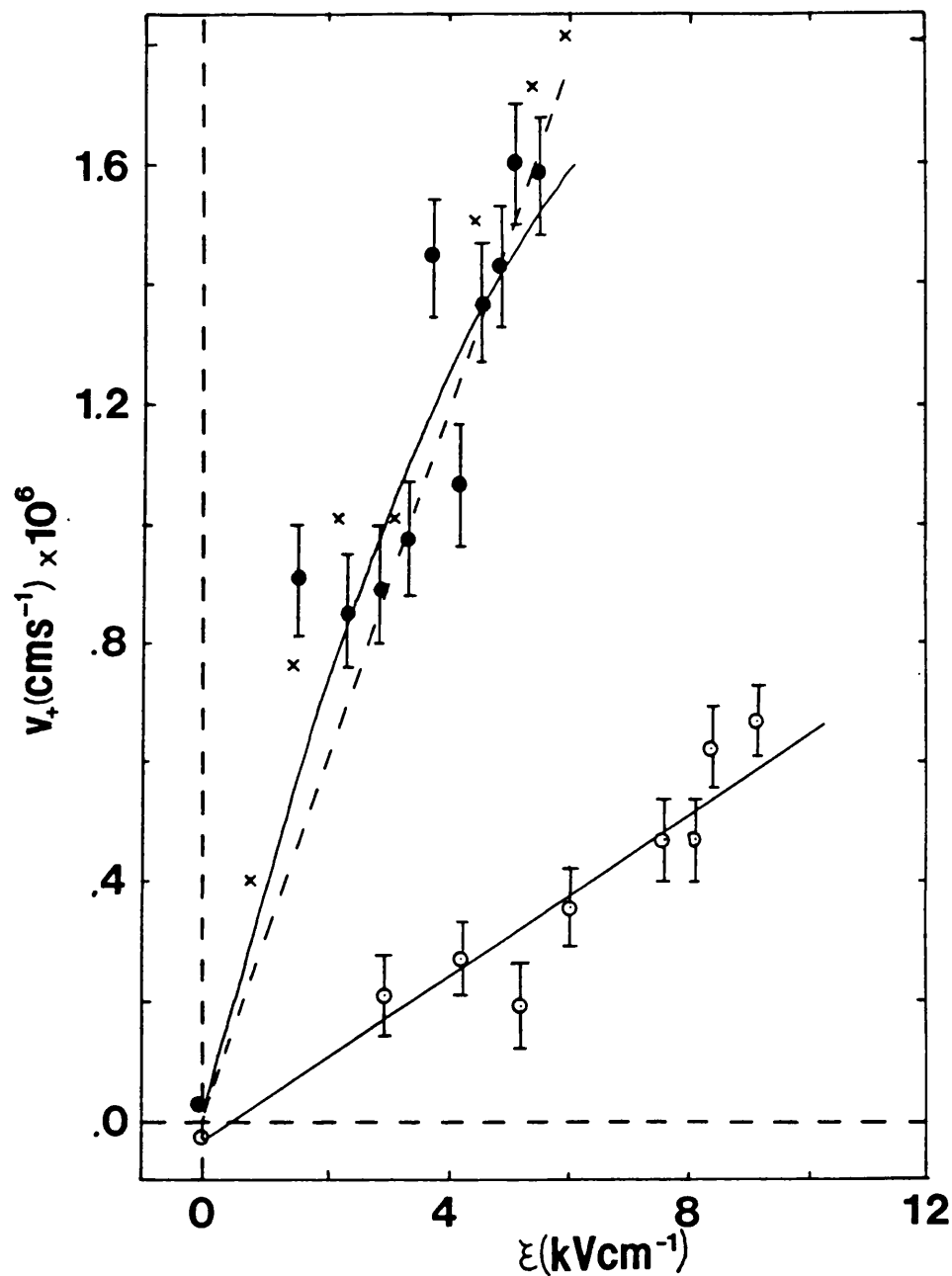


Figure 3.24 Positron drift velocity versus applied electric field, ξ , calculated from centroid data

- 295K
- 104K
- × 80K from Mills and Pfeiffer (1977)

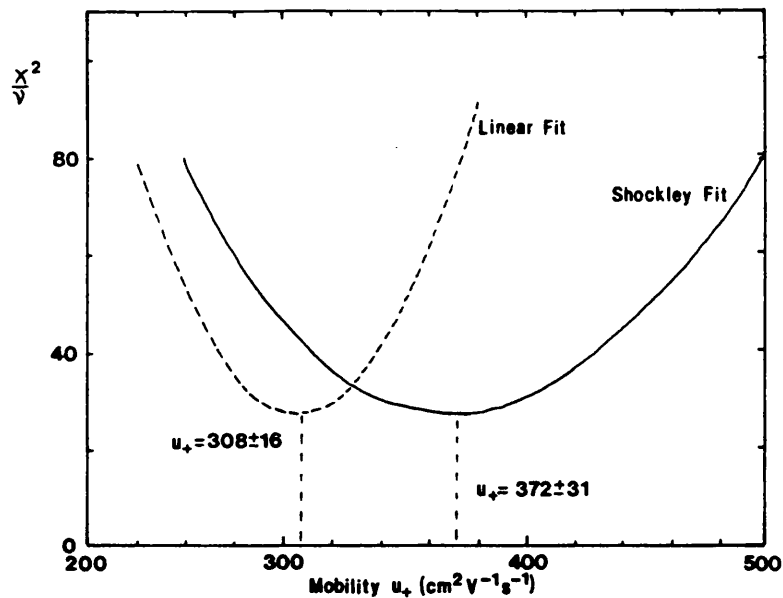


Figure 3.25 Variation of χ^2 with μ_+ for linear and Shockley expression (Equation 2:10) fits to the low temperature data

- Linear fit
- Shockley expression fit

3.6 DISCUSSION

Values of μ_+ derived from centroid data were $\approx 10\%$ less than the corresponding result obtained from RESOLUTION. Although smaller than the overall assigned error, the possibility of a systematic difference between the two methods of analysis cannot be discounted. The reason for this discrepancy is not obvious, although it may arise from the difficulty of allowing for the electric variation of both I_4 and τ_1 in the analysis using RESOLUTION. An examination of simulated e^+ electric field data obtained from a spectrum generating programme may resolve this discrepancy.

The centroid shift data were affected by instabilities arising from small changes in ambient temperature and the statistical error was not a good representation of the experimental error on each data point. Whenever a significant change in temperature

($\geq 1\text{K}$) was recorded over the course of a two day run, the centroid shift for that run was not used in the final analysis. RESOLUTION data were insensitive to temperature fluctuations, provided that the start channel used in the analysis was adjusted to allow for the change in time-zero. In all cases the final error assigned to μ_+ obtained from fits to the centroid data were less than the corresponding RESOLUTION value and were therefore used to make comparison with the other experimental mobility data discussed in Chapter 2.

The accuracy of the centroid data in particular could be improved by reducing the period of the switching cycle or by introducing some form of "on line" data correction. Conventional digital stabilisation would not be suitable for the centroid method, as it operates by fixing the distribution of the collected data.

The room temperature value of $\mu_+(295\text{K})=(68\pm 11)\text{cm}^2\text{V}^{-1}\text{s}^{-1}$ is in good agreement both with a $T^{-1.5}$ extrapolation of the result ($\approx 80\text{cm}^2\text{V}^{-1}\text{s}^{-1}$) obtained by Mills and Pfeiffer (1977) at 184K and the more recent value reported by Corbel *et al* (1989). These results are all in reasonable accord with the value of $\mu_+=(104\pm 12)\text{cm}^2\text{V}^{-1}\text{s}^{-1}$ deduced from the diffusion constant measurement reported by Nielsen *et al* (1985). However the value of $(460\pm 120)\text{cm}^2\text{V}^{-1}\text{s}^{-1}$ measured by Brandt and Paulin (1977) at 300K using an implantation method is evidently in disagreement. Prethermalisation drift, discussed in Chapter 2, would affect the current measurements and those of Brandt and Paulin (1977) to a similar extent, and so cannot be the explanation for the observed discrepancy. Linear and Shockley fits to the 104K data fall on either side of a $T^{-1.2}$ extrapolation of the 80K measurement of Mills and Pfeiffer (1977), so agreement between these studies is good at low temperatures.

Figure 3.26 shows a logarithmic plot of μ_+ versus T for the published mobility values in Si. A logarithmic fit to the data from the current study together with that of Mills and Pfeiffer (1977) at 80 and 184K gives a value for the temperature coefficient of mobility

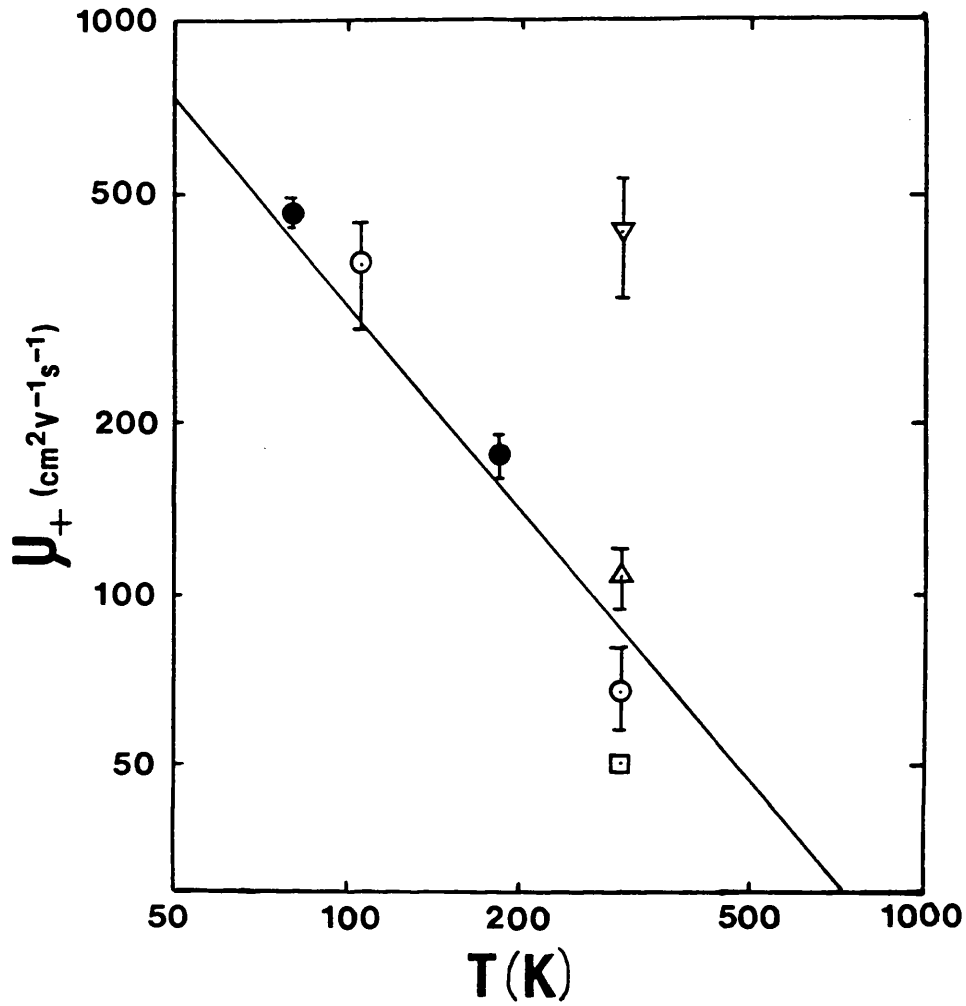


Figure 3.26 Experimental measurements of positron mobility, μ_+ , in Si at a temperature, T

- Current work
- Mills and Pfeiffer (1977)
- △ Nielsen *et al* (1985). Diffusion constant measurement.
- ▽ Brandt and Paulin (1977)
- Corbel *et al* (1989)

of $n=1.3\pm 1$. This is slightly less than the value of 1.5 predicted by a simple charge carrier-acoustic phonon scattering model. The value of n suggests that although e^+ motion in Si is predominantly governed by phonon interactions, some impurity scattering may also occur.

3.7 CONCLUSION

Positron mobility, μ_+ , has been determined in silicon using a technique based upon the drift of e^+ to an interface and the measurement of e^+ lifetime spectra. Values reported using lifetime, Doppler and e^+ beam techniques are in good agreement at all temperatures. However, there is still considerable scope for further measurements of μ_+ in Si and other materials, if a detailed understanding of e^+ motion in electric fields is to be achieved. More accurate measurements of μ_+ as a function of temperature would enable a more precise determination of n , and comparison of experimental and theoretical values of n , should the latter become available, would enable the relative importance of the various e^+ scattering processes to be established. An extension of measurements to low (liquid He) and high (>300K) temperatures might prove important in understanding e^+ behaviour in solid materials. At low temperatures impurity scattering will tend to dominate e^+ motion, particularly in highly doped samples. Jorch *et al* (1984) concluded that e^+ diffusion in Ge at high temperatures, could not be described by a simple acoustic phonon scattering model. Instead they suggested that more complicated interactions such as e^+ -polaron processes might be important. An extension of mobility measurement in Si, or Ge to high temperatures would therefore be of interest in verifying this conclusion. In this respect, recent advances with fast timing circuits using efficient crystals as γ -ray detectors (for example de Vries *et al* 1987) suggest that important gains both in timing resolution and counting rate are feasible. These will facilitate more precise determination of μ_+ using the lifetime technique. Consequently, the possible influence of systematic errors can be investigated more fully. Finally, it is noted that this experiment provides the first direct

evidence that a significant fraction ($\approx 7\%$) of e^+ from a ^{22}Na source can be drifted to an interface at 104K. This result is of considerable consequence in demonstrating the practicability of field assisted moderators for slow positron beam production: the subject of the next chapter.

CHAPTER 4

FIELD ASSISTED MODERATORS

4.1 INTRODUCTION

4.1.1 Conventional Positron Moderators

The first suggestion of producing near-thermal energy positrons from a surface by moderating energetic e^+ from a radioactive source is attributed to Madansky and Rasetti (1950). Assuming reasonable values for the positron diffusion length and mean implantation depth in a metal, they estimated that the efficiency of the process, approximately given by the ratio of these two quantities, was of the order of 5×10^{-3} .

To confirm this prediction, the authors attempted to detect thermal energy e^+ by supporting copper foils containing 10-30mCi of ^{64}Cu activity in a vacuum chamber and monitoring the coincidence rate originating from e^+ annihilations at a collector plate situated about 80cm from the source. The slow to fast e^+ ratio was increased by placing the tube in a uniform axial magnetic field which preferentially guided low-energy e^+ to the collector. The transport efficiency of the arrangement was determined by replacing the source with an electron emitting filament and measuring the current arriving at the collector.

Data were collected with the source biased alternatively 150V positive and negative with respect to the collector. Although the slow positron flux, given by the change in count rate between positively and negatively biased runs, was expected to be substantially greater than the fast e^+ background given by the count rate with negative bias, no statistically significant difference was observed for the Cu foils. Negative results were also obtained for a Pt filament, heated to desorb impurities, an evaporated layer of K and a liquid Ga sample.

Madansky and Rasetti (1950) suggested that the absence of a thermal flux of e^+ from β^+ bombarded surfaces may be due to

1. e^+ localisation at potential minima in the crystal lattice.
2. e^+ becoming trapped at the surface.
3. Positronium formation at the surface which would not be detected in the experiment.

The authors had therefore isolated some of the problems which were to hinder future development of e^+ beams, and twenty years of research were required to achieve moderation efficiencies approaching their estimated value.

Although Cherry (1958) succeeded in producing slow e^+ from a chromium plated mica surface bombarded with β^+ particles from a ^{22}Na source, the overall efficiency was low ($\approx 3 \times 10^{-8}$). Being unpublished, his work went largely unnoticed; the earlier work of Madansky and Rasetti (1950) often being quoted as evidence for the absence of e^+ re-emission from surfaces, until a paper by Madey (1968) renewed interest in the field. At the same time, Groce *et al* (1968) succeeded in forming a low intensity e^+ beam, which was used to make the first total e^+ scattering cross section measurements in He. In this arrangement, the source of fast e^+ was derived from a linear accelerator (linac) rather than a β^+ emitting isotope.

Costello *et al* (1972a,b) suggested that observations of low-energy positrons re-emitted from Au surfaces were a consequence of a negative positron work function, ϕ_+ for gold (see Figure 4.1). Tong (1972) simultaneously published a theoretical study of this mechanism and concluded that ϕ_+ was negative for high electron density metals such as Al, Mg, Cu and Au. However, a proper experimental verification of this mechanism as the dominant e^+ re-emission process for metallic surfaces was impossible until the initiation of detailed ultra high vacuum (UHV) studies of samples prepared and characterised *in situ* by Mills *et al* (1978). Details of this work are given in Chapter 5.

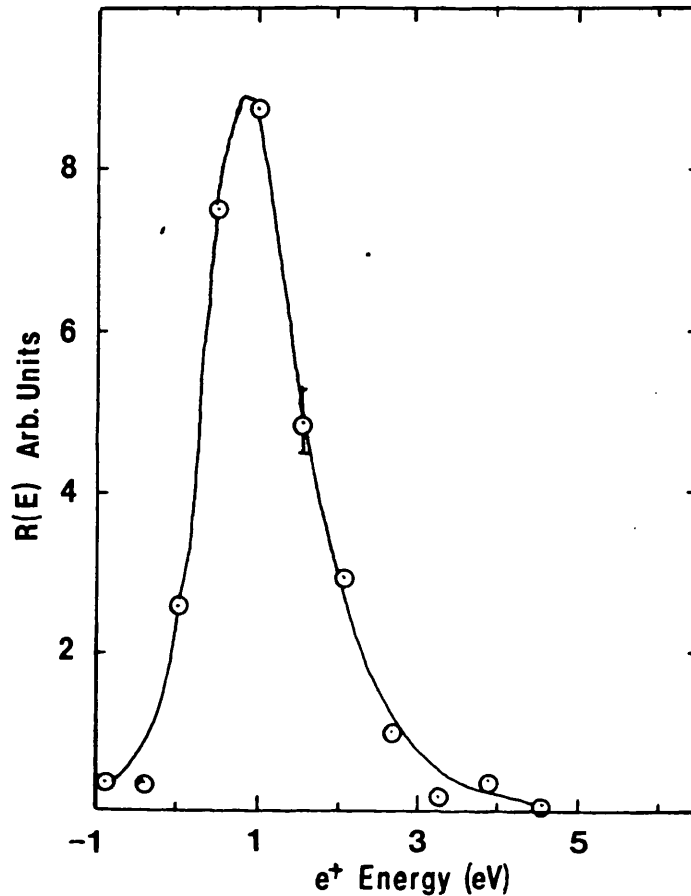


Figure 4.1 Re-emitted positron energy spectra for a tantalum-mica-gold moderator. (Costello *et al* 1972b)

An important stage in e^+ moderator development was the discovery of the MgO moderator by Canter *et al* (1972), prepared by coating a gold vane "venetian blind" arrangement with oxide from a burning Mg ribbon. A relatively high efficiency of 3×10^{-5} opened up many possibilities for low energy e^+ beam studies including total cross-section measurements and the observation of Ps formation at surfaces (Canter *et al* 1974).

Stein *et al* (1975) bombarded a boron target with 4.75MeV protons from a Van de Graaf generator to produce ^{11}C by the reaction



The β^+ produced by the decay of ${}^{11}_6\text{C}$ (see Table 1.3) were moderated in the B target to give re-emitted e^+ with a near-thermal energy spread ($\approx 1\text{eV}$). This spread is considerably narrower than that measured for MgO, although the moderation efficiency is significantly less ($\approx 10^{-7}$). The B moderator permitted e^+ studies to be extended to lower energies, enabling observation of a Ramsauer-Townsend minimum in the e^+ -Ar total cross section at a positron impact energy of about 2eV (Stein *et al* 1978).

At this time metallic moderators were also being used by Pendyala *et al* (1976) with an efficiency of $\approx 1 \times 10^{-6}$. Detailed UHV studies (see Chapter 5) resulted in a better understanding of the moderation process and realisation of the importance of high vacuum conditions and careful surface preparation. This knowledge permitted the development of new e^+ beams with improved efficiency ($\varepsilon \approx 10^{-3}$) and reduced energy spread ($\approx 25\text{eV}$) (Mills 1979). Based on the original ideas of Madansky and Rasetti (1950), Mills (1983) gave the following empirical relation for moderation efficiency, namely,

$$\varepsilon = y_0 \sqrt{D_+ \tau} \alpha_+
 \tag{4:2}$$

α_+ is the e^+ absorption parameter, ρ the moderator material density, $\sqrt{D_+ \tau}$, the positron diffusion length, and y_0 , the positron surface branching ratio. Research therefore concentrated on dense (high ρ), metallic single crystals (high $\sqrt{D_+ \tau}$), resulting in the development of the W(110) moderator by Vehanen *et al* (1983) with an efficiency of 3×10^{-3} .

More recently, experimental results have shown that the energy spread of e^+ re-emitted from Ni(100) surfaces (Gullikson *et al* 1985) is $\approx 35\text{meV}$. Although the moderation efficiency of this material is about half that observed for single crystal W targets, it may well become more widely used in arrangements which require low energy spreads (for example e^+ remoderators).

High efficiency single crystal moderators are normally operated in back-scattering geometry. However, there has been considerable interest in developing thin, single crystal foils for use in transmission mode. The principal advantages of this geometry are the elimination of source shadowing effects, which reduce the slow e^+ yield in back-scattering mode and the separation of incident and out-going optics in secondary moderator arrangements, which permits a greater brightness gain per remoderation stage. Several studies of positron moderation using single crystal foils have been reported, although, in all cases, efficiencies are significantly less than those predicted by theoretical calculations (for example Vehanen and Mäkinen 1985 and Appendix 1).

Lynn *et al* (1985b) and Gramsch *et al* (1987) annealed several polycrystalline and single crystal foils in high vacuum before introduction to an e^+ beamline. Efficiencies of up to 9×10^{-4} were obtained. The single crystal foils produced slow e^+ yields typically twice those measured for polycrystalline foils of the same material and thickness.

Zafar *et al* (1988) annealed single crystal W(100) foils with thicknesses between 1000 and $18\,000\text{\AA}$ in low vacuum by repeated heating between 2070 and 2670K and obtained a maximum efficiency of $(8.8 \pm 1.2) \times 10^{-4}$. Subsequently, Zafar *et al* (1989) extended this study to Ni(100) foils and using similar vacuum conditions obtained a maximum moderation efficiency of 6.5×10^{-4} . Although this efficiency is only 70% of that reported for W foils, the FWHM of the energy distribution is five times narrower and only a factor of two greater than that reported by Schultz *et al* (1986) for a similar moderator prepared by electron beam annealing in UHV. The authors thus established that good quality single

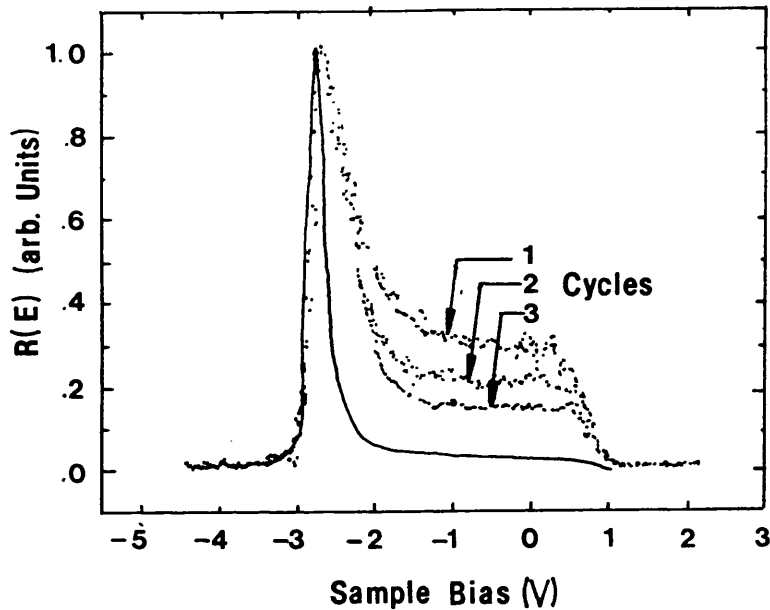


Figure 4.2 Re-emitted positron energy spectra for 1000Å W(100) foils

- Annealed by resistive heating in ultra high vacuum (3 cycles) (Chen *et al* 1985)
- Laser annealed in UHV (Jacobsen *et al* 1990)

crystal transmission moderators can be prepared using a simple annealing and handling technique. In all these studies, slow positron yields were found to be relatively unaffected by short exposures of the foils to air.

Jacobsen *et al* (1990) studied thin W(100) remoderators in high vacuum conditions. The foils were prepared by first cleaning with a laser pulse, followed by laser annealing at 1470K in a 10^6 torr O_2 atmosphere and finally heating for 1min at 2270K in a 10^9 torr vacuum. Using a variable energy (0-20keV) positron beam, the yield of remoderated e^+ from 1000, 2000 and 3100Å thick foils was measured and efficiencies obtained which were a factor of two greater than those previously reported by resistive heating. Furthermore, the laser annealed foils showed a substantially reduced energy-loss tail (see Figure 4.2). The inferior performance of the remoderators prepared by Chen *et al* (1985) can be attributed either to the introduction of thermal stresses in the foils during annealing

or contamination of the foil surfaces as a result of outgassing from the supporting electrodes. The efficiencies reported by Jacobsen *et al* (1990) are in agreement with theoretical predictions based on data measured for thick single crystal samples operated in back-scattering geometry. It would therefore be interesting to extend these studies to thicker foils for use as primary moderators. An improvement in performance similar to that recorded for thin remoderators would result in transmission moderators with efficiencies close to those obtained for semi-infinite crystals in back-scattering geometry.

Studies of solid rare gas films discussed in Chapter 1 (Gullikson and Mills 1986) led to the development of a highly efficient solid neon moderator (Mills and Gullikson 1986). The β^+ moderation efficiency of a flat layer of Ne condensed over a ^{22}Na deposit was 0.3%. When the flat source was surrounded by an open ended cylinder and the configuration covered with a solid Ne layer, the efficiency increased to 0.7%. The energy spread of re-emitted e^+ was $\approx 0.6\text{eV}$. Since e^+ are reflected at the vacuum-rare gas interface, the possibility of developing large area moderators has been considered (Charlton, M., 1989, private communication). Such an arrangement may give an efficiency in excess of 1%.

As indicated by Equation 4:2 the overall efficiency of a conventional moderator is limited by the ratio of positron diffusion length to mean implantation depth, which is of the order of 1% for well annealed metal and solid rare gas film targets. The mean implantation depth is governed by the endpoint energy of the fast positron source and the target density. The discovery of new β^+ emitting isotopes or pair production processes which create less energetic e^+ is unlikely, so considerable effort has been directed towards increasing the positron diffusion length in suitable (dense) moderating materials. However, current preparation techniques have substantially reduced defect concentrations in metals to the extent that the diffusion length is predominantly determined by other scattering mechanisms inherent in the crystal lattice (phonon and electronic excitations). Significant increases in L_+ are therefore unlikely for the metallic targets already studied. However

other possible moderating materials need to be considered. Suitable moderating materials require either a wide band-gap (for example solid rare gas films) or a negative e^+ work function (for example metallic moderators) as well as a high bulk e^+ diffusion constant, D_+ .

Positron diffusion lengths in Si and Ge are similar to those measured in metals, although their low density suggests that the overall moderation efficiency would be lower. Other semiconductors are less pure and D_+ is expected to be lower as a result of defect trapping and/or impurity scattering. Thermalisation times in semiconductors are considerably shorter than those in rare gas solids. To be suitable as moderators they would therefore require a negative e^+ work function. Surface studies of Si are described in Chapter 5.

Positron re-emission from insulators occurs predominantly via the "hot positron" mechanism described in Chapter 1. Rare gas solids have wide band-gaps and a simple structure, so thermalisation times are expected to be longer than for other insulators. It is therefore unlikely that insulators other than the rare gas moderators will make efficient moderators.

Several improvements to existing moderator technology have been suggested. An increase in moderation efficiency and a reduction in energy spread can be achieved by cooling to low temperatures. The use of composite moderators has also been considered. Vehanen *et al* (1983) suggested that fabrication of a Cu-W(110) hybrid moderator could combine the good emission characteristics of the former metal with the superior β^+ stopping power of the latter. They evaporated a few monolayers of Cu onto a W substrate and observed e^+ emission characteristic of a Cu(111) surface, although the overall efficiency was low due to e^+ trapping at the metal-metal interface. On annealing above 1200K, the efficiency increased to $\approx 1.0 \times 10^{-3}$ which is close to that expected for Cu(111) and the re-emitted e^+ spectra measured indicated that Cu islands had formed on the

W(110) surface (Schultz *et al* 1983). Several different evaporation and annealing methods were attempted, but in all cases the same features were observed and the overall efficiency was less than that predicted by theory.

Debowska *et al* (1985) suggested that a metal-metal hybrid moderator of the type developed by Vehanen *et al* (1983) acts as a positron rectifier. The potential drop at the interface allows e^+ transfer only in one direction. They presented calculations which indicated 40% enhancement in e^+ reaching the moderator surface. However experimental difficulties such as those encountered by Schultz *et al* (1983) suggested that practical demonstration of this effect will be difficult.

From the above discussion, it can be seen that the processes governing the efficiency of conventional positron moderators are well understood and there exists little scope for further significant improvement. Increases in intensity of e^+ beams based on current technology will therefore be achieved through the development of higher activity β^+ sources or use of expensive facilities such as linacs and nuclear reactors. Isotope separation may be more commonly utilised to develop sources with increased specific activity, thereby reducing the detrimental effect of self absorption in the source. A list of moderation efficiencies is given in Table 4.1.

4.1.2 Field Assisted Moderators

The transport of e^+ to a semiconductor or insulator surface can be enhanced by the application of an electric field to the material. The data presented in Chapter 3 show directly that in Si at 104K, 7% of implanted e^+ can be returned to an Au-Si interface. Using this data, or results from other studies reviewed in Chapter 2, the flux of e^+ reaching a surface after implantation can be estimated as a function of applied electric field, from the solution of the diffusion equation derived in Section 4.2. If a substantial proportion of this flux can subsequently be re-emitted into vacuum, it would provide the basis for a new type of moderator with significantly improved efficiency. Figure 4.3 shows

TABLE 4.1
Positron Moderator Efficiencies

Moderator	Experimental Details	Vacuum Conditions (torr)	Efficiency ϵ	Energy Spread ΔE (eV)
Cr ^{a)}	Metal coated mica	$\approx 10^{-7}$	3×10^{-8}	-
Au ^{b)}	"	"	10^{-7}	2
MgO ^{c)}	Coated Au vanes	"	3×10^{-5}	2.3
B ^{d)}	Target bombarded with protons to produce ^{11}C	"	10^{-7}	0.15
Al(100) ^{e)}	Sputtered and annealed <i>in situ</i>	$\approx 10^{-10}$	3×10^{-5}	0.1
Cu(111)+S ^{f)}	"	"	9×10^{-4}	0.3
Cu(111)+H ₂ S ^{g)}	"	"	1.5×10^{-3}	0.6
W ^{h)} (polycrystalline)	Resistively heated <i>in situ</i>	$\approx 10^{-7}$	10^{-3}	2.3
W(110) ⁱ⁾	Heated in O ₂ and vacuum	$\approx 10^{-10}$	3×10^{-3}	0.7
W(100) ^{j)} (transmission geometry)	"	"	4×10^{-4}	≈ 1
Ne ^{k)}	Ne gas condensed onto cooled Cu cylinder (6K)	$\approx 10^{-9}$	7×10^{-3}	.58
W(100) ^{l)}	Annealed in low vacuum	$\approx 10^{-2}$ (annealing) $\approx 10^{-7}$ (beamline)	$\approx 9 \times 10^{-4}$	$\approx 3\text{eV}$
Ni(100) ^{m)}	"	"	6.5×10^{-4}	0.3

References

- a) Cherry (1958)
- b) Costello *et al* (1972b)
- c) Canter *et al* (1972)
- d) Stein *et al* (1975)
- e) Mills *et al* (1978)
- f) Mills (1979b)
- g) Mills (1980)
- h) Dale *et al* (1980)
- i) Vehanen *et al* (1983)
- j) Lynn *et al* (1985b)
- k) Mills and Gullikson (1986)
- l) Zafar *et al* (1988)
- m) Zafar *et al* (1988)

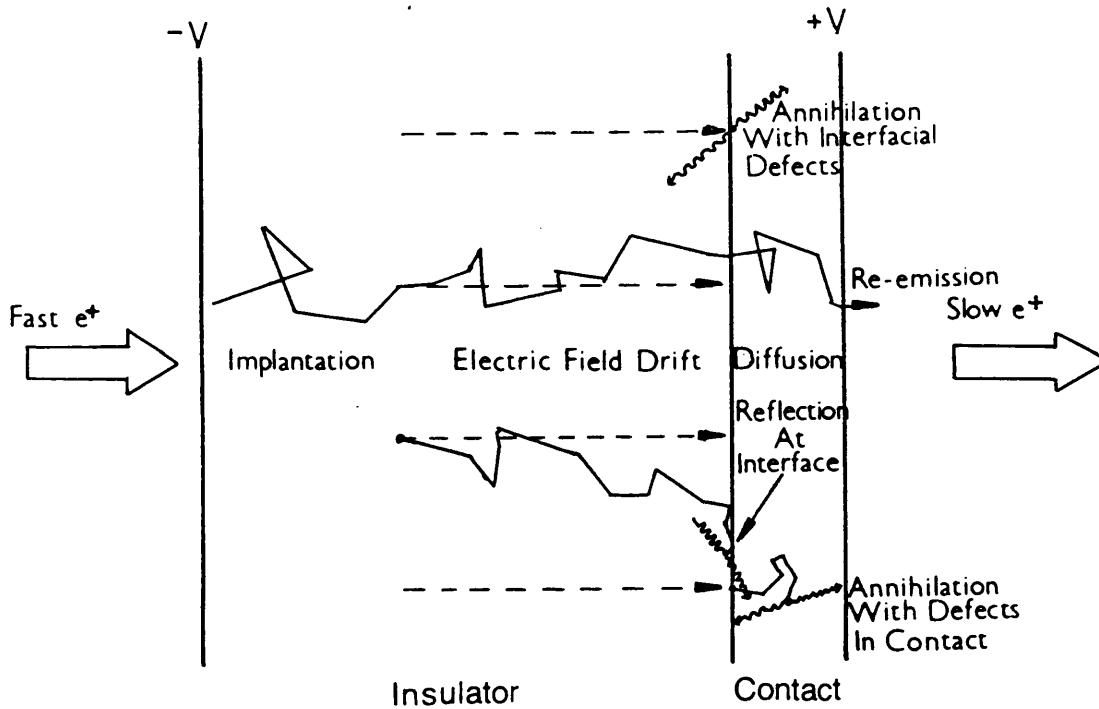


Figure 4.3 Schematic diagram of a field assisted positron moderator

schematically the operation of a "field assisted" (FA) moderator. The possibility of losses in efficiency due to e^+ trapping at the interface and in the conducting over layer are also shown.

The concept of field assisted moderation was originally proposed by Lynn and McKee (1979), who drifted e^+ in a conventional Si surface barrier detector with a 200\AA gold contact at the emitting face. Only a marginal increase in slow e^+ yield with applied field was observed and the low overall efficiency was consistent with the hypothesis that the slow positrons came from the Au layer and not the Si substrate. The apparent lack of success of this experiment can be attributed to

1. the presence of defects in the non epitaxially grown contact

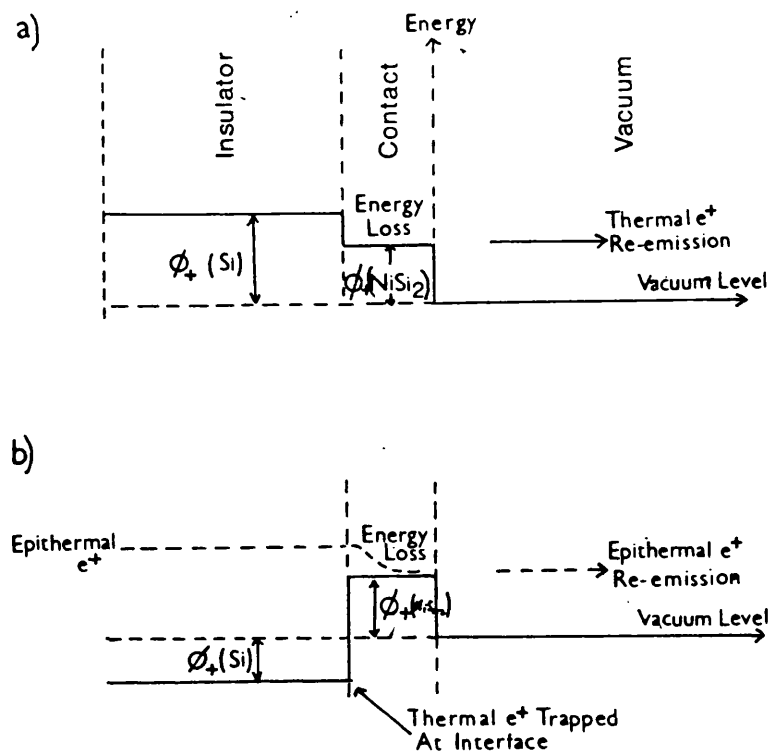


Figure 4.4 Energy levels for an Si- $NiSi_2$ field assisted moderator. The effect of near-surface band bending has been ignored

- a) $\phi_+(Si) < \phi_+(NiSi_2) < 0$. Re-emission of thermal e^+ is energetically favourable
- b) $\phi_+(Si) > \phi_+(NiSi_2)$. Thermal Positrons are trapped at the $NiSi_2$ interface, although epithermal e^+ re-emission may still occur

2. surface contamination due to the relatively poor vacuum used (5×10^{-7} torr)
3. an unfavourable energy barrier for e^+ transport from Si to Au.

In a recent publication, Beling *et al* (1987a) proposed that these problems could be overcome by using thin epitaxially grown metal-silicide layers in ultra high vacuum. In this system, the concentrations of defects at the interface and in the silicide overlayer can be negligible because of the near perfect lattice matching with the Si substrate. Despite

this advantage over non epitaxial systems, it may prove impossible to construct an efficient moderator using an Si-silicide structure since e^+ transport across the Si-silicide and/or silicide vacuum interface may be energetically unfavourable (See Figure 4.4). Re-emission of e^+ from surfaces is discussed in Chapter 5 and new data presented for Si(111) and Si(100).

4.2 SOLUTION OF THE DIFFUSION EQUATION

For most practical cases, positron drift and diffusion in defect free solid media can be described by solving the diffusion equation which, for one dimensional problems, takes the form

$$\frac{\partial n(x,t)}{\partial t} = D_+ \frac{\partial^2 n(x,t)}{\partial x^2} - v_+ \frac{\partial n(x,t)}{\partial x} - \lambda n(x,t) \quad 4:3$$

where $n(x,t)$, D_+ , v_+ , and λ are respectively the positron probability density, diffusion constant, drift velocity and annihilation rate.

Several authors (Mills and Murray 1980a, Sferlazzo 1985, Vehanen and Mäkinen 1985 and Jorch *et al* 1984) have obtained solutions to Equation 4:3 subject to various boundary conditions. Here, an exact solution of the equation is derived for a delta function e^+ implantation profile. The solution can be integrated over the relevant implantation profile to give expressions applicable to β^+ or mono-energetic e^+ impact.

Assuming perfectly absorbing boundaries at $x=0$ and $x=d$ and a Dirac delta function e^+ implantation profile at $x=x_0$ (see Figure 4.5), the appropriate boundary conditions are

$$\begin{aligned} \text{(a)} \quad & n(0,t) = n(x,t) = 0 \\ \text{(b)} \quad & n(x,0) = \delta(x - x_0) \end{aligned} \quad 4:4$$

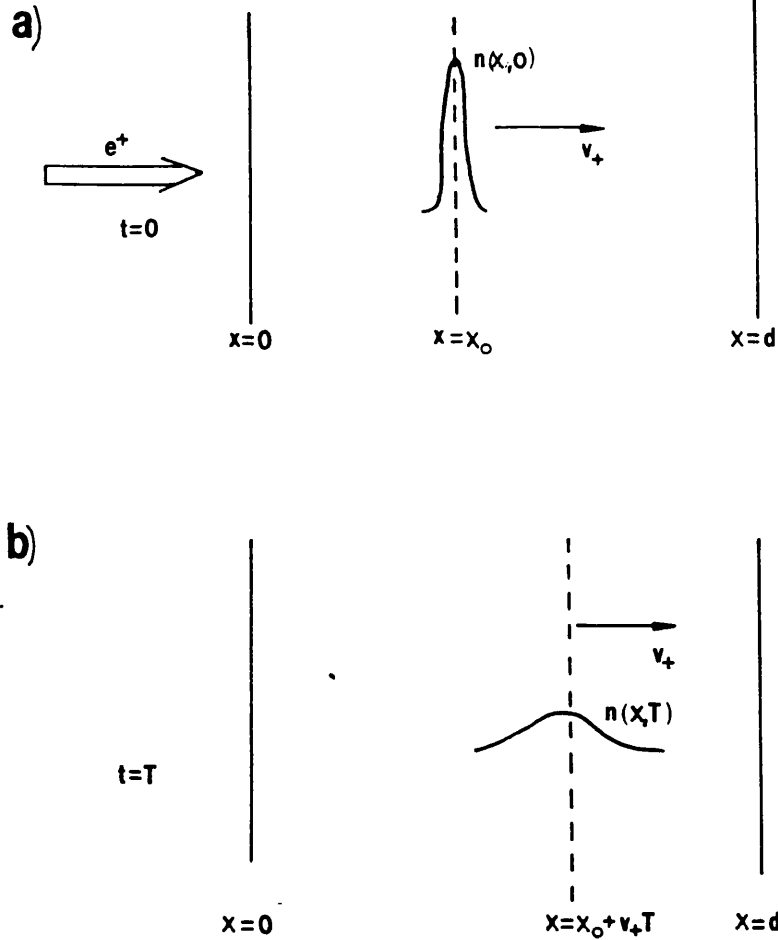


Figure 4.5 Variation of e^+ probability density, $n(x,t)$ with time following implantation of a δ function profile at $t=0$

- a) initial δ function profile at $t=0$
- b) profile at $t=T$

The differential equation can be solved by making the substitution

$$n(x,t) = X(x)T(t) \tag{4:5}$$

Separation of the variables gives

$$\frac{1}{T} \frac{dT}{dt} = -k^2 = \frac{D_+}{X} \frac{d^2X}{dx^2} - v_+ \frac{dX}{dx} - \lambda \tag{4:6}$$

where $-k^2$ is the separation constant. The first part can be solved immediately to give

$$T = T_0 e^{-k^2 t} \tag{4:7}$$

and the second part written in the form

$$[D \nabla^2 - v_+ \nabla - (\lambda - k^2)] = 0$$

where

$$\nabla = \frac{d}{dx}$$

4:8

Solving for ∇ gives

$$\begin{aligned} \nabla &= \frac{v_+}{2D_+} \pm \sqrt{\frac{k^2 - \lambda}{D_+} - \left(\frac{v_+}{2D_+}\right)^2} \\ &= \alpha + i\beta \end{aligned}$$

4:9

where

$$\alpha = \frac{v_+}{2D_+} \quad \beta^2 = \frac{k^2 - \lambda}{D_+} - \left(\frac{v_+}{2D_+}\right)^2$$

that is

$$k^2 = D_+(\alpha^2 + \beta^2) + \lambda$$

The solution is of the form

$$X(x) = A_n \exp(\alpha x) \sin(\beta x + \phi)$$

4:10

where ϕ and A_n are arbitrary constants to be determined from the above boundary conditions. From (a)

$$\phi = 0, \quad \beta = \frac{n\pi}{d} \quad n = 0, 1, 2, 3, \dots$$

4:11

So the general solution is

$$\begin{aligned} n(x, t) &= \exp\left[-D_+ \left\{ \left(\frac{v_+}{2D_+}\right)^2 + \lambda \right\} t\right] \exp\left[\frac{v_+ x}{2D_+}\right] \\ &\quad \times \sum_{n=1}^{\infty} A_n' \exp\left[-\left(\frac{\pi n}{d}\right)^2 D_+ t\right] \sin\left(\frac{\pi n x}{d}\right) \end{aligned}$$

4:12

From (b)

$$\delta(x - x_0) = \exp\left(\frac{v_+}{2D_+}\right) \sum_n A_n' \sin\left(\frac{\pi n x}{d}\right) \quad 4:13$$

Using

$$\int_{Y_1}^{Y_2} \delta(y - y') f(y) dy = f(y') \quad Y_1 < y' < Y_2 \quad 4:14$$

and, from Fourier methods,

$$A_n' = \frac{2}{d} \exp\left[-\frac{v_+ x_0}{2D_+}\right] \sin\left(\frac{\pi n x_0}{d}\right) \quad 4:15$$

gives

$$\begin{aligned} n(x, t) = & \frac{2}{d} \exp\left[-\left\{D_+ \left(\frac{v_+}{2D_+}\right)^2 + \lambda\right\}t\right] \exp\left[\frac{v_+}{2D_+}(x - x_0)\right] \\ & \times \sum_n \exp\left[\left(-\frac{\pi n}{d}\right)^2 D_+ t\right] \sin\left[\frac{n\pi x}{d}\right] \sin\left[\frac{n\pi x_0}{d}\right] \end{aligned} \quad 4:16$$

The flux at $x = d$ is given by

$$J(t) = -D_+ \frac{dn}{dx} \Big|_{x=d} \quad 4:17$$

so

$$\begin{aligned} J(t) = & \frac{2D_+}{d} \exp\left[-\left\{D_+ \left(\frac{v_+}{2D_+}\right)^2 + \lambda\right\}t\right] \exp\left[\frac{v_+}{2D_+}(d - x_0)\right] \\ & \times \sum_n \frac{n\pi}{d} (-1)^n \exp\left[-\left(\frac{\pi n}{d}\right)^2 D_+ t\right] \sin\left[\frac{n\pi x_0}{d}\right] \end{aligned} \quad 4:18$$

Defining the fraction of e^+ reaching $x = d$ by

$$q_d = \int_0^{\infty} J(t) dt \quad 4:19$$

gives

$$q_d = \frac{2D_+}{d} \exp\left[\frac{v_+}{2D_+}(d-x_0)\right] \sum_n \left\{ \frac{n\pi}{d} (-1)^n \sin\left[\frac{n\pi x_0}{d}\right] \right. \\ \left. \times \int_0^{\infty} \exp\left[-\left\{\left(\frac{\pi n}{d}\right)^2 D_+ + \lambda\right\}t\right] dt \right\} \quad 4:20$$

Hence

$$q_d = \frac{2}{\pi} \exp\left[\frac{v_+}{2D_+}(d-x_0)\right] \sum_n \left[\frac{n \sin\left(\frac{n\pi x_0}{d}\right) (-1)^{n+1}}{n^2 + \left(\frac{a}{\pi}\right)^2} \right] \quad 4:21$$

where

$$a = d \left[\left(\frac{v_+}{2D_+}\right)^2 + \frac{\lambda}{D_+} \right]^{\frac{1}{2}}$$

This series solution can be reduced to an analytical expression by use of the identity

$$\sinh qy \equiv \sum_{n=1}^{\infty} B_n' \sin ny \quad -\pi \leq y \leq \pi \quad 4:22$$

Applying Fourier methods to Equation 4:22 gives

$$\frac{2}{q^2 + n^2} (-1)^{n+1} m \sinh q\pi = \pi B_n' \quad 4:23$$

therefore

$$B_n' = \frac{2}{\pi} \cdot \frac{m}{q^2 + n^2} (-1)^{n+1} \sinh q\pi$$

Hence

$$\sinh qx = \frac{2}{\pi} \sinh q\pi \sum_n (-1)^{n+1} \cdot \frac{n \sin nx}{n^2 + q^2} \quad 4:24$$

so from Equation 4:21

$$q_d = \exp\left[\frac{v_+}{2D_+}(d - x_0)\right] \cdot \frac{\sinh\left(\frac{ax_0}{d}\right)}{\sinh a} \quad 4:25$$

The fraction of e^+ reaching the $x=0$ boundary, q_0 , can be similarly determined or deduced from Equation 4:25 by making the substitution $x=d-x_0$ which gives

$$q_0 = \exp\left[\frac{v_+}{2D_+}x_0\right] \frac{\sinh\left[\frac{a(d-x_0)}{d}\right]}{\sinh a} \quad 4:26$$

Equations 4:25 and 4:26 can be integrated over x_0 to give a solution for a general implantation profile $P(x)$. The solution takes the form.

$$q_d = \frac{1}{\sinh a} \int_0^d \exp\left[\frac{v_+}{2D_+}x_0\right] \sinh\left[\frac{ax_0}{d}\right] P(x_0) dx_0 \quad 4:27$$

When $v_+=0$, this expression reduces to the solution derived by Vehanen and Mäkinen (1985) using a Green's function method and slightly different boundary conditions. For an exponential implantation profile of the form

$$P(x) = \frac{1}{L} \exp\left[-\frac{x}{L}\right] \quad 4:28$$

The fractions of e^+ reaching the $x=0$ and $x=d$ boundaries respectively are

$$q_0 = \frac{\exp\left[\frac{v_+ d}{2D_+}\right]}{dL\left(\frac{\lambda}{D_+} - \frac{1}{L^2} - \frac{v_+}{LD_+}\right)} \left[a \coth a - b \coth b + \exp(-b) \left\{ \frac{b}{\sinh b} - \frac{a}{\sinh a} \right\} \right]$$

and

$$q_d = \frac{\exp\left[\frac{v_+ d}{2D_+}\right]}{dL\left(\frac{\lambda}{D_+} - \frac{1}{L^2} - \frac{v_+}{LD_+}\right)} \left[\frac{b}{\sinh b} - \frac{a}{\sinh a} + \exp(-b) \{ a \coth a - b \coth b \} \right] \quad 4:29$$

where

$$b = \frac{d}{L} + \frac{v_+ d}{2D_+}$$

4.3 REQUIREMENTS OF A FIELD ASSISTED MODERATOR

A schematic diagram of a FA transmission moderator is shown in Figure 4.3. The moderation process is similar to that of a conventional moderator, although the method of transport of e^+ from their trajectory endpoints (see Section 1.3.3) to the surface is electric field drift rather than diffusion. In order to establish the electric field, a thin conducting layer is required on the emitting surface through which e^+ must pass.

An approximate expression for the efficiency of a FA moderator, given by a modified form of Equation 4:2 is

$$\varepsilon = y_0(v_+ \tau) \alpha_+$$

where

$$v_+ = \mu_+(\xi) \xi$$

4:30

μ_+ is the positron mobility in the moderator and y_0 the positron branching ratio, which can be suitably modified to allow for reflection at the solid-solid interface and losses in the conducting overlayer. The essential properties of a field assisted moderator can be summarised as follows.

1. The bulk material must possess a high positron mobility, μ_+ , and be capable of sustaining high electric fields. Experimental measurements of μ_+ were discussed in Chapters 2 and 3.
2. The application of an electric field to the moderator requires either a contact or conducting layer through which e^+ must pass. Positrons trapped in defects in this region will reduce the overall moderator efficiency. The layer should therefore be thin and most probably epitaxial.
3. Positron energy levels in the bulk and contact must be favourable for transmission through the solid-solid and solid-vacuum interfaces (see Figure 4.4).
4. As for conventional moderators, efficiency increases with density and mean e^+ lifetime in the moderator.

In Sections 4.4 and 4.5 possible FA moderating systems are considered on the basis of previously published data.

4.4 SILICON FIELD ASSISTED MODERATORS

The e^+ transport and surface properties of Si are the most extensively studied of any non-metallic material. Si was also chosen by Lynn and McKee (1979) for the first experimental study of a FA moderator.

The non-polar nature of the Si lattice gives weak phonon coupling and thus a high free carrier mobility. Previous measurements of μ_+ in Si were reviewed in Chapter 2 and a new method of measuring this quantity described in Chapters 2 and 3. These studies show that μ_+ is significant at room temperature ($\approx 80\text{cm}^2\text{V}^{-1}\text{s}^{-1}$), which is the largest value measured in any material apart from paraffin wax. As observed for other charge carriers, positron mobility increases rapidly with decreasing temperature ($\approx 400\text{cm}^2\text{V}^{-1}\text{s}^{-1}$ at 100K).

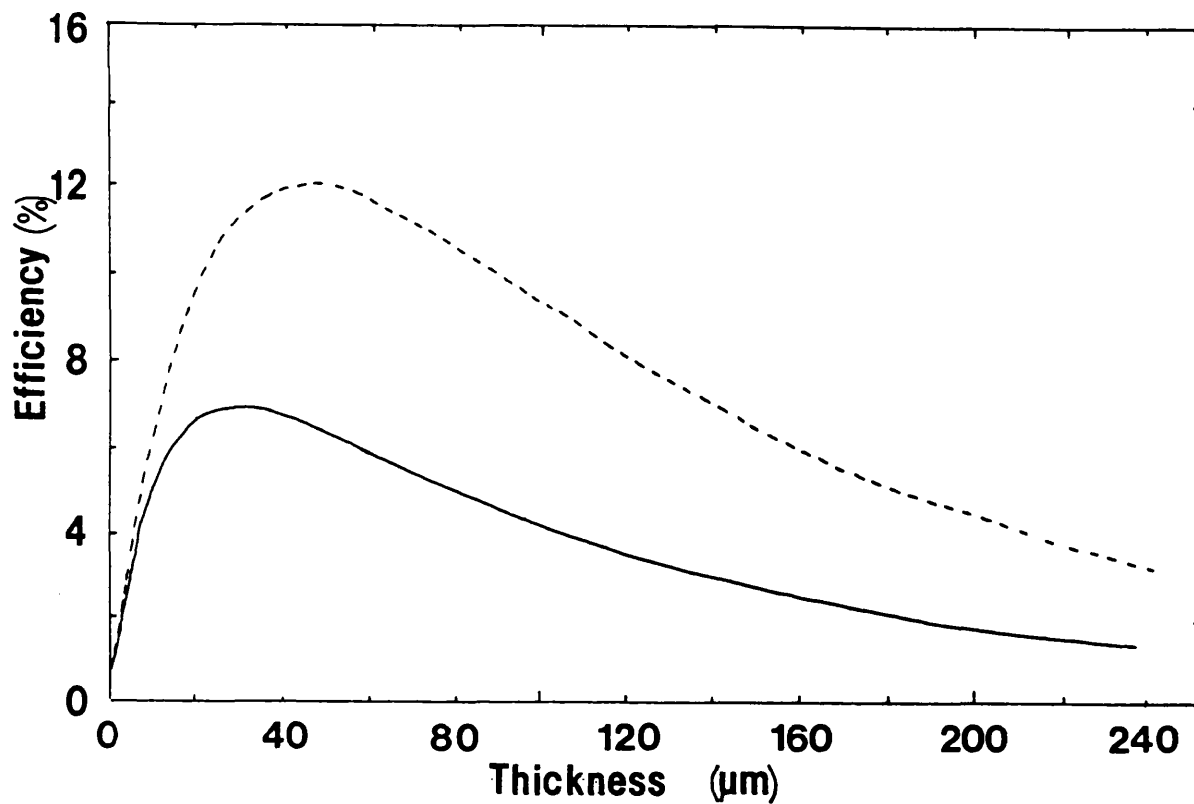


Figure 4.6 Transmitted slow positron yield versus Si film thickness for e^+ drift velocities of 5×10^4 and $1 \times 10^5 \text{ms}^{-1}$

— $v_+ = 5 \times 10^4 \text{ms}^{-1}$

- - - $v_+ = 1 \times 10^5 \text{ms}^{-1}$

These values appear to be concordant with acoustic phonon scattering, although at low temperatures there is some evidence of impurity scattering. If the latter process is significant, Si has the advantage over many materials in that high purity samples are commercially available at relatively low cost.

Using equation 4:29 and experimental values of μ_+ , the fraction of e^+ transported to an interface in a Si FA moderator can be calculated. Figure 4.6 shows the transmitted e^+ yield as a function of wafer thickness for two values of v_+ . The distribution shows a rapid rise in efficiency at low thicknesses due to an increase in the fraction of incident β^+ stopping within the Si film. For drift velocities of 5×10^6 and $1 \times 10^7 \text{cms}^{-1}$, the maximum

100

efficiencies are 6.5 and 12% respectively. At greater thicknesses, the fraction of e^+ transmitted decreases as an increasing proportion of β^+ particles annihilate in the Si bulk before reaching the contact.

Figure 4.7 shows the variation of efficiency with electric field for a 50 μm thick sample at 80K. μ_+ is taken from the work of Mills and Pfeiffer (1977). At low fields, the transmitted efficiency increases rapidly, reaching $\approx 11\%$ at a field of $1 \times 10^5 \text{Vm}^{-1}$. At higher fields, the increase in efficiency is less due to the predicted saturation of v_+ (see Section 2.3). Practical difficulties in maintaining these fields may be encountered. The FA moderator structure is essentially that of a surface barrier detector for which Awcock and Young (1964) report typical breakdown fields of 25kVcm^{-1} due to minority carrier injection. This is an order of magnitude below the intrinsic breakdown field strength of Si. Careful preparation of Si surfaces prior to contact formation will increase the breakdown strength of the structure. A further possibility is to form a "Mesa" or "guard-ring" structure of the type used in avalanche photodiodes (Figure 4.8).

The feasibility of drifting a significant fraction of e^+ to a Si surface or interface is well established both theoretically and experimentally. However, the ability to transport a significant fraction of this flux through the conducting surface layer is less clear. A full understanding of e^+ interactions at Si surfaces has yet to be attained, although the results of several experimental studies have been reported. The earliest measurement of positron re-emission from an Si surface was published by Mills *et al* (1978). These data were similar to retarding field spectra recorded for metallic surfaces (see Figure 5.2) and the authors concluded that Si had a work function of $\approx -1 \text{eV}$. Since the initiation of the current investigation of FA moderators, several further studies of the principal Si surface orientations have been reported. Although several authors concluded that some Si surfaces have negative positron work functions, there is no direct evidence of substantial re-emission of e^+ implanted from β^+ sources. Research in this area is reviewed in Chapter 5 and the results of the current work on Si(111) and Si(100) surfaces presented.

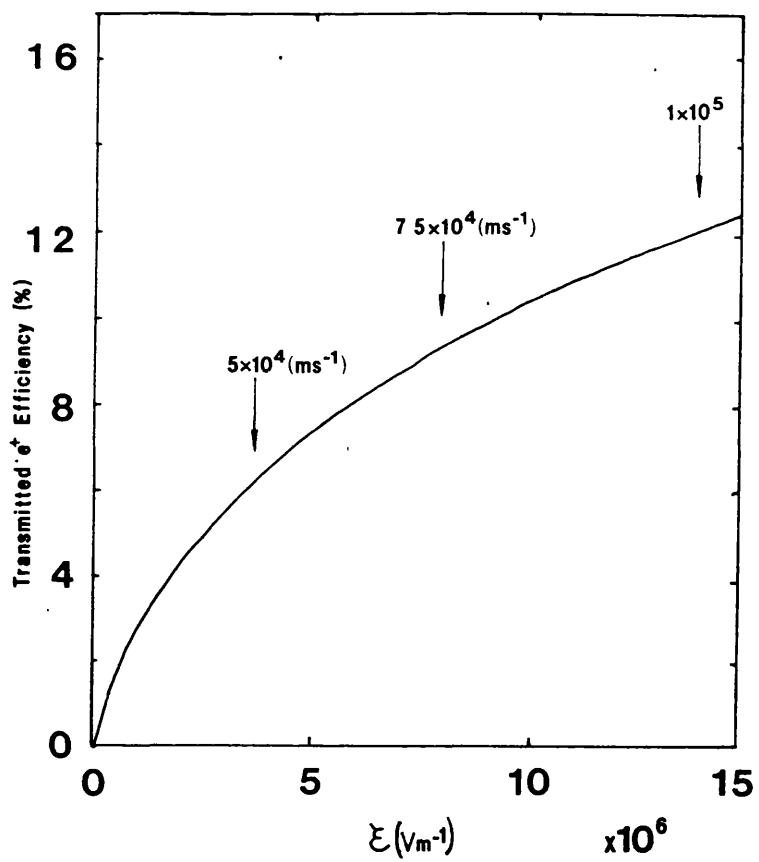


Figure 4.7 Transmitted slow positron yield with applied electric field for a $50\mu m$ Si film. Arrows indicate the positron drift velocity derived from Equation 2:10

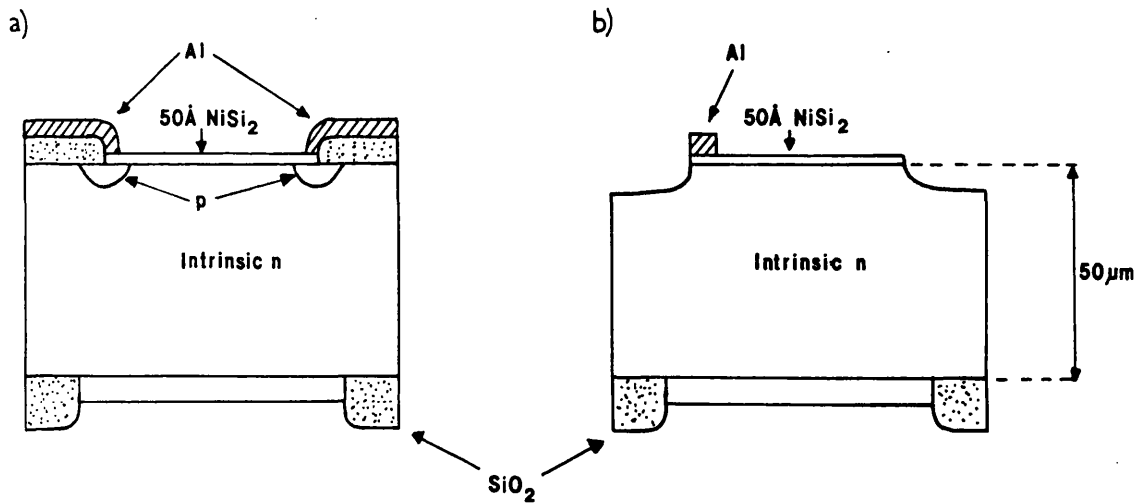


Figure 4.8 Avalanche photodiode structures

- a) Guard ring
- b) Mesa

Particularly in the case of degenerately doped samples, the behaviour of e^+ near to Si surfaces is strongly influenced by "band bending" arising from the high concentration of electronic surface states. The presence of a conducting overlayer will disrupt these states and create a Schottky barrier at the interface. In this case, the behaviour of e^+ near to the interface may be significantly different from that observed near to Si surfaces. Although some investigation of e^+ processes at solid-solid interfaces have been reported (see Chapters 1 and 5), further work is still required before an adequate understanding of e^+ behaviour at such interfaces can be established.

Positron trapping at the Si-Au interface in the sample studied by Lynn and McKee (1979) has been suggested as an explanation of the null result recorded by this experiment. Beling *et al* (1987a) proposed that the NiSi_2 -Si(111) system might provide the basis for a FA moderator and they presented calculations in support of this hypothesis. Justification for this choice is that, given the current experimental knowledge of e^+ behaviour in semiconducting and insulating materials, this system appears to offer the best chance of satisfying the criteria outlined in Section 4.3.

The physical and chemical properties of NiSi_2 and CoSi_2 layers have been extensively studied and are well understood (for example Murarka 1983). Sub-100Å silicide layers with good uniformity and near perfect epitaxy can be grown by evaporation of the appropriate metal onto a Si(111) substrate under UHV conditions (Tung *et al* 1982). For NiSi_2 , the epitaxial layer is subsequently formed by annealing at about 800K (Van Loenen *et al* 1985). Figure 4.9 shows a transmission electron micrograph of an 18Å NiSi_2 layer recorded by Van Loenen *et al* (1985). The abrupt interface and highly uniform overlayer are clearly shown.

Silicide-silicon structures are thermally and chemically stable at room temperature, so it might be possible to transfer samples from one vacuum system to another, with only a small amount of sputtering and annealing necessary to clean the surface. It has also been

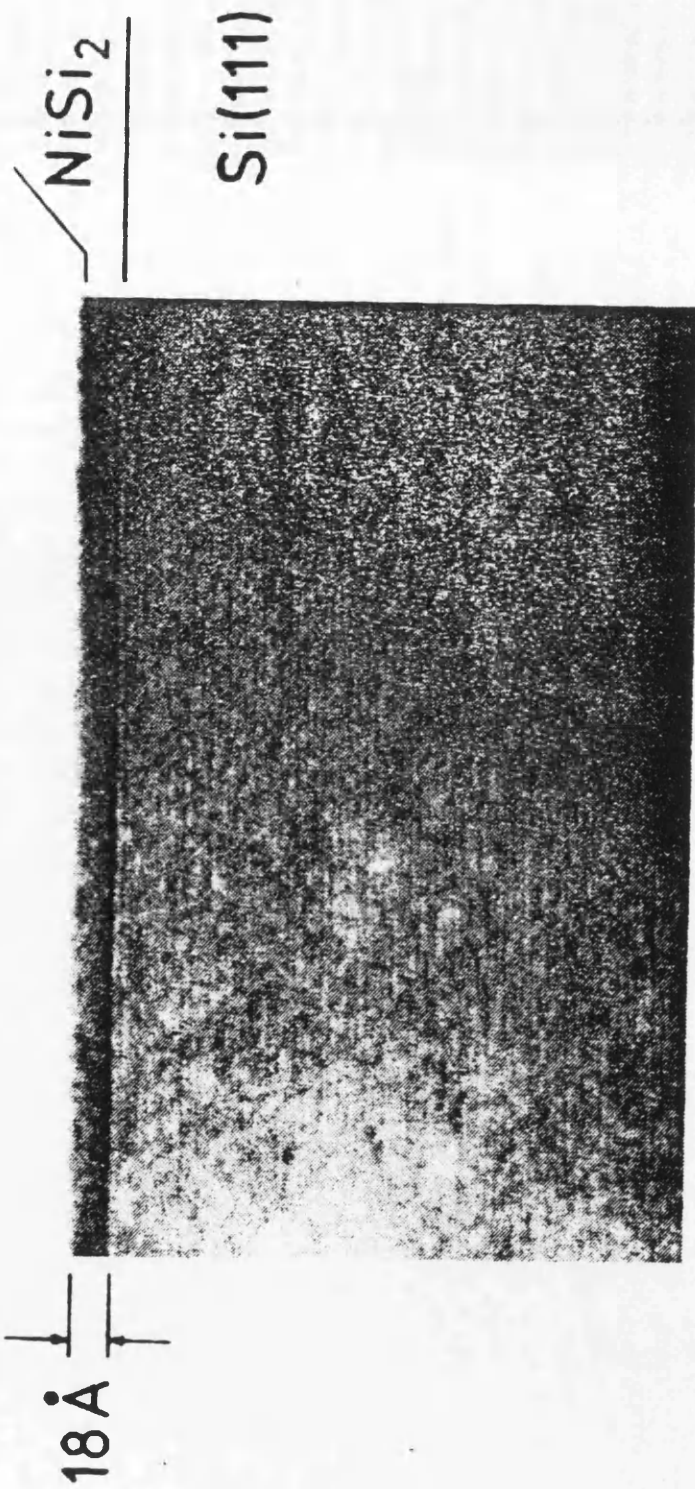


Figure 4.9 Transmission electron micrograph of an 18 \AA NiSi_2 layer on $\text{Si}(111)$
(Van Loenen *et al* 1985)

suggested (Lynn, K.G., 1987, private communication) that, after silicide formation, a sample could be given a protective coating of a volatile material such as As. The sample could then be transferred to a new chamber or beamline and this layer evaporated by gentle heating to give a clean silicide surface.

No experimental investigation of e^+ behaviour in Si-NiSi₂ structures has been reported following the publication of Beling *et al* (1987a). However, results of a UHV study of positron re-emission from CoSi₂ have been published (Gullikson *et al* 1988b; see Figure 5.5). This work, discussed in detail in Chapter 5, showed a negative positron work function for a 250Å CoSi₂ layer grown on an Si(111) substrate. Similarity between the properties of CoSi₂ and NiSi₂ would therefore suggest a negative work function for surfaces of the latter material. If this is the case, positrons implanted into the Si substrate of a Si-NiSi₂ structure can be expected to be re-emitted through the silicide layer provided that the Si work function is more negative than that of the silicide, although the yield may be reduced by residual defects in the NiSi₂ overlayer. The positron yield from CoSi₂ measured by Gullikson *et al* (1988b) diminished rapidly with increasing implantation energy, suggesting that e^+ trapping occurred in the silicide or silicon-silicide interface. If this reduction in yield was a result of e^+ trapping in defects in the overlayer, a thinner layer ($\leq 30\text{\AA}$) in which dislocations are naturally absent could still be used in a FA moderator. However there remains the strong possibility that e^+ become trapped at an unfavourable interfacial energy barrier. In this case a Si-silicide structure would be unsuitable as a FA moderator and other structures need to be considered.

4.5 OTHER POSSIBILITIES

4.5.1 Polar Insulators

The behaviour of e^+ in insulators with applied electric fields is at present little understood. The polar nature of alkali halides and other materials is expected to result in low positron

mobilities due to polaron state formation (Nieminen 1975). This process may provide the explanation of the negative results obtained in studies of e^+ mobility in insulators (see Chapter 2). However, in many insulators, breakdown fields in excess of 1MVcm^{-1} are common, which may impart a significant drift velocity despite a low e^+ mobility. At the largest attainable fields, positron motion might become ballistic as observed for electrons in SiO_2 by Brorson *et al* (1985). In this study, vacuum emission of e^- from 100-1000Å thick oxide layers stressed by fields in excess of 2MVcm^{-1} was observed.

Experimental results reported by Mills and Crane (1984) showed appreciable slow e^+ emission for several insulators bombarded by keV energy e^+ (see Figure 1.10a)). It remains to be seen whether the application of electric fields enhances the yield of slow e^+ reaching an insulator interface or surface. It is planned to develop the experimental method described in Chapter 3 to investigate e^+ motion in a variety of insulating materials.

Due to the cubic structure of the alkali halides and some other insulators, epitaxial growth is possible in many cases. Examples are, Ni, Pt and Pd on a NaCl substrate. MgO and LiF in addition may have negative work functions (Mills and Crane 1984 and Van House and Zitzewitz 1984) so epitaxial (for example MgO-Al (Green *et al* 1969)) systems with favourable energy levels exist. It should be noted that if ballistic motion does occur in these materials, epitaxy may not be a requirement, although Brorson *et al* (1985) indicate that there is a strong interaction between vacuum emitted e^- and the thin metal exit contact.

4.5.2 Rare Gas Solids

The high efficiency and large energy spread of re-emitted positrons from rare gas solids has been explained by Gullikson and Mills (1986) in terms of a "hot positron model" (see Chapter 1). They argue that long e^+ thermalisation times in these materials ensure a high escape probability despite a positive positron work function. The application of large electric fields may enhance this re-emitted e^+ fraction by

1. increasing the thermalisation time further and/or
2. imposing a drift velocity on the random motion during thermalisation.

In order to establish the effect of an electric field on e^+ motion in these materials, Monte Carlo calculations were carried out for which the following assumptions were made:

1. positrons begin a random walk at a random depth weighted according to an exponential implantation profile;
2. initial positron energy lies between 0 and E_{th} , the Ps formation threshold. The energy for each event is weighted according to a chosen profile $P(E,0)$;
3. scattering is isotropic and the energy loss per collision, δE , constant. The mean free path for the i^{th} step is independent of energy E_i ;
4. The effect of the electric field is to
 - i) add a small drift distance

$$x_i = \frac{1}{2} \frac{e \mathcal{E}}{m} t_{Si}^2 \quad 4:31$$

and

- ii) increase the e^+ energy by

$$e \mathcal{E} x_i \quad 4:32$$

where t_{Si} is the time between collisions for the i^{th} step;

5. positrons reaching the surface are assumed to escape provided their perpendicular component of energy is greater than the positron work function, ϕ_+ . The escape probability is given by the quantum mechanical transmission of a plane wave past a step potential of height ϕ_+ ;
6. positrons with energies in excess of E_{th} are assumed to form stable Ps and the calculations for that particular event are terminated. The total Ps yield is given by adding the zero field yield of 10% taken from (Schrader *et al* 1984) to the field dependent part obtained from the Monte Carlo simulations.

Typically, between 1×10^3 and 1×10^6 events were required to give reasonable statistical accuracy ($\approx 3\%$) for the re-emitted energy distribution, $R(E)$. Computing time was reduced by assuming that e^+ implanted greater than a critical depth had a negligible return probability and their paths were not calculated.

Although Mills and Gullikson (1986) showed that solid neon is the most efficient rare gas moderator, results are presented here only for argon, for which there is a complete published set of relevant electronic and positronic properties.

Figure 4.10 shows the variation of $R(E)$ with initial energy profile $P(E,0)$. Apart from the delta function, which is clearly a poor representation of $P(E,0)$, the exact choice is not critical. Figure 4.11 shows $R(E)$ as a function of implantation energy. The distributions are area normalised and the percentage of e^+ re-emitted is given in the figure caption. Although the total yield decreases rapidly with increasing implantation energy, the normalised re-emitted e^+ energy spectrum is practically unchanged. Agreement between the Monte Carlo calculations and the experimental data of Gullikson and Mills (1986), which is also shown in the figure, is excellent considering the simplicity of the model used.

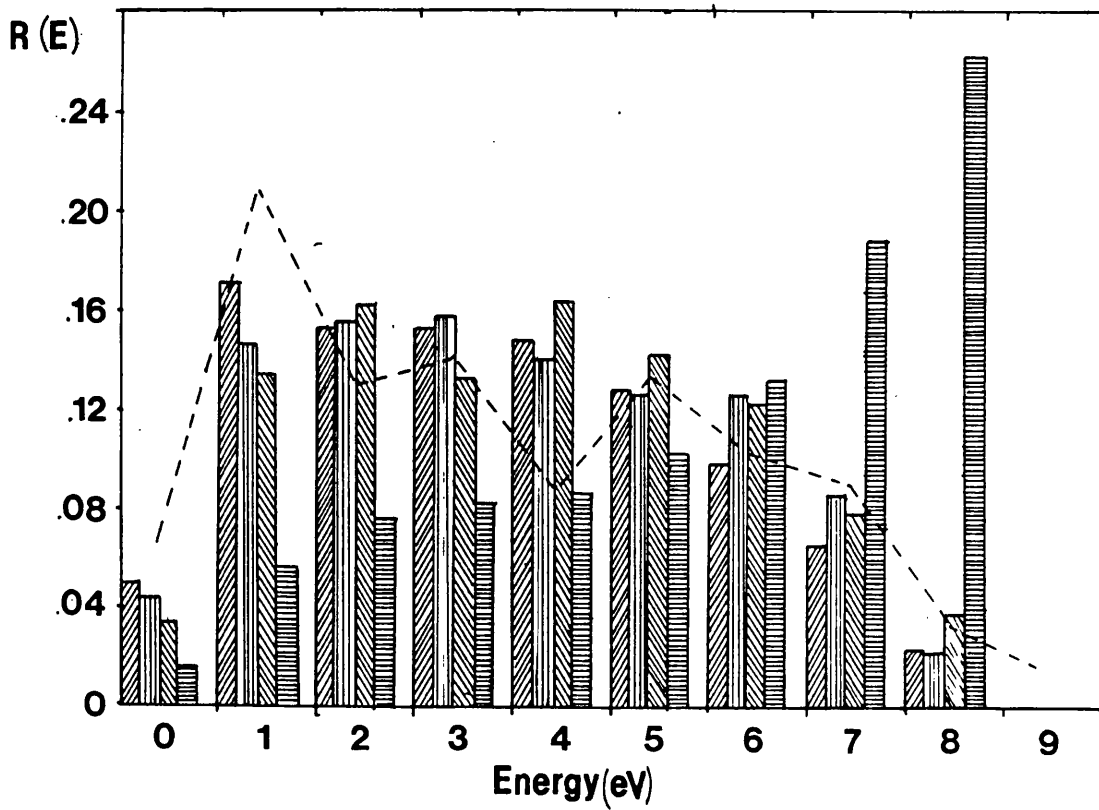
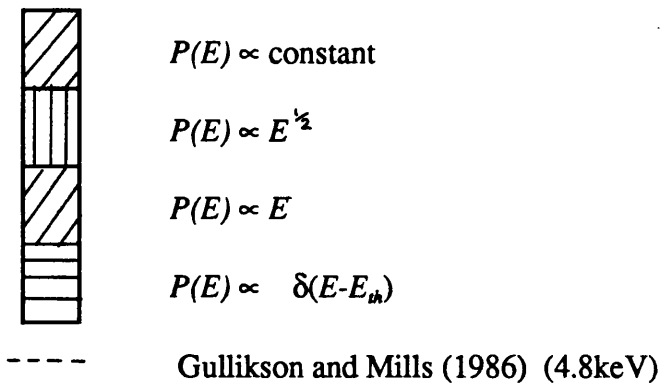


Figure 4.10 Re-emitted energy distribution, $R(E)$, for e^+ from Ar for several different initial energy distributions, $P(E,0)$. Data obtained from Monte Carlo simulations



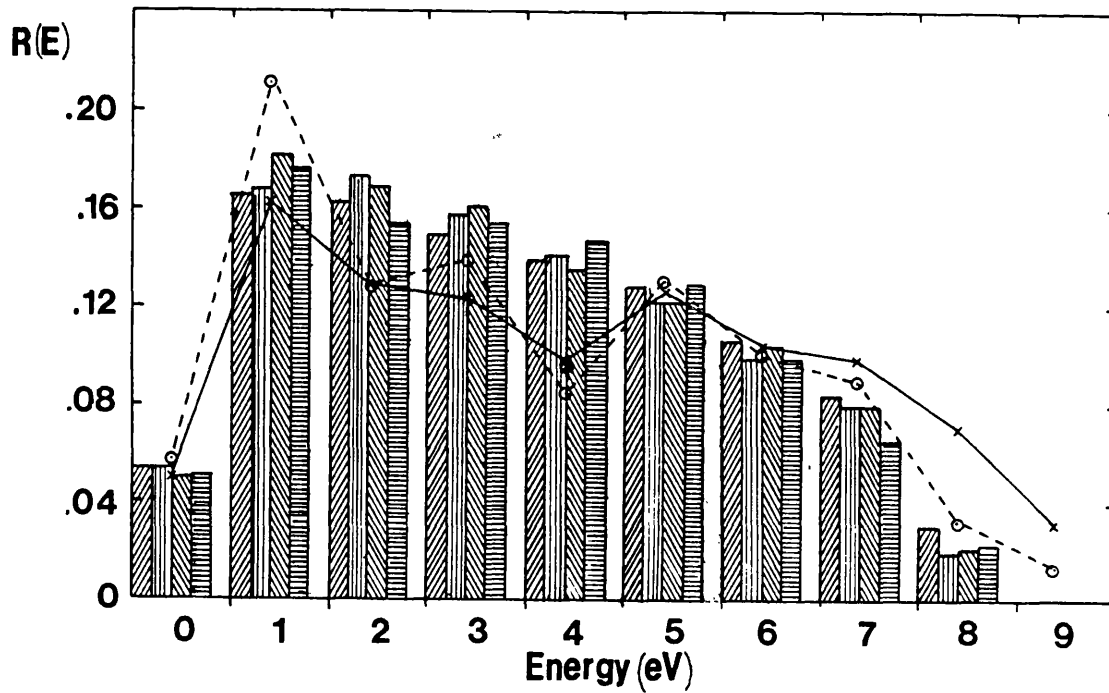
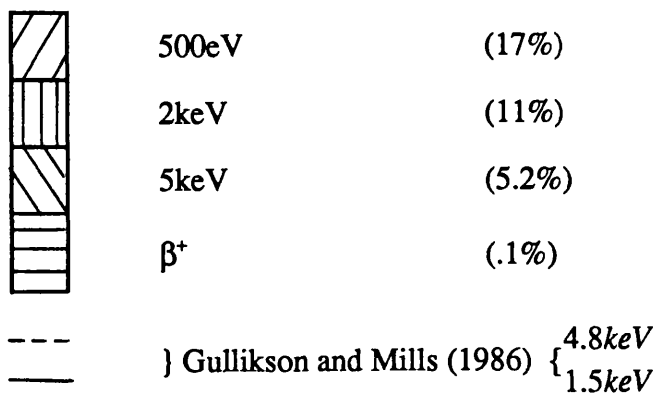


Figure 4.11 Re-emitted energy distribution, $R(E)$, for e^+ implanted into Ar with .5, 2, 5keV and β^+ energies. Data obtained from Monte Carlo simulations



The variation of $R(E)$ with applied electric field is shown in Figure 4.12. The data show a gradual shift to high energies with increasing field. Between 1×10^6 and $1 \times 10^7 \text{Vm}^{-1}$ the overall efficiency increases by about 35% (see Figure 4.13). Above $1 \times 10^7 \text{Vm}^{-1}$ the efficiency rapidly falls as e^+ are heated into the Ore gap by the electric field. The corresponding rapid increase in Ps fraction from the zero field value of 10% to $\approx 80\%$ at $1 \times 10^8 \text{Vm}^{-1}$ is shown in Figure 4.14. The figure includes the variation of f with applied electric field measured by Marder *et al* (1956) in 1.2 atmospheres of gaseous Ar. In the latter case, the zero field Ps fraction is $\approx 30\%$, which is approximately a factor of three greater than that measured in solid Ar. The similar variation of f with in solid and gaseous Ar is remarkable and demonstrates the validity of the simple model used for the present calculations.

From the calculations it can be concluded that only a marginal advantage in efficiency is gained by the application of an electric field to a rare gas moderator. Any improvement is probably less than that attainable using a large area moderator (Charlton, M., 1989, private communication). In contrast to the previous FA moderators, the front contact would be replaced by a grid or foil and a potential difference established between this and the rare gas film substrate. The low dielectric constant ($\epsilon_r \leq 2$) suggests that for a 1mm grid-substrate separation and a rare gas film with a thickness of several thousand Å, a potential difference of $\approx 1-10\text{kV}$ would be required to cause an observable change in slow e^+ yield. These fields are probably experimentally attainable without causing electrical breakdown. Although the advantage of a field assisted rare gas moderator is minimal, a study of electric field induced e^+ re-emission from such films would be of interest in understanding positron motion and Ps formation in solids.

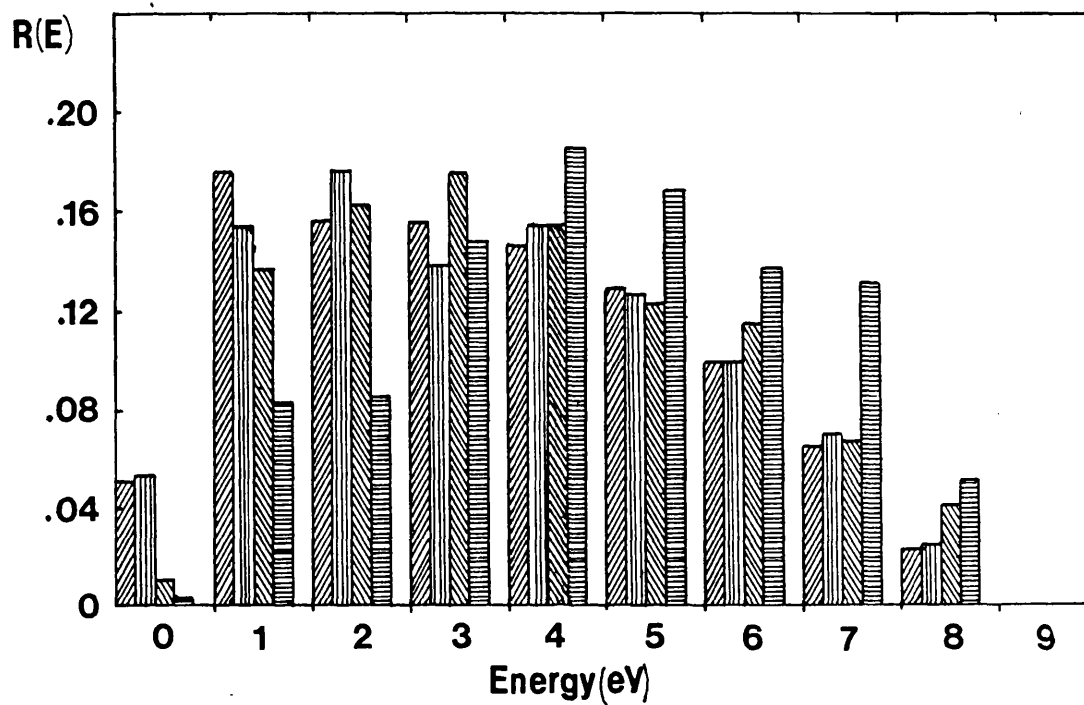
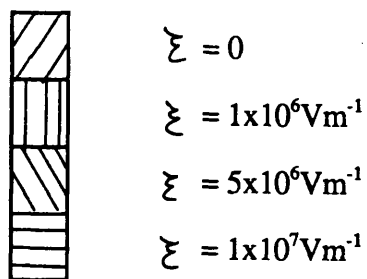


Figure 4.12 Re-emitted energy distribution, $R(E)$ for e^+ from Ar stressed by electric fields of 0 , 1×10^6 , 5×10^6 and $1 \times 10^7 \text{ Vm}^{-1}$.



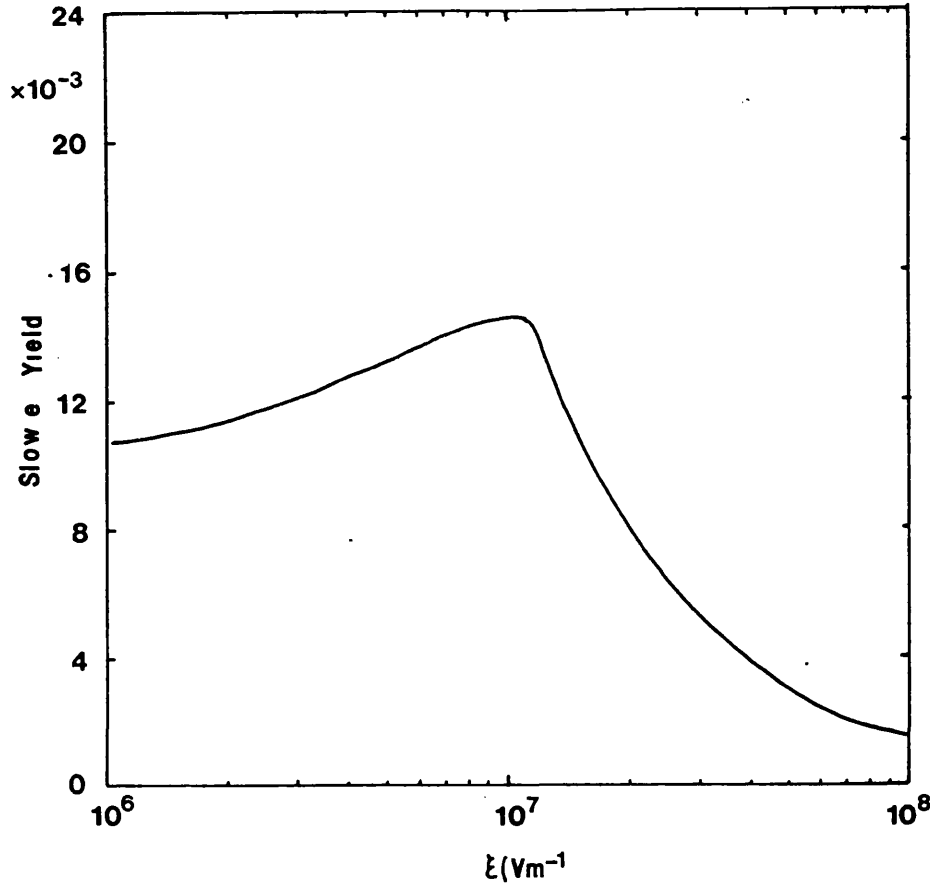


Figure 4.13 Re-emitted slow positron yield versus applied electric field.
Data obtained from Monte Carlo simulations

4.6 CONCLUSION

The feasibility of producing field assisted e^+ moderators by the application of large electric fields to semiconductors or insulators has been considered and the possibility of substantial gains in efficiency demonstrated theoretically. Based on the current knowledge of e^+ behaviour in non-metallic materials, a Si-NiSi₂ structure was considered to provide the best possibility of producing a FA moderator. It now appears that the predicted efficiency will not be observed experimentally due to an unfavourable energy

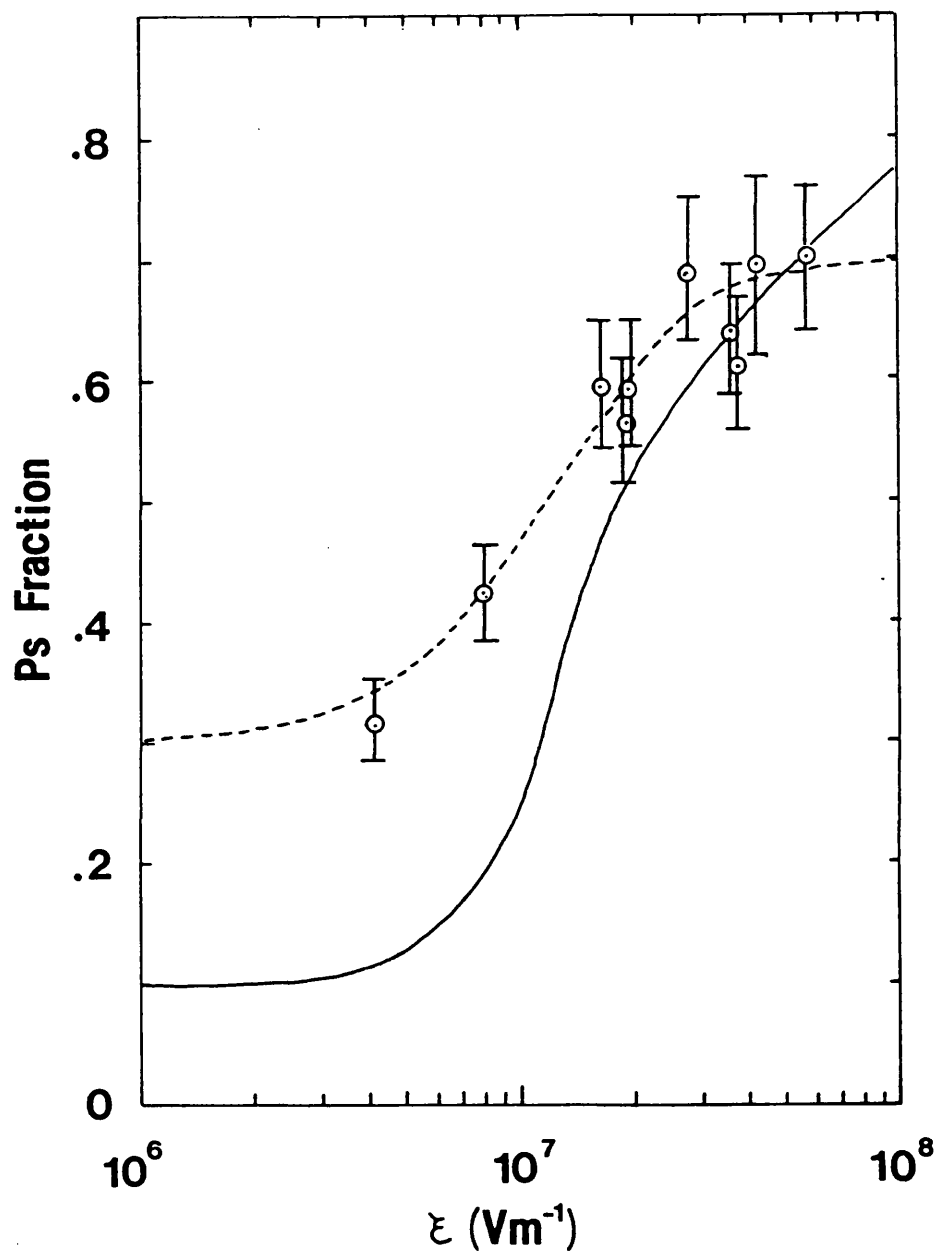


Figure 4.14 Variation of Ps fraction in Ar with applied electric field

- Monte Carlo simulation for solid Ar (current work)
- Experimental data for gaseous Ar at 1.2atm (Marder et al 1956)

barrier at the Si-silicide interface. Other systems have also been considered, but, at present, there is insufficient experimental data to be able to predict moderation efficiencies.

CHAPTER 5

A STUDY OF SLOW POSITRON RE-EMISSION FROM SURFACES IN ULTRA HIGH VACUUM

5.1 INTRODUCTION

Although early experiments on positron re-emission from surfaces established that a useful flux of slow positrons could be generated by bombarding a solid with β^+ particles, measurements were not of sufficient accuracy to determine conclusively the mechanisms involved. A complicating factor was that many of the materials studied were insulators such as MgO (Canter *et al* 1972), polyethylene (Madey 1969) and chromium plated mica (Cherry 1958), so surface charging effects can be important. It was suggested by Madey (1968) that this process enhanced the re-emission of e^+ from polyethylene. Observations of a high Ps yield *in vacuo* for an MgO coated foil irradiated by a β^+ source (Curry and Schawlow 1971) prompted Canter *et al* (1972) to suggest that e^+ re-emission from this surface was a result of the diffusion and break-up of bulk Ps at the vacuum interface. Although Griffith *et al* (1978) and Mills and Crane (1984) provided further evidence for this mechanism, it is now believed that the hot positron model used by Gullikson and Mills (1986) to explain re-emission of e^+ from rare gas solids provides the most probable explanation of this process.

5.1.1 Metallic Surfaces

Following the experiments of Costello *et al* (1972a,b), which showed substantial re-emitted positron yields from several surfaces, Tong (1972) made a theoretical study of thermal positrons in metals and concluded that a fraction could be emitted with energies up to several eV by a direct surface mechanism. This he attributed to the existence of a negative e^+ work function, ϕ_+ , analogous to the familiar concept of the electron work function, ϕ_- , associated with the photoelectric threshold, for example. Leakage of the free electron gas into the vacuum region and the excess positive background due to the ion

cores in the solid give rise to a surface dipole layer, Δ , which is attractive to electrons *in vacuo* near the surface (see Figure 5.1a). The bulk chemical potential, μ , which comprises effects due to the attractive electron ion potential and exchange between the electrons also contributes to the work function giving

$$\phi_- = \Delta - \mu_- \quad 5:1$$

For positrons the dipole layer is repulsive and thus tends to remove positrons from the solid. The corresponding expression for ϕ_+ is

$$\phi_+ = -\Delta - \mu_+ \quad 5:2$$

where μ_+ , the positron chemical potential, is determined by e^+ -correlation effects and the repulsive e^+ -ion potential (see Figure 5.1b)). The two terms nearly cancel to produce, in some cases, a slightly negative work function which gives rise to spontaneous e^+ re-emission.

Conclusive experimental evidence of the e^+ work function mechanism was published by Mills *et al* (1978) and Mills (1978). In contrast to previous experiments, these studies involved atomically clean surfaces, carefully prepared under high vacuum conditions. Retarding potential spectra for e^+ from Al(100), evaporated Cr and Si(100) surfaces are reproduced in Figure 5.2. Mills and Murray (1980) subsequently measured the angular distribution of e^+ from Cu(111) + S and Al(100) targets bombarded with keV e^+ in ultra high vacuum (UHV). These data show that the majority of slow e^+ emitted from negative surfaces of metals emerge in a narrow cone consistent with an effective temperature, $T^* \approx 4T$, where T is the lattice temperature (see Section 1.3.7a)). The authors suggested that the high effective temperature was due to incomplete thermalisation of the implanted e^+ prior to re-emission.

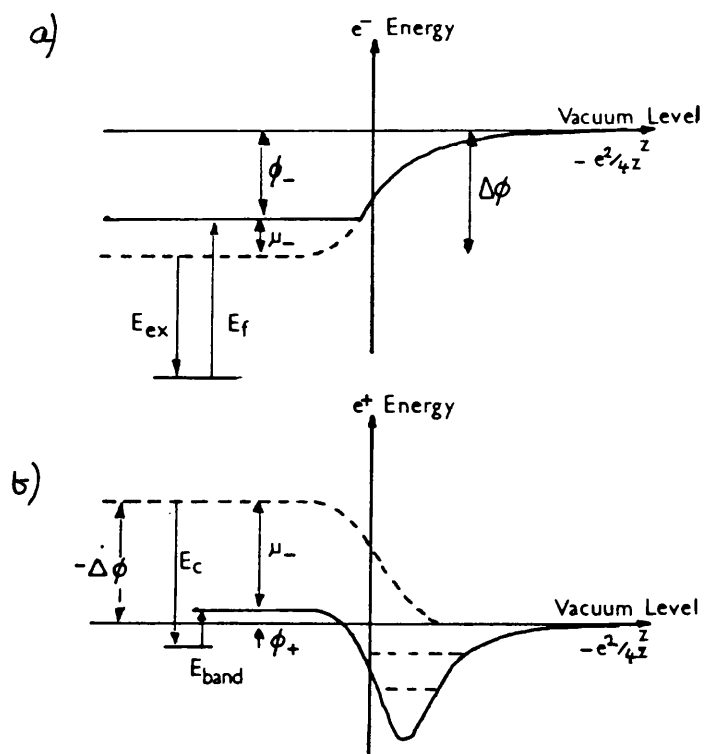


Figure 5.1 Electron and positron energy levels near to a metallic surface

- a) Electrons
- b) Positrons

The importance of the surface dipole moment, Δ , was demonstrated in experiments reported by Murray *et al* (1980). By heating a copper crystal *in vacuo*, controlled amounts of sulphur were adsorbed on the sample surface and the coverage determined by Auger spectroscopy. Changes in ϕ_+ and ϕ_- with S coverage were found to be equal and opposite which, from equations 5:1 and 5:2, corresponds to a change in Δ . This work therefore verified that the peak observed in the e^+ energy distribution from negative affinity surfaces is indeed a measure of the bulk positron work function. More recently Schultz *et al* (1983) measured changes in ϕ_+ and ϕ_- of (-290 ± 140) and (250 ± 140) mV following CO coverage of an initially clean Pt(100) surface. These values are consistent with a changing surface dipole due to the presence of adsorbates.

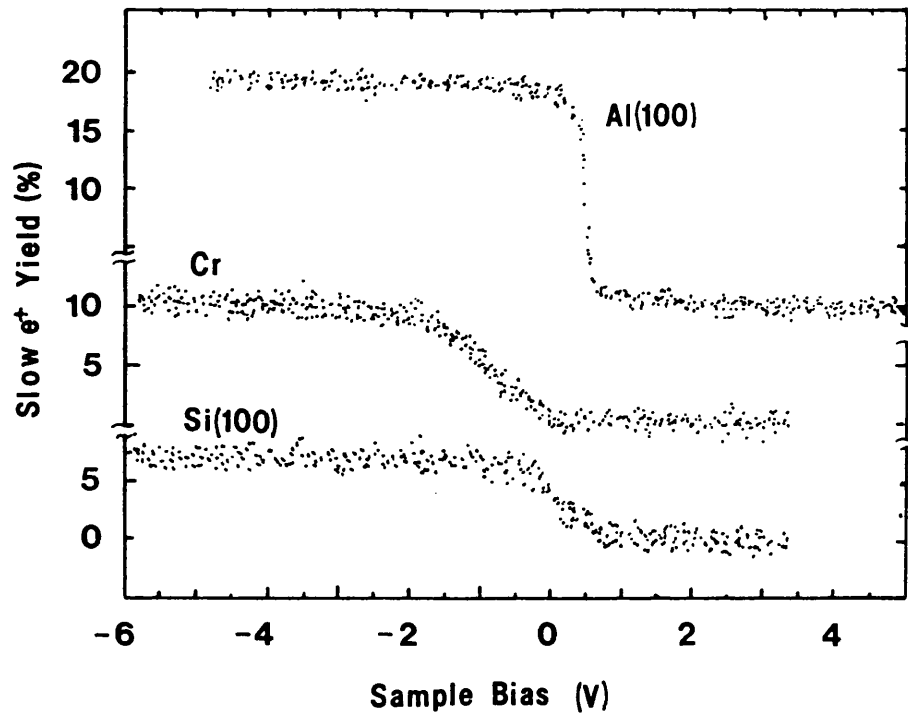


Figure 5.2 Retarding potential curves of e^+ re-emission from clean Al(100), Cr and Si(100) surfaces (Mills *et al* 1978)

Early studies of e^+ re-emission from clean metallic surfaces (for example Murray and Mills 1980) indicated that there was a small inelastic fraction of e^+ leaving the surface, giving rise to a low-energy tail in the measured energy distribution. Several possible energy-loss processes have been suggested

1. electron-hole excitations (Nieminen and Oliva 1980)
2. phonon excitations (Nieminen and Oliva 1980)
3. surface roughness
4. vibrational excitation of residual surface contamination (Fischer *et al* 1983, 1986)
5. the effect of thermal or static displacements of surface ion cores (Murray and Mills 1980)

6. e^+ escape following surface trapping (Pendry 1980).

However, experiments performed in uniform axial magnetic fields only record the energy fraction E_{perp} corresponding to the e^+ velocity component perpendicular to the surface. Consequently, the studies discussed above could not distinguish between inelastic scattering and the apparent energy loss in E_{perp} due to large angle elastic scattering. Fischer *et al* (1983, 1986) overcame this problem by employing a hemispherical analyser and an electrostatic e^+ beam to measure total-energy spectra from well characterised Ni(100), Cu(111) and W(110) surfaces. These measurements were completely consistent with the energy and angular widths resulting from thermal broadening alone. On cooling the samples, the elastic re-emission peak narrowed, although the finite resolution of the analyser made it impossible to determine T^* accurately (see Figure 5.3a).

On exposure of an Ni(100) surface to CO at a partial pressure of 2×10^{-8} torr, a small energy loss peak was recorded at (248 ± 10) meV (see Figure 5.3.b)). This peak, consistent with measurements of electron energy loss (EELS), was attributed to vibrational excitation of C-O bonds. Similar peaks were also obtained for a H₂O covered NiO(111) surface. These observations of energy loss to discrete vibrational modes of adsorbed molecules has opened up the possibility of re-emitted positron energy loss spectroscopy (REPELS) as a novel surface probe. This technique may offer some advantages over its more conventional electron analogue, EELS (Fischer *et al* 1986). These authors also recorded continuous energy-loss, which may result from electron-hole excitations or, in the case of NiO(111), surface disorder. These observations suggest that REPELS may also be applicable as a surface structure probe.

Gullikson *et al* (1985) demonstrated that measurements of the total energy distribution of re-emitted e^+ can be obtained in a guiding magnetic field if a permanent magnet is placed behind the sample to ensure that the field in this region is significantly stronger than that at the analyser. In this case, the low-energy tails recorded in e^+ retarding potential spectra

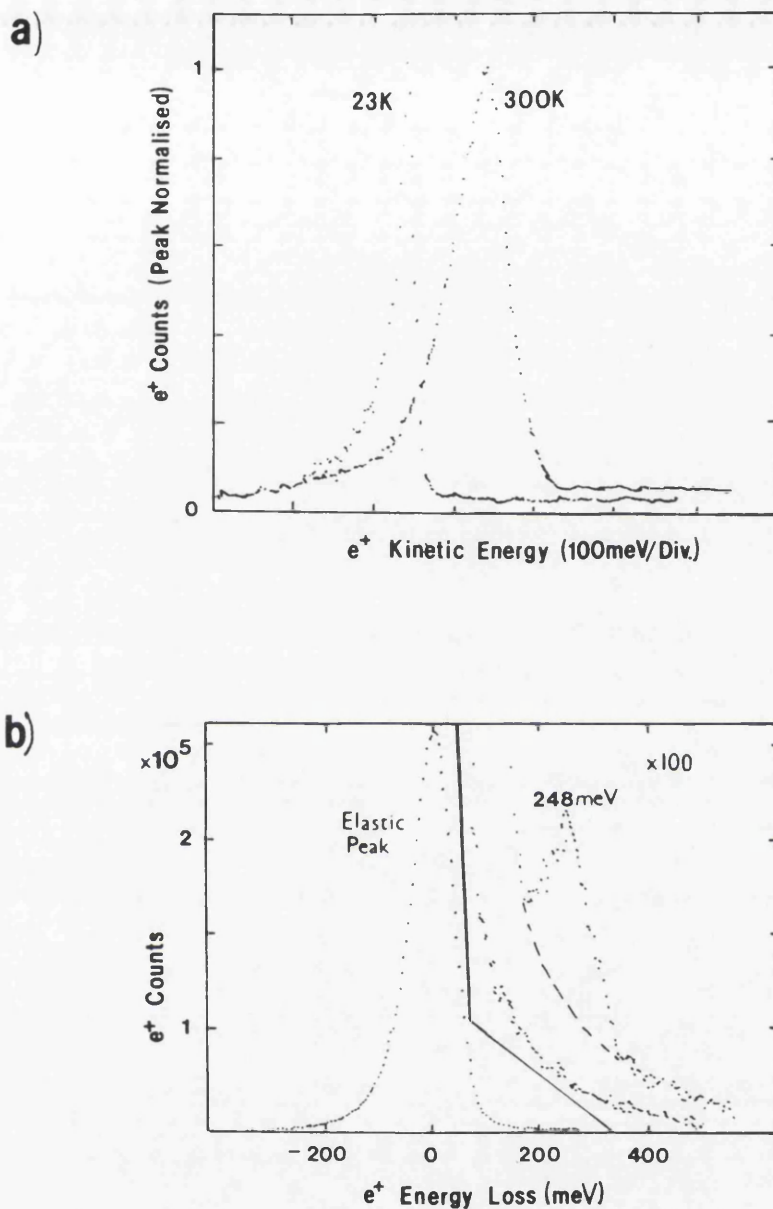


Figure 5.3 Studies of e^+ re-emission from Ni(100) surfaces

- Peak normalised energy distribution for e^+ re-emitted from clean Ni(100) at 300 and 23K
- Expanded view of the energy distribution of e^+ re-emitted from clean and CO exposed Ni(100) surfaces, showing an inelastic energy-loss peak at 248meV due to excitation of a C-O vibrational state

(Fischer et al 1986)

obtained without the magnet in place were practically eliminated. From measured total energy spectra, the authors concluded that inelastic e^+ -surface scattering at clean Ni(100) and W(110) surfaces was negligible, in agreement with Fischer *et al* (1986).

Although the existence of negative e^+ work functions for many metal surfaces is well established, the precise nature of the e^+ -surface interaction is not fully understood, despite being the subject of much experimental and theoretical work. Since ϕ_+ determines the positron interaction time with the surface electron density, y_0 and f_0 , the positron and positronium surface branching ratios, are expected to be work function dependent. Mills and Murray (1980b) measured the variation of y_0 with changes in ϕ_+ , induced by the adsorption of S onto Cu surfaces, as discussed above, and by changes in temperature for Al surfaces. However, Gullikson *et al* (1988a) suggested that these measurements may be in error due to changes in bulk trapping and diffusion rates caused by changes in experimental conditions required to vary ϕ_+ . Consequently, these authors changed ϕ_+ by adsorbing K onto initially clean Ni(100) and Cu(111) surfaces. A value of ϕ_+ for the clean surface was determined by a retarding field method and the absolute yield measured using a NaI detector to monitor e^+ annihilations in the sample. K, from a getter source, was then deposited onto the sample at a constant rate and a continuous sequence of 32 channel retarding field spectra recorded using a channel-electron-multiplier (CEM)/multiscalar arrangement. The y_0 values were corrected for the fraction of e^+ which annihilated in the bulk before diffusing to the sample surface. The zero of ϕ_+ was taken to be the point at which the yield, y_0 , extrapolated to zero.

Fits to the data were performed using the resonance trapping model of Yu and Lang, (1983) originally developed to describe ion neutralisation, and a density of final states model, in which positron and positronium formation are assumed to be determined by the density of available final states. Agreement between the data and both models was good (see Figure 5.4), apart from at low energies where effects due to the thermal distribution of e^+ in the solid and non-thermal re-emission became significant. By including an

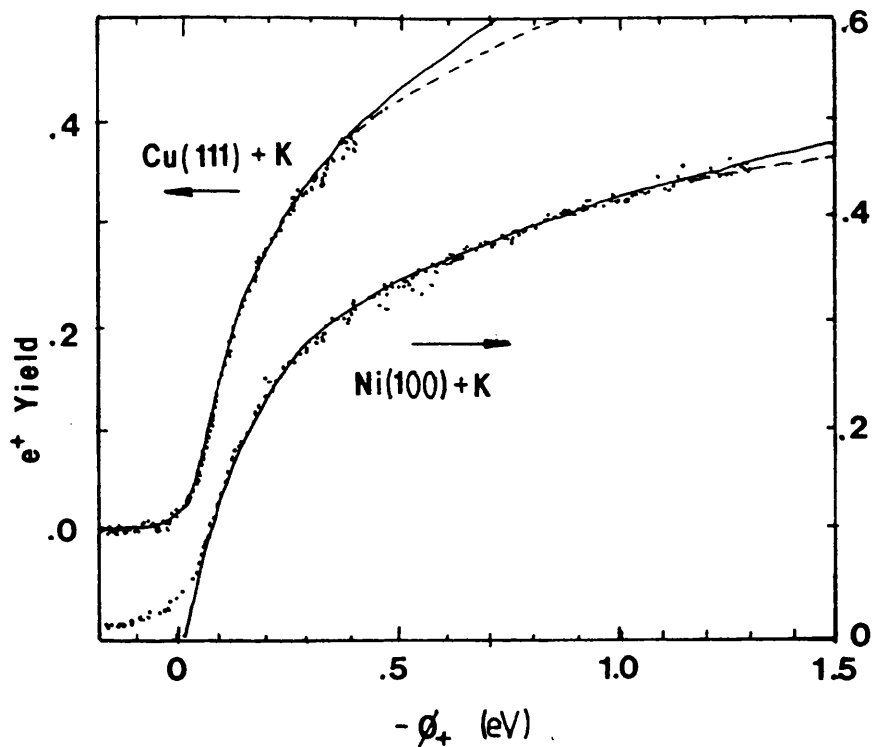


Figure 5.4 The variation of slow e^+ yield with work function, ϕ_+ , for K exposed Cu(111) and Ni(100) surfaces. Curves through the data are fits to theoretical models

- Resonance tunnelling model of Yu and Lang (1983)
- - - A final density of states model

(Gullikson et al 1988)

effective positron temperature of $\approx 380\text{K}$ and a non thermal fraction of 0.4, the fit to the model of Yu and Lang was substantially improved. Gullikson *et al* (1988a) concluded that the data was of insufficient accuracy to distinguish between different re-emission models, although it clearly demonstrated a $\sqrt{|\phi_+|}$ variation in y_0 , suggesting that e^+ velocity is the important quantity in determining the probability of e^- pick-up.

Gullikson *et al* (1988b) studied the re-emission of e^+ implanted into a 250\AA epitaxial film of metallic CoSi_2 on Si. The sample was prepared by evaporation of Co onto a clean Si(111) substrate followed by annealing at 920K *in situ* to form the silicide. The sample

was then transferred to a magnetically guided slow positron beam and cleaned by bombarding it with $10\mu\text{Acm}^{-2}$ current density of 500eV Ar^+ ions for 2 minutes followed by a 3 minute anneal at 1050K . After cleaning, contamination monitored by Auger electron spectroscopy was less than 10% of a monolayer of C and O. The positron yield against incident beam energy is shown in Figure 5.5a). Extrapolation to zero energy gave a positron branching ratio of $(23\pm 1)\%$. The rapid decrease in yield with e^+ implantation energy suggested a low e^+ diffusion length of several hundred angstroms, which was attributed to one or more of the following effects:

1. e^+ may have been trapped in defects in the CoSi_2 layer or at the Si-silicide interface;
2. e^+ may have been attracted into the potential well caused by the Schottky barrier at the interface;
3. e^+ initially implanted through the silicide layer into the Si bulk may have been inhibited from returning into the silicide layer by an electric field at the interface;
4. The positron work function of the silicon may be higher than that of the silicide, so that e^+ become trapped at the interface.

By varying the potential on a retarding electrode situated in front of the sample, Gullikson *et al* (1988b) obtained the spectrum shown in Figure 5.5b). Assuming that the positron energy distribution extends to zero, the zero energy point of the spectrum is given by the point at which the count rate just starts to decrease as the bias is increased. Generally, this does not occur at zero bias because of the contact potential difference between the sample and the retarding grid due to the difference in electron work functions. This effect is apparent in the figure. Using this data, Gullikson *et al* (1988b) estimated that $\phi_+ = (-.046\pm .07)\text{eV}$. In order to observe the energy loss of re-emitted e^+ from CoSi_2 , a strong permanent magnet was placed behind the sample. This ensured that most of the velocity of the re-emitted e^+ was directed parallel to the magnetic guiding field. The differentiated

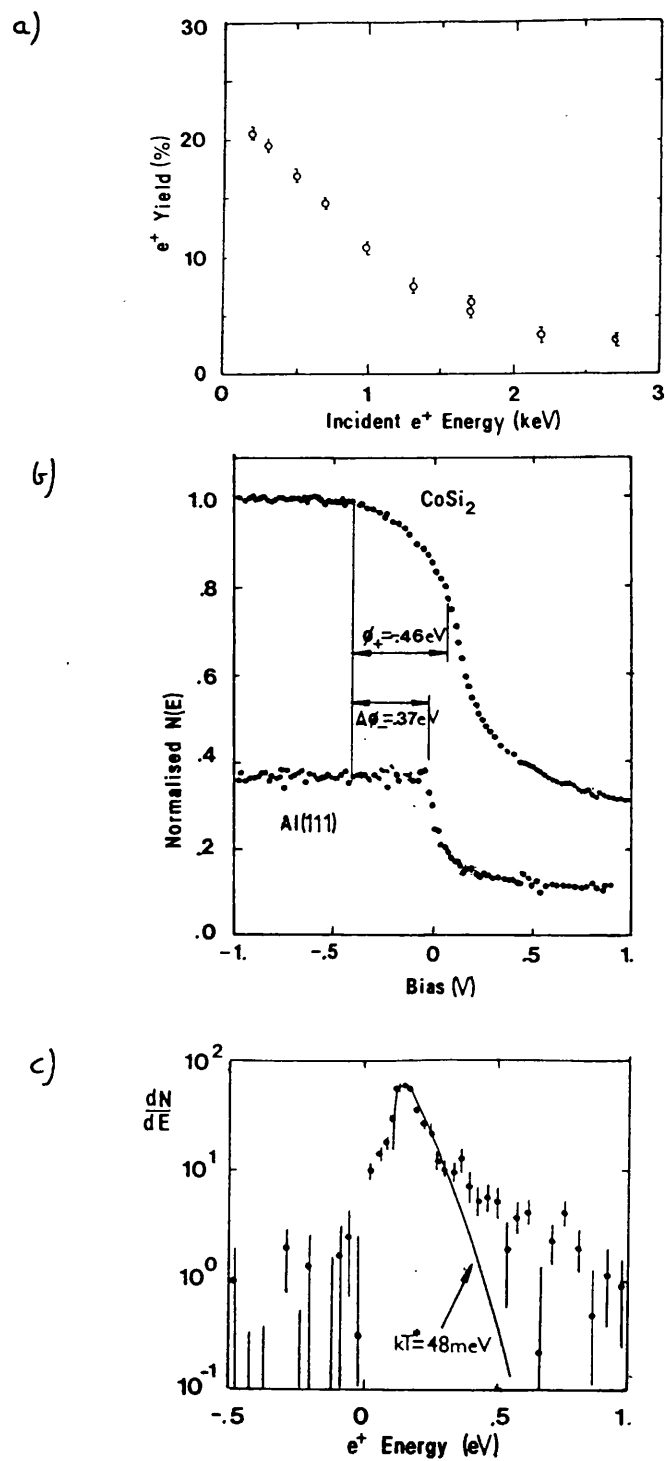


Figure 5.5 Positron re-emission from a clean 250Å CoSi₂ layer on Si(111)

- a) Variation of e⁺ yield with implantation energy
- b) Retarding potential spectrum for CoSi₂ and Al(111) samples
- c) Energy distribution of e⁺ re-emitted from the sample

(Gullikson et al 1988b)

energy spectrum obtained by this method (see Figure 5.5c)) was well fitted by a Maxwellian distribution, giving a low e^+ effective temperature of 48meV. The energy loss tail was found to be small as observed for single component metals with clean surfaces.

5.1.2 Insulating and Semiconducting Surfaces

Apart from that for silicon, there is little experimental information concerning e^+ -surface processes of insulating and semiconducting materials. Experimental e^+ re-emission studies for ionic insulators by Mills and Crane (1984) and rare gas solids by Gullikson and Mills (1986) have been discussed previously in Chapters 1 and 4. Re-emitted energy spectra from these materials show little resemblance to those obtained for metallic surfaces with negative positron affinities and the broad distributions are believed to be characteristic of epithermal e^+ processes (Lynn and Nielsen (1987), Gullikson and Mills (1986)). However some samples, particularly LiF, showed a sharp peak at low energy, which may be a result of a negative work function. Mills and Crane (1984) observed a series of e^+ Bragg peaks for most of the samples they studied and, from considerations of the inner potential, they determined e^+ work functions of -0.7 and +0.5eV for LiF and CaF₂ respectively. However in a subsequent, more detailed, low energy diffraction study of vacuum cleaved NaF and LiF crystals, Mills and Crane (1985) found ϕ_+ positive for both materials. The origin of the low energy e^+ distribution for LiF is therefore still uncertain and merits further investigation.

Several studies of e^+ re-emission from silicon surfaces have been reported and in some cases, the authors conclude that a negative work function exists for at least some of its common crystal orientations. However, caution must be exercised in interpreting the data, particularly in the case of low energy e^+ beam studies, for which significant re-emission of non thermal e^+ may occur. The energy distribution of epithermal e^+ in Si is small because of its narrow band gap (1.1eV) compared to those of the insulators

studied by Mills and Crane (1984) and Gullikson and Mills (1986). This will give rise to a significantly narrower distribution of re-emitted e^+ than those shown in Figure 5.1 and could therefore be mistaken for a negative work function process. As discussed in Section 5.2, surface states and near surface impurity concentration gradients lead to electric fields at the surface which can either enhance or inhibit e^+ motion towards the surface. In considering experimental data these points must be taken into account.

Mills *et al* (1978) cleaned a highly doped Si(100) surface by heating at a temperature close to its melting point in UHV and obtained the retarding field spectrum reproduced in Figure 5.2. This distribution appears similar to those for metallic surfaces with negative work functions suggesting, that similar re-emission mechanisms are involved.

Gol'danski *et al* (1988) employed a long slit angular correlation instrument with a resolution of 0.7mrad to measure the distribution of annihilation γ -rays, $f_2(\theta)$ from Si(100) surfaces. Using a 4.5 Ω cm p-type sample as a reference, $f_1(\theta)$, they determined the difference $\Delta f(\theta) = f_2(\theta) - f_1(\theta)$ for both n- and p-type samples over a range of dopant concentrations. For all dopant levels apart from $p \approx 1 \times 10^{16}$ holes cm^{-3} (1 Ω cm p-type) $\Delta f(\theta) = 0$ to within statistical accuracy. For this sample, $\Delta f(\theta)$ showed a narrow peak near $\theta = 0$ mrad (see Figure 5.6). This effect was attributed to the annihilation of e^+ or Ps in stationary states associated with the one dimensional potential well at the Si surface. For the other samples, the absence of any peak was explained by the escape into vacuum of all e^+ reaching the surface. Gol'danski *et al* (1988) attributed this behaviour to a change in sign of ϕ_+ at a hole concentration $p \approx 1 \times 10^{16} \text{cm}^{-3}$. For n-type, intrinsic and p-type Si with $p > 1 \times 10^{16} \text{cm}^{-3}$, ϕ_+ is negative, whereas for $p \leq 1 \times 10^{16} \text{cm}^{-3}$, ϕ_+ is positive and e^+ are trapped in surface states.

In this work no mention of the sample preparation was made so, presumably, the surfaces were not atomically clean. If a native oxide layer were present, emission of e^+ into vacuum was improbable and other mechanisms which might account for the observed

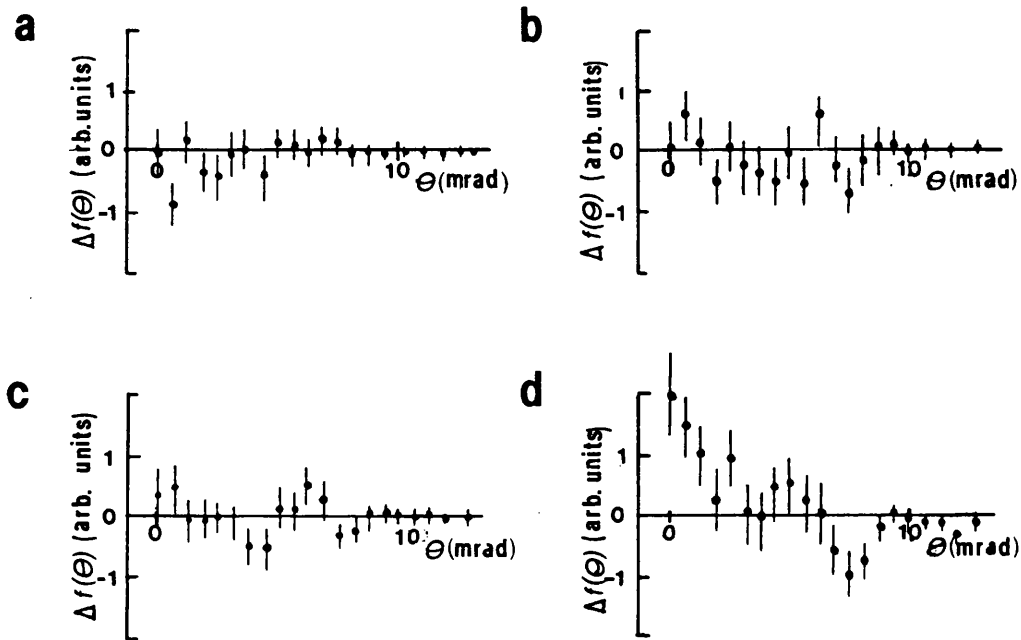


Figure 5.6 Difference between angular distributions of annihilation γ -rays, $\Delta f(\theta) = f_2(\theta) - f_1(\theta)$ for n- and p-type doped Si(100). The ACAR distribution recorded for a 4.5 Ω cm n-type sample was used as a reference, $f_1(\theta)$. $f_2(\theta)$ as follows

- a) 15 Ω cm n-type Si
- b) 12k Ω cm high resistivity compensated Si
- c) 4 Ω cm p-type Si
- d) 1 Ω cm p-type Si

(Gol'danski *et al* 1988)

behaviour should be considered. If it is assumed that $\phi_+ > 0$ for all Si surfaces, the disappearance of the sharp peak at $\theta = 0$ can still be explained by the creation of near-surface electric fields which inhibit the transport of e^+ to the surface. The magnitude of these fields depends on the sample resistivity and is therefore carrier concentration dependent.

Experimental evidence for the effect of electric fields on positron motion at surfaces has been presented by Mills (1978) and Nielsen *et al* (1985). In the former study, an anomalously low value of the positron diffusion length for a Si sample prepared by heat treatment was reported. Mills and Murray (1980) explained this result by the presence of an internal electric field residing near the surface. They concluded that this field would be established by a p-type carrier concentration of $p=5 \times 10^{19} \text{cm}^{-3}$ and that it would act to oppose the motion of e^+ towards the surface, as required. The formation of a highly conductive p-type inversion layer following high temperature heat treatment of Si was first reported by Allen *et al* (1959) and has been well documented since. Nielsen *et al* (1985) reported an anomalously low diffusion parameter, E_0 , for both Si(111) and Si(100) surfaces following sputtering and annealing at 1300K (E_0 is defined in Equation 1:24). Samples annealed at a lower temperature (1100K) showed substantially higher values for E_0 . Furthermore, following annealing at the higher temperature, a sharp increase in E_0 from room temperature to about 500K was observed, which was thought to be caused by a breakdown of the surface electric field as the sample conductivity increased. This effect was reversible with no observable hysteresis on cooling.

Chen *et al* (1987) used mono-energetic positrons with incident energies up to 25eV to monitor the surface oxidation of Si. Measurements of positron reflectivity and positronium formation were reported for oxygen coverages from sub-monolayer to 3500Å of SiO₂ on the Si. Although no details are given, these authors concluded from considerations of positron Bragg scattering that their results for the clean Si(111) surface were consistent with a value of $\phi_+ < 0.2\text{eV}$ reported by Chen (1987) for the same crystal orientation.

Electron work functions for clean (100), (110) and (111) Si faces are 4.82, 4.70 and 4.67eV respectively, indicating a significant dependency on crystal orientation. However it is difficult to reconcile the large (1 to 1.2eV) difference between $\phi_+(100)$ (Mills *et al* 1978) and $\phi_+(111)$ (Chen 1987 and Chen *et al* 1987) as being simply a surface orientation

phenomenon. On the other hand, Gol'danski *et al* (1988) report a change of sign in ϕ_+ at a critical dopant level, suggesting that for both p- and n-type (100) samples, $\phi_+ \approx 0$. The differences between this measurement and those for the (111) orientation are therefore consistent with the measured difference in ϕ_+ for these two faces.

Boev *et al* (1987) have performed calculations of electron and positron energy levels in solids using a local density approximation (LDA) method. Knowledge of these levels enables determination of positron and positronium work functions as well as the positron diffusion constant, D_+ . Values are generally in good accord with those measured experimentally. However, for Si(100) and Si(111) the calculations give 2.04 and 2.21eV respectively, in poor agreement with all the experimental values discussed above. Boev *et al* (1987) suggest that this discrepancy may be due to the effect of surface charging which would hinder accurate measurement of ϕ_+ for non metallic surfaces. Further experimental studies and more detailed calculations are necessary to resolve this problem.

5.2 SILICON SURFACE STRUCTURE

The silicon surface is complicated by the presence of surface states which result in near-surface band bending and related electric fields. Further difficulties arise due to the interaction of the surface with adsorbed species and the possibility of migration of impurities into or from the underlying bulk. Consequently, surface properties are more closely related to bulk properties of the semiconductor than in the case of metals and the simple surface dipole model introduced in Section 5.1.1 to explain e^+ re-emission is inadequate. For Si, studies of surface electronic properties are well documented because of their importance in developing structures for the semiconductor device industry. These studies can be used with the data published for e^+ (see Section 5.1.2) to make predictions of the likely e^+ behaviour at elemental semiconductor surfaces.

In an ideal Si lattice structure, the outermost s and p levels are mixed, producing hybridised sp^3 bonds. Overlapping hybridised orbitals from neighbouring tetrahedrally co-ordinated sites give rise to bonding and antibonding levels which ultimately broaden into valence and conduction bands respectively. Between these lies a forbidden band gap in which no delocalised electron states are permitted. Since Si has co-ordination number four, the valence band is filled and the conduction band empty, which explains the high intrinsic conductivity of the pure crystal. The Fermi level, E_f , resides near the band gap centre as shown in Figure 5.9a). On doping the crystal with donor (n-type) impurities, electrons are released into the conduction band and the Fermi level rises until in degenerate cases it resides close to the conduction band minimum. Conversely, on p-type doping the Fermi level falls.

For an ideal surface defined by an infinite two-dimensional plane cutting through the lattice, surface atoms are unable to form four bonds without re-ordering of the surface structure. In the absence of surface states the bands extend to the surface without bending. In the (111) orientation each surface atom has one free "dangling" bond. This structure is unstable both to the chemisorption of impurities and to surface reconstruction, thus giving rise to the well documented 2×1 and 7×7 structures (Kahn 1983). These processes reduce the number of dangling bonds and thus stabilise the surface. Information concerning surface structure is usually derived from studies such as low energy electron diffraction (LEED), electron microscopy and ion scattering (Zangwill 1988). In absorption studies, these techniques are augmented by contaminant sensitive probes which include electron energy loss spectroscopy (EELS) and Auger neutralisation.

In contrast, electronic properties of the surface are mainly deduced from measurements of contact potential and ultraviolet photoelectron spectroscopy (UPS). The former technique measures the work function of the surface whereas the latter method provides information on the occupancy of the various electronic levels near the surface. The two techniques are complementary as shown in Figure 5.7a) for an "ideal" surface. The work function, ϕ , is

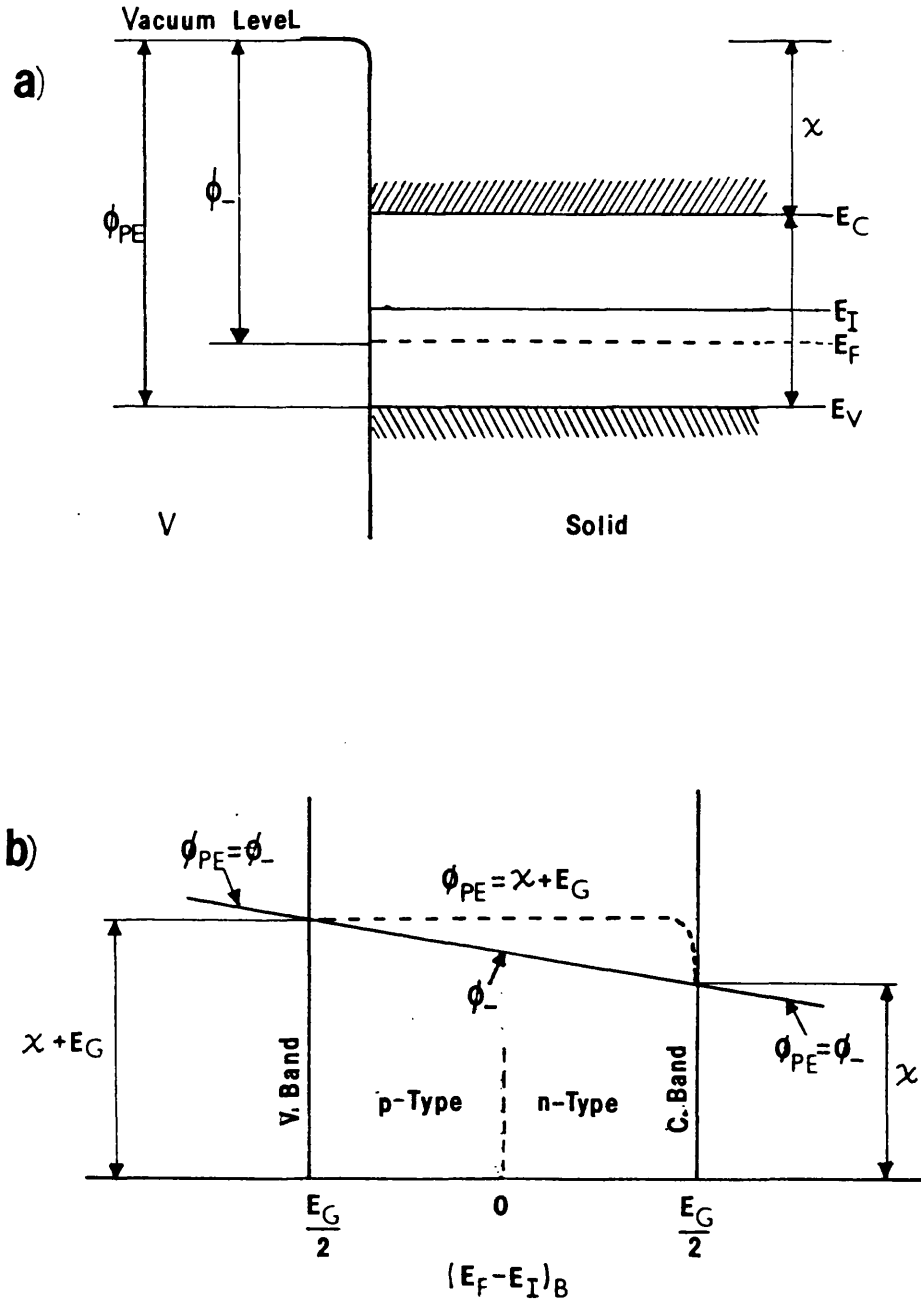


Figure 5.7 a) Surface energy levels, work function, ϕ_- , and photoelectric threshold, ϕ_{PE} for an "ideal" Si surface without surface states
 b) Variation of ϕ_- and ϕ_{PE} predicted by the "ideal" model

a measure of the Fermi level with respect to the vacuum level and the photoelectric threshold, Φ_{PE} , gives the position of the highest significantly occupied e^- energy level. In degenerate n and p cases $\phi \approx \Phi_{PE}$ since the highest filled state (the conduction and valence bands respectively) will be at the Fermi level. This is similar to metals where E_f always resides within an allowed energy band. In non-degenerate cases, where E_f resides within the band gap, Φ_{PE} and ϕ will differ as shown in Figure 5.7b). ϕ follows the position of E_f in the gap unlike Φ_{PE} which is dominated by photoemission from the valence band and is therefore a constant:

$$\Phi_{PE} = \chi + E_g \quad 5:3$$

where χ and E_g , the electron affinity and band gap respectively, are considered to be independent of doping.

Simultaneous measurements of Φ_{PE} and ϕ as a function of doping were published by Allen and Gobeli (1962) and are reproduced in Figure 5.8. These measurements, which extended from degenerate p (p^{++}) to degenerate n (n^{++}), failed to show the variations predicted by the ideal model (see Figure 5.7), so these authors concluded that the presence of a high density of surface states was required to provide an adequate explanation. In their model, the undoped Si surface is characterised by a band of surface states which, to satisfy conditions of charge neutrality, must lie near mid gap and be half filled to a level coincident with E_f (Figure 5.9a)). Upon n-type doping, E_f rises towards the conduction band (see Fig 5.9b)) so electrons vacate the high lying dopant levels and populate the lower lying unfilled surface states. This process continues until the Fermi level falls to restore equilibrium. Conversely, on p-type doping E_f is lowered towards the valence band and electrons flow out from previously occupied surface states until equilibrium is re-established (Figure 5.9c)). The surface state density is high enough (≈ 1 state per

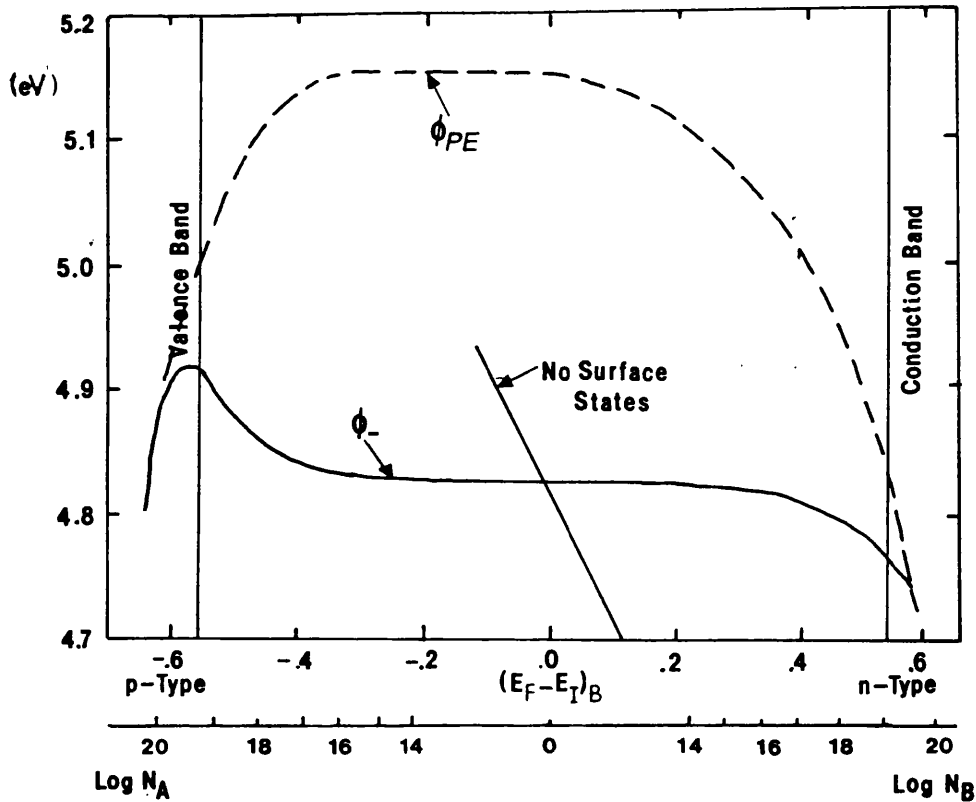


Figure 5.8 Measurements of work function, ϕ_0 , and photoelectric threshold, ϕ_{PE} versus bulk doping. Figure also shows the variation of ϕ_0 expected for a surface without surface states (Allen and Gobeli (1962))

surface atom) to "pin" E_f within a narrow energy range. In both n and p cases, the migration of surface charge causes a space charge layer in the underlying bulk, which consequently produces band bending, as predicted by Poisson's equation.

From the measurements of Allen and Gobeli (1962) it can be seen that while the Fermi level in the bulk moves 1.2eV from degenerate n to degenerate p, ϕ_0 changes at the extremes only from 4.7 to 4.9 eV. This is strong evidence for pinning of E_f by the surface states. The expected variation of ϕ_0 without pinning is also shown in Figure 5.8. The apparent drop in ϕ_0 at extreme p doping could not have been caused by the surface states and was instead attributed to a change in χ . This viewpoint is in agreement with the

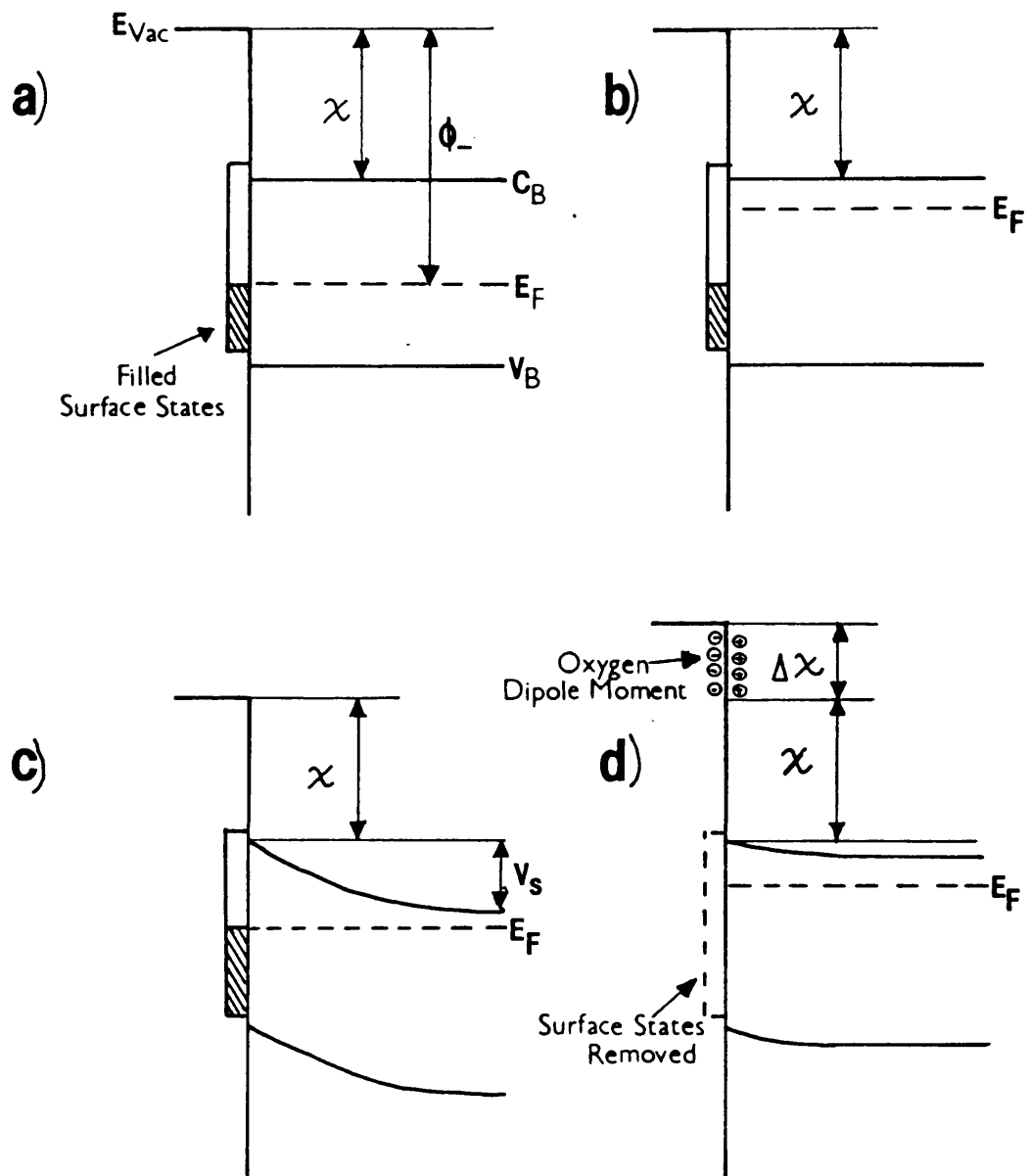


Figure 5.9 Electron energy levels in Si

- Energy bands for a clean undoped Si surface
- Disequilibrium between n-type bulk and surface
- Band bending and pinning of the Fermi level, E_f
- Energy bands for an Si surface after oxygen exposure

findings of Wagner and Spicer described below. The photoelectric threshold, Φ_{PE} , remained constant over a large range of resistivities. In this region the 0.3eV difference between Φ_{PE} and ϕ showed that E_f was held 0.3eV above the valence band maximum. At high n and p concentrations, Φ_{PE} tends towards ϕ as expected from the ideal model described above. In the p^{++} case, this was explained by the valence band crossing E_f within one electron escape depth ($\approx 20\text{\AA}$) of the surface. Subsurface electrons lying just below E_f can therefore escape from the valence band. For n^{++} doping the more gradual decrease in Φ_{PE} could not be explained by this process. Instead it was suggested that surface states close to E_f became progressively filled as the bulk energy bands bend downwards relative to E_f , with increasing doping, giving rise to sufficient emission from this level to cause the fall in Φ_{PE} . Allen and Gobeli (1962) reported a gradual rise in both ϕ and Φ_{PE} with oxygen exposure, reaching saturation after an increase of $\approx 0.5\text{eV}$ with several hundred Langmuirs, L, of coverage ($1\text{L} = 10^{-6}\text{torr s}^{-1}$). This change was believed to be due to an increase in χ due to the orientation of oxygen dipole moments with their negative end pointing outwards from the surface.

Wagner and Spicer (1972, 1974) performed a detailed ultra-violet photoelectron spectroscopy (UPS) study of n^{++} , n^- and p^{++} Si(111) surfaces as functions of oxygen coverage. The electron distribution curves (EDCs) for clean and oxygen saturated n^{++} surfaces are shown in Figure 5.10. The high energy (right hand) part of the clean surface EDC corresponds to electrons emitted from surface states. By measuring the relative area of this region Wagner and Spicer (1972, 1974) calculated that the surface state density corresponded to one electron per surface atom. This was in agreement with a Poisson equation calculation of the amount of charge required to give the correct amount of band bending. The disappearance of this part of the distribution can immediately be related to the removal of the surface states as the dangling bonds combine with the chemisorbed oxygen. The sharp peaks in the centre of the distribution are associated with bulk transitions. Following O_2 exposure, these were shifted by an amount V_s due to the

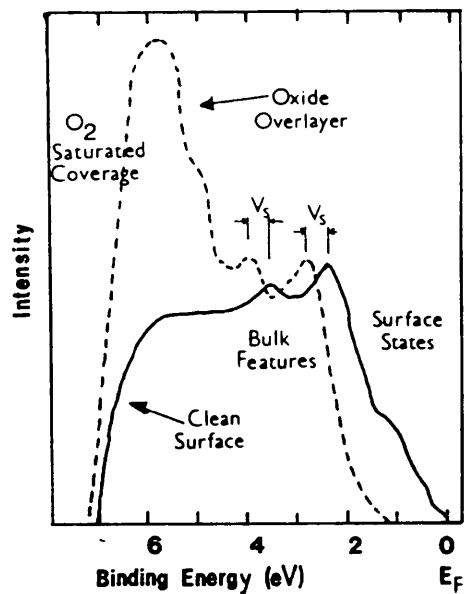


Figure 5.10 Electron distribution curves obtained from an ultraviolet photoelectron spectroscopic (UPS) study of a degenerate n^{++} Si(111) surface

- Clean surface
- - - Oxygen saturated surface

(Wagner and Spicer 1974)

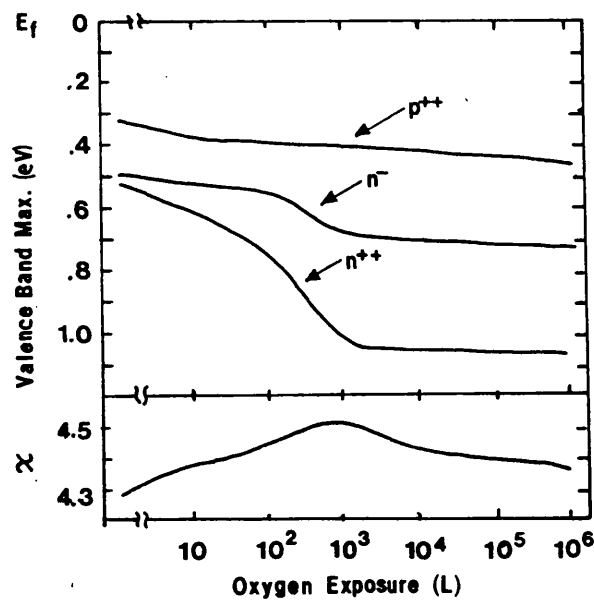


Figure 5.11 a) Position of the Fermi level relative to the valence band maximum for p^{++} , n^- and n^{++} doped samples as a function of oxygen exposure

b) Electron affinity, χ , versus oxygen exposure

(Wagner and Spicer 1974)

unbending of the bands. The large low energy peak, which was well formed after 10^3 L exposure, continued to grow with further exposure. This part of the EDC was observed to be quantitatively similar to UPS measurements of thermally grown SiO_2 and was therefore attributed to the formation of an oxide layer.

By monitoring changes in the peak positions of the EDCs with increasing O_2 exposure, Wagner and Spicer (1974) determined χ and the position of E_f relative to the valence band maximum for n^{++} , n^- and p^{++} doped surfaces. These are shown in Figure 5.11.

5.3 EXPERIMENTAL DETAILS

Most of the understanding of positron-surface interactions has been obtained by bombarding the target material with low to medium energy positrons (100eV-10keV). The present work was concerned with the development of primary moderators, so the positron source used was a β^+ emitter rather than a variable energy beam. Although in this case e^+ were implanted deeper into the samples, thus reducing the flux returning to the surface, the major advantage was that the measured yields truly represent the primary moderation efficiency for the material under study. The relatively simple set up also benefited from being contained in a single vacuum chamber, enabling clean UHV conditions to be easily maintained using relatively small pumps. A schematic illustration of the experimental arrangement is shown in Figure 5.12.

The stainless steel chamber was pumped by a 6" Edwards diffusion pump charged with high grade oil (Santovac 5). Backstreaming of pump vapour was inhibited by incorporating a Vacuum Generators UHV cold trap between the pump and main chamber. Following bakeout, this was constantly kept filled with liquid nitrogen using an automatic feed system. The chamber was also equipped with an auxiliary 500ls^{-1} AEI titanium sublimation pump. This was operated during sample annealing to maintain a good vacuum (typically $< 5 \times 10^{-10}$ torr) and also occasionally to reduce the system base pressure.

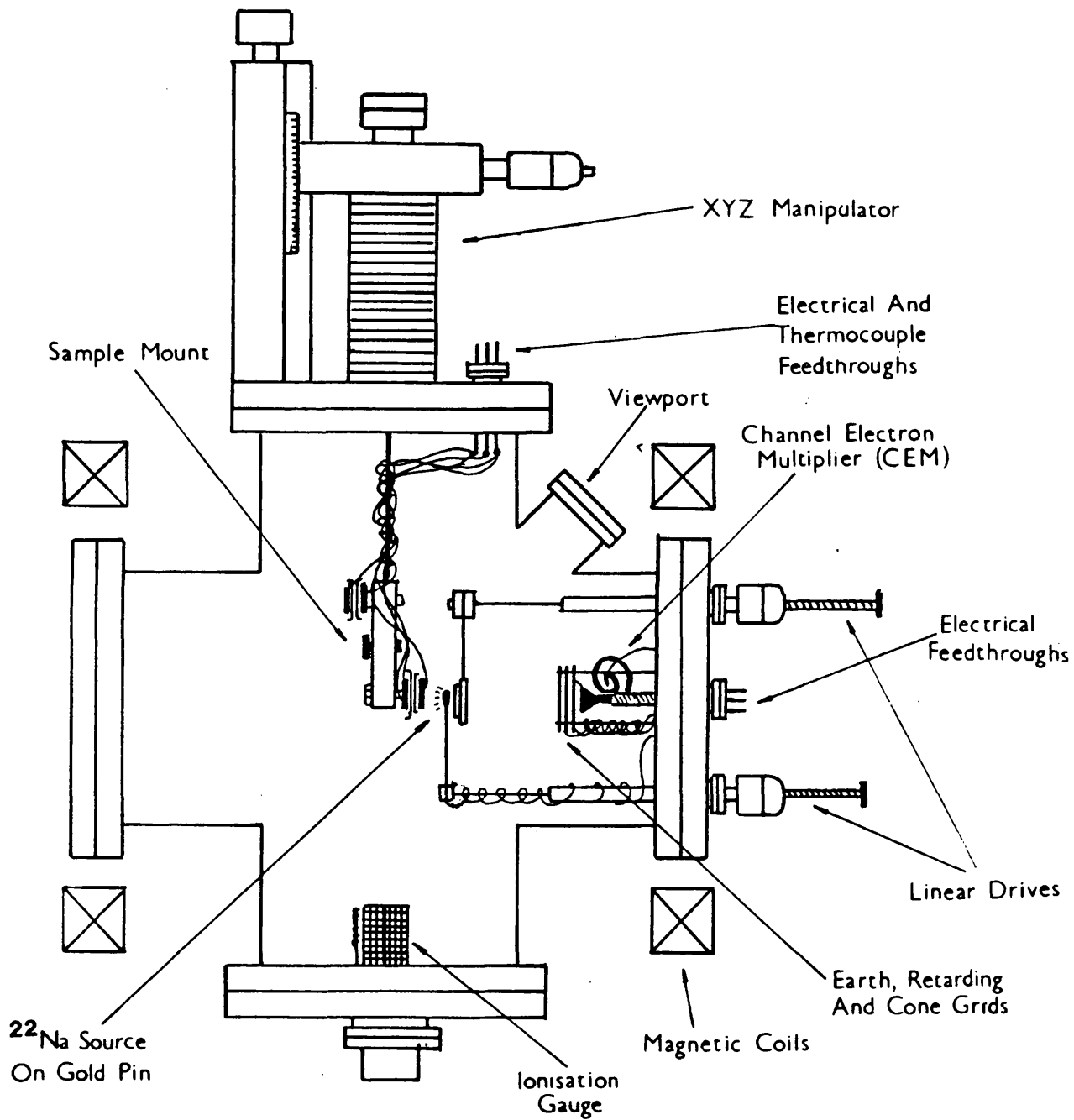


Figure 5.12 Schematic diagram of the experimental arrangement used to study e^+ re-emission from Ni, Si(111) and Si(100) surfaces

The system pressure was monitored using a Bayard-Alpert ionisation gauge with variable emission current ranges and a degas facility. Residual gas analysis was performed with a Spectramass Selectorr quadrupole mass spectrometer with a minimum partial pressure detection limit of 2×10^{-11} torr. The latter instrument could also be used as a helium leak detector in a special "mass four" mode.

Care was taken to use only UHV compatible materials, mainly stainless steel and high purity copper (OFHC) inside the chamber. Prior to assembly, components were scrubbed in detergent followed by successive washes in inhibisol, acetone and propanol. Cleaning of small parts was carried out in an ultrasonic bath. Ceramic components occasionally became carbonised as a result of system bakeout and sample annealing, so they were cleaned ultrasonically in concentrated KOH solution, followed by a rinse in deionised water. The system was bolted together using high purity copper gaskets, indium or gold seals.

Prior to bakeout the system reached a pressure of about $2-5 \times 10^{-8}$ torr after about 12 hours of pumping. Residual gas analysis showed that the major partial pressure was that of water vapour. Further reduction of the base pressure into the UHV region was achieved by baking the chamber. A double walled oven was constructed from aluminium sheet and the insulating region between the wall filled with glass fibre wool. Following bakeout, the front portion of the oven was swung back onto the rear part to allow access to the experimental chamber. Heat was provided by twelve 1kW electric elements mounted in front of aluminium radiation shields on the inner oven walls. The bakeout temperature was monitored by two thermocouples which regulated the heat input to the front and rear portions of the oven. The power output of each heater was individually regulated by a 'Simmerstat'. Additional thermocouples connected to various parts of the chamber monitored the temperature during bakeout and the Simmerstats were adjusted to achieve a uniform temperature throughout the oven. A protective thermocouple shut off all the power if the oven temperature rose too high. Feedthroughs, viewports and manipulators

were covered with aluminium foil to reduce thermal stresses due to direct heating. The maximum bakeout temperature was limited to 500K to avoid risk of damage to the manipulator.

After switching on the oven, it took between eight and twelve hours to reach this temperature, at which time the pressure had increased to between 5 and 10×10^{-5} torr. Subsequently the pressure began to drop until after two to three days, it reached 6×10^{-8} torr and the oven was turned off. After cooling for 6-10 hours, the pressure fell to between 1 and 3×10^{-10} torr.

Residual gas analysis showed strong peaks at mass numbers 2, 28 and 44, corresponding to H_2 , CO and CO_2 which were evolved from gauge filaments and the stainless steel chamber. These peaks are characteristic of most UHV arrangements. Hydrocarbon contamination from the diffusion pump was negligible provided the cold trap was kept filled.

Samples were clamped onto commercial mounts (VG EBH2) supported on a precision manipulator capable of motion in x, y and z directions, and rotation about the z axis. This arrangement was later modified to enable several samples to be supported in the system at one time. The mounts incorporated thoria coated iridium filaments to permit electron beam annealing up to 1470K. Below 1270K the sample temperature was measured with a type K thermocouple and for higher temperatures an optical pyrometer was employed. In the region 1170-1270K both methods were in good agreement. Since annealing was always carried out below 1470K, no correction for the sample emissivity was necessary.

The system was equipped with a 0-10keV ion gun for argon sputtering. Research grade gas was supplied to the gun via a stainless steel gas line and precision leak valve. Before operating the gun, the line was pumped and flushed with gas several times. In earlier runs, low levels of impurities in the Ar were recorded on the mass spectrometer. To reduce these contaminants, a SAES 171 non evaporable getter was subsequently incorporated

into the system. Prior to admitting gas into the UHV chamber, the getter was activated by passing a current through it whilst under vacuum. After activation, gas was admitted into the getter chamber through a liquid nitrogen/acetone cold trap and allowed to "see" the getter for several minutes before opening the leak valve to the main chamber. With an Ar pressure of 10^{-5} torr partial pressures due to impurities were no greater than those measured with the system at its UHV base pressure. The same gas line was used to admit high purity O_2 into the system for studies of oxidised Si surfaces. The getter could not be used to purify this gas, although the cold trap reduced water vapour and volatile hydrocarbon contaminants.

A small ($\approx 50\mu\text{Ci}$) ^{22}Na source deposited on one side of a small gold pin was used to implant the e^+ into the samples. The gold pin was supported on a linear motion drive, which could be retracted during sample annealing. Following some of the earlier runs slight radioactive contamination of the samples and mount was observed. To avoid this recurring, the source was sealed using a $1\mu\text{m}$ Ni foil. It was estimated that this foil stopped $\leq 10\%$ of β^+ particles emitted by the source.

Positrons re-emitted from the samples were accelerated by a potential difference applied between the sample and a moveable earth grid positioned immediately behind the source, which was maintained at the sample potential. For detection, e^+ were guided by a 100 gauss magnetic field to a channel electron multiplier (CEM) situated about 10cm from the sample. A biasing grid in front of the CEM enabled measurements of positron energy to be made. With the source-sample-grid configuration used, the transport efficiency and energy resolution of the re-emitted e^+ were relatively poor, especially at energies $< 10\text{eV}$. The optimum accelerating potential of about 10V was used for most runs. Much of the data were collected using a simple bias on/ bias off method. CEM pulses were recorded on a scalar with a sufficiently high bias applied to the retarding grid

to ensure that no re-emitted slow e^+ reached the CEM. The run was then repeated with the bias removed and the difference in counts between the two runs was thus a measure of the slow e^+ yield.

For Ni the slow event signal rate was generally similar to that of the background arising from fast e^+/e^- and γ -ray events, so relatively short run times were required (typically 100s). For Si the re-emitted yields were always low and run times ≥ 1000 s were required to observe any signal above background statistics. For some runs a voltage ramp was employed in conjunction with an MCA in multichannel scaling mode. The ramp dwelt on each voltage step in the set range for a preset length of time and CEM pulses were stored in one channel of the MCA. The ramp then stepped to the next voltage and advanced the MCA input to the next channel. This process was repeated to cover the whole 512 channels of the MCA memory and a complete retarding field spectrum could be accumulated in 5×10^3 - 5×10^4 s.

The energy distribution of the re-emitted e^+ was obtained by differentiation of the retarding field spectra. An attempt to perform this operation by computer was unsatisfactory and the most reliable method proved to be by calculating the gradients of tangents drawn on the plotted spectra.

5.4 SAMPLE PREPARATION

Several techniques have been developed for the preparation of clean surfaces in a UHV environment. The most important ones are summarised below.

1. For some materials, such as the alkali halides, attainment of good vacuum is sufficient to clean the surface under study. Contaminating species are desorbed from the surface and the sticking probability of the residual gas is low enough for recontamination not to occur.

2. Some single crystals can be easily cleaved (such as LiF) thus providing a simple and direct method of preparing a clean surface. Cleaved surfaces may not undergo the reconstructions brought about by high temperature annealing and can therefore show different surface properties (for example Si(111)).
3. High temperature annealing is sufficient to remove contaminants such as O, C and S from many surfaces. Generally these contaminants are desorbed as volatile species such as oxides, sulphides or carbides, although in some cases they may diffuse into the sample bulk leaving sub-monlayer levels of contamination behind.
4. In cases where the surface layer is stable at high temperatures, contamination may be removed in a more volatile form by heating in a surrounding reactive atmosphere. This technique has been exploited by Vehanen *et al* (1983) in the preparation of W(110) crystals as positron moderators. The high temperature annealing of bulk defects caused the segregation of carbon to the crystal surface. This was subsequently removed by heating to 500°C in 10^{-8} torr of oxygen. Further heating to 1000°C was sufficient to desorb the resulting oxygen coverage, leaving a clean surface.
5. Strong bonding contaminants can be removed by the bombardment of noble gas ions, particularly Ar^+ . Low energy ions are commonly produced by fast electron bombardment or field ionisation of a 10^{-3} to 10^{-4} torr Ar atmosphere. Higher energy ions are normally produced in a gun which consists of an ionisation region and simple electrostatic ion optics to accelerate and focus the beam. In many cases, a magnetic field is also applied to focus the beam. Ion guns have the advantage of being directional and thus lessen the risk of sample contamination due to sputter products from other parts of the system. Near-surface damage caused by the energetic ions is removed either by simultaneous or subsequent annealing. This can lead to surface migration of bulk impurities, so a suitable choice of

bombardment and annealing conditions must be made which allows re-ordering without unacceptable levels of contamination. In many cases, sputter-anneal cycles of between 10 and 100 repetitions are required to attain atomically clean surfaces.

6. Some studies of clean surfaces have used samples prepared *in situ* by evaporation or chemical reaction. When the surface becomes contaminated, a fresh layer of material can be re-deposited.

The choice of technique depends on the nature of the contaminant as well as the chemical and physical properties of the substrate. It is normally determined empirically by the use of standard methods of surface analysis such as LEED/Auger, X-ray or UV photoelectron spectroscopy. In the present study of Ni and Si surfaces, no surface analysis techniques were available so samples were prepared by following previously published methods.

5.4.1 Nickel

Nickel was the first element to be subjected to precise surface analysis (Davisson and Germer 1927) and remains one of the most intensively studied. Musket *et al* (1982) give a thorough review of the preparation of many clean elemental surfaces in UHV including the three principal Ni orientations. They note that the most common contaminants are carbon, sulphur and oxygen. Although Klimesch and Henzler (1979) succeeded in preparing a clean Ni(111) by annealing at 1450K for 400s in UHV, most workers have adopted a series of sputter-anneal cycles. The exact choice of conditions varies considerably but usually involves between 15 and 100 cycles with annealing temperatures between 1000 and 1300K for polycrystalline and 620 and 1170K for single crystal surfaces. In many cases it was reported that residual carbon proved persistent and frequently had to be desorbed as CO₂ by subsequent annealing in an O₂ atmosphere. This in turn tended to cause oxygen migration into the bulk which was removed by high temperature treatment in hydrogen.

5.4.2 Silicon

Atomically clean silicon surfaces of all common orientations have been prepared both by ion bombardment and high temperature annealing. In the case of the (111) phase, cleavage has also been utilised.

Using a combination of surface sensitive techniques Allen *et al* (1959) studied the effect of high temperature annealing of silicon and concluded that reproducible results characteristic of clean surfaces were obtained following annealing at 1550K or above for several minutes. However, the permanent p-type layer, several microns thick, formed at the surface was suspected to be an effect of the high temperature heat treatment rather than an intrinsic property of the surface itself. Subsequent experiments performed by Allen *et al* (1960) indicated strongly that this p-layer was formed by the transfer of boron from the walls of the borosilicate glass vacuum vessel and not the segregation of impurities from the Si bulk. However, as discussed in Section 5.1.2, the anomalously low value of E_0 in Si obtained following high temperature heating reported by Nielsen *et al* (1985) was attributed to the formation of a similar p-layer. These studies were presumably carried out in a modern stainless steel system, so a different source of boron must be involved. One possibility is that of the steel itself or the tantalum mount. Alternatively some other impurity may be responsible for this effect.

Cleaning of Si surfaces by low energy Ar ion bombardment was first reported by Dillon and Farnsworth (1958). After thoroughly outgassing the sample and mount at elevated temperatures, Ar was introduced to a pressure of 10^{-3} to 10^{-4} torr. With a few hundred volts accelerating potential, ion currents of 10 - $100\mu\text{Acm}^2$ were measured at the sample. The optimum conditions for clean Si surface preparation were found to be series of several such bombardments followed by annealing at 970K for one to two minutes. Chung *et al* (1976) demonstrated that higher energy Ar^+ ions can also be used to produce clean Si surfaces. In this study, sputtering with a $4\mu\text{A}$ 2keV ion beam followed by an anneal at 1070K for 30 minutes produced clean surfaces as characterised by LEED and

electron energy-loss spectroscopy. Nielsen *et al* (1985) used a 1keV ion energy and an 1100K anneal to produce clean (111) and (100) surfaces as observed by LEED and Auger spectroscopy. Higher annealing temperatures produced effects attributed to the p-type inversion layer discussed above.

5.5 RESULTS

5.5.1 Nickel

Slow positrons re-emitted from Ni and W surfaces were primarily used to optimise experimentally variable parameters such as sample bias, source bias, magnetic guiding field, CEM cone potential and source-sample position. Since the β^+ to slow e^+ conversion efficiency and re-emitted e^+ energy spectra have been measured previously, these materials also served as a "calibration source" of positrons, with which the energy resolution and transport efficiency of the system could be determined. Although some data were taken initially using W foils, polycrystalline and single crystal Ni samples were mainly used. The W foils were annealed by flashing the foils several times to intense white heat in a separate low vacuum chamber before placement in the UHV system. Ni foils were prepared *in situ* either by annealing or by Ar^+ ion sputtering and annealing.

Figure 5.13 shows the variation of slow positron count rate, R , from a W foil as a function of sample potential for several different magnetic fields. In all cases the source was held at the sample potential and the magnetic field produced by two coils in a Helmholtz configuration. The data show that the highest count rates were obtained between 10 and 20V. At these potentials there is also a strong variation in R with magnetic field. Below 10V, R rapidly decreased and was negligible below $\approx 5V$. For a single coil similar yields were obtained at high currents ($\approx 2A$), although retarding field spectra showed that the energy resolution of the system was badly degraded. Most data were subsequently taken with a sample potential of 10V.

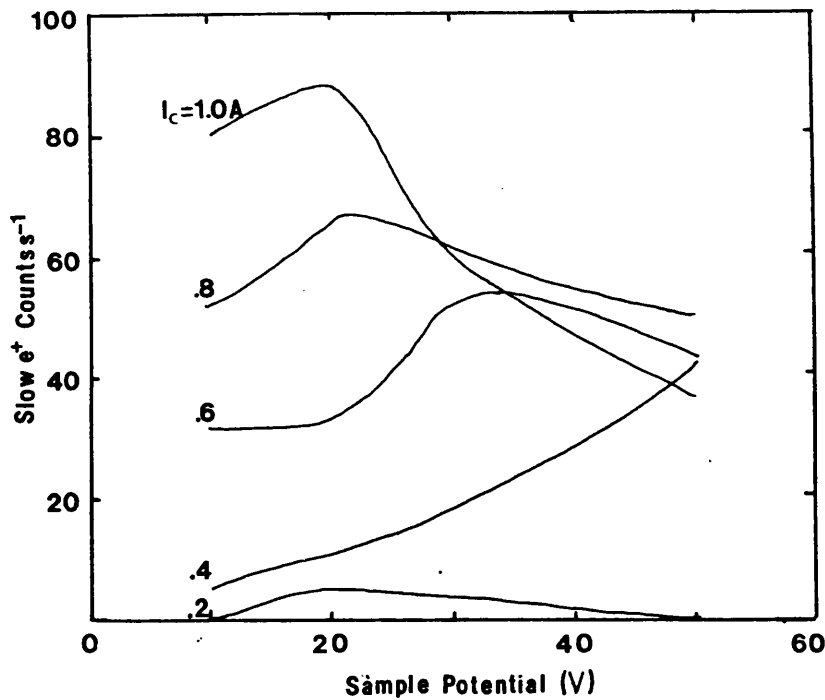


Figure 5.13 Slow positron count rate, R , versus sample potential for coil currents of 0.2 to 1.0A

Figure 5.14 shows the variation of slow positron yield with source potential for a 15 000Å Ni(100) layer grown epitaxially on an NaCl substrate. The sample potential was maintained at 10V. The data show that the maximum count rate is attained with source and sample potentials equal. For higher source potentials there is a rapid decrease in slow e^+ yield.

Since the linear drives supporting the source and earth grid were not graduated and the grid obscured the source in the viewport, exact positioning of these components was impossible. The optimum configuration was found before each run by systematically varying the position of the source or grid and measuring the slow e^+ count rate. The source was typically ≈ 3 to 5mm from the sample and the earth grid ≈ 2 to 3mm behind the source. These positions were found to be noncritical to within ± 1 mm.

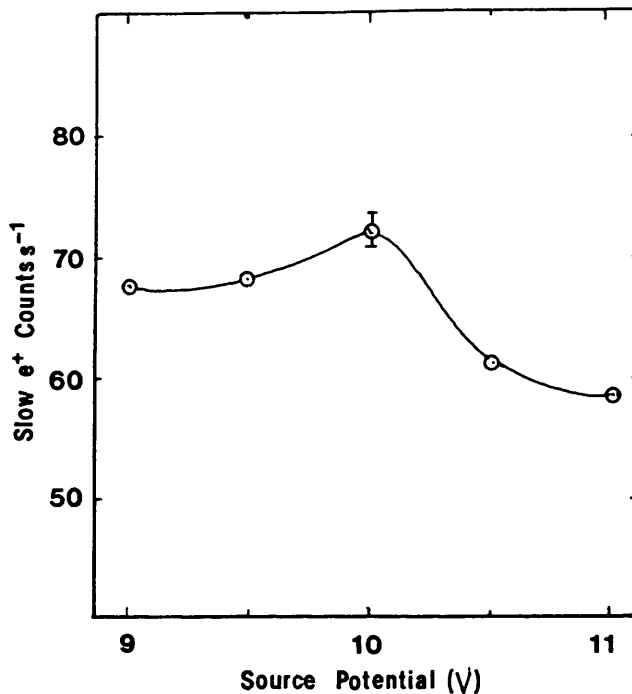


Figure 5.14 Variation of slow positron yield with source potential for a 15000Å Ni(100) layer grown epitaxially on an NaCl substrate. Sample bias held at 10V

Figure 5.15 shows the variation of slow positron yield and slow to fast e⁺ ratio versus CEM cone potential. The potential applied to the CEM collector was also varied to maintain a constant potential of 3350V across the detector. Both quantities increased significantly with cone potential over the range 200-700V. Data were normally collected with 500V applied to the cone, since at higher potentials there was a risk of electrical breakdown inside the vacuum chamber.

Figure 5.16a) shows a typical annealing cycle for a polycrystalline Ni sample heated to 720K for 6minutes. The rate of temperature rise was limited to avoid a rapid increase in system pressure to above about 10⁻⁷torr. This pressure rise was due to outgassing of heated components in the vacuum system. The rate of cooling was determined by the loss of heat from the sample and mount after the electron beam was switched off.

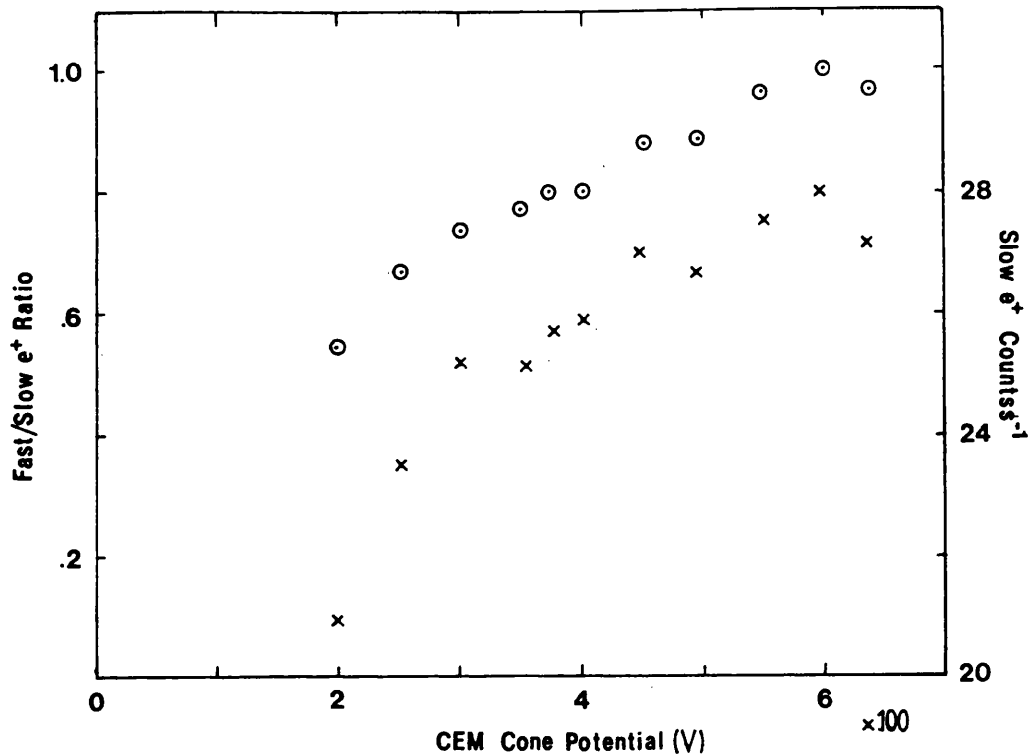
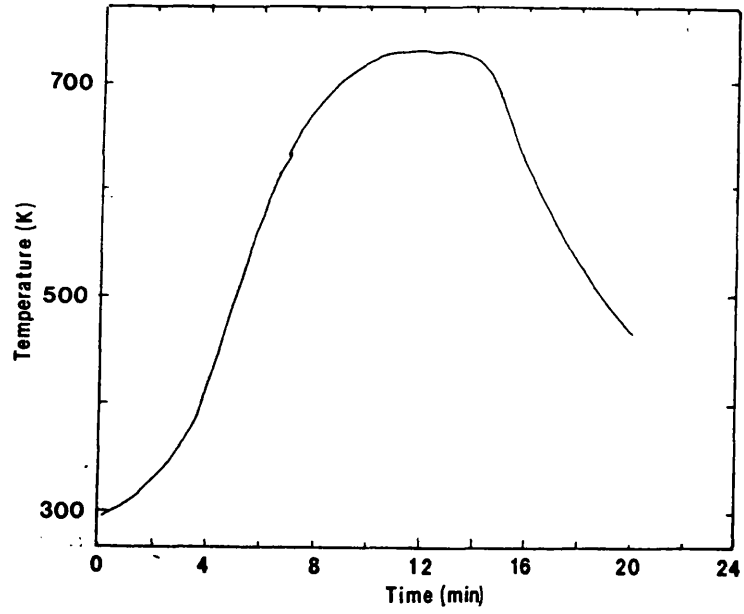


Figure 5.15 Slow positron yield and slow to fast e^+ ratio versus CEM cone potential

- × Slow positron yield (e^+s^{-1})
- Slow to fast e^+ ratio

Figure 5.16b) shows the variation of slow positron yield with annealing time for a polycrystalline foil heated to 720K. The non-zero value of R recorded before the first anneal suggests that the foil was partially annealed during manufacture. After a total annealing time of 12mins, R saturated and could not be improved further by heating to higher temperatures. Subsequent Ni samples were generally heated to between 870 and 920K for several mins to saturate R . Although the possibility of a systematic error in measuring the annealing temperature of this first sample cannot be discounted, due to poor thermal contact, for example, it was noted that the sample failed to reach dull red heat which occurs at $\approx 900K$. Furthermore, it was necessary to anneal at higher temperatures ($\approx 920K$) following sputtering, to achieve a good slow positron yield. This

a)



b)

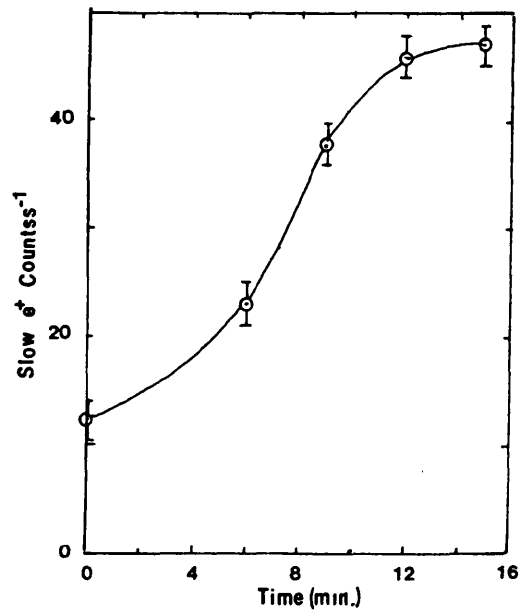


Figure 5.16 a) Annealing cycle used for a polycrystalline Ni sample heated to 720K
b) Slow positron yield from a polycrystalline Ni sample versus annealing time at 720K

is in agreement with subsequent measurements on other foils. The precise annealing procedure required to form an efficient e^+ moderator is determined by both the removal of

1. bulk defects, which typically requires heating to $\approx 70\%$ of the sample melting point (melting point for Ni $\approx 1700\text{K}$) (J. Chevallier, private communication 1987) and
2. surface adsorbed contaminants, which may not be achieved by heating alone.

Consequently, annealing conditions will depend on the initial state of the sample as well as the level of contamination in the vacuum system. Large variations in the preparation process of different samples of the same material in different experimental conditions can therefore be expected. This may be the explanation for the low annealing temperature required to prepare the first Ni sample studied.

Zafar *et al* (1989) and Schultz *et al* (1986) reported high yields of slow positrons from thin single crystal Ni(100) foils following annealing for several minutes at or above 920K. Gramsch *et al* (1987) used a higher temperature of 1670K, which is extremely close to the melting point of Ni. Zafar *et al* (1989) annealed the Ni foils in poor vacuum ($\approx 10^{-2}$ torr) which may require different conditions from those needed to produce Ni moderators *in situ* in UHV. Furthermore, direct comparison between polycrystalline and single crystal foils of different thickness may not be judicious. Likewise, comparison of the present annealing procedure used for Ni with others assessed using standard techniques of surface analysis (for example Musket *et al* 1982 and references therein) is difficult to make since the latter studies invariably used sputter-anneal cycles and/or heating in an O_2 atmosphere to remove the last traces of S, C and O surface species. The laborious techniques described to produce atomically clean surfaces suggest that annealing in UHV may not alone remove these chemisorbed species. However, experimental results reported by Smith (1970) and Park and Farnsworth (1964) suggest that CO and O are removed from Ni surfaces by heating to ≈ 600 and 730K respectively. It is not certain whether the

presence of such impurities in sub-monolayer quantities significantly changes the slow positron yield, although the presence of CO on single crystal Ni(100) surfaces has been shown to produce an energy-loss peak on the normal elastic peak measured for the clean surface (Fischer *et al* 1986). The resolution of the present arrangement was insufficient to be able to register any change in re-emitted e^+ energy spectra due to this effect.

Figure 5.17a) shows a retarding field spectra for e^+ re-emitted from a polycrystalline Ni surface after annealing at 720K for 15minutes. The re-emitted e^+ energy, obtained by differentiation of this data, is shown in Figure 5.17b). From this distribution, a value of $\phi_+ = -1.5\text{eV}$ is estimated for polycrystalline Ni, which is in reasonable agreement with previous measurements for single crystal samples (see Table 5.1). The energy spread of e^+ re-emitted from polycrystalline Ni is expected to be greater than the near-thermal spreads measured for single crystal samples (Gullikson *et al* 1985). However, the majority of the 1.1eV spread obtained from Figure 5.17b) arises from the poor resolution of the experimental arrangement rather than energy-loss intrinsic to the metal surface. The poor resolution is probably a result of distortion of electric field lines between the sample and earth grid by the source. This results in e^+ moving non-axially in the magnetic guide field and the transverse component of momentum is not measured by the retarder. Fischer *et al* (1984) reported a work function of -1.6eV for a CO exposed Ni surface, which is significantly more negative than the value recorded for a clean surface of the same crystal orientation. In the present study, an attempt was made to expose a clean Ni surface to CO produced by degassing the ionisation gauge filament. However, no significant shift in ϕ_+ was recorded.

After observing that R had saturated following successive high temperature anneals, the sample was sputtered with 8-10keV Ar^+ ions for several minutes at normal incidence. With a 1×10^{-7} torr Ar atmosphere in the system, a current of 20-100 μA was measured at the sample. After sputtering, no appreciable slow positron yield was measured from the sample, indicating that the Ar^+ ions had generated a large concentration of defects close

TABLE 5.1
Positron Surface Properties

Material	Face	$\phi_s(\text{th})$ (eV)	$\phi_s(\text{exp})$ (eV)	γ_0 (%)
Al	(100)	-.32	-.16(3)	20
		-.5	-.19(5)	21
	(110)	-.19		9
	(111)	-.15	+0.065	6
Au	(111)	+1.1	>0	0
Cu	(100)	+0.22		
	+S		-1.2	
	(110)	+0.33	-.13(8)	
	+S		-.4	
	(111)	-.13	-.4(1)	39(5)
	+S		-.33	28(3)
Ni	(100)	-.77	-1.0	39(2)
		-.4	-1.3	45(5)
	+O		-.95	
	CO		-1.6	
	S		-1.6	
	(110)	-.59	-1.4(1)	
	(111)	-.90		
		-.4		
	polycr.		<0	
	W	(100)		-3.0
(110)			-3.0	33
+C			-2.9(1)	
+O			-4.1(2)	
(111)		-2.1	-2.6(1)	40(5)
polycr.			-4.0(1)	53(5)
Si	(100)	+2.04	=0	
	(111)	+2.21	=0	10
CoSi ₂			-.46(5)	23(1)
Ne			+0.6(1)	70(3)
Ar			+1.55(5)	67(3)
Kr			+2.0(5)	63(3)
Xe			+2.3(5)	50(3)
SiO ₂				15
LiF			-.7	
NaF			+0.5	

Data taken from Table VIII in Schultz and Lynn (1988).

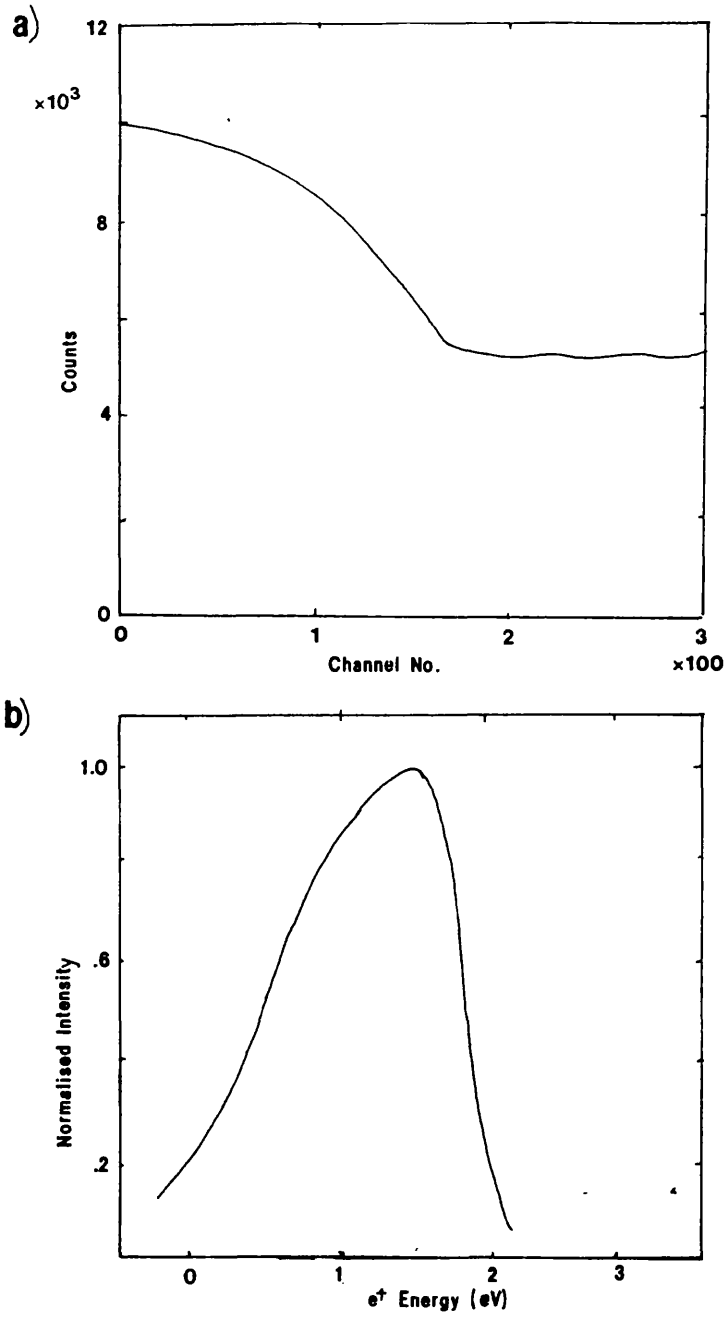


Figure 5.17 a) Retarding potential spectrum for a polycrystalline Ni sample annealed at 720K for 15min
 b) Re-emitted e^+ energy spectrum obtained by differentiation of the data in Figure 5.17a)

to the metal surface. The variation of R with annealing time is shown in Figure 5.18. The annealing temperature was 870K unless stated otherwise. A significant slow positron yield was only obtained after annealing at 870K for several minutes. R saturated at $\approx 70\text{e}^+\text{s}^{-1}$ after a cumulative annealing time of 1.5hours and was unchanged by a subsequent anneal at 1020K for 5minutes. The saturation value of R is significantly greater than the value obtained without sputtering. Further sputter-anneal cycles at energies between 400eV and 10keV gave lower yields, typically between 35 and 45 e^+s^{-1} , which are similar to the values obtained without sputtering. The reason for the high value of R after the first sputter-anneal cycle is therefore unclear. Re-emitted energy spectra for Ni samples prepared by this method are similar to that shown in Figure 5.17.

Slow e^+ re-emission from a 15 000Å Ni(100) film grown epitaxially on a NaCl substrate was also studied. The foil was left supported on the substrate to lessen the risk of damage whilst being mounted in the system. Prior to annealing a significant slow positron yield of $\approx 17\text{e}^+\text{s}^{-1}$ was measured and the energy spread of $\approx 0.8\text{eV}$ was about 30% less than that observed for polycrystalline samples. After annealing the sample at 870K for 30minutes, R increased to $\approx 60\text{e}^+\text{s}^{-1}$. The re-emitted e^+ energy spread was $\geq 1\text{eV}$, which was probably a result of creases forming in the Ni film, which lifted away from the substrate. Further annealing at temperatures of $\approx 970\text{K}$ in vacuum and a 10^{-8}torr O_2 atmosphere increased R to $\approx 70\text{e}^+\text{s}^{-1}$. The energy spread was unchanged to within the accuracy of the experiment.

Assuming the source contained 50 μCi of ^{22}Na activity, it produced 1.9×10^6 fast positrons per second. The fast to slow conversion efficiencies of single crystal and polycrystalline Ni samples were therefore typically 4×10^{-5} and 2×10^{-5} respectively, which is an order of magnitude less than that reported by Zafar *et al* (1989) and Gramsch *et al* (1987) for thin foils of the same material used in transmission mode, and nearly two orders of magnitude less than the efficiency of thick Ni single crystals operated in back scattering geometry. The low efficiency can be explained by

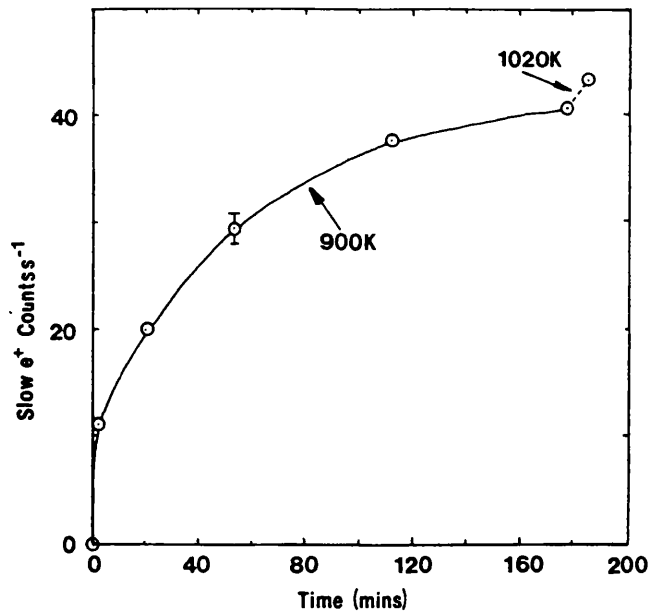


Figure 5.18 Slow positron yield versus annealing time for a sputtered polycrystalline Ni sample

1. a low transport efficiency of slow e^+ from sample to CEM, particularly as a result of shadowing and field line distortion by the source
2. a low solid angle subtended by the sample at the source
3. losses in the four 90% transmission grids situated between the sample and CEM
4. self adsorption in the source.

The last point may be particularly important because of the small size of the source ($\approx 3 \times 2 \text{ mm}^2$) required to reduce the adverse effect of shadowing.

In order to estimate the efficiency of Si as a positron moderator, it is therefore necessary to correct for the above losses, which could be substantially reduced in a system different design. During experiments on Si samples, the system was calibrated using a Ni

moderator, supported on a second sample mount, before each run. The slow positron yield from Ni of $\approx 25e^+s^{-1}$ was substantially less than that measured in the earlier studies of Ni discussed previously. This is a result of the exponential decay in source strength over the duration of the studies and a reduction of fast e^+ flux from the source due to the thin Ni foil used to seal the source. The efficiency of clean and oxygen exposed samples was estimated by assuming that a flux of 25 slow e^+s^{-1} corresponded to an efficiency of 2.5×10^{-4} , which is the value reported by Gramsch *et al* (1987) for a polycrystalline sample.

5.5.2 Silicon

a) Results

Re-emission of e^+ from 10k Ω cm n-type Si(111), 10k Ω cm p-type Si(111), and 4-6 Ω cm Si(100), dopant type unknown was studied. In all cases, the yield of e^+ was small ($\leq 1e^+s^{-1}$), so long run times were required to produce statistically significant data. Although some data were collected using a voltage ramp, no information on the energy distribution of re-emitted e^+ could be deduced. Consequently, most of the data were collected using a simple bias on/ bias off method. For each data point, an alternate series of 100s runs were collected at each bias, so that the stability in count rate could be monitored.

The 10k Ω cm n-type Si(111) sample was progressively annealed at increasing temperature over the range 1120-1390K, the temperature at which the sample melted. In all cases, the slow positron yield, R , was $\leq 0.5e^+s^{-1}$. During these measurements, the sample presumably remained contaminated, since clean Si surfaces are only generated by heating above 1550K (see Section 5.4.2). The low melting point of the sample at 1390K was attributed to a reaction between Si and the Mo mount. For this reason, samples were subsequently prepared by Ar^+ sputtering and annealing at lower temperatures ($\approx 1070K$).

The latter procedure also overcame problems associated with formation of a p-type inversion layer at the Si surface following prolonged heating at high temperature. This phenomenon was discussed in Section 5.1.2.

A second 10k Ω cm n-type Si(111) sample was sputtered with a 6 μ A, 2keV ion beam for 1hour and then annealed at 1070K for 15min. This procedure is similar to that chosen by Chung *et al* (1976) and Nielsen *et al* (1985) to produce atomically clean Si surfaces, characterised by LEED and Auger spectroscopy. After cleaning, a yield of $\approx 0.5e^+s^{-1}$ was measured from the sample. Similar yields were obtained after repeated cleaning of the sample using similar sputter/anneal conditions.

A 10k Ω cm p-type Si(111) sample was studied in more detail. Several cleaning cycles comprising sputtering at 45-60° incidence for 30-60minutes followed by annealing at 1070K for 30minutes produced a consistent yield of $0.2e^+s^{-1}$. After measuring R for each freshly cleaned surface, the sample was exposed to an atmosphere of $\approx 10^{-7}$ torr of CO and CO₂, generated by degassing the ionisation gauge filament for several minutes. Although there was some evidence to suggest that this process increased the slow positron yield, measurements were not of sufficient accuracy to establish a systematic variation in R arising from contamination of the surface. These measurements were hindered by a reduction in CEM gain following degassing.

After several sputter/anneal cycles, high purity O₂ was admitted into the UHV chamber. The exposure of the Si surface to O₂ was calculated from the pressure recorded by the ionisation gauge as a function of time. The variation of positron yield with total O₂ exposure is shown in Figure 5.19. The data are an average of two complete runs taken in succession. Between these runs, the sample was cleaned by sputtering with 2keV Ar⁺ ions for 20minutes followed by annealing at 1070K for a further 20minutes. The two sets of data were statistically in agreement.

Figure 5.20 shows the variation of R with oxygen exposure for an Si(100) sample prepared under similar sputter/anneal conditions. As with the Si(111) study, the data are an average of two successive runs which were statistically in agreement.

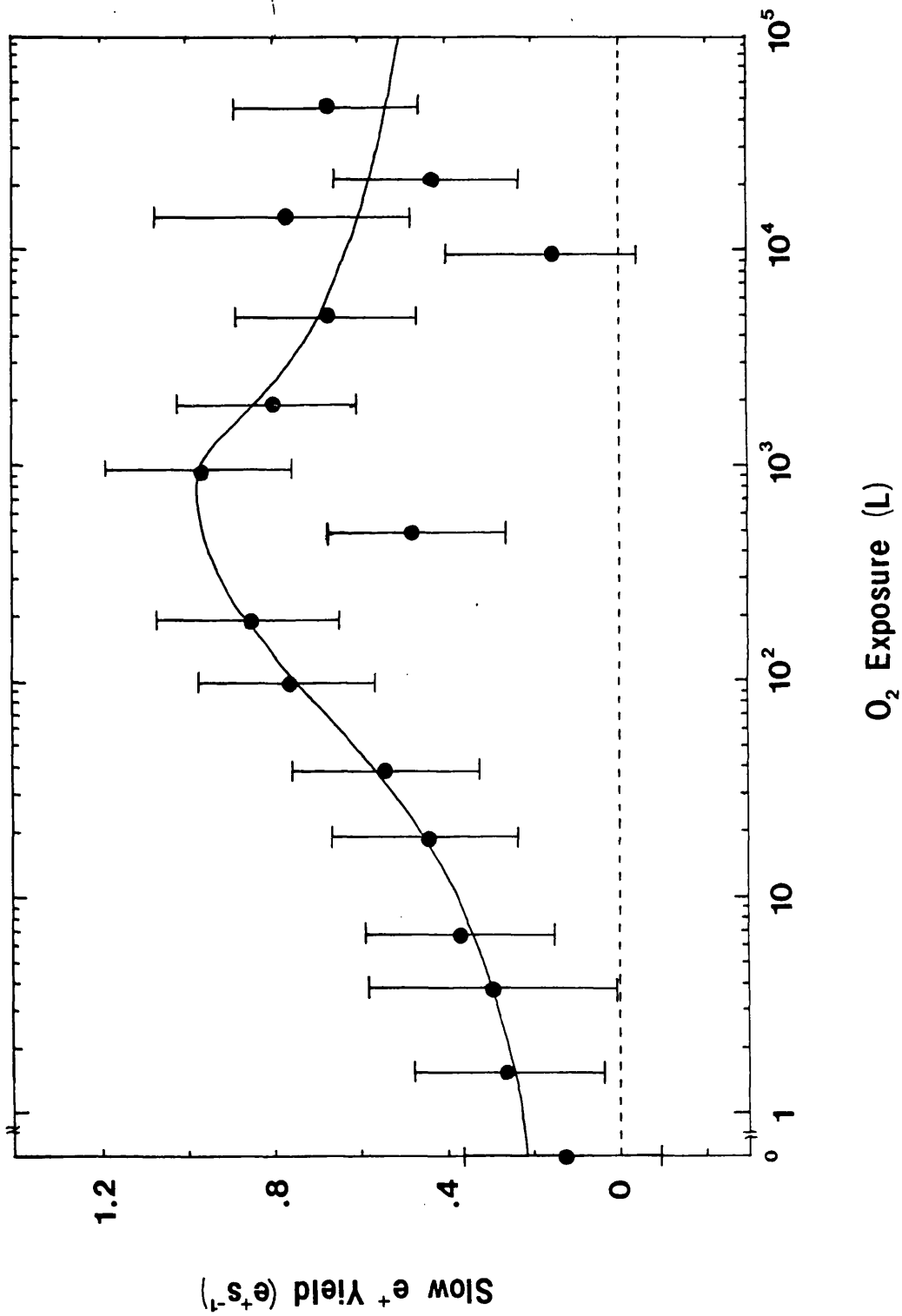


Figure 5.19 Slow positron yield versus oxygen exposure for a 10kΩcm p-type Si(111) sample

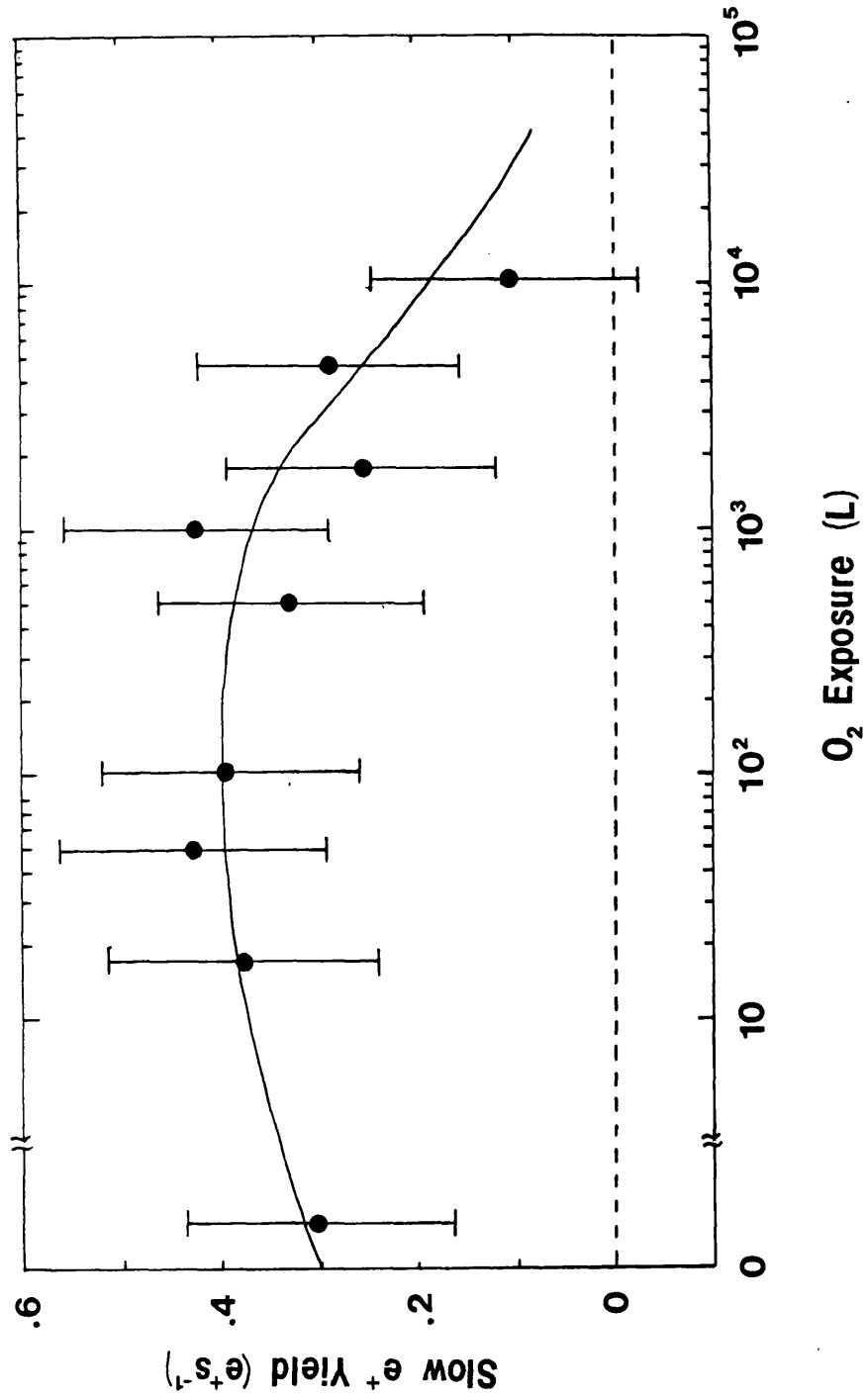


Figure 5.20 Slow positron yield versus oxygen exposure for a 4-6Ωcm Si(100) sample. The carrier type is unknown

b) Discussion

For sputter/annealed (111) and (100) surfaces, the slow positron yields, R , were approximately 0.2 and $0.3e^+s^{-1}$ respectively. In comparison, the yields from annealed polycrystalline Ni foils varied between 30 and $50e^+s^{-1}$. Allowing for losses due to the design of the present system, it was assumed that a yield of $1e^+s^{-1}$ corresponded to a fast to slow conversion efficiency of 1×10^{-5} (see Section 5.5.1). The moderation efficiency of the two Si orientations studied is therefore $\approx 10^{-6}$. The low efficiency may be a result of

1. positron trapping at the surface due to defects or impurities
2. the existence of strong electric fields which oppose e^+ motion towards the surface
3. a positive positron work function for Si.

Referring to the first of these points, the trapping of e^+ in surface defects or in the surface potential well minimum, as a result of inelastic scattering with surface adsorbed impurities cannot be discounted, especially considering that no surface analysis was available in the current study. However, the sputter/anneal procedure used to clean the sample was similar to that used by Chung *et al* (1976) and Nielsen *et al* (1985) to produce atomically clean surfaces, characterised by LEED and Auger spectroscopy. Furthermore, as discussed later in the current section, the variation of positron yield with oxygen exposure can be explained by a change in surface dipole moment arising from the contamination of an initially clean surface. It is therefore concluded that the Si surfaces were clean immediately after the sputter/anneal procedure and that e^+ trapping at the surface did not occur.

In all cases, the width of the near-surface depletion region produced by the trapping of electrons into surface states is $\geq 10^3 \text{Å}$ and is therefore significantly greater than the e^+ mean free path in the Si acoustic phonon field ($\approx 10 \text{Å}$). Consequently, e^+ moving along a curved energy band will relax before reaching the surface. In degenerately doped samples

($\rho \approx 0.001 \Omega \text{cm}$), the width of the depletion region is considerably less ($\approx 12 \text{\AA}$) and e^+ and e^- experience the effect of the strong near-surface electric fields without undergoing relaxation. This behaviour was observed by Allen and Gobel (1962) and Wagner and Spicer (1974) using photoemission techniques (see Section 5.2). The possibility of a p-type inversion layer at the surface of the samples studied can also be discounted because of the low annealing temperature used in the present study.

The low moderation efficiency for the Si samples studied is thus unlikely to be a result of a negative e^+ work function mechanism, especially in view of the high e^+ diffusion constant (see Chapter 2). Instead, it is proposed that ϕ_+ is positive and that re-emission of epithermal e^+ occurs as observed by Gullikson and Mills (1986) for the rare gas solids (see Section 1.3.7b)). According to their model, epithermal e^+ in bulk Si will be distributed between 0 and 1.1 eV (the band gap energy). Provided that $\phi_+ < 1.1 \text{ eV}$, re-emission of e^+ occurs with energies between 0 and $(1.1 - \phi_+) \text{ eV}$. The narrow Si band gap and the high implantation energy used in the present study result in yields of epithermal e^+ several orders of magnitude less than those measured for the rare gas solids. Yields from the (111) orientation are expected to be less than those from the (100) surface because of the difference in ϕ_+ for the two surfaces (see Section 5.1.2). This is observed to be the case.

The validity of the hot e^+ model for e^+ re-emission from Si could be established unequivocally if precise measurements of the re-emitted e^+ energy spectra could be obtained. This was not possible with the current system because of the low e^+ count rate. In addition, the energy resolution of the system was insufficient to be able to distinguish between thermal and epithermal e^+ . The only other published measurement of e^+ re-emission from a Si surface was reported by Mills *et al* (1978), who studied a highly doped Si(100) sample, cleaned by heating close to its melting point. Using a positron implantation energy of 1 keV, the energy distribution obtained in Figure 5.2 was obtained. The relatively narrow distribution of re-emitted e^+ energies was attributed to a negative e^+ work function of $-1.0 \pm 0.2 \text{ eV}$. However, a more recent experimental study reported by

251

Nielsen *et al* (see Section 1.3.7b)) showed that a significant proportion of e^+ implanted with keV energies into metallic samples are re-emitted as epithermal e^+ . Considering that the rate of e^+ energy-loss in Si is expected to be less than that in a metal at sub-eV energies, it can be concluded that Mills *et al* (1978) observed epithermal rather than thermal e^+ . If this is the case, the measured energy spread suggests that $\Phi_+ \approx 0$. Further studies of e^+ emission from Si surfaces following low-energy implantation would therefore be of considerable interest.

The variation of R with oxygen exposure for Si(111) and Si(100) surfaces is shown in Figures 5.19 and 5.20 respectively. As discussed above, the effect of band bending is negligible since the samples were weakly doped. For the (111) orientation, R follows the variation in χ recorded by Wagner and Spicer (1974) (see Figure 5.11) for coverages up to 0.5 monolayers. This is a result of equal and opposite changes in ϕ_+ and χ due to the increasing dipole moment contribution from the adsorbed oxygen atoms. At higher coverages, the rapid decrease in R may be due to surface scattering of e^+ by the oxygen over layer. Although the change in R for the (100) surface was less, the overall variation was similar to the (111) case.

Monte Carlo calculations presented in Chapter 4 used a simple model describing implantation, energy-loss and diffusion of epithermal e^+ in rare gas solids to predict re-emitted energy spectra. If measurements of e^+ mean free path and energy-loss per collision were available for Si, similar calculations could be used to predict e^+ yields and work function, ϕ_+ . Without this data an estimate of ϕ_+ can still be made. Following implantation of an e^+ ensemble, it is assumed that there is a uniform distribution of e^+ energies in the Si bulk between 0 and 1.1eV (see Figure 5.21a). With increasing time, the mean energy of the distribution decreases and a proportion of e^+ diffuse back to the surface. Assuming the energy distribution of epithermal e^+ reaching the surface is of the form shown in Figure 5.21b), the fraction, R , of the e^+ re-emitted is given by

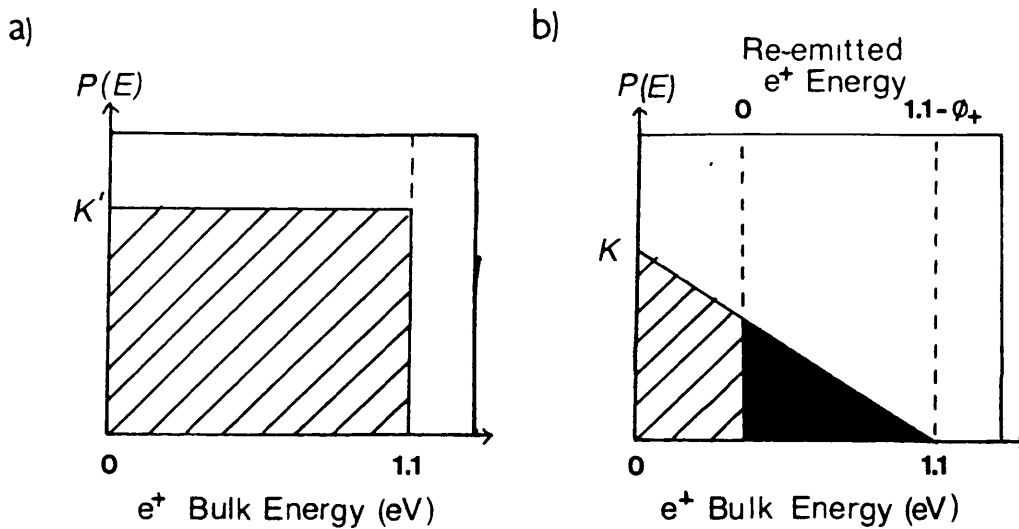


Figure 5.21 Energy distribution of e^+ in Si

- a) Immediately after implantation
- b) After diffusion back to the surface. Positrons with energies $>(1.1 - \phi_+)$ eV can escape

K and K' are arbitrary constants

$$R = (1.1 - \phi_+) \cdot \frac{(1.1 - \phi_+)}{1.1} K \cdot \frac{1}{2} \quad 5:4$$

In this simple argument, the effect of internal reflection is ignored. The work function difference between Si(111) and (100) is 0.15eV and the e^+ yields from clean surfaces 0.2 and $0.3e^+s^{-1}$ respectively. Therefore

$$\frac{3}{2}(1.1 - \phi_+(111))^2 = (1.1 - \phi_+(100))^2 \quad 5:5$$

$$\frac{3}{2}(1.1 - \phi_+(111))^2 = (1.25 - \phi_+(111))^2$$

Taking the root of the quadratic equation which lies between 0 and 1.1eV gives $\phi_+(111)=0.34\text{eV}$ and hence $\phi_+(100)=0.19\text{eV}$. ϕ_+ can also be deduced from the change in e^+ yield with oxygen exposure. Assuming the change in ϕ_+ between 0 and 10^3L exposure is equal to the corresponding change in χ ($\approx 0.2\text{eV}$), then $\phi_+(111)=0.9\text{eV}$. However for Si(100) no solution is obtained for $\phi_+(100)$ in the range 0 to 1.1eV. Values of ϕ_+ obtained by the two methods are clearly not in agreement and, given the accuracy of the data, the validity of the simple argument presented above cannot be established. However, the current data suggests that precise measurements of the epithermal energy distribution for different orientations of Si under clean and oxygen exposed conditions could be used in conjunction with the Monte Carlo model developed in Chapter 4 to provide information on epithermal energy-loss in Si and to estimate a value for ϕ_+ .

5.6 CONCLUSION

In this chapter, the first measurements of slow e^+ re-emission from Si subjected to β^+ irradiation have been described. The data suggest that the two orientations of Si studied have positive positron work functions and would therefore be unsuitable as positron moderators. Although an intense electric field may heat positrons thermalising in the Si bulk, it is unlikely that this process would substantially increase the positron yield re-emitted from the sample surface.

Measurements of positron yield versus oxygen exposure for Si(111) and Si(100) surfaces are consistent with a changing surface dipole moment due to the oxygen adsorption. Useful data would be obtained by repeating the experiments with a variable energy positron beam. It would be particularly interesting to extend the study to degenerately doped n and p-type material for which the effects of near-surface band bending become significant. In the n^{++} case, e^+ bands bend sharply downwards within 20\AA of the surface and e^+ may escape from the crystal without relaxation. For extreme doping this would

effectively decrease ϕ_+ by $\approx 0.5\text{eV}$ and re-emission of thermal e^+ may become energetically favourable. This may provide an explanation for the relatively high e^+ yield measured by Mills *et al* (1978) for a highly doped Si(100) sample implanted with keV energy e^+ .

CHAPTER 6

CONCLUSION

The primary objective of the present work was to assess the possibility of developing a new type of positron moderator, based upon the electric field drift of e^+ in a insulator or semiconductor. Although some progress towards this aim was made, it remains unclear whether a practical field assisted (FA) moderator can be produced.

Studies of e^+ behaviour in solid media originated in the 1950s and 1960s using angular correlation of annihilation radiation (ACAR), e^+ lifetime spectroscopy and Doppler broadening measurements. These experiments showed that the majority of energetic e^+ implanted into bulk materials rapidly slow down to near thermal energies and subsequently diffuse freely in the solid before annihilating with an electron. Since the annihilation γ -rays convey information relating to the final e^+e^- state, they provide a useful means of studying the electronic structure of solids. The discovery by MacKenzie *et al* (1967) that e^+ are trapped in crystal defects brought about an upsurge in e^+ solid state research and the field has continued to expand rapidly.

Before the development of the first intense e^+ beams in the early 1970s, research was mainly restricted to studies of homogeneous bulk structures, although e^+ lifetime studies in powdered and neutron irradiated materials provided some information on e^+ -surface interactions. The discovery of the MgO e^+ moderator by Canter *et al* (1972) enabled more detailed studies of e^+ interactions at surfaces to be initiated and also created the possibility of investigating near-surface defect profiles with e^+ . There has been considerable interest in developing e^+ beams as probes of near-surface structure using techniques such as REPELS and e^+ microscopy.

Conventional e^+ moderators rely on diffusion to transport a small fraction of e^+ implanted into a solid to a surface where, under favourable conditions, they can be re-emitted into vacuum with eV energies. Since the pioneering work of Madansky and Rasetti (1950), it has been realised that the efficiency of a moderator, ϵ , is governed by the ratio of e^+ diffusion constant to mean implantation depth for the β^+ source used. Assuming realistic values for these two quantities, Madansky and Rasetti (1950), estimated that $\epsilon \approx 5 \times 10^{-3}$. A considerable amount of research has since been devoted to developing efficient e^+ moderators and this theoretical estimate has only been recently attained with the discovery of the solid rare gas moderator by Mills and Gullikson (1986). As discussed in Chapter 4, there appears to be little scope for further improvement in conventional moderator efficiencies. Based on current technology, e^+ beam intensities are limited to $\approx 10^6 e^+ s^{-1}$ in the laboratory and $\approx 10^9 e^+ s^{-1}$ using linear accelerators or ^{64}Cu sources produced in a high flux reactor. The latter value is still several orders of magnitude less than intensity of commercially available e^- beams, so potential advantages offered by e^+ surface analysis techniques (see Table 1.1) have to be offset against the increased cost and reduced intensity of e^+ beam facilities.

In general, the motion of e^+ in semiconductors and insulators is less well understood than in metals. Measurements of positron mobility, μ_+ , provide a good method of determining the dominant e^+ scattering mechanisms in solid media. Early attempts to measure positron drift velocities in insulating materials were unsuccessful, until Mills and Pfeiffer (1976, 1977) reported large positron mobilities in Si and Ge. Subsequent studies have shown appreciable drift velocities in several other insulators and semiconductors. Published data suggest that reliable measurements of μ_+ are difficult to make and substantial discrepancies in values of μ_+ determined by different techniques have been reported. It is not yet clear whether the disagreement arises from systematic errors in particular experimental methods, or from variations in material properties of often uncharacterised samples of the same material. In an attempt to address this problem, a new method of

measuring μ_+ , based on positron lifetime spectroscopy was developed and used to make measurements of positron drift in high purity Si samples. The results obtained at the two temperatures studied are in good accord with results reported by Mills and Pfeiffer (1977), Nielsen *et al* (1985) and Corbel *et al* (1989). However, the cause of the significant discrepancy between values of μ_+ obtained from these studies and that measured by Brandt and Paulin (1977) using a shift in implantation profile method remains unexplained.

It is envisaged that the lifetime method will be used to observe e^+ motion in a variety of other materials. Measurements in GaAs are currently in progress. However, there is still considerable scope for further work on Si, especially if the accuracy of the data can be improved. Detailed measurements of μ_+ as functions of temperature and dopant concentration should be made. Comparison of experimental and theoretical values of n , the temperature coefficient of positron mobility, would establish the relative importance of the various e^+ scattering processes. In particular, an extension of the measurements to liquid He temperatures, where impurity scattering becomes increasingly important, and to high temperatures ($>300\text{K}$) would be interesting. In Ge, measurements of the positron diffusion constant, D_+ , in the range $300 < T < 1020\text{K}$ suggest that e^+ -polaron formation could be an important process in elemental semiconductors.

The count rate and/or time-resolution of the spectrometer used in the current study could be improved by replacing the plastic scintillators with BaF_2 crystals. The analysis of generated e^+ lifetime spectra, described in Chapter 3, suggests that this would reduce the error in μ_+ , which is predominantly determined by the uncertainty in the interfacial lifetime τ_4 .

It is important to note that the method developed in the present work to determine μ_+ provides a direct measure of the fraction of e^+ which, after implantation, drift in an applied

electric field to an insulator-metal interface. The measurements are therefore directly applicable to the development of field assisted moderators. For Si at 104K, this fraction was $\approx 7\%$ at the highest fields studied.

The development and present state of e^+ moderator technology was reviewed in Chapter 4. The possibility of developing FA moderators was discussed and the failure of Lynn and McKee (1979) to observe field enhanced e^+ re-emission from an Si surface barrier detector attributed to e^+ trapping in defects in the non-epitaxially grown contact. Based on current knowledge, it was argued that Si offers the best prospect of developing a FA moderator. For this material, the concentration of defects in the thin contact on the exit surface of the moderator could be reduced by using a thin epitaxially grown $NiSi_2$ layer on a Si(111) substrate.

Studies of e^+ re-emission from $CoSi_2$ (Gullikson *et al* 1988b) suggest that $NiSi_2$ probably has a negative positron work function, ϕ_+ . If this is the case, the success of a Si(111)- $NiSi_2$ moderator depends on the behaviour of e^+ at the solid-solid interface.

Measurements of positron work function, ϕ_+ , were reviewed in Chapter 5. Although several authors conclude that ϕ_+ is negative for Si(111) and (100) surfaces, the data are inconsistent. In the only direct study of positron re-emission from Si, Mills *et al* (1978) concluded that the substantial yield of e^+ observed from a highly doped Si(100) sample was a result of a negative positron work function for the surface. However, the data need to be re-evaluated following the more recent measurements of epithermal e^+ re-emission from insulating surfaces with positive e^+ work functions (Gullikson and Mills (1986), Mills and Crane 1984).

The ultra high vacuum system described in Chapter 5 was constructed to study the re-emission of e^+ from Si surfaces bombarded with β^+ particles. Although a small yield of slow e^+ was observed from clean Si(111) and Si(100) surfaces, the moderation

efficiency was extremely low ($\approx 10^{-6}$) and the measurements are considered to be the result of epithermal e^+ re-emission rather than a negative work function for Si. Measurements of slow positron yield versus oxygen exposure for both Si surfaces studied were consistent with a changing surface dipole due to oxygen adsorption. The low e^+ yields suggest that $\phi_+ > 0$ for all exposures studied.

The signal to noise ratio, energy resolution and count rate of the experimental arrangement could be improved by replacing the gold pin source with an annular arrangement and by arranging for a more uniform magnetic guide field. With a more efficient transport system, the CEM could be located further from the source, thereby reducing the fast e^+ and γ -ray backgrounds. These could be further reduced by installing an ExB filter or bent solenoid arrangement in conjunction with lead or tungsten alloy shielding.

It would be interesting to extend measurements to degenerately doped Si samples, for which band bending becomes significant. In the n^{++} case, e^+ bands bend sharply downwards near the surface and e^+ may escape without relaxation. This effect would effectively decrease ϕ_+ by 0.5eV and may provide an explanation for the large yield of re-emitted e^+ measured by Mills *et al* (1978). Further studies of adsorption should be performed using other gases. More precise data could be generated by repeating these studies using a variable energy e^+ beam. In this case, measurements of re-emitted e^+ energy spectra could be used to estimate ϕ_+ and to study e^+ thermalisation in semiconductors. In order to develop a comprehensive understanding of e^+ processes in non-metallic solids, the work should be extended to other semiconductors and insulators such as LiF and MgO, which may have negative e^+ work functions.

It now appears that an Si field assisted moderator will not provide an efficient source of slow e^+ , due to an unfavourable e^+ work function at all Si surfaces. For other materials, at present, there is insufficient data relating to the bulk and surface behaviour of e^+ to be able to predict whether a practical field assisted moderator can be developed.

APPENDIX 1

APPLICATION OF THE DIFFUSION EQUATION TO MONO-ENERGETIC POSITRON IMPLANTATION INTO SINGLE CRYSTAL FOILS

Estimates of remoderation efficiency of thin single crystal metal foils can be obtained from the diffusion equation solutions derived in Chapter 4. These predictions are of considerable importance in developing efficient brightness enhanced positron beams (see Section 1.1.4).

Monte Carlo simulations preformed by Valkealahti and Nieminen (1983, 1984) suggest that, in the range 0-10keV, mono-energetic positron implantation is well described by a profile originally proposed by Makhov (1960a,b,c) for electron impact (see Section 1.3.3). This has the form

$$P(x) = \frac{mx^{m-1}}{x_0^m} \exp\left[-\left(\frac{x}{x_0}\right)^m\right] \quad \text{A1:1}$$

where $m \approx 1.9$ for most materials and x_0 is related to the mean implantation depth, \bar{x} , by the gamma function, $\Gamma(z)$ expression

$$\bar{x} = \Gamma\left(1 + \frac{1}{m}\right) x_0 \quad \text{A1:2}$$

\bar{x} can be expressed in terms of the incident e^+ energy, E, by the formula

$$\bar{x} = AE^n \quad \text{A1:3}$$

where A and n are constants characteristic of a particular material. Values of m , A and n derived from Monte Carlo calculations are in reasonable accord with thin foil transmission experiments (for example Mills and Wilson 1982), although the experimental data tend to exaggerate the initial part of the profile due to backscattering effects.

Remoderator efficiencies were calculated by substituting Equations A1.1-3 into Equation 4.27. In general the integration cannot be solved exactly, so numerical methods had to be employed. A Numerical Algorithms Group (NAG) library subroutine DO1AJF, accessed from a FORTRAN coded main programme, returned the value of the integral and an estimate of the absolute error. Computational accuracy was checked by comparing results with the exact analytical expressions obtained for $m=1$ and 2. Between these limits numerical results showed no discontinuities which might have indicated poor performance.

Slow positron yields for Cu and W are presented in Figures A1.1 and A1.2 together with the transmitted fast e^+ fraction, F_{fp} , given by

$$F_{fp} = \int_d^{\infty} P(x)dx \quad \text{A1:4}$$

The parameters used are shown in Table A1.1 and are the same as those adopted for previous calculations reported by Vehanen and Mäkinen (1985). Agreement between both these sets of data and the values published by Sferlazzo (1985) for Cu is good.

In Figure A1.3 values calculated for a 1500\AA Ni foil are compared with experimental results of Schultz *et al* (1986). In this case values of A , m and n are based on those given the Monte Carlo simulations, discussed above and in Section 1.3.3. The diffusion constant is the experimental value obtained by Vehanen *et al* (1984) and y_0 taken from Gullikson *et al* (1988). Considering the uncertainty in the parameter values chosen and their likely variation from sample to sample, the agreement between theory and experiment is good.

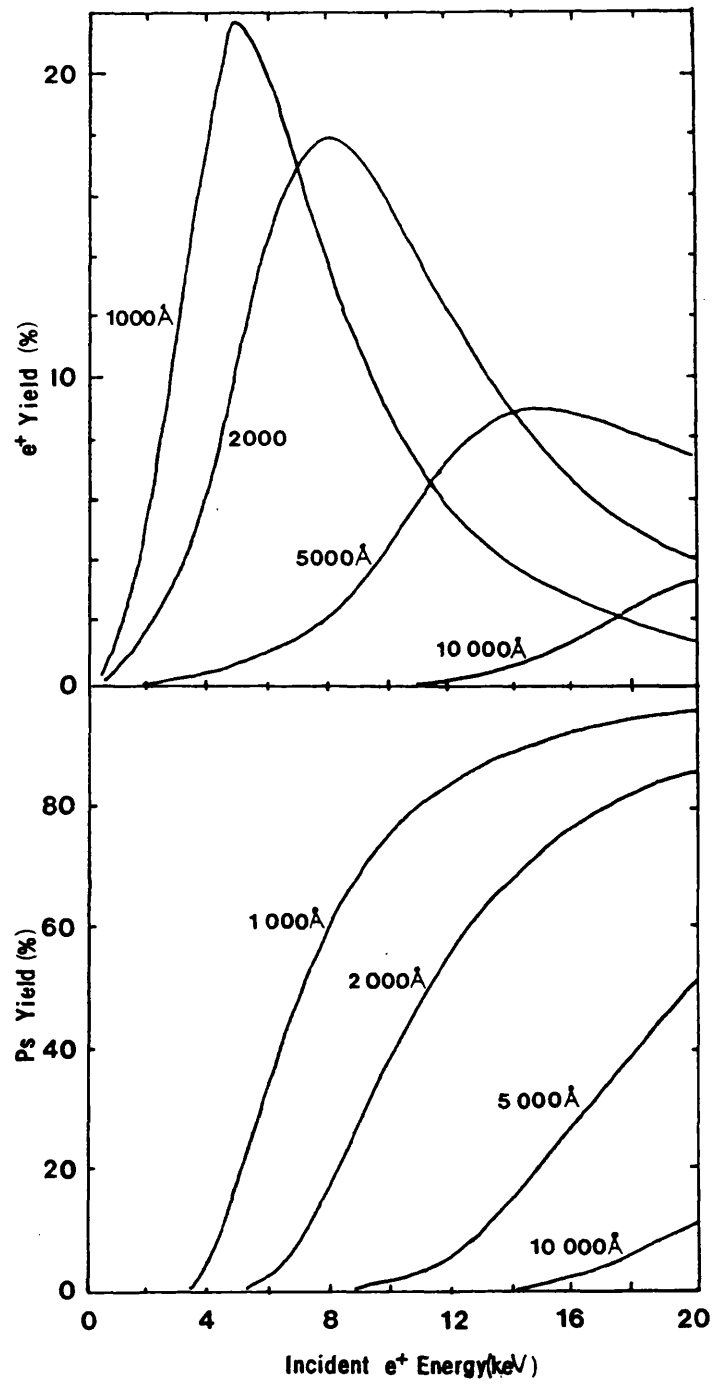


Figure A1.1 Calculated slow e⁺ yields and fast e⁺ transmission probabilities for Cu foils

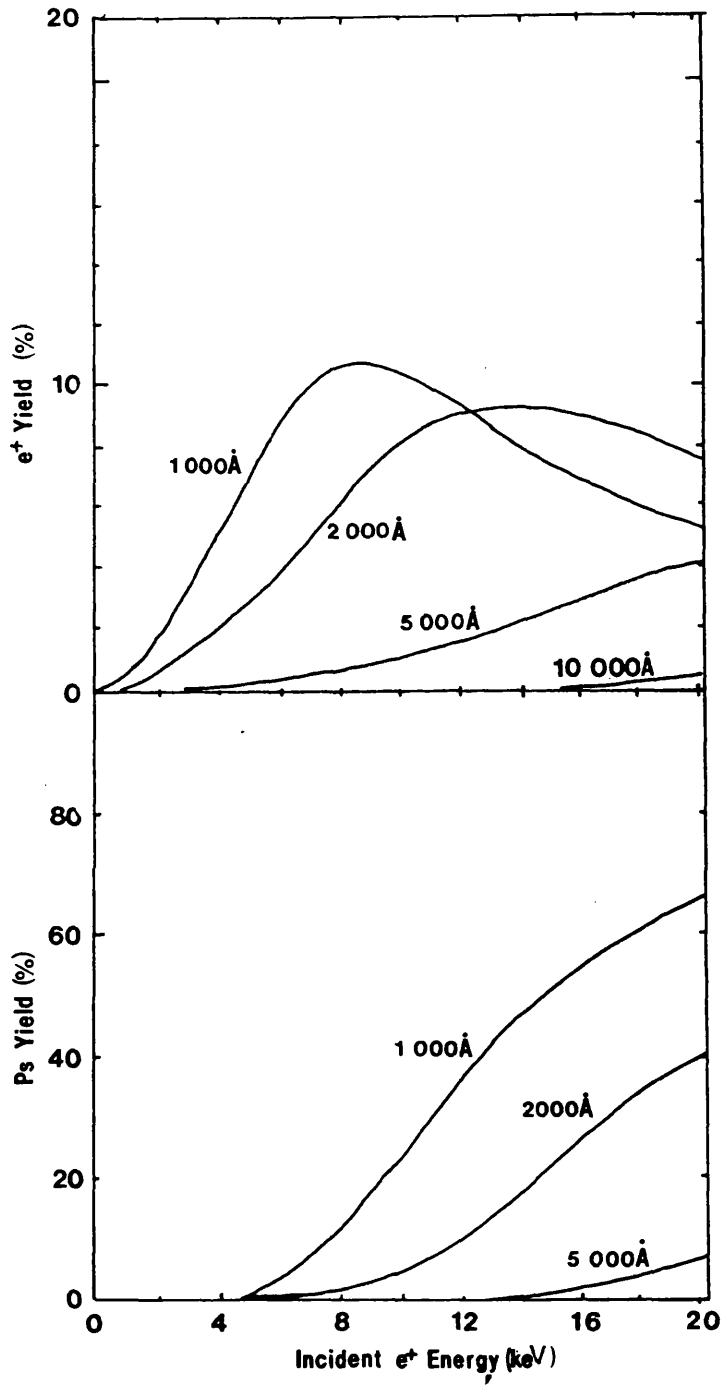


Figure A1.2

Calculated slow e⁺ yields and fast e⁺ transmission probabilities for W foils.

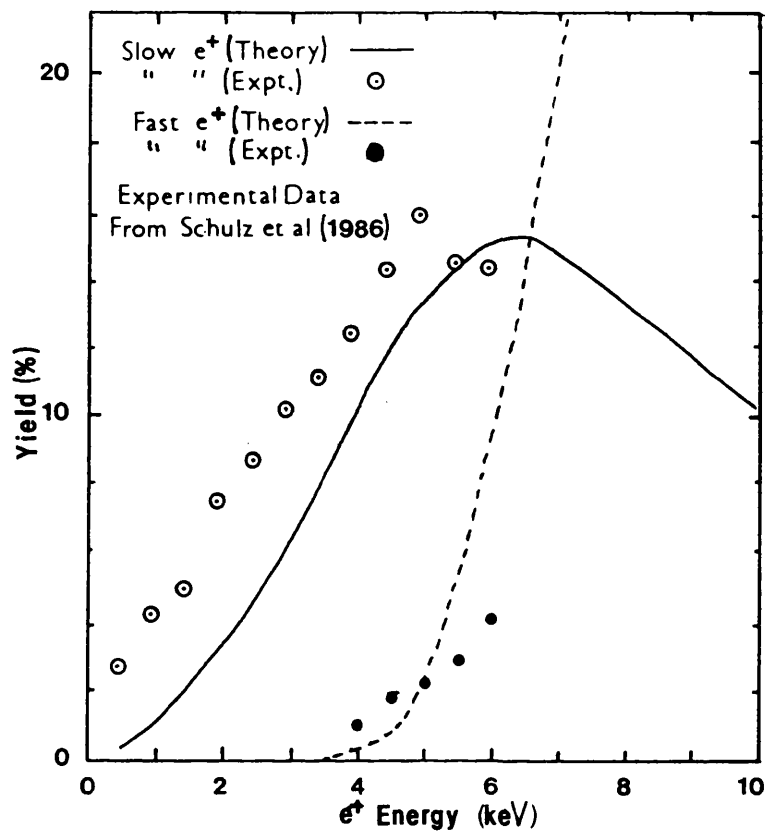


Figure A1.3 Comparison of theoretical and experimental e^+ moderation efficiencies for a 1500\AA Ni(100) foil.

TABLE A1.1

Parameters Used in Transmission Remoderator Efficiency Calculations

Foil	n	m	A μgcm^{-2}	y_0	L_+ \AA	ρ gcm^{-3}
Cu(111)	1.6	1.7	4	.55	1100	8.9
W(110)	1.53	1.2	4	.33	1350	19.3
Ni(100)	1.6	1.9	4	.45	1100	8.9

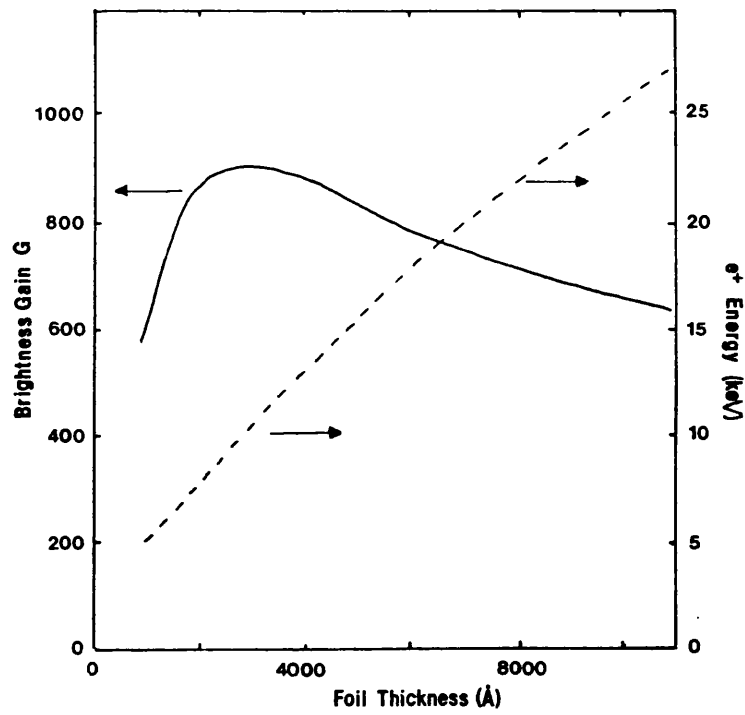


Figure A1.4 Brightness gain, G , and optimum primary beam energy as functions of foil thickness for Ni(100)

The brightness per volt, R , of an e^+ beam with intensity I , energy, E diameter, D and angular divergence, θ , is given by (see Section 1.4.4)

$$R = \frac{I}{D^2 \sin^2 \theta E} \quad \text{A1:5}$$

The important parameter in determining the quality of the remoderated beam is the brightness gain, G . Making the assumption of constancy of angular spread, θ , at the moderator and remoderator surfaces, Vehanen and Mäkinen (1985) give the expression

$$G = \epsilon \left(\frac{D_m}{D_r} \right)^2 = \epsilon \frac{E}{|\phi_+|} \quad \text{A1:6}$$

where ϵ is the remoderation efficiency, D_m and D_r , the primary and remoderator diameters respectively, E the primary beam energy, and ϕ_+ , the e^+ work function of the moderators. Figure A1.4 shows the maximum brightness gain, G , for Ni(100) as a function of foil thickness, d . G is seen to be fairly insensitive to changes in d , despite a substantial decrease in ϵ over the range calculated. This is a result of an increase in optimum primary beam energy with increasing, d . The brightness per volt could be further improved by employing additional remoderator stages.

REFERENCES

- Allen, F.G., Buck, T.M. and Law, J.T., 1960, *J. Appl. Phys* **31**, 979.
- Allen, F.G., Eisinger, J., Hagstrum, H.D. and Law, J.T., 1959, *Appl. Phys.* **30**, 1563.
- Allen, F.G. and Gobeli, G.W., 1962, *Phys. Rev.* **127** 150.
- Anderson, C.D., 1932, *Phys. Rev.* **41**, 405.
- Awcock, M.L. and Young, D.C, 1963, UK AERE Report R4710.
- Baker, J.A. and Coleman, P.G., 1988, *J. Phys. C* **21**, L875.
- Ball, J.E., MacKenzie, I.K. and Stone, R.J., 1989, in Dorikens-Vanpraet *et al*, eds., pp857-859.
- Beling, C.D., Simpson, R.I., Charlton, M., Jacobsen, F.M., Griffith, T.C., Moriarty, P. and Fung, S., 1987a, *Appl. Phys.* **A42**, 111.
- Beling, C.D., Simpson, R.I., Stewart, M.G., Wang, Y.Y, Fung, S., Wai, J.C.H. and Sun, T.N. 1987b, *phys. stat. sol.* **102**, 537.
- Beling, C.D., Simpson, R.I. and Charlton, M., 1987c in Humberston, J.W. and Armour, E.A.G., pp175-183.
- Bergersen, B., Pajanne, E., Kubica, P., Stott, M.J. and Hodges, C.H., 1974, *Solid State Comm.* **15**, 1377.
- Berko, S., 1983, in Brandt and Paulin, eds., pp64-143.
- Berko, S. and Erskine, 1967, *Phys. Rev. Lett.* **19**, 307
- Berko, S. and Hereford, F.L., 1956, *Rev. Mod. Phys.* **28**, 299.
- Berko, S. and Mader, J., 1975, *J. Appl. Phys.* **5**, 287.
- Berko, S. and Pendleton, H.N., 1980, *Ann. Rev. Nucl. Part. Sci.* **30** 543.
- Bethge, H., Pippel, E. and Woltersdorf, J., 1976, *phys. stat. sol. (a)***37**, 457.
- Bisi, A., Gambarini, G. and Zappa, L., 1981, *Lett. Nuovo Cimento* **31**, 58.
- Blackett, P.M.S. and Occhialini, G.P.S., 1933, *Proc. Roy. Soc.* **A139**, 699.

- Boas, M.L., 1966, *Mathematical Methods in the Physical Sciences*, (Wiley, New York), p335.
- Boev, O.V., Puska, M.J. and Nieminen, R.M., 1987, *Phys. Rev.* B36, 7786.
- Brandes, G.R., Canter, K.F., Horsky, T.N., Lippel, P.H. and Mills, A.P., Jr., 1988a, *Rev. Sci. Instrm. Meth.* 59, 228.
- Brandes, G.R., Canter, K.F., Horsky, T.N. and Mills, A.P., Jr., 1988b, *Appl. Phys.* A46, 335.
- Brandt, W., 1982, *Lett. Nuovo Cimento* 33, 499.
- Brandt, W. and Dupasquier, A., eds., 1983, *International School of Physics 'Enrico Fermi' (1981: Varenna, Italy). Positron Solid State Physics (Proceedings of the International School of Physics 'Enrico Fermi'; course 83)*, (North Holland, Amsterdam).
- Brandt, W. and Paulin, R., 1972, *Phys. Rev.* B5, 2430.
- Brandt, W. and Paulin, R., 1977, *Phys. Rev.* B15, 2511.
- Brandt, W. and Reinheimer, J., 1970, *Phys. Rev.* B2, 3104.
- Brandt, W. and Reinheimer, J., 1971, *Phys. Lett.* A35, 109.
- Britton, D.T., Huttenen, P.A., Mäkinen, J., Soininen, E. and Vehanen, A., 1989, *Phys. Rev. Lett.* 62, 2413.
- Brorson, S.D., DiMaria, D.J., Fischetti, M.V., Pesavento, F.L., Solomon, P.M. and Dong, D.W., 1985, *J. Appl. Phys.* 58, 1302.
- Brown, A.P., Jensen, K.O. and Walker, A.B., 1989, in Dorikens-Vanpraet *et al*, eds., pp332-4.
- Brown, A.P., Walker, A.B. and West, R.N., 1987, *J. Phys.* F17, 2491.
- Canter, K.F., Brandes, G.R., Horsky, T.N., Lippel, P.H. and Mills, A.P. Jr., 1987, in Humberston and Armour pp153-60.
- Canter, K.F., Brandes, G.R., Horsky, T.N., Lippel, P.H. and Mills, A.P. Jr., 1989, in Dorikens-Vanpraet *et al*, eds., pp18-27.
- Canter, K.F., Coleman, P.G., Griffith, T.C. and Heyland, G.R., 1972, *J. Phys.* B5, L167.

- Canter, K.F., G.R., Horsky, T.N., Lippel, P.H., Crane, W.S. and Mills, A.P. Jr., 1986, in *Positron (Electron) Gas Scattering*, Kaupilla, W.E., Stein, T.S. and Wadehra, J.M., eds., (World Scientific, Singapore), p202.
- Canter, K.F., Mills, A.P., Jr., and Berko, S., 1974, *Phys. Rev. Lett.* **33**, 7.
- Carbotte, J.P. and Arora, H.L., 1967, *Can. J. Phys.* **45** 387.
- Charlton, M., 1985, *Rep. Prog. Phys.* **48**, 737.
- Charlton, M. and Jacobsen, F.M., 1987, *Appl. Phys.* **A43**, 235.
- Chen, D.M., 1987, PhD dissertation, (City College New York, unpublished).
- Chen, D.M., Berko, S., Canter, K.F., Lynn, K.G., Mills, A.P., Jr., Roellig, L.O., Sferlazzo, P., Weinert, M. and West, R.N., 1987, *Phys. Rev. Lett.* **58**, 921.
- Chen, D.M., Lynn, K.G., Pareja, R. and Nielsen, B., 1985, *Phys. Rev.* **B31**, 4123.
- Chen, Y-C., Lynn, K.G. and Nielsen, B., 1987, *Phys. Rev.* **B37**, 3105.
- Cherry, W., 1958, PhD dissertation (Princeton University, unpublished).
- Chung, Y.W., Siekhaus, W. and Somarjai, 1976, *Surf. Sci.* **58**, 341.
- Coleman, P.G., Sharma, S.C., and Diana, L.M., eds., 1982, *Positron Annihilation*, (North Holland, Amsterdam).
- Corbel, C., Hautojärvi, P., Mäkinen, J., Vehanen, A. and Mathiot, D., 1989, *J. Phys.* **C1**, 6315.
- Costello, D.G., Groce, D.E., Herring, D.F. and McGowan, J.W., 1972a, *Can. J. Phys.* **50**, 23.
- Costello, D.G., Groce, D.E., Herring, D.F. and McGowan, J.W., 1972b, *Phys. Rev.* **B5**, 1433.
- * Dannefaer, S., Mascher, P. and Kerr, D., 1989, in Dorikens-Vanpraet *et al*, eds., p714.
- Davisson, C.J. and Germer, C.H., 1927, *Phys. Rev.* **30**, 705.
- DeBenedetti, S. and Corben, H.C., 1954, *Ann. Rev. Nucl. Sci.* **4**, 191.
- DeBenedetti, S., Cowan, C.E., Konneker, W.R. and Primakoff, H., 1950, *Phys. Rev.* **77**, 205.
- Debowska, M., Ewertowski, R. and Swiatkowski, W., 1985, *Appl. Phys.* **A36**, 47
- * Curry, S.M. and Schawlow, A.L., 1971, *Phys. Lett.* **37A**, 5.

- Deutch, B.I., Jacobsen, F.M., Andersen, L.H., Hvelplund, P., Knudsen, K., Holzscheiter, M.H., Charlton, M. and Laricchia, G., 1988, *Physica Scripta* T22, 248.
- Deutsch, M., 1951, *Phys. Rev.* **82**, 455, **83**, 866.
- De Vries, J., 1987, PhD dissertation, (University of Delft, Netherlands, unpublished).
- De Vries, J. and Kelling, F.E.T., 1987, *Nucl. Instrm. and Meth.* A262, 385.
- De Vries, J. and Kelling, F.E.T., 1988, *IEEE Trans. on Nucl. Sci.* **35**, 392.
- De Vries, J., Schippers, J.M. and Lourens, W., 1985, *Nucl. Instrm. Meth.* A238, 182.
- De Vries, J., Zecca, A., Brusa, R.S., Grisenti, R.G., Oss, S. and van Veen, A., 1989 in Dorikens-Vanpraet *et al*, eds., pp654-6.
- DeWald, A.B., Frost, R.L., Ringel, S.A., Schaffer, J.P., Rohatgi, A., Nielsen, B. and Lynn, K.G., 1988, *J. Vac. Sci. Technol.* A6, 2248.
- Dirac, P.A.M., 1930a, *Proc. Roy. Soc.* A126, 360.
- Dirac, P.A.M., 1930b, *Proc. Camb. Phil. Soc.* **26**, 361.
- Dorikens-Vanpraet, Dorikens, M. and Segers, D., eds., 1989, *Positron Annihilation: Proceedings of the 8th International Conference on Positron Annihilation, Gent 1988*, (World Scientific, Singapore).
- Dupasquier, A., 1983, in Brandt, W. and Dupasquier, A, pp510-564.
- Dupasquier, A. and Quartapelle, L., 1987, *Appl. Phys.* A44, 239.
- Dupasquier, A. and Zecca, A., 1985, *Rivista de Nuovo Cimento* **8**, p1-.
- Eldrup, M., MacKenzie, I.K., McKee, B.T.A. and Segers, D., 1989 in Dorikens-Vanpraet *et al*, eds., pp216-226.
- Eldrup, M., Vehanen, A., Schultz, P.J. and Lynn, K.G., 1985, *Phys. Rev.* B32, 7048.
- Evans, R.D., 1955, *The Atomic Nucleus*, (McGraw-Hill, New York), p628.
- Fieschi, R., Gainotti, A., Ghezzi, C. and Manfredi, M., 1968, *Phys. Rev.* **175**, 383.
- Fischer, D.A., Lynn, K.G. and Frieze, W.E., 1983, *Phys. Rev. Lett.* **50**, 1149.
- Fischer, D.A., Lynn, K.G. and Gidley, D.W., 1986, *Phys. Rev.* B33, 4479.
- Gainotti, A., and Ghezzi, C., 1970, *Phys. Rev. Lett.* **24**, 349.
- Gainotti, A., and Ghezzi, C., 1972, *J. Phys. C*, **5** 779.

- Gidley, D.W., Köymen, A. and Capehart, T.W., 1982, *Phys. Rev. Lett.* **49**, 1779.
- Gol'danski, V.I., Novikov, Y.A., Rakov, A.V. and Shantarovich, V.P., 1988, *JETP Lett.* **47**, 610.
- Gramsch, E., Throwe, J. and Lynn, K.G., 1987, *Appl. Phys. Lett.* **51**, 1862.
- Green, A.K., Dancy, J. and Bauer, E., 1969, *J. Vac. Sci. Tech* **7**, 1.
- Green, J. and Lee, J., 1964, *Positronium Chemistry* (Academic Press, New York).
- Griffith, T.C., 1986, *Adv. in At. and Mol. Phys.* **22**, 37
- Griffith, T.C. and Heyland, G.R., 1978, *Phys. Rep.* **39C**, 169.
- Griffith, T.C., Heyland, G.R., Lines, K.S. and Twomey, T.R., 1978, *Phys. Lett.* **A69**, 1969.
- Gryzynski, M., 1965, *Phys. Rev.* **A138**, 305, 322, 336.
- Gullikson, E.M. and Mills A.P., Jr., 1986, *Phys. Rev. Lett.* **57**, 376.
- Gullikson, E.M., Mills A.P., Jr. and Brown, B.L., 1985, *Phys. Rev.* **B12**, 5484
- Gullikson, E.M. and Mills A.P., Jr. and Murray, C.A., 1988a, *Phys. Rev.* **B38**, 1705.
- Gullikson, E.M. and Mills A.P., Jr. and Phillips, J.M., 1988b, *Surf. Sci.* **195**, L150.
- Hautojärvi, P., ed., 1979, *Positrons in Solids: Topics in Current Physics*, **12**, (Springer, Berlin).
- Heinrich, F., 1978, *Helv. Phys. Acta* **51**, 433.
- Heinrich, F. and Schiltz, A., 1982, in Coleman, P.G., Sharma, S.C. and Diana, L.
- Hodges, C.H., 1970, *Phys. Rev. Lett.* **25**, 284.
- Hodges, C.H. and Stott, M.J., 1973, *Solid State Comm.* **12**, 1153.
- Howell, R.H., 1987, in Humberston and Armour, pp215-222.
- Howell, R.H., Fluss, M.J., Rosenberg, I.J. and Mayer, P., 1985b, *Nucl. Instrm. Meth.* **B10**, 373.
- Howell, R.H., Mayer, P., Rosenberg, I.J. and Fluss, M.J., 1985a, *Phys. Rev. Lett.* **54**, 1698.
- Howell, R.H., Rosenberg, I.J. and Fluss, M.J., 1986, *Phys. Rev.* **B34**, 3069.
- Hulett, L.D., Jr., Dale, J.M. and Pendyala, S., 1984, *Mat, Sci, Forum* **2**, 133.

- Humberston, J.W., 1979, *Adv. in At. and Mol. Phys.* **15**, 101.
- Humberston, J.W. and Armour, E.A.G., eds., 1987, *Atomic Physics with Positrons (Nato ASI series. Series B, Physics, Vol 169)*, (Plenum, New York).
- Huomo, H., Vehanen, A., Bentzon, M.D. and Hautojärvi, P., 1987, *Phys. Rev.* **B35** 8252.
- Hyodo, T. and Stewart, A.T., 1984, *Phys. Rev.* **B29**, 4164.
- Jackman, T.E., 1974, MSc dissertation (University of Guelph, unpublished) (see MacKenzie, 1983).
- Jacobini, C. and Reggiani, L., 1979, *Adv. in Phys.* **28**, 493.
- Jacobsen, F.M., 1986, *Chem. Phys.* **101**, 259.
- Jacobsen, F.M., Charlton, M., Chevallier, J., Deutch, B.I., Laricchia, G. and Poulsen, M., 1990, to be published in *Appl. Phys.*
- Jorch, H.H., Lynn, K.G. and McMullen, T., 1984, *Phys. Rev.* **B30**, 93.
- Kahn, A., 1983, *Surf. Sci. Rep.* **3**, 193.
- Killeen, T.L., 1975, PhD dissertation (University of London, unpublished).
- Kirkegaard, P., Eldrup, M., Mogensen, O.E. and Pedersen, N.J., 1981, *Comp. Phys. Comm.* **23**, 307.
- Kirkegaard, P., Pedersen, N.J. and Eldrup, M., 1989, in Dorikens-Vanpraet *et al*, eds., pp642-644.
- Klimesch, P. and Henzler, M., 1979, *Surf. Sci* **90**, 57.
- Knop, G. and Paul, W., 1966, in *Alpha, Beta and Gamma Ray Spectroscopy*, Siegbahn, K., ed., (North-Holland, Amsterdam) **1**, p1.
- Kubica, P. and Stewart, A.T., 1975, *Phys. Rev. Lett.* **34**, 852.
- Kuzminikh, V.A. and Vorobiev, S.A., 1979, *Nucl. Instrm. Meth.* **167**, 483.
- Lang, G. and DeBenedetti, S., 1957, *Phys. Rev.* **108**, 914.
- Laricchia, G., Charlton, M., Davies, S.A., Beling, C.D. and Griffith, T.C., 1987, *J. Phys.* **B20**, L99.
- Laval, M., Moszynski, M., Allemand, R., Cormoreche, Guinet, P., Odru, R. and Vacher, J., 1982, *Nucl. Instrm. and Meth.* **206**, 169.

- Linderoth, S., Hansen, H.E., Nielsen, B. and Petersen, K., 1984, *Appl. Phys.* **A33**, 25.
- Logan, L.R., Schultz, P.J., Davies, J.A. and Jackman, T.E., 1988 *Nucl. Instrm Meth.* **B33**, 58.
- Lou Yongming, Gu Binglin, Zhu Jialin, Lee Chang, Xiong Jiajiong and Johansson, B., 1989, in Dorikens-Vanpraet *et al*, eds., pp335-7.
- Lynn, K.G., 1979, *Phys. Rev. Lett.* **43**, 391.
- Lynn, K.G., 1982, in Brandt, W. and Dupasquier, A., pp609-643.
- Lynn, K.G., Chen, D.M., Nielsen, B., Pareza, R. and Myers, S., 1986, *Phys. Rev.* **B34**, 1449.
- Lynn, K.G. and Dickman, J.E., 1978, *Bull. Am. Phys. Soc.* **23**, 427.
- Lynn, K.G. and Frieze, W.E., 1984, in *Positron Scattering in Gases (Nato ASI series. Series B, Physics vol. 107)*, Humberston, J.W. and McDowell, M.R.C., eds., (Plenum, New York) pp165-180.
- Lynn, K.G. and Lutz, H., 1980, *Phys. Rev.* **B22**, 4143.
- Lynn, K.G., McKay, T., and Nielsen, B., 1987, *Phys. Rev.* **B36**, 7107.
- Lynn, K.G. and McKee, B.T.A., 1979, *Appl. Phys.* **19**, 247.
- Lynn, K.G., Mills, A.P., Jr., West, R.N., Berko, S., Canter, K.F. and Roellig, L.O., 1985, *Phys. Rev. Lett.* **54**, 1702.
- Lynn, K.G. and Nielsen, B., 1987, *Phys. Rev. Lett* **58**, 81.
- Lynn, K.G. and Nielsen, B. and Quateman, 1985, *Appl. Phys Lett.* **47**, 239.
- Lynn, K.G., Weber, M., Roellig, L.O., Mills, A.P., Jr., and Moodenbaugh, 1987, in Humberston and Armour, eds., pp161-174.
- MacKenzie, I.K., 1983, in Brandt and Dupasquier, pp196-264.
- Mackenzie, I.K. and Campbell, 1972, *Nucl. Instrm. Meth.* **101**, 149.
- Mackenzie, I.K. and Ghorayshi, P.Z., 1985, *Solid State Comm.* **55**, 125.
- MacKenzie, I.K., Khoo, T.L., McDonald, A.B. and McKee, B.T.A., 1967, *Phys. Rev. Lett.* **19**, 946.
- Mackenzie, I.K., Shulte, C.W., Jackman, T. and Campbell, J.L, 1973, *Phys. Rev.* **A7**, 135

- Madansky, L. and Rasetti, F., 1950, Phys. Rev. **79**, 397.
- Madey, J.M.J., 1969, Phys. Rev. Lett. **22**, 784.
- Makhov, A.F., 1960a,b,c, Sov. Phys. Solid State **2**, 1934, 1942, 1945.
- Many, A., Goldstein, Y. and Grover, N.B., 1971, *Semiconductor Surfaces*, (North Holland, Amsterdam).
- Marder, S., Hughes, V.W., Wu, C.S. and Bennett, W., 1956, Phys. Rev. **103**, 1258.
- McGervey, J.D., Welsch, G., Kögel, G. and Schödlbauer, D., 1989, in Dorikens-Vanpraet *et al*, eds., pp425-427.
- Mills, A.P. Jr., 1978, Phys. Rev. Lett. **41**, 1828.
- Mills, A.P. Jr., 1979a, Solid State Comm. **31**, 623.
- Mills, A.P. Jr., 1979b, Appl. Phys. Lett. **35**, 427.
- Mills, A.P. Jr., 1980, Appl. Phys. **23**, 189.
- Mills, A.P. Jr. and Crane, W.S, 1984, Phys. Rev. Lett. **53**, 2165.
- Mills, A.P. Jr. and Crane, W.S, 1985, Phys. Rev. **B31**, 3988.
- Mills, A.P. Jr. and Gullikson, E.M., 1986, Appl. Phys. Lett. **49**, 1121.
- Mills, A.P. Jr. and Gullikson, E.M., Pfeiffer, L. and Rockward, W.S., 1986, Phys. Rev. **B33**, 7799.
- Mills, A.P. Jr. and Murray, C.A., 1980a, Appl. Phys. **21**, 323.
- Mills, A.P. Jr. and Murray, C.A., 1980b, Bull. Am. Phys. Soc. **25**, 392.
- Mills, A.P. Jr. and Pfeiffer, L., 1976, Phys. Rev. Lett. **36**, 1389.
- Mills, A.P. Jr. and Pfeiffer, L., 1977, Phys. Lett. **63A**, 118.
- Mills, A.P. Jr. and Pfeiffer, L., 1979a, Phys. Rev. Lett. **43**, 1961.
- Mills, A.P. Jr. and Pfeiffer, L., 1979b, Phys. Lett. **69A**, 471.
- Mills, A.P. Jr. and Pfeiffer, L. and Platzman, P.M., 1983, Phys. Rev. Lett. **51**, 1085.
- Mills, A.P. Jr. and Platzman, P.M., 1980, Solid State Comm. **35**, 321.
- Mills, A.P. Jr., Platzman, P.M. and Brown B.L., 1978, Phys Rev. Lett. **41**, 1076.
- Mills, A.P. Jr. and Wilson R.J., 1982, Phys. Rev. **A26**, 490.
- Mogensen, O.E., 1974, J. Chem. Phys. **60**, 998.

- Mogensen, O.E., 1983, Phys. Lett. **96A**, 250.
- Mohorovicic, S., 1934, Astron. Nachr. **253**, 94.
- Moszynski, M. and Bengtson, 1979, Nucl. Instrm. Meth. **158**, 1.
- Mourino, M. and Brandt, W., 1979, Bull. Am. Phys. Soc. **24**, 72
- Mourino, M., Löbl, H. and Paulin, R., 1979, Phys. Lett. **71A**, 106.
- * Murray, C.A. and Mills, A. P., Jr., 1980, Solid State Comm. **34**, 789.
- Murray, C.A., Mills, A. P., Jr. and Rowe, J.E., 1980, Surf. Sci **100**, 647.
- Musket, McLean, W., Colmenares, C.A., Makowiecki, D.M. and Siekhaus, W.J., 1982, Appl. Surf. Sci **10**, 143.
- Nielsen, B., Lynn, K.G., Vehanen, A. and Schultz, P.J., 1985, Phys. Rev **B32**, 2296.
- Nielsen, B., Lynn, K.G. and Chen, Y-C., 1986, Phys. Rev. Lett. **57**, 1789.
- Nielsen, B., Lynn, K.G., Chen, Y-C. and Welch, D.O., 1987, Appl. Phys. Lett. **51**, 1022.
- Nieminen, R.M. and Oliva, J., 1980, Phys. Rev. **B22**, 2226.
- Ore, A., 1949, Univ. i Bergen Arbok Natuvidensabelig Rekke, **9**.
- Ore, A. and Powel, J.L., 1949, Phys. Rev. **75**, 1696.
- Park, R.L., and Farnsworth, H.E., 1964, J. Appl. Phys. **35**, 2220.
- Paulin, R., Ripon, R. and Brandt, W, 1973, Phys. Rev. Lett. **31**, 1214.
- Pendry, J.B., 1980, J.Phys. **C13**, 1159.
- Pendyala, S., Bartell, D., Girouard, F.E. and McGowan, J.W., 1976 Can. J. Phys. **54**, 1527.
- Platzman, P.M. and Tzoar, 1986, Phys. Rev. **B33**, 5900.
- Plotkowski, K., Panek, T.J. and Kansy, J., 1988, Il Nuovo Cimento **10**, 933.
- Poth, H., 1987, in Humberston and Armour pp307-319.
- Puska, M.J. and Manninen, M., 1987, J. Phys. **F17**, 2235.
- Rich, A., Conti, R., Frieze, W., Gidley, D.W., Griffin, H., Skalsey, M., Steiger, T., Van House, J., Zheng, W. and Zitzewitz, P.W., 1987, in Humberston and Armour, eds., pp321-332.
- Rich, A. and Van House, J., 1988, J. Elec. Micros. Tech. **9**, 209.
- * Murarka, S.P., 1983, "Silicides for VLSI Applications", (Academic Press, Orlando)

- Rosenberg, I.J., Weiss, A.H. and Canter, K.F., 1980, Phys. Rev. Lett. **44**, 1139.
- Schrader, D.M., Loewenschuss, A., Jean, J.Y., Nakamoto, K. and Pollard, B.P., 1982, in Coleman, P.G., Sharma, S.C., and Diana, L.M., eds., p657.
- Schultz, P.J., 1988, Nucl. Instrm. Meth. **B30**, 94.
- Schultz, P.J., Gullikson, E.M. and Mills, A.P., Jr., 1986, Phys. Rev. **B34**, 442.
- Schultz, P.J., Jackman, T.E., Jorch, H.H. and Lynn, K.G., 1983, unpublished (see Schultz and Lynn, 1988).
- Schultz, P.J. and Lynn, K.G., 1982, Phys. Rev. **B26**, 2390.
- Schultz, P.J. and Lynn, K.G., 1988, Rev. Mod. Phys. **60**, 701.
- Schultz, P.J., Lynn, K.G., Frieze, W.E. and Vehanen, A., 1983, Phys. Rev. **B27**, 6626.
- Schultz, P.J. and Lynn, K.G. and Nielsen, B., 1985, Phys. Rev. **B32**, 1369.
- Schultz, P.J., Tandberg, E., Lynn, K.G., Nielsen, B., Jackman, T.E., Denhoff, M.W. and Aers, G.C., 1988, Phys. Rev. Lett. **61**, 187.
- Schödlbauer, D., Kögel, G., Sperr, P. and Triftshäuser, W., 1987, phys. stat. sol. **a102**, 549.
- Sferlazzo, P., 1985, Appl. Phys. **A36**, 93.
- Sferlazzo, P., Berko, S. and Canter, K.F., 1985, Phys. Rev. **B32**, 6067.
- Shearer, J.W. and Deutsch, M., 1949, Phys. Rev. **76**, 462.
- Shirai, Y. and Takamura, J., 1987, Mater. Sci. Forum **15**, 1.
- Shockley, W., 1951, Bell Syst. Tech. J. **30**, 990.
- Shulman, M.A., Beardsley, G.M. and Berko, S., 1975, Appl. Phys. **5**, 367.
- * Smith, A.W., 1970, J. Coll. and Int. Sci. **34**, 101.
- Stein, T.S., Kaupilla, W.E., Pol, V., Smart, J.H. and Jeison, G., 1978, Phys. Rev. **A17**, 1600.
- Stein, T.S., Kaupilla, W.E. and Roellig, L.O., 1974, Rev. Sci. Inst. **45**, 951.
- Stein, T.S., Kaupilla, W.E. and Roellig, L.O., 1975, Phys. Lett. **51A**, 327.
- Stone, R.J., MacKenzie, I.K. and Ball, J.E., 1989, in Dorikens-Vanpraet *et al*, eds., pp854-856.
- * Simpson, R.I., Stewart, M.G., Belling, C.D. and Charlton, M., 1989, J. Phys. C: Con. Mat. **1**, 101.

- Sueoka, O. and Koide, S., 1976, *J.Phys. Soc. Jpn.* **41**, 116.
- Sze, S.M., 1981, 2nd edition, *Physics of Semiconductor Devices*, (Wiley, New York).
- Teixeira Dias, J.P., Jesus, J., Lopes Gil, C., de Lima, A.P., 1989, in Dorikens-Vanpraet *et al*, eds., pp629-631.
- Tong, B. Y., 1972, *Phys. Rev.* **B5**, 1436.
- Tung, R.T., Poate, J.M., Bean, J.C., Gibson, J.M. and Jacobson, D.C., 1982, *Thin Solid Films* **93**, 77.
- Valkealahti, S. and Nieminen, R.M., 1983, *Appl. Phys.* **A32**, 95.
- Valkealahti, S. and Nieminen, R.M., 1984, *Appl. Phys.* **A35**, 51.
- Van House, J. and Zitzewitz, P.W., 1984, *Phys. Rev.* **A29**, 96.
- Van Loenen, E.J., Fischer, A.E.M.J., Van der Veen, J.F. and Legoues, F., 1985, *Surf. Sci* **154**, 52.
- Vehanen, A., Lynn, K.G., Schultz, P.J., Cartier, E., Guntherodt, H-J. and Parkin, D.M., 1984, *Phys. Rev.* **B29**, 2371.
- Vehanen, A., Lynn, K.G., Schultz, P.J. and Eldrup, M, 1983, *Appl. Phys.* **A32**, 163.
- Vehanen, A. and Mäkinen, J., 1985, *Appl. Phys.* **A36**, 97.
- Wagner, L.F. and Spicer, W.E., 1972, *Phys. Rev. Lett.* **28**, 1381.
- Wagner, L.F. and Spicer, W.E., 1974, *Phys. Rev.* **B9**, 1512.
- Weber, M., Tang, S., Berko, S., Brown, B.L., Canter, K.F., Lynn, K.G., Mills, A.P., Jr., Roellig, L.O. and Viescas, A.J., 1989, in Dorikens-Vanpraet *et al*, eds., pp28-30.
- Weiss, A.R., Mayer, R., Jibaly, M., Lei, C., Mehl, D. and Lynn, K.G., 1989, to be published.
- West, R.N., 1973, *Adv. Phys.* **22**, 263.
- Westbrook, C.I., Gidley, D.W., Conti, R.S. and Rich, A., 1987, *Phys. Rev. Lett.* **58**, 1328.
- Weyl, H., 1934, 2nd edition, *Gruppentheorie und Quantenmechanick*, p234.
- Wheeler, J.A., 1946, *Ann N.Y. Acad. Sci.* **48**, 219.
- Wilson, R.J., 1983, *Phys. Rev.* **B27**, 6974.
- Yang, C.N., 1950, *Phys. Rev.* **77**, 242.

Yu, M.L. and Lang, N.D., 1983, *Phys. Rev. Lett.* **50**, 127

Zafar, N. Chevallier, J., Jacobsen, F.M., Charlton, M. and Laricchia, G., 1988, *Appl. Phys.* **A47**, 409.

Zafar, N. Chevallier, J., Laricchia, G. and Charlton, M., 1989, *J. Phys.* **D22** 868.

Zangwill, A., 1988, *Physics at Surfaces*, (Cambridge University Press, Cambridge).